Trapped Ultracold Atoms with Tunable Interactions

by

Javier von Stecher

B.A., Universidad de Buenos Aires, 2002

A thesis submitted to the

Faculty of the Graduate School of the

University of Colorado in partial fulfillment

of the requirements for the degree of

Doctor of Philosophy

Department of Physics

2008

This thesis entitled:
Trapped Ultracold Atoms with Tunable Interactions
written by Javier von Stecher
has been approved for the Department of Physics

Chris H. Greene

Murray J. Holland

Date 07/07/2008

The final copy of this thesis has been examined by the signatories, and we find that both the content and the form meet acceptable presentation standards of scholarly work in the above mentioned discipline.

von Stecher, Javier (Ph.D., Physics)

Trapped Ultracold Atoms with Tunable Interactions

Thesis directed by Prof. Chris H. Greene

In this dissertation, we analyze both many- and few-body systems under external confinement with tunable interactions. First, we develop a density-renormalization approach for describing two-component fermionic systems with short-range interactions. This renormalized zero-range interaction eliminates the instabilities produced by a bare Fermi pseudopotential and provides a simple description of the interactions from the weakly interacting BCS region up to unitarity.

In the second part of the thesis, we focus on few-body systems in the BCS-BEC crossover. To obtain the solutions, we implement two different numerical techniques: a correlated-Gaussian-basis-set expansion and a fixed-node diffusion Monte Carlo technique. We also develop an innovative numerical technique for obtaining solutions to the four-body problem in the hyperspherical representation.

Our solutions provide an accurate description of few-body trapped systems. The analysis of two-, three-, and four-body systems, for instance, provides a few-body perspective on the BCS-BEC crossover problem. The analysis of the spectrum of such systems allows us to visualize important pathways for molecule formation. We then use the four-body solutions to extract key properties of the system such as the dimer-dimer scattering length and the effective range.

We also explore the qualitative change of behavior in the BCS-BEC crossover by analyzing the spectrum and structural properties. We investigate the dynamics of these few-body systems and analyze them using a Landau-Zener model. At unitarity, we study the universal properties of few-body systems and verify the absence of many-body bound states up to N=6.

Finally, we present preliminary results on the four-boson system. We analyze the structure of the spectrum and find a family of four-body states attached to the three-body thresholds. These four-body states follow the universal scaling properties of the Efimov states. We explore the collisional implications of these four-body states and find relations between the atom-dimer and dimer-dimer collisional properties. In particular, we predict that these four-body states will produce resonances in the dimer-dimer scattering length.

Para Leila y Faustino.

Acknowledgements

First, I want to thank Chris Greene, for his perseverance and confidence in this project. I especially want to acknowledge his patience with me at the beginning of my research, when it seemed fruitless. During my research with him, I always felt I could only absorb just a small fraction of his comprehensive knowledge of atomic physics. His passion for physics combined with his rigorous research methodology make him an inspirational figure for my work. Most importantly, I will always be grateful to Chris for constantly putting my career above all other things.

During my first years of research in Chris Greene group, I was lucky to share the office with Josh Dunn and Stefano Tonzani. They were the most helpful colleagues a person could wish for. They were reliable sources of knowledge when I was taking my first steps in computer programming. I appreciate their generous team spirit and the way in which they welcomed me to the group.

I also want to thank the various collaborators who made this work possible. Seth Rittenhouse and Jose D'Incao were always very generous in sharing their knowledge of few-body physics and hyperspherical methods. I especially want to thank Doerte Blume. I had the pleasure of collaborating with her during her visit to JILA in 2007. Not only did she teach me a lot about Monte Carlo techniques and ultracold gases in general, but she also showed me how to be more effective in my research. She was always critical (in a positive way) of my research, and that helped me grow as a physicist.

I want to thank Julie Phillips for her careful and patient editing of this disserta-

tion.

I thank my parents, brothers, and sister for their constant support and company. Finally, and foremost, I want to thank my wife, Leila, for generously understanding my passion for my work and for living every moment of my career as if it were hers. None of this would have been possible without her wise advice and love.

I would like to thank the National Science Foundation for funding my research as a graduate student.

Contents

Chapter

Tables

Table

Figures

Figure

Chapter 1

Introduction

Superconductivity is a striking phenomenon discovered in 1911 by Heike Kamerlingh Onnes [132]. Superconducting materials at very low temperatures are characterized by zero electrical resistance and the expulsion of the magnetic field from their interior. Since the discovery of superconductivity, important efforts have been devoted to the theoretical understanding the of mechanism that leads to it. It took more than 40 years until physicists arrived at a solid understanding of this mechanism. During the 1950s, condensed matter physicists developed the phenomenological Ginzburg-Landau theory [112] and the microscopic Bardeen-Cooper-Schrieffer (BCS) theory [10]. These theories form the basis of our current theoretical understanding of superconductivity and superfluidity. Superfluids are neutral gases with analogous properties to superconductors, i.e., superfluids are irrotational gases with zero viscosity.

The BCS theory in particular was a great triumph since it was able to explain the microscopic quantum mechanical mechanism that leads to superconductivity. BCS theory views superconductivity as a macroscopic quantum mechanical effect in which the interacting particles feel an effective attraction that leads them to form pairs. These pairs, usually called Cooper pairs [47], would not bind in free space. They are bound by the influence of the medium, and their binding energy depends on the density of the system. This binding energy produces a gap in the single-particle excitation spectrum that is the key for the understanding of many superconducting properties.

An interesting question arises if we consider what would happen if the attraction in the superconducting or superfluid system is changed. If the attraction increases the interacting particles could be bound, possibly even in free space, and the system would evolve into a system of diatomic molecules. This scenario was first considered by Eagles [59] and Leggett [113] who realized that the BCS theory could be extended to any interaction strength; furthermore, it would predict a smooth transition between the system of particles and the system of molecules. These seminal studies were followed by Nozieres and Schmitt-Rink [129] and Sá de Melo, Randeria, and Engelbrecht [155] who also considered temperature effects on these systems.

This transition from an atomic to a molecular system entails a qualitative change in the system. The constituent particles of the superconducting system described by BCS theory are fermions. However, when two fermions are bound, they form a bosonic molecule. An ultracold system of bosons is described by Bose-Einstein condensation (BEC). Therefore, the transition between interacting particles described by BCS theory and the system of molecular bosons described by the BEC theory is usually called the BCS-BEC crossover. Fermions and bosons are characterized by completely different statistical behaviors. Therefore, the BCS-BEC crossover describes the transition between two different statistical regimes. For that reason, the BCS-BEC crossover problem is theoretically both very appealing and very challenging.

For starters, there are no condensed-matter or nuclear systems in nature that allow the experimental study of the BCS-BEC crossover. An ideal system that would allow the experimental realization of the BCS-BEC crossover should be cold enough to reach quantum degeneracy and have interactions that can be externally controlled.

The experimental achievements of BEC [5, 30, 50] and Fermi degeneracy [53, 177] in ultracold gases opened the door to the analysis of superfluidity in a controllable manner. In particular, Fermi gases with weak attractive interactions should be described by BCS theory and exhibit superfluidity. Since fermions of the same component repel

each other because of Pauli repulsion, it is necessary to create and cool a two-component Fermi gas to achieve attractive interactions, as it was done in Ref. [53].

In these first experiments, the interactions between fermions were not strong enough to attain superfluidity. It was necessary to find a way to change the interactions of the system. It was soon realized that interactions in cold atoms could be experimentally tuned using Fano-Feshbach resonances [69, 70, 74]. In the vicinity of a Fano-Feshbach resonance, the scattering length, i.e., the parameter that characterizes the interaction strength, depends strongly on external magnetic field. Therefore, by making small changes in the external magnetic field, we can widely tune the interaction and even change its sign. Fano-Feshbach resonances were first utilized to tune the interactions in a bosonic gas [96, 48], but strongly interacting regimes were also soon obtained in fermionic systems using a Fano-Feshbach resonance [130, 24].

After all this experimental progress, the condensation of atom pairs in a two-component Fermi gas was observed. The first observations were in the BEC region [82, 99, 194, 25], where the pairs formed real molecules. Next, pairs were also condensed in the BCS region [144, 195]. After these encouraging results, experimentalist tried to verify the superfluid nature of the system. Measurement of collective excitations [12, 104] and the pairing gap [44] were consistent with the superfluidity ansatz. However, those predictions can also be attributed to a normal state. The experimental verification of superfluidity in a Fermi gas in the BCS-BEC crossover directly probed the irrotational nature of the fluid by rotating the system and observing quantized vortices [193].

In another remarkable experimental accomplishment, cold atoms were loaded in optical lattices [81], i.e., strong periodic potentials. These optical lattices provide new ways to control the system such as changing the distance between the minima of the periodic potential (usually called the lattice sites), or changing the dimensionality of the system, or controlling the number of atoms in each lattice site. Most experiments focussed on the experimental realization of the Hubbard Hamiltonian [81]. However,

optical lattices were also used to measure properties of a two-body trapped system [168].

The theoretical exploration of the BCS-BEC crossover has also significantly increased in the last few years. In contrast with dilute bosonic systems, for which the Gross-Pitaevskii equation provides a highly successful many-body theory, fermionic systems in the BCS-BEC crossover lack a comprehensive many-body theory. Therefore, it has been necessary to resort to numerical or approximate methods. For instance, an extension of the BCS theory proposed by Eagles [59] and Leggett [113] is only qualitatively correct and has been consistently used as a starting point for most sophisticated analytical models. One of the most reliable descriptions of this system was obtained through Monte-Carlo techniques [36, 7]. The Monte-Carlo results are generally used to test theories or models as well as experimental results. In addition, there is an impressive amount of theoretical work on the BCS-BEC crossover problem that cannot be covered in this introduction; however this work will be partially explored in this dissertation.

Our approach to the BCS-BEC crossover problem is unique, since it tries to avoid conventional many-body approaches and focusses on the few-body physics. In contrast with many-body theories, which usually focus only on the ground state and have to rely on approximations, few-body calculations can describe the complete spectrum without resorting to approximations. From a few-body perspective, the solution of the four-fermion problem represents the next big challenge -a challenge we partially meet in this dissertation. Although the three-body problem might be considered as largely "solved" by existing numerical techniques, only specific and limited solutions to the four-body system exist. Furthermore, the four-body problem is the smallest system that can describe most of the physics of the BCS-BEC crossover, from a gas of attractive fermions to a system of two interacting bound boson pairs. Here, we present such a solution.

However, we do not limit ourselves to the four-body system. We extend our calculations to smaller and larger systems, in the process providing a comprehensive

analysis of few-body trapped systems. Our results are organized this thesis as follows:

Chapter 2 presents the theoretical elements that are particularly relevant to this dissertation. The basic elements of ultracold scattering theory are introduced. The concept of a zero-range pseudopotential is discussed and applied to the description of two particles in a trap. A brief description of BCS theory is presented. Finally, the hyperspherical representation is presented.

Chapter 3 develops three different numerical techniques used throughout this dissertation. Quantum Monte Carlo techniques are described at the beginning of the chapter. Special attention is devoted to the qualitative understanding of the method and the proper selection of trial wave functions that describe fermionic systems in the BCS-BEC crossover. Then, the correlated Gaussian (CG) method is discussed. The general ideas and implementation of the CG method are presented here and many of the details are included in a set of Appendices. Finally, the implementation of the correlated-Gaussian hyperspherical (CGHS) method is presented. This method combines the ideas of the standard CG method with the hyperspherical method. This method was developed near the end of my thesis research and the results have not yet been published.

Chapter 4 presents our initial attempts to describe two-component Fermi gases in the BCS region. Analysis of the perturbative regime in an open-shell system is described. Then, a density renormalization technique is presented. Finally, different mean-field methods – namely Thomas-Fermi, variational-trial wavefunction, and Hartree-Fock with bare and renormalized interactions – are used to analyze the behavior of trapped Fermi gases. The work presented in this chapter has been published in Refs. [148, 149, 183].

Chapter 5 analyzes the topology of the spectrum and dynamics of few-body trapped systems ($N \leq 4$). The spectrum of these few-body systems is analyzed throughout the BCS-BEC crossover region. Then, the dynamics of these systems are probed by tuning the scattering length throughout the BCS-BEC crossover region. The numerical results are analyzed with the Landau-Zener theory and compared with experimental

results. The results for the four-body system presented here have been published in Ref. [182], and the rest of the results remain unpublished.

Chapter 6 analyzes more quantitatively the spectrum of few-body trapped systems. The CG results are compared with Quantum Monte Carlo predictions. From these calculations, the dimer-dimer scattering length and effective range are obtained. Finally, structural properties in the BCS-BEC crossover are analyzed. The studies presented here have been published in Refs. [184, 185].

Chapter 7 focusses on the properties of trapped fermionic systems at unitarity. The theoretical predictions of the properties at unitarity are reviewed. These properties are verified using different numerical methods. The numerical calculations are extended to larger trapped systems using Quantum Monte Carlo methods, and the results are analyzed using a local density approximation. The excitation gap and the universal parameter β is extracted. This work has been published in Refs. [19, 185].

Finally, in the last chapter, Chapter 8, we shift gears and present preliminary results on the four-boson system. We analyze the spectrum as a function of the scattering length. Then we consider the collisional aspects of the four-boson system: dimer-dimer collisions and atom-trimer collisions. This work was performed in collaboration with J. P. D'Incao and Chris H. Greene and has not been published yet.

Chapter 2

Theoretical introduction

2.1 Introduction

In this chapter, we review important theoretical elements used in this dissertation. First, we review important aspects of ultracold collisions, the definition of scattering length, and the selection of the appropriate interaction potential for numerical calculations. Second, we analyze the solution of two particles in a trap interacting through a zero-range pseudopotential. This solution represents an ideal case because of its simplicity and the way in which scattering-length dependence is introduced. We will use the two-particle solution extensively throughout the thesis.

Third, we present mean-field BCS theory in Sec. 2.4. The BCS theory is the standard theory for describing the BCS-BEC crossover from a many-body viewpoint. For that reason, it is important to consider it here and review its strengths and limitations. Finally, we introduce the hyperspherical framework. The hyperspherical framework becomes very useful once some intuition is built around it. A simple analysis of hyperspherical potential curves usually provides a qualitative understanding of the system. Also, an exact solution can be obtained by solving coupled differential equations involving the hyperspherical potential curves. In additions, properties of strongly interacting trapped system can be easily understood from the hyperspherical perspective. The hypersherical representation will be used throughout this dissertation.

2.2 The interaction potential

In this section, we analyze the collisional properties of ultracold gases with s-wave interactions. We focus on the single-channel model that is used throughout this thesis.

2.2.1 Scattering properties of ultracold gases

The scattering properties of ultracold alkali atoms can be understood considering the simple case of two particles interacting with a central potential $V(r)$. Since the relative coordinate Schrödinger equation has spherical symmetry, the wave function can be written as

$$\psi_k(\mathbf{r}) = \frac{u_k(r)}{r} Y_{lm}(\Omega). \tag{2.1}$$

Here, k is the momentum of the collision, and $Y_{lm}(\Omega)$ are the well-known spherical harmonics. Using Eq. 2.1, the radial Schrödinger equation that describes the collision takes the form

$$\left[-\frac{\hbar^2}{2\mu} \frac{d^2}{dr^2} + V_{eff}(r) - \frac{\hbar^2 k^2}{2\mu} \right] u_k(r) = 0, \tag{2.2}$$

where μ is the reduced mass, and energy of this collision is $E = k^2/2\mu$. The two particles feel an l-dependent effective potential,

$$V_{eff}(r) = V(r) + \frac{\hbar^2 l(l+1)}{2\mu r^2}, \tag{2.3}$$

where l is the relative angular momentum between the particles. The second term in Eq. (2.3) is called the centrifugal barrier.

For each angular momentum l there is a scattering solution to Eq. (2.2), and all these solutions contribute to the scattering observables. However, at ultracold temperatures only the $l = 0$ contribution is important. We can neglect higher angular momentum solutions because the centrifugal barrier introduces an effective repulsion between the particles. The centrifugal barrier controls particle interaction at large distances is controlled if the long-range behavior of the bare interaction $V(r)$ decays faster

than $1/r^2$. At low energies (ultracold temperatures), particles colliding with $l > 0$ do not feel the interaction of the bare potential $V(r)$ because they cannot overcome the centrifugal barrier. Therefore, particles colliding with $l > 0$ can be considered noninteracting, reducing significantly the complexity of the problem.

The ultracold collisional properties of the two-body system are characterized by the long-range behavior of the radial-scattering solutions. The asymptotic solutions of the radial equation take form

$$u_k(r)_{r\to\infty} \approx \frac{A(k)}{k} \sin[k\, r + \delta(k)], \tag{2.4}$$

where $\delta(k)$ is the phase shift that characterizes all the two-body scattering properties. For example, the scattering cross section for two distinguishable particles is given by

$$\sigma(k) = \frac{4\pi}{k^2} \sin^2[\delta(k)]. \tag{2.5}$$

Therefore, it is important to understand the behavior of the phase shift in the ultracold limit.

The phase shift is characterized by the interaction potential. For alkali atoms, the long-range behavior of the interaction between is generally described by a van der Waals force of the form $V_6(r) = -C_6/r^6$. This r^{-6} long-range behavior decays fast enough that it can be treated as a "short-range" potential. Short-range potentials have nice scattering properties at low energy. In particular, the s-wave scattering phase shift $\delta(k)$ depends linearly in the collision momentum k as it goes to zero. This property allows us to define the s-wave scattering length as

$$a_s = -\lim_{k\to 0} \frac{\tan[\delta(k)]}{k}. \tag{2.6}$$

All the scattering properties reduce to a simple expression involving the s-wave scattering length a_s, in the ultracold limit. For example, the scattering cross section [Eq. (2.5)] for two distinguishable particles in the ultracold limit reduces to $\sigma(0) = 4\pi a_s^2$, which is exactly the classical prediction of the cross section for hard spheres with radius a_s.

Since all scattering properties depend only on a_s, the shape of the real potential of the interacting alkali atoms is irrelevant for describing ultracold scattering. Furthermore, different potentials with the same scattering length will then have identical scattering properties. Consequently, the behavior of dilute ultracold atoms can be considered to be universal. Such universal behavior give us some flexibility in selecting a potential to simplify the numerical calculations. In general, we use a potential of the form $V(r) = V_0 v(r)$. Here, $v(r)$ is a purely attractive potential of a simple form like a Gaussian or a square well, and V_0 is the potential depth that can be tuned to the desired scattering-length value a_s. The potential $v(r)$ has a range r_0, and its ultracold scattering properties will behave universally if $a_s \gg r_0$.

There is also a simple interpretation of the scattering length in terms of the zero-energy wave function $u_0(r)$. In the zero-energy limit, the long range behavior of u_0 is

$$u_0^A(r)_{r\to\infty} \approx u_0^A(r) = A(0)(r - a_s). \tag{2.7}$$

Therefore, the asymptotic behavior of $u_0(r)$, called $u_0^A(r)$, is a straight line that crosses zero at $r = a_s$. Figure 2.1 provides a qualitative understanding of the scattering length by analyzing the zero-energy wave function. In Figs. 2.1 (a) and (b), the red curves are the potential $V_0(r)$, which is a Gaussian interaction potential in this case. The black curves are the zero-energy solutions $u_0(r)$, and the dashed blue lines are the extrapolated asymptotic behavior $u_0^A(r)$. Figure 2.1 (c) presents the behavior of the scattering length as a function of the potential depth V_0.

Another important quantity for the qualitative understanding of the scattering length is the phase accumulated in the interacting region. This accumulated phase is related to the "curvature" of $u_0(r)$ in that region. For a shallow potential depth, the phase accumulated is very small since the potential is not strong enough to produce important changes. Therefore, this potential produces a small curvature in $u_0(r)$ leading

to a negative scattering length [see Fig. 2.1 (a)]. In contrast, for larger values of V_0, the accumulated phase is large enough that $u_0(r)$ turns around in the interacting region and has node at $r = a_s$, a positive scattering length. Therefore, there is a critical accumulated phase, associated with a critical potential depth at which the scattering length changes from positive to negative. That critical accumulated phase is $\pi/2$ and occurs when the curvature of $u_0(r)$ is just enough to produce asymptotic behavior parallel to the coordinate r. In this particular case, the scattering length diverges, as shown by the dashed vertical line in Fig. 2.1 (c).

The divergence of the scattering length is also associated with the existence of a bound state right at the zero-energy threshold. Therefore, for deeper potentials, i.e., positive scattering lengths, the potential holds a weakly bound state. The properties of this weakly bound state only depend on a_s as long as $a_s \gg r_0$. For example, this weakly bound state has a binding energy of $E_b = 1/(2\mu a_s^2)$ [schematically shown in Fig. 2.1 (c)] and a size of $\sim a_s/2$.

However, realistic potentials differ significantly from the model potential presented above. A complete description of ultracold two-body collisions usually requires the analysis of a multichannel system where the hyperfine splitting is incorporated. In experiments with ultracold gases, the scattering length a_s is tuned using Fano-Feshbach resonances. A description of Fano-Feshbach resonances requires at least a two-channel model. The incoming collision occurs in the lower channel while the upper channel is closed. The resonance occurs at the energy at which the uncoupled closed channel has a bound state. For ultracold systems, the collision energy is very close to threshold. Therefore, Fano-Feshbach resonances occur when a bound state of the uncoupled closed channel coincides with the open channel threshold. As in the single channel case, the bound state at threshold produces divergence of the scattering length. For positive scattering lengths, the bound state is below threshold. This state is analogous to the weakly bound state of the one-channel model, i.e., its properties are only characterized

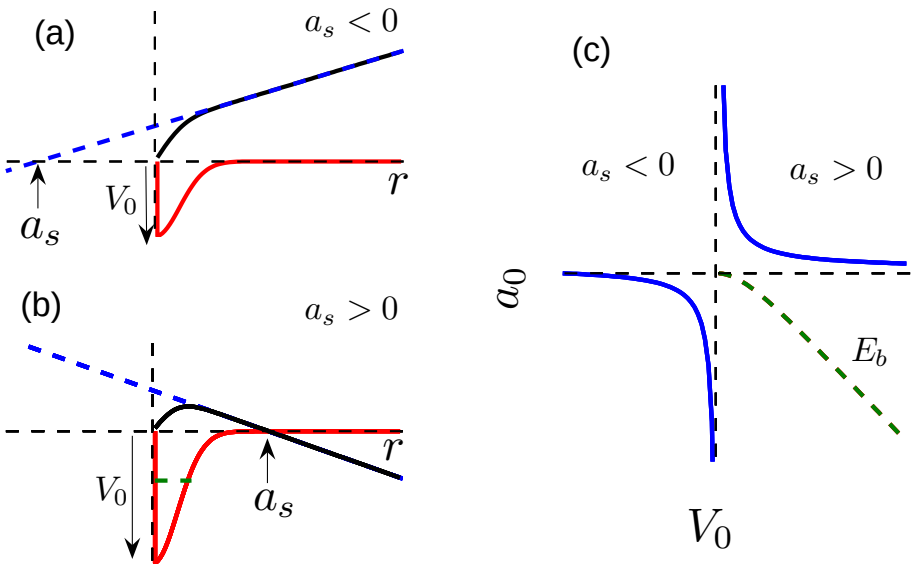

Figure 2.1: Behavior of the scattering length and the zero-energy wave function as functions of the potential depth. In panels (a) and (b), the red curve corresponds to the potential interaction. The black curve is the zero-energy $u_0(r)$, and the dashed blue line represents the extrapolated long range behavior of $u_0(r)$ [Eq. 2.4].(c) Schematic behavior of the scattering length as a function of the potential depth. The solid blue line is the scattering length, and the dashed green line is the binding energy of the weakly bound dimer.

by the scattering length.

Realistic multichannel calculations are important for predicting the interaction properties of a particular pair of alkali atoms (see e.g. [106]), i.e., the scattering-length dependence on the magnetic field, the position of resonances, the regions of universality, etc. Once a large scattering-length region has been theoretically or experimentally identified for a particular pair of alkali atoms, we can use a simple single-channel potential to model the interaction. Furthermore, we can even use a zero-range pseudopotential that explicitly introduces the scattering length dependence. The description of the zero-range pseudopotential is described in the next subsection.

2.2.2 Zero-range interactions

From the analysis of ultracold collisions with large scattering lengths presented above, we can understand the zero-range pseudopotential used to mimic the interaction. This pseudopotential is valid in the universal regime. The universal regime is achieved in a dilute system [1] when $r_0 \ll a_s$. Since this range is very small and does not enter in the theory, we can replace the realistic potential with a zero-range pseudopotential. By introducing pseudopotentials that only depend on the scattering length, we make explicit the universal behavior of the interaction.

To obtain the pseudopotential, we consider the scattering wave function solution. In the limit of $r_0 \to 0$, the asymptotic behavior of the scattering solution, Eq. (2.7), is valid for all r values. In particular, consider a many-particle system. When two particles get very close together while other particles remain far apart, then the behavior of the many-body wave function is controlled by the scattering of the two particles given by Eq. (2.7). This reasoning leads to the Bethe-Peierls contact condition [15],

$$\lim_{r_{ij}\to 0} \Psi(\mathbf{r}_1, ..., \mathbf{r}_i, ..., \mathbf{r}_j, ...) \propto \frac{u_0^A(r_{ij})}{r_{ij}} = C\left(\frac{1}{r_{ij}} - \frac{1}{a_s}\right). \tag{2.8}$$

[1] Dilute system refers in this case to the condition $r_0 \ll r_{mean}$, where r_{mean} is the mean interparticle distance.

Here, r_{ij} is the distance between particles i and j, and C is a smooth function of the remaining coordinates. The boundary condition of Eq. (2.8) can be achieved through a zero-range pseudopotential of the form [95]

$$v(\mathbf{r}) = \frac{2\pi\hbar^2 a_s}{\mu}\delta(\mathbf{r})\frac{\partial}{\partial r}r. \tag{2.9}$$

This pseudopotential, or contact condition, tries to reproduce the long-range behavior of the scattering solution. To some extent, it represents an ideal interaction that has the minimum ingredients for describing an ultracold system.

In the next section, we apply the zero-range pseudopotential to the system of two trapped particles.

2.3 Spectrum of two particles in a trap

A system of two particles in a trap with tunable interactions provides a qualitative understanding of trap few-body systems and is a useful tool for describing more complicated systems.

Consider the system of two particles in an harmonic trap with masses m_1 and m_2 interacting in the s-wave channel. Both particles experience a trapping potential characterized by the same frequency. Thus, when we select the appropriate center of mass and relative vectors, i.e., $\mathbf{R}_{CM} = (m_1\mathbf{r}_1 + m_2\mathbf{r}_2)/M$ and $\mathbf{r} = \mathbf{r}_1 - \mathbf{r}_2$, the center-of-mass motion decouples from the system and is characterized by a reduced mass $\mu = m_1 m_2/M$.

We also assume that the interaction potential $V(r)$ is spherically symmetric and short range. When the range of the interaction is much smaller than the two-body scattering length a_s and the characteristic trap length ($a_{ho} = \sqrt{\hbar/2\mu\omega}$) that controls the mean interparticle distance, then the interaction can be replaced by a zero-range pseudopotential from Eq. (2.9).

The center-of-mass motion is described by a one-particle noninteracting system

of mass $M = m_1 + m_2$, and the energies are $E_{CM} = (2n + l + 3/2)\hbar\omega$, where n and l are radial and angular quantum numbers. The relative motion also has a spherical symmetry that allows us to consider each relative angular momentum l_{rel} separately. However, we are only interested in $l_{rel} = 0$ solutions since the pseudopotential [Eq. (2.9)] was designed to describe s-wave collisions. The remaining $l_{rel} > 0$ solutions can be considered noninteracting.

Taking advantage of the spherical symmetry, we write the relative wave function as

$$\Psi(\mathbf{r}) = \frac{1}{\sqrt{4\pi}} \frac{u(r)}{r}. \tag{2.10}$$

The radial Schrödinger equation for $l_{rel} = 0$ collisions is given by

$$\left(-\frac{\hbar^2}{2\mu} \frac{d^2}{dr^2} + \frac{1}{2}\mu\omega^2 r^2 + v(r) \right) u(r) = E_r u(r). \tag{2.11}$$

There are different techniques for solving Eq. (2.11). In the method outlined in Ref. [35], the zero-range interaction is interpreted as a boundary condition given by

$$\frac{u'(0)}{u(0)} = -\frac{1}{a_s}. \tag{2.12}$$

Therefore, the system can be described by a noninteracting Hamiltonian, and all the interaction effects are introduced as the boundary condition given by Eq. (2.12). The radial wave function $u(r)$ can be then expanded in solutions of the noninteracting system, i.e., harmonic-trapped solutions. Using properties of the Laguerre polynomials that describe the harmonic trapped solutions, the imposed boundary condition, Eq. (2.12), leads to a transcendental equation that relates the energies with the scattering length:

$$\sqrt{2} \frac{\Gamma\left(-\frac{E_r}{2\hbar\omega} + \frac{3}{4}\right)}{\Gamma\left(-\frac{E_r}{2\hbar\omega} + \frac{1}{4}\right)} = \frac{a_{ho}}{a}. \tag{2.13}$$

Here, Γ is the gamma function. Note that the energies only depend on the ratio a_0/a_{ho}. Figure 2.2 presents the spectrum predicted in Eq. (2.13) as a function of a_{ho}/a_s. Interestingly, we observe smooth behavior in the strongly interacting regime $[-1 \lesssim a_{ho}/a_s \lesssim 1]$.

In the positive scattering length, we observe the molecule formation described by the lowest energy curve. The appearance of the molecule affects all the higher states connecting the n vibrational trapped state at $a_s \sim 0^-$ [left extreme of Fig. 2.2] to the $n-1$ vibrational trapped state at $a_s \sim 0^+$ [right extreme of Fig. 2.2].

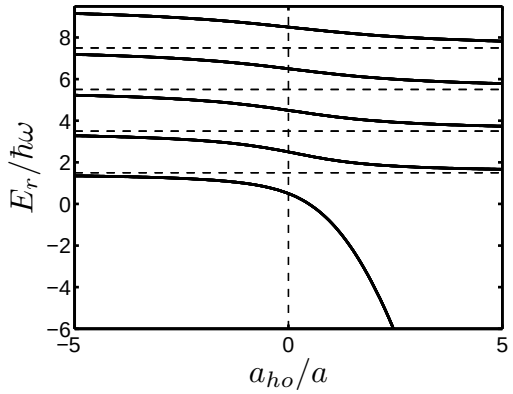

Figure 2.2: Spectrum of the relative motion of two particles in a trap as a function of the inverse scattering length a_{ho}/a_s.

It is interesting to analyze the limiting behaviors of the lowest energy of the system. In the small and negative scattering length limit, the lowest energy is

$$E_0/\hbar\omega = 3 + \sqrt{\frac{2}{\pi}}\frac{a_s}{a_{ho}} + \frac{2-2\ln(2)}{\pi}\left(\frac{a_s}{a_{ho}}\right)^2 + \dots \,. \tag{2.14}$$

The first term is the noninteracting energy with the center-of-mass contribution included. The second term can be obtained using the Fermi pseudopotential and is associated with a mean-field effect.

In the small and positive scattering-length region, the ground-state energy is

$$E_0/\hbar\omega = -\left(\frac{a_{ho}}{a_s}\right)^2 + 3/2 - \frac{7}{8}\left(\frac{a_s}{a_{ho}}\right)^2. \tag{2.15}$$

The first term is the molecule-binding energy, $-\hbar\omega a_{ho}^2/a_s^2 = -\hbar^2/ma^2$, and the second is the zero-point energy of the molecule.

After analyzing the energies, we now consider the wavefunction. The zero-range pseudopotential approximation also allow us to obtain analytical expressions for the

wave functions, e.g.,

$$\Psi(\mathbf{r}) = A \exp\left(-\frac{r^2}{4a_{ho}^2}\right) U\left(-\frac{E_r}{2\hbar\omega} + \frac{3}{4}, \frac{3}{2}, \frac{r^2}{2a_{ho}^2}\right). \tag{2.16}$$

Here, U is the confluent hypergeometric function, and A is a normalization constant. A series expansion of Eq. (2.16) around $r \approx 0$ shows that the wave function obeys the Bethe-Peierls boundary condition where

$$\Psi(\mathbf{r}) \approx \frac{A}{\sqrt{2}\pi a_{ho}^{3/2}} \left(\frac{a_{ho}}{r} - \sqrt{2}\frac{\Gamma\left(-\frac{E_r}{2\hbar\omega} + \frac{3}{4}\right)}{\Gamma\left(-\frac{E_r}{2\hbar\omega} + \frac{1}{4}\right)}\right) + \mathcal{O}(r) = \frac{A}{\sqrt{2}\pi a_{ho}^{3/2}} \left(\frac{a_{ho}}{r} - \frac{a_{ho}}{a_s}\right) + \mathcal{O}(r). \tag{2.17}$$

Note that we have used Eq. (2.13) to obtain the scattering-length dependence in Eq. (2.17).

A second method for obtaining solutions of the two-particle trapped system is based on quantum defect theory techniques [17]. Since the potential $v(r)$ is only nonzero at the origin, the solution $u(r)$ of Eq. (2.11) should be a linear combination of the regular and irregular solutions of the noninteracting system. This linear combination at a given energy is chosen so that the logarithmic derivative boundary condition, i.e., Eq.(2.12), is obeyed. This procedure leads to a transcendental equation equivalent to Eq. (2.13) and provides an interesting new insight into the problem.

2.4 BCS theory

In 1956, Cooper found that two opposite-spin fermions immersed in a Fermi sea with arbitrarily weak attractive interactions would form a bound pair [47]. The large degeneracy of states in the Fermi surface allows such formation. This idea was extended to many fermion pairs by Bardeen, Cooper, and Schieffer when they developed what is now known as the BCS theory [10, 11]. An important prediction of the BCS theory was the existence of an energy gap (pairing gap) in the single particle excitation spectrum. Cooper pairs and the pairing gap are key ingredients in our modern understanding of superconductivity and superfluidity.

A particularly interesting problem arises when interactions in fermionic systems can be tuned. In such cases, we can access the BCS-BEC crossover. Eagles [59] and Leggett [113] were the first to realize that BCS theory is capable of qualitatively describing both limiting behaviors and predicting an smooth transition between them. Here, we outline the main results relevant to this dissertation.

To arrive at the BCS equations we assume that the wave function takes the form [113] of

$$\Psi(\mathbf{r_1}, ..., \mathbf{r_N}) = \mathcal{A}\{\psi(r_{1,1'}), \psi(r_{2,2'}), ..., \psi(r_{N/2,N'/2}). \tag{2.18}$$

Next, we consider a system of distinguishable fermions for which the spin part factors out, and unprimed and primed indices refer to spin-up and spin-down particles, respectively. To obtain the BCS equations, we apply a variational approach using an extension of Eq. (2.18) where the pair wave function ψ is the variational parameter [113]. The extended version of Eq. (2.18) does not correspond to definite number of particles, and the minimization process constrains the wave function to a mean number of particles. Alternatively, the BCS equation can be obtained by solving the effective BCS Hamiltonian using a Bogoliubov transformation. Both methods lead to the same set of coupled equations. The first equation is usually called the gap equation and relates the gap Δ and the interaction strength (in this case characterized by the two-body scattering length a_s):

$$\frac{m}{4\pi\hbar^2 a_s} = \int \frac{d\mathbf{k}}{(2\pi)^3} \left(\frac{1}{2\epsilon_k} - \frac{1}{2E_k} \right). \tag{2.19}$$

Here, we define $\epsilon_k = \hbar^2 k^2/2m$ and $E_k = \sqrt{\Delta^2 + (\epsilon_k - \mu)^2}$, where μ is the chemical potential. Note that a momentum renormalization has been carried out to obtain Eq. (2.19). The second equation describes the one-component density ρ_1 as

$$\rho_1 = \frac{1}{2} \int \frac{d\mathbf{k}}{(2\pi)^3} \left(1 - \frac{\epsilon_k - \mu}{E_k} \right). \tag{2.20}$$

The density is written in general as $\rho_1 = k_F^3/(6\pi^2)$, and the system is then characterized by a single dimensionless parameter $k_F a_s$. In Eqs. (2.19) and (2.20), the gap Δ and the

chemical potential μ are obtained by fixing the scattering length a_s and the density μ. These coupled equations can be solved analytically [123], but the general solution is not particularly enlightening. Here, we solve these equations numerically.

Several observables can be obtained once Δ and μ are known. In particular, we are interested in the energy of the system, which is given by

$$E_0 = \int \frac{d\mathbf{k}}{(2\pi)^3} \left(\epsilon_k \left(1 - \frac{\epsilon_k - \mu}{E_k} \right) - \frac{\Delta^2}{2E_k} \right). \tag{2.21}$$

The first term describes the kinetic contribution, and the second describes corrections due to the interactions. The behavior of the energy in the BCS-BEC crossover can be easily obtained numerically. The numerical results of E_0 are presented in Fig. 4.11. Furthermore, the limiting behaviors of the energy and the first-order corrections can be obtained analytically. For $|k_F a_s| \ll 1$ and $a_s < 0$, i.e., in the weakly interacting BCS limit, the energy is

$$E_0/N = \frac{3}{5} E_F \left(1 + \frac{40}{e^4} e^{\pi/k_F a_s} \right). \tag{2.22}$$

Here, the first term corresponds to the noninteracting energy where $E_F = k_F^2/2m$. The second term is the first-order correction, which is exponentially small in $k_F a_s$. In chapter 4 , we will see that the Hartree term, neglected in this approximation, predicts a first-order correction linear in $k_F a_s$. Thus, the Hartree term is the leading correction in the weakly interacting BCS regime.

In contrast, in the weakly interacting molecular BEC limit, i.e., for $|k_F a_s| \ll 1$ and $a_s > 0$, the energy is

$$E_0/N = -\frac{\hbar^2}{2ma^2} + \frac{3}{5} E_F \left(\frac{5 k_F a}{9\pi} + ... \right). \tag{2.23}$$

The first term is half the binding energy of the weakly bound molecules. The second term describes a repulsive interaction between molecules with a dimer-dimer scattering length of $a_{dd} = 2a_s$. More accurate calculations, like the ones presented in Chapter 6 , show that the interaction is indeed repulsive, but the dimer-dimer scattering length is

$a_{dd} \approx 0.6 a_s$. Therefore, both the BCS and BEC first-order corrections predicted by the BCS model are incorrect. However, this simple model can still describe the transition from fermionic atoms to bosonic molecules.

Now we shift gears and we introduce the hyperspherical representation which will be use to describe both few- and many-body systems.

2.5 Hyperspherical representation

The hyperspherical formulation has been mainly developed to describe few-body systems [51, 52, 119, 116, 159, 42]. However, some properties of Bose and Fermi gases have been successfully explained with this formulation within the K harmonic approximation [20, 149]. Therefore, the hyperspherical formulation is particularly suitable for studying the transition from few- to many-body systems since it provides a unified framework for treating this transition. The study of both few- and many-body systems can be, in turn, greatly simplified using an adiabatic approximation. In this approximation, the description of a many-body system can be reduced to a simple one-dimensional Schrödinger equation.

The hyperspherical formulation will be extensively used in this dissertation. In Chapter 3, we present an efficient way to numerically implement the full hyperspherical formulation for few-body systems. In Chapters 5 and 6, we present preliminary hyperspherical calculations that allow a qualitative interpretation of the spectrum in the BCS-BEC crossover and the dimer-dimer collisional properties. In Chapter 7, we verify important properties of unitary trapped systems derived from the hyperspherical framework. Finally, in Chapter 8, we use the full solution in the hyperspherical framework to analyze the spectrum and collisional properties of the four-boson system. Here, we outline the hyperspherical method.

The main objective of the hyperspherical method is to solve the time-independent Schrödinger equation in a convenient and efficient way. To do this, we calculate eigenval-

ues and eigenfunctions of the fixed-hyperradius Hamiltonian, constructing an adiabatic hyperspherical representation. These eigenvalues and eigenfunctions are then used to construct a set of one-dimensional coupled equations in the hyperradius R. The hyperradius is a smooth collective coordinate. In a system described by N coordinate vectors $\mathbf{r}_1, \ldots, \mathbf{r}_N$, the hyperradius R is defined by

$$\mu R^2 = \sum_{i=1}^{N} m_i \mathbf{r}_i^2. \tag{2.24}$$

Here, μ is the hyperradial reduced mass, and m_i are the masses corresponding to the particle i. The remaining coordinates are described by a set of hyperangles, generally called Ω.

The dimension of this system is $d = 3\,N$. The total wave function ψ is rescaled by R, $\Psi = R^{(d-1)/2}\psi$, so that the hyperradial equation resembles a coupled one-dimensional Schrodinger equation. In the adiabatic representation, the wave function $\Psi_E(R, \Omega)$ is expanded in terms of a complete orthonormal set of angular wave functions Φ_ν and radial wave functions $F_{\nu E}$, such that

$$\Psi_E(R, \Omega) = \sum_{\nu} F_{\nu E}(R) \Phi_\nu(R; \Omega). \tag{2.25}$$

The adiabatic eigenfunctions, or channel functions Φ_ν, depend parametrically on R and are eigenfunctions of a $3\,N - 1$ partial differential equation:

$$\left(\frac{\hbar^2 \Lambda^2}{2\mu R^2} + \frac{(d-1)(d-3)\hbar^2}{8\mu R^2} + V(R, \Omega) \right) \Phi_\nu(R; \Omega) = U_\nu(R) \Phi_\nu(R; \Omega). \tag{2.26}$$

Here, Λ is the grand angular momentum operator, which is related to the kinetic term by

$$-\sum_i \frac{\hbar^2 \nabla_i^2}{2m_i} = -\frac{\hbar^2}{2\mu} \frac{1}{R^{d-1}} \frac{\partial}{\partial R} R^{d-1} \frac{\partial}{\partial R} + \frac{\Lambda^2 \hbar^2}{2\mu R^2}. \tag{2.27}$$

The $U_\nu(R)$ obtained in Eq. (2.26) are effective hyperradial potential curves of a set of one-dimensional differential equations:

$$\left[-\frac{\hbar^2}{2\mu} \frac{d^2}{dR^2} + U_\nu(R) \right] F_{\nu E}(R) - \frac{\hbar^2}{2\mu} \sum_{\nu'} \left[2P_{\nu\nu'}(R) \frac{d}{dR} + Q_{\nu\nu'}(R) \right] F_{\nu' E}(R) = E F_{\nu E}(R). \tag{2.28}$$

These differential equations [Eq. (2.28)] are coupled through the $P_{\nu\nu'}(R)$ and $Q_{\nu\nu'}(R)$ couplings defined as

$$P_{\nu\nu'}(R) = \langle \Phi_\nu(R;\Omega) | \frac{d}{dR} | \Phi_{\nu'}(R;\Omega) \rangle \Big|_R, \tag{2.29}$$

$$Q_{\nu\nu'}(R) = \langle \Phi_\nu(R;\Omega) | \frac{d^2}{dR^2} | \Phi_{\nu'}(R;\Omega) \rangle \Big|_R. \tag{2.30}$$

Since the basis set expansion of the wave function, Eq. (2.25), is complete in the $3\,N$-dimensional space, Eqs. (2.26) and (2.28) reproduce exactly the original d-dimensional Schrödinger equation. As in most numerical methods, the solutions are approximated by truncating the Hilbert space. In this case, the Hilbert space is truncated by considering a finite number of channels in Eq. (2.28). This approximation can be easily tested analyzing the convergence with respect to the number of channels included in the calculation.

The utility of the hyperspherical representation relies on the assumption that the hyperradius R is a smooth variable. In such cases, only a few channels are relevant, and the couplings are small and have a smooth behavior. Furthermore, a fairly good approximation to the solutions can be achieved by truncating the expansion in Eq. (2.25) to a single term:

$$\Psi_E(R,\Omega) = F_{\nu E}(R)\Phi_\nu(R;\Omega). \tag{2.31}$$

This adiabatic hyperspherical approximation leads to an effective one-dimensional Schrödinger equation,

$$\left[-\frac{\hbar^2}{2\mu}\frac{d^2}{dR^2} + W_\nu(R) \right] F_{\nu E}(R) = E F_{\nu E}(R), \tag{2.32}$$

where the effective potential is

$$W_\nu(R) = U_\nu(R) - \frac{\hbar^2}{2\mu} Q_{\nu\nu}(R). \tag{2.33}$$

Here, the first term is the hyperradial potential curve, and the second term is the kinetic contribution of the hyperradial dependence of the channel function, which is always positive. If the potential curves are well spaced and do not have strong avoided

crossings, then the adiabatic approximation can be very good. This approximation comes from a truncation of the Hilbert space and, for that reason, follows the variational principle. Any energy solution obtained with this method is an upper bound of the exact energy solution.

Another useful approximation is obtained by neglecting the second term in Eq. (2.33), i.e., replacing $W_\nu(R)$ by $U_\nu(R)$ in Eq. (2.32). This is usually called the hyperspherical Born-Oppenheimer approximation. As in the standard Born-Oppenheimer approximation, the approximated energy represents a lower bound of the exact energy [46].

Next, we consider the noninteracting limit.

2.5.1 The noninteracting limit: hyperspherical harmonics

The eigenfunctions of an N-particle system acquire a simple form in the noninteracting limit. Since Λ is an operator that acts only on the Ω coordinates, the solutions of Eq. (2.41), Φ_ν, become independent of R. Therefore, any derivative of the channel function with respect to R is zero, all the coupling terms vanish, and the adiabatic approximation becomes exact. In other words, the kinetic operator [Eq. (3.47)] is separable in Ω and R and, for that reason, its solutions take the form of Eq.(2.31), with Φ_ν independent of R.

The solutions of Λ^2, $\Phi_\lambda(\Omega)$ are usually labeled by λ and called hyperspherical harmonics. Here λ is the solution of

$$[\Lambda^2 - \lambda(\lambda + d - 2)]\Phi_\lambda(\Omega) = 0. \tag{2.34}$$

For each symmetry and each number of particles, there is a λ_{min} and particular degeneracies corresponding to that problem. To obtain the λ_{min} and degeneracies, we can compare the energies of the trapped system in both the single particle and the hyperspherical representation. In the trapped system, the external potential is simply $V(R,\Omega) = \omega^2/2 \sum_{i=1}^{d} m_i x_i^2 = \omega^2 \mu R^2/2$. This potential commutes with the Λ^2 operator

and does not introduce any coupling. Therefore, the channel functions of the free system $\Phi_\lambda(\Omega)$ also describe a trapped system. Then, the wave functions of the trapped system take the form

$$\Psi_{\lambda n}(R,\Omega) = F_{\lambda n}(R)\Phi_\lambda(\Omega), \tag{2.35}$$

where $F_{\lambda n}(R)$ obeys the effective one-dimensional Schrödinger equation,

$$\left(\frac{-\hbar^2}{2m}\frac{\partial}{\partial R^2} + V_{eff}(R)\right) R^{(d-1)/2}F(R) = ER^{(d-1)/2}F(R). \tag{2.36}$$

Here, the effective potential is

$$V_{eff}(R) = \frac{(d-1)(d-3)}{8\mu R^2} + \frac{\lambda(\lambda+d-2)}{2\mu R^2} + \frac{\mu\omega^2 R^2}{2}. \tag{2.37}$$

Defining $\ell = \lambda + (d-3)/2$, the effective potential takes the known form

$$V_{eff}(R) = \frac{\ell(\ell+1)}{2\mu R^2} + \frac{\mu\omega^2 R^2}{2}, \tag{2.38}$$

which is identical to the radial Schrödinger equation of a particle with angular momentum ℓ and mass μ in a spherical trap of frequency ω. Thus, the energies are

$$E_{\ell,n} = (\ell + 2n_R)\hbar\omega = \left(\lambda + \frac{d}{2} + 2n_R\right)\hbar\omega. \tag{2.39}$$

A useful method to obtain the λ values and their degeneracies compares the solutions of Eq. (2.39) with those obtained from the single particle framework [159]. By comparing both energy solutions, we obtain the relation

$$\lambda + 2n_R = \sum_{i=1}^{N_J}(l_i + 2n_i). \tag{2.40}$$

Here, N_J is the number of Jacobi vectors. Considering all the possible options in the right-hand-side solutions, we can infer the solutions in the left-hand side. The degeneracy of λ can be obtained by combining all the possible l_i and n_i on the right hand side of Eq. (2.40) allowed by the symmetrization rules of the wave function.

As an example, consider the system of three distinguishable particles. We remove the center-of-mass coordinate and are left with two Jacobi coordinates. Thus, Eq. (2.40)

is simply

$$\lambda + 2n_R = l_1 + 2n_1 + l_2 + 2n_2. \tag{2.41}$$

We focus on the $L = 0$ states. The case $\lambda = 0$ is not degenerate and corresponds to $l_1 = l_2 = n_1 = n_2 = 0$. The next case is $\lambda = 2$ (The $\lambda = 1$ can only be formed with $L > 0$). The single particle representation predicts three cases ($l_1 = l_2 = n_1 = 0$ and $n_2 = 1$; $l_1 = l_2 = n_2 = 0$ and $n_1 = 1$; $l_1 = l_2 = 1$ and $n_1 = n_2 = 0$). One of these cases corresponds, in the hyperspherical representation, to a hyperradial excitation of the $\lambda = 0$ case. The other two are degenerate states of $\lambda = 2$. The eigenvalue of the Λ^2 operator $\lambda(\lambda + d - 2) = 12$. This procedure can be continued to higher λ values.

Chapter 3

Numerical Techniques

3.1 Introduction

In this Chapter, we present the numerical methods used in this Thesis. We focus initially on the Monte Carlo methods. In the fixed-node diffusion Monte Carlo section, we pay special attention to the importance of physical intuition for the construction of the guiding wave functions. In particular, we present the different trial wave functions used to describe trapped Fermi gases in the BCS-BEC crossover. Then we present a powerful technique to describe few-body trapped systems where the solutions are expanded in correlated Gaussian (CG) basis set. Finally, we present an innovating method which combines the hyperspherical technique with the CG method. This chapter presents these numerical methods in a general way; and it is complemented with a set of Appendices: A, B C, D E, F, G.

3.2 Fixed-node diffusion Monte Carlo approach

In 1949, Metropolis and Ulam presented the basic idea of what they called **The Monte Carlo Method** [126]. They proposed a general statistical approach to the study of differential equations. In particular, motivated by the work of Fermi, they noted that the Schrödinger equation could be expressed as a diffusion equation and simulated by a system of "particles" that move randomly and multiply themselves.

Since then, quantum Monte Carlo methods, i.e., applications of Monte Carlo

techniques to solve the Schrödinger equation, have been extensively used and perfected. There have been important developments such as the implementation of important sampling [125, 101] and different ways [4, 146, 39, 111] to overcome the limitations of the Monte Carlo methods to deal with wave functions that have nodes or, equivalently, changes of sign. These limitations are usually called the "sign problem" and affect the study of fermionic systems whose ground state wave functions have nodes.

In this section, we present the fixed-node diffusion Monte Carlo (FN-DMC) method [4] that overcomes the "sign problem" by forcing the ground state solution to have the same nodes as a suitably-chosen trial wave function. This trial wave function is crucial for a reliable estimation of the physical observables. Many of the details of the implementation of the FN-DMC method can be found extensively in the literature [84]. Here, we present the general ideas that describe the FN-DMC method. Then, we discuss in detail the trial wave functions used to describe trapped two-component Fermi gases.

3.2.1 Imaginary time propagation and diffusion Monte Carlo

We present the concepts of imaginary time propagation and its application to the diffusion Monte Carlo method. Then, we discuss general aspects of the FN-DMC method.

Consider the time-dependent Schrödinger equation for a Hamiltonian $\mathcal{H}$,

$$i\hbar\frac{\partial\Phi(\mathbf{x},t)}{\partial t} = (\mathcal{H} - E_T)\Phi(\mathbf{x},t). \tag{3.1}$$

For convenience, we have introduced an energy shift E_T. The quantity $\mathbf{x} = \{\mathbf{x}_1, ...\mathbf{x}_N\}$ includes the coordinates of all the particles. The solutions of Eq. (3.1) for a time-independent Hamiltonian take the form,

$$\Phi(\mathbf{x},t) = \sum_k C_k \Psi_k(\mathbf{x}) e^{-i(E_k - E_T)t}. \tag{3.2}$$

Equation (3.1) can be extended to imaginary time, $\tau = it$, and be written as

$$-\hbar\frac{\partial\Phi(\mathbf{x},\tau)}{\partial\tau} = (\mathcal{H} - E_T)\Phi(\mathbf{x},\tau). \tag{3.3}$$

The solutions of Eq. (3.3) are simply $\Phi(\mathbf{x},t)$ from Eq. (3.2) extended to imaginary time:

$$\Phi(\mathbf{x},\tau) = \sum_{k=0}^{\infty} C_k\Psi_k(\mathbf{x})e^{-(E_k-E_T)\tau}. \tag{3.4}$$

After a propagation in imaginary time, the term with lowest $E_k - E_T$ will become the most prominent term in Eq. (3.5). The lowest energy is, of course, the ground-state energy E_0, and the dominant term would be proportional to the ground state Ψ_0. In particular, we can set $E_T = E_0$ in Eq. (3.5) and obtain

$$\Phi(\mathbf{x},\tau) = C_0\Psi_0(\mathbf{x}) + \sum_{k=1}^{\infty} C_k\Psi_k(\mathbf{x})e^{-(E_k-E_0)\tau}. \tag{3.5}$$

In this case, $\Phi(\mathbf{x},\tau)$ converges to a steady state proportional to $\Psi_0(\mathbf{x})$.

The concept of imaginary time propagation and the derivation in Eqs. (3.1-3.5) are completely general and independent of the method used to make the propagation. The diffusion Monte Carlo method takes advantage of these properties of the Schrodinger equation in imaginary time and its similarities with the classical diffusion equation. Consider Eq. (3.3) with the Hamiltonian now explicitly written as

$$\frac{\partial\Phi(\mathbf{x},\tau)}{\partial t} = \frac{\hbar^2}{2m}\nabla^2\Phi(\mathbf{x},\tau) + (E_T - V(\mathbf{x}))\Phi(\mathbf{x},\tau). \tag{3.6}$$

If the term $(E_T - V(\mathbf{x}))$ is ignored, then Eq. (3.6) is the usual diffusion equation. Ignoring the kinetic term leads to a first-order rate equation. Both the diffusion and rate processes can be simulated separately by the Monte Carlo method, but there is no general exact solution for Eq. (3.6). However, a propagation of Eq. (3.6) in a differential $\delta\tau$, the leading order correction can be understood as a sum (or product) of the independent diffusion and rate processes. In other words, the exact propagation operator factorizes in a diffusion and rate term in the small time-step limit.

There is a close analogy between a diffusion Monte Carlo simulation and the experimental study of the behavior of a gas. To theoretically obtain the temperature and other global properties of a gas, we solve the corresponding diffusion equation. Alternatively, we could release the real gas from an initial configuration and wait until it reaches equilibrium and experimentally measure the temperature and the other global properties. The second approach is more like the diffusion Monte Carlo simulation. However, instead of experimentally studying the "gas," it numerically simulates a gas that obeys the diffusion equation [Eq. (3.6)]. The simulation starts from an initial configuration of an artificial gas, the diffusion Monte Carlo method propagates this gas until it reaches equilibrium. The gas remains in equilibrium for some measuring time during which its properties are computed. At equilibrium, the gas describes the ground state of the system and any observable of the ground state can be obtained.

The constituent parts of this artificial gas are usually called "walkers", and they describe a configuration of the N-particle system. For example, a Schrodinger equation of a 3D N-body system, a walker represents a given configuration of all the bodies, i.e., $\mathbf{x} = \{\mathbf{x}_1, ...\mathbf{x}_N\}$, and live in a $3N$ dimensional space. The diffusion process is simulated by producing a random displacement of the initial configuration, or walker, with a probability dictated by the diffusion term in Eq. (3.6). The rate process is simulated by allowing the walkers to die or to duplicate themselves.

Although solving Eq. (3.6) is in principle possible with the "pure" diffusion Monte Carlo method, the fluctuations are generally very large. However, the fluctuations can be greatly reduced by the Monte Carlo technique of importance sampling [125, 101]. In this procedure, an initial guess Ψ_T, usually called the trial wave function or guiding function, is used to bias the "walkers" to reproduce the distribution $f(\mathbf{x}, \tau) = \Phi(\mathbf{x}, \tau)\Psi_T(\mathbf{x})$. An equation similar to Eq. (3.6) describes the imaginary time evolution of $f(\mathbf{x}, \tau)$ (see detailed description in Ref. [84]). If Ψ_T is a good approximation to the exact ground state, then the fluctuations will be greatly reduced. Therefore, the construction of Ψ_T

is a very important step in FN-DMC calculations.

Another vital aspect of the importance sampling technique is that Ψ_T can be used to overcome the sign problem. In general, the propagation in imaginary time does not take into account the symmetry of the wave function. Thus, independently of the type of particles we are considering, such a propagation will converge to the same ground state, the **nodeless** bosonic ground state. This is unsatisfying if we are interested in fermionic systems. To remedy this difficulty, we can force the wave function to have the same nodal structure of a guiding wave function, Ψ_T. This method is usually called FN-DMC. To within statistical uncertainties, the FN-DMC algorithm provides an upper bound to the exact ground-state energy, i.e., to the lowest-lying state with the same symmetry as Ψ_T. If the nodal surface of Ψ_T coincides with that of the exact eigenfunction, then the FN-DMC method produces the exact eigen energy of the system.

An important step in the FN-DMC calculation is the optimization of Ψ_T. The variational Monte Carlo (VMC) method is used to test and optimize the trial wave function. In the VMC method, the energy expectation value of Ψ_T is evaluated using Monte Carlo integration techniques. The trial wave function is characterized by a set of parameters that are optimized by minimizing the energy of the trial wave function. The optimized Ψ_T is then used as a guiding function in the FN-DMC process.

A detailed description on how the VMC and FN-DMC methods are implemented will not be presented here but can be found in Ref. [84].

3.2.2 Trial Wave functions for a Trapped Two-Component Fermi Gas

The selection of the guiding wave function is a crucial step in the FN-DMC calculations. Physical intuition is used to select a suitable wave function. For homogeneous two-component Fermi gases, there are a couple of guiding wave functions that have been used to describe the gaslike ground state at different regimes of the crossover [7, 36]. The "Jastrow-Slater" wave function is used to describe a system in the weakly interact-

ing BCS limit ($a_s < 0$ and $|k_F a_s| \ll 1$) while the "paired" wave function describes the weakly interacting molecular BEC ($a_s > 0$ and $|k_F a_s| \ll 1$). Here, we extend the use of such wave functions for trapped systems.

We begin with the Jastrow-Slater wave function,

$$\Psi_J(\mathbf{r}_1, \mathbf{r}_2, ..., \mathbf{r}_N) = \prod_{ii'} J(\mathbf{r_i} - \mathbf{r_{i'}}) \Psi_{NI}(\mathbf{r}_1, \mathbf{r}_2, ..., \mathbf{r}_N) \tag{3.7}$$

Here, i and i' correspond to different-spin fermions, and Ψ_{NI} is the noninteracting ground state wave function. Alternatively, we can replace Ψ_{NI} by the noninteracting wave function with an effective oscillator length that can be different from the bare trap length of the problem. This effective scattering length is used as a variational parameter. For strongly attractive systems, we find that the optimal effective oscillator length is smaller than the bare trap length. This reduction of the effective oscillator length is a consequence of the squeezing of the gas produced by the attraction in the system.

The Jastrow term, i.e., $\prod_{ii'} J(\mathbf{r_i} - \mathbf{r_{i'}})$, describes the correlation between spin-up and spin-down particles. The Jastrow term is constructed to be nodeless for the trial wavefunction Ψ_J. Therefore, the purpose of the Jastrow term in the FN-DMC calculations is only to reduce the statistical fluctuations. In constrast, in the VMC calculations, the energies depend on the form of the Jastrow correlations.

Since Ψ_{NI} is in most cases degenerate, and there are different ways to construct it. In Eq. (3.7), the noninteracting wave function is a product of two Slater determinants, one for each component,

$$\Psi_{NI} = \mathcal{A}(\phi_{n_x n_y n_z}(\mathbf{r}_1), \cdots, \phi_{n_x n_y n_z}(\mathbf{r}_{N_1}))\ \mathcal{A}(\phi_{n_x n_y n_z}(\mathbf{r}_{1'}), \cdots, \phi_{n_x n_y n_z}(\mathbf{r}_{N_2'})) =$$
$$\det \begin{vmatrix} \phi_{111}(\mathbf{r}_1) & \cdots & \phi_{111}(\mathbf{r}_{N_1}) \\ \vdots & & \vdots \\ \phi_{n_x n_y n_z}(\mathbf{r}_1) & \cdots & \phi_{n_x n_y n_z}(\mathbf{r}_{N_1}) \end{vmatrix} \det \begin{vmatrix} \phi_{111}(\mathbf{r}_{1'}) & \cdots & \phi_{111}(\mathbf{r}_{N_2'}) \\ \vdots & & \vdots \\ \phi_{n_x n_y n_z}(\mathbf{r}_{1'}) & \cdots & \phi_{n_x n_y n_z}(\mathbf{r}_{N_2'}) \end{vmatrix} \tag{3.8}$$

The determinant form is particularly suitable for numerical evaluation. Furthermore,

the evaluation of the derivatives can be greatly simplified using the inverse of the Slater matrix (see e.g., Appendix B in Ref. [84]). Each Slater matrix is formed with the harmonic oscillator orbitals. In general, it is convenient to use harmonic oscillator orbitals obtained in Cartesian coordinates, $\phi_{n_x n_y n_z}$. For closed shells, it is straightforward to select the harmonic oscillator orbitals. For open shells, the selection of the orbitals is more cumbersome since the ground state is degenerate. However, this degeneracy can be broken by perturbation theory with the zero-range Fermi pseudo-potential as discussed in Sect. 4.2. Thus, ideally we could use the ground state obtained from this perturbation approach as Ψ_{NI}. However, such Ψ_{NI} is an expansion of the product of Slater determinants and is very expensive to compute. Therefore we look for alternative trial wave functions to describe some of the degenerate noninteracting systems.

Now we turn the discussion to a different type of trial wave function. The behavior of the two-component Fermi gas on the BEC side is qualitatively different. For attractive potentials with small, positive a_s, comparatively strongly-bound two-body dimers exist and the system is expected to form a molecular Bose gas of dimers. Such a system is not described even qualitatively correctly by the guiding function Ψ_J, which assumes that every spin-up fermion is "simultaneously" correlated with every spin-down fermion. Therefore, we use instead a "paired" guiding function Ψ_P [36, 7],

$$\Psi_P(\mathbf{r}_1, \mathbf{r}'_1, ..., \mathbf{r}_N) = \mathcal{A}\left\{\Psi_2(\mathbf{r}_1, \mathbf{r}_{1'})\Psi_2(\mathbf{r}_2, \mathbf{r}_{2'})...\Psi_2(\mathbf{r}_{N/2}, \mathbf{r}_{N/2'})\right\}, \tag{3.9}$$

where $\mathcal{A}$ is the antisymmetrizer operator. The paired guiding function is much better suited for describing a Fermi gas that behaves as a weakly interacting molecular Bose gas. In this case, Ψ_P correlates the first spin-up fermion with the first spin-down fermion, the second spin-up fermion with the second spin-down fermion, and so on; then it antisymmetrizes this "paired state." For its part, the guiding function Ψ_P is expected to accurately describe the system when the size of the dimer pairs becomes small compared to the oscillator lengths.

In Eq. (3.9), we have assumed that we have an even-N system where the number of spin-up and spin-down particles is the same. The other case we are going to consider is the odd-N system where $N_1 = N_2 + 1$. Ψ_P can be extended to treat odd-N systems by simply adding a single particle orbital ϕ_{nl} [23, 36],

$$\Psi_P(\mathbf{r}_1, \mathbf{r}'_1, ..., \mathbf{r}_N) = \mathcal{A}\left\{\Psi_2(\mathbf{r}_1, \mathbf{r}_{1'})\Psi_2(\mathbf{r}_2, \mathbf{r}_{2'})...\Psi_2(\mathbf{r}_{N_1-1}, \mathbf{r}_{N'_2}), \phi_{nl}(\mathbf{r}_{N_1})\right\}. \quad (3.10)$$

We consider a number of different single particle orbitals ϕ_{nl} in spherical coordinates, and determine the optimal nl values by performing a series of FN-DMC calculations. For the lowest n and l (the m quantum number is set to zero), the unnormalized orbitals are $\phi_{00}(\vec{r}) = e^{-r^2/2b^2}$, $\phi_{01}(\mathbf{r}) = e^{-r^2/2b^2} z/a_{ho}$, $\phi_{20}(\mathbf{r}) = e^{-r^2/2b^2}(1 - 2(r/a_{ho})^2/3)$ and $\phi_{02}(\mathbf{r}) = e^{-r^2/2b^2}(3(z/a_{ho})^2 - (r/a_{ho})^2)$. The b parameter can be treated variationally. If $b = a_{ho}$, the ϕ_{nl} agree with the noninteracting trapped orbitals.

Another important point that must be decided is the angular momentum of the trial wave function Ψ_P. Since each pair function $\Psi_2(\mathbf{r}_1, \mathbf{r}_{1'})$ has vanishing relative orbital angular momentum, the total angular momentum L of Ψ_P is 0 for even N and $N_1 = N_2$. For odd N, L of ψ_P is determined by the angular momentum of ϕ_{nl}, i.e., $L = l$.

Both paired wave functions, Eqs. (3.9,3.10), are constructed in from a two-body wave function. The two-body wave function, Ψ_2, can be obtained from the trapped two-particle system. Interestingly, the ground-state wave function of two particles in a trap can be separated exactly into a Jastrow term and noninteracting orbitals, in which

$$\Psi_2(\mathbf{r_1}, \mathbf{r_2}) = \psi(\mathbf{r_1})\psi(\mathbf{r_2})J(\mathbf{r_1} - \mathbf{r_2}), \quad (3.11)$$

where ψ is the non-interacting ground state orbitals. We will show that this relation is valid when the center-of-mass wave function and the noninteracting orbitals have a Gaussian form, like in the trapped system. For this discussion, we will not consider normalization factors or proportionality constants. If we define $\mathbf{R}_{CM} = (1/2)(\mathbf{r_1} + \mathbf{r_2})$ and $\mathbf{r} = (\mathbf{r_1} - \mathbf{r_2})$ we know that the pair wave function can be separated in the center-of-mass and relative-coordinate terms, $\Psi_2(\mathbf{r_1}, \mathbf{r_2}) = \Psi(\mathbf{R}_{CM})\phi(\mathbf{r})$. Also, we know that

the center-of-mass wave function is unaffected by the two-body interaction and is

$$\Psi(\mathbf{R}_{CM}) = \exp(-\frac{\mathbf{R}_{CM}^2}{a_{ho}^2}) = e^{-\frac{\mathbf{r}_1^2}{2a_{ho}^2}} e^{-\frac{\mathbf{r}_2^2}{2a_{ho}^2}} e^{\frac{\mathbf{r}^2}{4a_{ho}^2}} = \psi(\mathbf{r}_1)\psi(\mathbf{r}_2) e^{\frac{\mathbf{r}^2}{4a_{ho}^2}}, \tag{3.12}$$

where $\psi(\mathbf{r}_1) = e^{-\frac{\mathbf{r}_2^2}{2a_{ho}^2}}$ is the 1s (ground-state) orbital. Thus, the total wave function is

$$\Psi(\mathbf{R}_{CM})\phi(\mathbf{r}) = \psi(\mathbf{r}_1)\psi(\mathbf{r}_2) e^{\frac{\mathbf{r}^2}{4a_{ho}^2}} \phi(\mathbf{r}) = \psi(\mathbf{r}_1)\psi(\mathbf{r}_2) J(\mathbf{r}), \tag{3.13}$$

where

$$J(\mathbf{r}) = e^{\frac{\mathbf{r}^2}{4a_{ho}^2}} \phi(\mathbf{r}). \tag{3.14}$$

The evaluation of the relative coordinate wave function, $\phi(\mathbf{r})$, usually requires a numerical calculation.

These two-body solutions are used to build both the Jastrow and the paired wave function. In the Jastrow wave function, the Jastrow term is expected to describe short-range correlations. Therefore, the two-body solutions are matched outside the range of the interaction to a function that decays rapidly to a constant. For our calculations, we use $A\exp(-c\,r) + B$. The parameters A and B are selected so that the $J(r)$ and $J'(r)$ are continuous at the matching point r_m. In general, both c and r_m can be used as variational parameters in a VMC calculation. In the weakly interacting BCS side, we observe that the results are roughly insensitive to the values of c and r_m if we set r_m to a few times the range of the potential. In the noninteracting case, i.e., for $a_s = 0$, the guiding function Ψ_J with $J(r) = 1$ coincides with the exact eigenfunction. For weakly attractive Fermi systems, the attractive nature of the two-body potential introduces correlations but does, to a good approximation, leave the nodal surface unchanged. Indeed, we find that the variational energy for Ψ_J in this regime is nearly indistinguishable from the FN-DMC energies, indicating that the Jastrow product over all pair functions accounts properly for the two-body correlations of the system. Furthermore, it suggests that the Jastrow-Slater wave function is very close to the exact wave function in this regime.

The exponentially growing term of the Jastrow function [Eq. (3.14)] compensates the exponential decaying behavior of ϕ due to the trapping potential. Therefore, $J(r)$ decays with a power law behavior at $a_s < 0$. As we will see in the following this type of long-range behavior is similar to the Jastrow term obtained from the free system. Thus, it is sensible to replace the Jastrow term obtained for the trapped system with the one for the free system.

For the initial calculations for $N = 8$ in Ref. [183], we used a Gaussian interaction and the numerical solutions of the trapped system to obtain the Jastrow function. These simulations can be significantly sped up, if we use a square-well potential and the analytical Jastrow function of the free system. In this case, the Jastrow function $J(r)$ is given by the free-space two-body solution [7]. For positive scattering lengths a_s, $J(r)$ coincides with the free-space–two-body bound-state solution. For negative a_s, $J(r)$ is the free-space scattering solution, calculated at the scattering energy E_{rel}. For $N = 6, 8$ at unitarity, we treat E_{rel} as a variational parameter and find a reduction of the energy of 1 or 2% for a finite E_{rel} compared to $E_{rel} = 0$. For larger N, we simply use $E_{rel} = 0$ which implies that outside the range of the interaction the Jastrow term goes like $J(r) \propto (1/r - 1/a_s)$.

Another description of the system is given by an alternative wave function Ψ_{CB}, proposed by Chang and Bertsch [40]. This wavefunction combines the ideas of Eqs. (3.7, 3.9). For closed shell noninteracting systems, Eq. (3.15) can be written as a single Slater determinant of paired functions. Finally, the guiding function Ψ_{CB} is constructed following Eqs. (3) and (4) of Ref. [40]. At unitarity, for most N systems either Ψ_J or Ψ_P provide the lowest energy so we do not use Ψ_{CB}. However, for $N = 11$, we find that Ψ_{CB} gives the lowest energy.

The calculations presented in Sec. 4.6 were done for closed shell ($N = 8$), and consequently we used Eq. (3.15). As an example, we compare the energies at unitarity obtained with the Jastrow-Slater, E_J, and the paired wave function E_P. The results

are $E_J = 12.63(2)$ and $E_P = 12.58(2)$. In this case we see that the energies are very close.

For N=4, the constructed guiding wave function that describes the system on the BCS side has been inspired by the picture for a homogeneous system, i.e.

$$\Psi_{(N=4)} == \prod_{ii'} J(\mathbf{r_i} - \mathbf{r_{i'}}) \det \begin{vmatrix} \psi(\mathbf{r_1})\psi(\mathbf{r'_1})\cos(kr_{11'}) & \psi(\mathbf{r_1})\psi(\mathbf{r'_2})\cos(kr_{12'}) \\ \psi(\mathbf{r_2})\psi(\mathbf{r'_1})\cos(kr_{21'}) & \psi(\mathbf{r_2})\psi(\mathbf{r'_2})\cos(kr_{22'}). \end{vmatrix} \quad (3.15)$$

The Jastrow term describes the short-range interactions. The determinant part describes a nodal surface similar to that of the noninteracting system if the parameter k is chosen to be very small, i.e., $k \sim 10^{-5}/a_{ho}$. This trial wave function can be thought of as a variant of the Chang and Bertsch guiding function. We empirically verified that such a guiding function produces accurate results (see Sec. 6.2).

Finally, in the strongly-interacting regime, i.e., for $|a_s| \to \infty$, it is not **a priori** clear which of the two guiding functions provides a better description of the system.

3.3 Correlated Gaussian Method

Now we turn to an alternative method for solving the few-body Schrödinger equation variationally which does not rely on Monte Carlo techniques. Different types of Gaussian basis functions have long been used in many different areas of physics. In particular, the usage of Gaussian basis functions is one of the key elements of the success of *ab initio* calculations in quantum chemistry. The idea of using an explicitly correlated Gaussian to solve quantum chemistry problems was introduced in 1960 by Boys [26] and Singer [157]. The combination of a Gaussian basis and the stochastical variational method SVM was first introduced by Kukulin and Krasnopol'sky [110] in nuclear physics and was extensively used by Suzuki and Varga [179, 178, 180, 181]. These methods were also used to treat ultracold many-body Bose systems by Sorensen, Fedorov and Jensen [162]. A detailed discussion of both the SVM and CG methods can be found in Sorensen's Master's thesis [161] and, in particular, in Suzuki and Varga's

book [173]. In the following, we present the CG method and its application to few-body trapped systems.

Consider a set of coordinate vectors that describe the system $\{\mathbf{x}_1, ..., \mathbf{x}_N\}$. In this method, the eigenstates are expanded in a set of basis functions,

$$\Psi(\mathbf{x}_1, \cdots, \mathbf{x}_N) = \sum_A C_A \, \Phi_A(\mathbf{x}_1, \cdots, \mathbf{x}_N) = \sum_A C_A \, \langle \mathbf{x}_1, \cdots, \mathbf{x}_N | A \rangle \, . \tag{3.16}$$

Here A is a matrix with a set of parameters that characterize the basis function. In the second equality we have introduced a convenient ket notation. Solving the time-independent Schrödinger equation in this basis set reduces the problem to a diagonalization of the Hamiltonian matrix:

$$\mathcal{H}\vec{C}_i = E_i \mathcal{O}\vec{C}_i \tag{3.17}$$

Here, E_i are the energies of the eigenstates, $\vec{C}_i$ is a vector form with the coefficients C_A and $\mathcal{H}$ and $\mathcal{O}$ are matrices whose elements are $\mathcal{H}_{BA} = \langle B|\mathcal{H}|A\rangle$ and $\mathcal{O}_{BA} = \langle B|A\rangle$. For a 3D system, the evaluation of these matrix elements involves $3N$-dimensional integrations which are in general very expensive to compute. Therefore, the effectiveness of the basis set expansion method relies mainly on the appropriate selection of the basis functions. As we will see, the CG basis functions permit a fast evaluation of overlap and Hamiltonian matrix elements; they are flexible enough to correctly describe physical states.

To reduce the dimensionality of the problem we can take advantage of its symmetry properties. Since the interactions considered are spherically symmetric, the total angular momentum, L, is a good quantum number. For simplicity, we will restrict ourselves to $L = 0$ solutions. This restriction allow us to reduce the Hilbert space by introducing restrictions to the basis functions. In particular, if the basis functions only depend on the interparticle distances, then Eq. (3.16) can only describe states with zero angular momentum and positive parity ($L^P = 0^+$). Furthermore, we can consider

that the center-of-mass motion decouples from the system. In such cases, the CG basis functions take the form

$$\Phi_{\{\alpha_{ij}\}}(\mathbf{x}_1, \cdots, \mathbf{x}_N) = \psi_0(\mathbf{R}_{CM})\mathcal{S}\left\{\exp\left(-\sum_{j>i=1}^{N}\alpha_{ij}r_{ij}^2/2\right)\right\}, \tag{3.18}$$

where $\mathcal{S}$ is a symmetrization operator and r_{ij} is the interparticle distance between particles i and j. The set of parameters $\{\alpha_{ij}\}$ are related with the matrix elements of A. Here, ψ_0 is the ground state of the center-of-mass motion. For trapped systems, ψ_0 takes the form, $\psi_0(\mathbf{R}_{CM}) = e^{-R_{CM}^2/2a_{ho}^M}$. Because of its simple Gaussian form, the ψ_0 can be absorbed in the exponential factor. Thus, in a more general way, the basis function can be written in terms of a matrix A that characterizes them,

$$\Phi_A(\mathbf{x}_1, \mathbf{x}_2, ..., \mathbf{x}_N) = \mathcal{S}\left\{\exp(-\frac{1}{2}\mathbf{x}^T.A.\mathbf{x})\right\} = \mathcal{S}\left\{\exp(-\frac{1}{2}\sum_{j>i=1}^{N}A_{ij}\mathbf{x}_i.\mathbf{x}_j)\right\}, \tag{3.19}$$

where $\mathbf{x} = \{\mathbf{x}_1, \mathbf{x}_2, ..., \mathbf{x}_N\}$, and A is a symmetric matrix. The matrix elements A_{ij} are directly related with the α_{ij} (see Appendix C). Because of the simplicity of the basis functions, Eq. (3.18), the matrix elements of the Hamiltonian can be calculated analytically.

The key idea that allows the analytical evaluation of the matrix elements is selecting the set of coordinates that simplifies the evaluations. For basis functions of the form of Eq. (3.19), the matrix elements are characterized by a matrix M in the exponential. In such case, the matrix element integrand can be greatly simplified if we write it in terms of the Jacobi vectors that diagonalize that matrix M. This change of coordinates permits, in many cases, the analytical evaluation of the matrix elements. The explicit evaluation of the matrix elements can be found in Appendices A and B.

There are two properties of the CG method that worth mentioning. First, the CG basis set is linearly-dependent and over-complete, so a systematic increase in the number of basis functions will converge to the exact eigenvalues [161]. Secondly, the basis functions Φ_A are squared integrable only if the matrix A is positive definite. We can

further restrict the basis function by introducing a real widths d_{ij} such that $\alpha_{ij} = 1/d_{ij}^2$. With this transformation, we make sure that A is positive definite. Furthermore, these widths are proportional to the mean interparticle distances of the basis function. Thus, it is easy to select them after considering the physical length scales relevant to the problem. Even though we have restricted the Hilbert space with this transformation, we have numerical evidence that that the results converge to the exact eigenvalues.

The linear dependence in the basis set causes problems in the numerical diagonalization of the Hamiltonian matrix equation 3.17. There are different ways to minimize or eliminate such problems which are explained in the Appendix E.

Finally, we want to stress the importance of the appropriate selection of the interaction potential. For the problems considered in this dissertation, the interactions are expected to be characterized only by the scattering length, i.e., to be independent of the shape of the potential. For that reason, we can select a model potential that permits rapid evaluation of the matrix elements. We found that a model potential with a Gaussian form,

$$V_0(r) = -d \exp\left(-\frac{r^2}{2r_0^2}\right), \tag{3.20}$$

is particularly suitable for this basis set expansion. If the range r_0 is much smaller than the scattering length, then the interactions are effectively characterized only by the scattering length. The scattering length is tuned by changing the strength of the interaction potential, d, while the range, r_0, of the interaction potential remains unchanged. This is particularly convenient in this method since it implies that we only need to evaluate the matrix elements once and we can use them to solve the Schrödinger equation at any given potential strength (or scattering length). Of course, this procedure will give accurate results only if the basis set is complete enough to describe the different configurations that appear at different scattering lengths.

In general, a simple version of this method includes four basic steps: the gen-

eration of the basis set, the evaluation of the matrix elements, the elimination of the linear dependence and the evaluation of the spectrum. The SVM, presented in Appendix F, combines the first three of these steps in a optimization procedure where the basis functions are selected randomly.

3.4 Correlated Gaussian Hyperspherical method

Several techniques to solve few-body systems have been developed in the last decades [68, 173, 121, 190, 119]. Among these method, the Correlated Gaussian (CG) technique, presented in the previous Section, has proven to be capable of describing trapped few-body system with short-range interactions. Because of the simplicity of the matrix element calculation, the CG method provides an accurate description of the ground and excited states up to $N = 6$ [19]. However, CG can only describe bound states. For this reason, it is numerically convenient to treat trapped systems where all the states are quantized. The CG cannot (without substantial modifications) describe states above the continuum nor the rich behavior of atomic collisions such as dissociation and recombination.

The hyperspherical representation, on the other hand, provides an appropriate framework to treat the continuum. In the adiabatic hyperspherical representation, the Hamiltonian is solved as a function of the hyperradius R, reducing the many-body Schrödinger equation to a single variable form with a series of different couple effective potentials. The asymptotic behavior of the potentials and the channels describe different dissociation or fragmentation pathways, providing a suitable framework for analyzing collisional physics. However, the standard hyperspherical methods expand the channel functions in splines or finite element basis functions [133, 192, 65, 172], and the calculations become computationally very demanding for $N > 3$ systems.

Ideally, we would like to combine the fast matrix element evaluation of the CG basis set with the capability of the hyperspherical framework to treat the continuum.

Here, we explore how the CG basis set can be used within the hyperspherical framework. We call the use of CG basis function to expand the channel functions in the hyperspherical framework the CG hyperspherical method (CGHS).

In the hyperspherical framework, we need to evaluate matrix elements of the Hamiltonian at fixed R. To evaluate such matrix elements, consider first how the matrix element evaluation is carried out in the standard CG approach.

In the CG method, we select, for each matrix element evaluation, a set of coordinate vectors that simplifies the integration, i.e., the set of coordinate vectors that diagonalize the basis matrix M which characterizes the matrix element. The flexibility to choose the best set of coordinate vectors for each matrix element evaluation is key to the success of the CG method.

This selection of the optimal set of coordinate vectors is formally applied by an orthogonal transformation from an initial set of vectors $\mathbf{x} = \{\mathbf{x}_1, ..., \mathbf{x}_N\}$ to a final set of vectors $\mathbf{y} = \{\mathbf{y}_1, ..., \mathbf{y}_N\}$: $T\mathbf{x} = \mathbf{y}$, where T is the orthogonal transformation matrix. The hyperspherical method is particularly suitable for such orthogonal transformations because the hyperradius R is an invariant under them. Consider the hyperradius defined in terms of a set of mass scaled Jacobi vectors [51, 52, 172, 124], $\mathbf{x} = \{\mathbf{x}_1, ..., \mathbf{x}_N\}$,

$$\mu R^2 = \mu \sum_i \mathbf{x_i}^2, \tag{3.21}$$

If we applied an orthogonal transformation to a new set of vectors $\mathbf{y}$, then

$$\mu R^2 = \mu \sum_i \mathbf{x_i}^2 = \mu \mathbf{y} T^T T \mathbf{y} = \mu \sum_i \mathbf{y_i}^2 \tag{3.22}$$

where we have used that $T^T T = I$, and I is the identity. Therefore, in the hyperspherical framework we can also select the most convenient set of coordinate vectors for each matrix element evaluation. This will be the key to reducing the dimensionality of the matrix element integration. This transformation is the equivalent of saying that, for each matrix element evaluation, we can select the set of hyperangles (Ω) that simplify the matrix-element evaluation.

As an example of how the dimensionality of matrix-element integration is reduced, consider a three dimensional N-particle system with the center of mass removed and $L = 0$ solutions. We will show that this technique reduces a $(3N - 7)$ numerical integration [1] to a sum over the symmetrization permutation of $(N - 3)$ numerical integrations (see Sec. 3.4.2 and Appendix G). This result implies that for $N = 3$ the matrix element evaluation can be done analytically and that for $N = 4$, it requires a sum of one-dimensional numerical integrations.

The next three subsections discuss the implementation of the CGHS. Many of the techniques used in the standard CG method can be directly used in the CGHS. For example, the selection and symmetrization of the basis function can be directly applied in the CGHS. Also, the optimization through the VMS method can be used to optimize the basis set at different values of the hyperradius R. Subsection 3.4.1 describes how the hyperangular Schrödinger equation (Eq. 2.26) can be solved using a basis set expansion. Subsection 3.4.2 shows, as an example, how the unsymmetrized matrix elements can be calculated analytically for a three particle system (the calculation of the unsymmetrized matrix elements for $N = 4$ is presented in the Appendix G). Finally, subsection 3.4.3 discuss in general how this method is implemented.

3.4.1 Expansion of the channel function in a basis set

In the hyperspherical method (see Sec. 2.5), channel functions are solutions of the adiabatic Hamiltonian $\mathcal{H}_A(R;\Omega)$,

$$\mathcal{H}_A(R;\Omega)\Phi_\nu(R;\Omega) = U_\nu(R)\Phi_\nu(R;\Omega). \tag{3.23}$$

[1] The (3N-7) numerical integration results from the following reasoning: initially we have 3N numerical integration but 3 dimensions are removed by decoupling the center of mass motion, 3 dimension are removed fixing the Euler angles and 1 dimension is removed fixing R.

The eigenvalues of this equation are the hyperspherical potential curves $U_\nu(R)$. The adiabatic Hamiltonian has the form,

$$\mathcal{H}_A(R;\Omega) = \frac{\hbar^2\Lambda^2}{2\mu R^2} + \frac{(d-1)(d-3)\hbar^2}{8\mu R^2} + V(R,\Omega). \tag{3.24}$$

Here, $d = 3N_J$ where N_J is the number of Jacobi vectors.

A standard way to solve Eq. (3.23) is to expand the channel functions in a basis,

$$|\Phi_\mu(R;\Omega)\rangle = \sum_i c^i_\mu(R)\,|B_i(R;\Omega)\rangle\,. \tag{3.25}$$

Here μ labels the channel function. The $|B_i(R;\Omega)\rangle$ are the basis functions. With this expansion, Eq. (3.23) reduces to the eigenvalue equation

$$\mathcal{H}_A(R)\vec{c}_\mu = U_\mu(R)\mathcal{O}(R)\vec{c}_\mu. \tag{3.26}$$

The vectors $\vec{c}_\mu = \{c^1_\mu, ..., c^D_\mu\}$, where D is the dimension of the basis set. $\mathcal{H}_A$ and $\mathcal{O}$ are the Hamiltonian and overlap matrices whose matrix elements are given by

$$\mathcal{H}_A(R)_{ij} = \langle B_i|\mathcal{H}_A(R;\Omega)|B_j\rangle\,\Big|_R, \tag{3.27}$$

$$\mathcal{O}(R)_{ij} = \langle B_i|B_j\rangle\,\Big|_R. \tag{3.28}$$

Once the hyperradial potential curves are calculated, we still need to evaluate the non-adiabatic couplings between the channel functions. The P and Q couplings, defined in Sec. 2.5, are

$$P_{\nu\mu} = \langle\Phi_\nu(R)|\frac{d}{dR}\Phi_\mu(R)\rangle\,, \tag{3.29}$$

$$Q_{\nu\mu} = \langle\frac{d}{dR}\Phi_\nu(R)|\frac{d}{dR}\Phi_\mu(R)\rangle\,. \tag{3.30}$$

In the basis set expansion, the couplings P and Q can be calculated as matrix multiplication. Using the expansion in Eq. (3.25),

$$\frac{d}{dR}\,|\Phi_\mu(R)\rangle = \sum_i \frac{dc^i_\mu(R)}{dR}, |B_i(R)\rangle + c^i_\mu(R)\,|\frac{dB_i(R)}{dR}\rangle\,. \tag{3.31}$$

For simplicity, we have omitted the angular dependence. The P coupling takes the form

$$P_{\nu\mu} = \sum_{ij} c_\nu^j(R) \frac{dc_\mu^i(R)}{dR} \langle B_j(R)|B_i(R)\rangle + c_\nu^j(R) c_\mu^i(R) \langle B_j(R)|\frac{dB_i(R)}{dR}\rangle \tag{3.32}$$

which can be written as simple matrix multiplication,

$$P_{\nu\mu} = \vec{c}_\nu^T \mathcal{O}(R) \dot{\vec{c}}_\mu + \vec{c}_\nu^T \mathcal{P}(R) \vec{c}_\mu. \tag{3.33}$$

Here and in the following, $\dot{\vec{c}}$ is the derivative of $\vec{c}$ with respect to R and $\mathcal{P}(R)$ is defined in Eq. (3.36). The same procedure can be done for the Q couplings with

$$\begin{aligned} Q_{\nu\mu} = \sum_{ij} & \frac{dc_\nu^j(R)}{dR} \frac{dc_\mu^i(R)}{dR} \langle B_j(R)|B_i(R)\rangle + \frac{dc_\nu^j(R)}{dR} c_\mu^i(R) \langle B_j(R)|\frac{dB_i(R)}{dR}\rangle \\ & c_\nu^j(R) \frac{dc_\mu^i(R)}{dR} \langle \frac{dB_j(R)}{dR}|B_i(R)\rangle + c_\nu^j(R) c_\mu^i(R) \langle \frac{dB_j(R)}{dR}|\frac{dB_i(R)}{dR}\rangle \end{aligned} \tag{3.34}$$

and can also be written as a matrix multiplication.

$$Q_{\nu\mu} = \dot{\vec{c}}_\nu^T \mathcal{O}(R) \dot{\vec{c}}_\mu + \dot{\vec{c}}_\nu^T \mathcal{P}(R) \vec{c}_\mu + \vec{c}_\nu^T \mathcal{P}^T(R) \dot{\vec{c}}_\mu + \vec{c}_\nu^T \mathcal{Q}(R) \vec{c}_\mu. \tag{3.35}$$

In Eqs. (3.33, 3.35) we have used the overlap matrix $\mathcal{O}$ and defined the matrices $\mathcal{P}$ and $\mathcal{Q}$ whose matrix elements are

$$\mathcal{P}(R)_{ij} = \langle B_j(R)|\frac{dB_i(R)}{dR}\rangle\,, \tag{3.36}$$

$$\mathcal{Q}(R)_{ij} = \langle \frac{dB_j(R)}{dR}|\frac{dB_i(R)}{dR}\rangle\,. \tag{3.37}$$

The derivatives of the $c_\mu^j(R)$ coefficients that form the $\dot{\vec{c}}_\mu$ are calculated numerically using the three point rule.

3.4.2 Unsymmetrized Matrix Elements evaluation of three particles

A basis function in terms of the interparticle distances is

$$\Psi(r_{12}, r_{13}, r_{23}) = \exp(-\frac{r_{12}^2}{2d_{12}^2}) \exp(-\frac{r_{13}^2}{2d_{13}^2}) \exp(-\frac{r_{23}^2}{2d_{23}^2}). \tag{3.38}$$

These basis functions do not depend on the center-of-mass coordinate and can only reproduce the $J^P = 0^+$ spectrum. For equal mass systems, we can write Eq.(3.38) in terms of the following Jacobi coordinates:

$$\mathbf{x_1} = \frac{1}{\sqrt{2}}(\mathbf{r}_1 - \mathbf{r}_2), \tag{3.39}$$

$$\mathbf{x_2} = \sqrt{\frac{2}{3}}\left(\mathbf{r}_3 - \frac{\mathbf{r}_1 + \mathbf{r}_2}{2}\right). \tag{3.40}$$

The basis functions [Eq. (3.38)] can be written as

$$|A\rangle = \exp(-\frac{\mathbf{x}^T.A.\mathbf{x}}{2}) = \exp(-\frac{\mathbf{x_1}.\mathbf{x_1}a_{11} + 2\mathbf{x_1}.\mathbf{x_2}a_{12} + \mathbf{x_2}.\mathbf{x_2}a_{22}}{2}) \tag{3.41}$$

where $\mathbf{x} \equiv \{\mathbf{x}_1, \mathbf{x}_2\}$ and A is a 2 by 2 symmetric matrix whose elements are $a_{11} = 2/d_{12}^2 + 1/2(1/d_{13}^2 + 1/d_{23}^2)$, $a_{12} = a_{21} = \sqrt{3}(1/d_{23}^2 - 1/d_{13}^2)$, and $a_{22} = 3/2(1/d_{13}^2 + 1/d_{23}^2)$. In Eq. (3.41), we can clearly see that the state $|A\rangle$ depends only on the distances x_1, and x_2 plus the angle θ_{12} between them, $\cos\theta_{12} = \mathbf{x_1}.\mathbf{x_2}/x_1x_2$.

We want to obtain the matrix elements corresponding to these basis function at fixed hyperradius R. We define the hyperradius to be $R^2 = \mathbf{x}_1^2 + \mathbf{x}_2^2$. The integrand of the overlap matrix element is

$$B.A = \exp(-\frac{x^T.(A+B).x}{2}). \tag{3.42}$$

We change to the Jacobi basis set that diagonalizes $A + B$ and we call β_1 and β_2 the eigenvalues and $\mathbf{y} \equiv \{\mathbf{y}_1, \mathbf{y}_2\}$ the eigenvectors. In this new coordinate basis, Eq. (3.42) has a simple form,

$$B.A = \exp(-\frac{\beta_1 y_1^2 + \beta_2 y_2^2}{2}). \tag{3.43}$$

We integrate over the angles of the vectors $\mathbf{y}_1$ and $\mathbf{y}_2$ and we fix the hyperradius, so $y_1 = R\cos\theta$ and $y_2 = R\sin\theta$. In this set of coordinates, the matrix element at fixed R is

$$\langle B|A\rangle \Big|_R = (4\pi)^2 \int_0^{\pi/2} \exp(-\frac{\beta_1 R^2\cos^2\theta + \beta_2 R^2\sin^2\theta}{2})\cos^2\theta\sin^2\theta d\theta \tag{3.44}$$

This integration has an analytical form,

$$\langle B|A\rangle \Big|_R = 8\pi^3 \frac{\exp(-\frac{\beta_1+\beta_2}{4}R^2)}{R^2(\beta_1-\beta_2)} I_1\left(R^2\frac{\beta_1-\beta_2}{4}\right) \tag{3.45}$$

To simplify the interaction matrix element evaluation, we can use a Gaussian model potential as we have done in the CG method. In this case, the interaction term can be evaluated in the same way we have calculated the overlap term since the interaction is also a Gaussian. Each pairwise interaction can be written as $V_{ij} = V_0 \exp(-\frac{r_{ij}^2}{2d_0^2}) = V_0 \exp(-x^T.M^{(ij)}.x/(2d_0^2))$ (see Appendix C for the definition of $M^{(ij)}$). Therefore, to calculate the interaction matrix element, we need to evaluate

$$\langle B|V_{ij}|A\rangle = V_0 \int d\Omega \exp(-\frac{x^T.(A+B+M^{(ij)}/d_0^2).x}{2}). \tag{3.46}$$

This integration can be done following the same steps of the overlap matrix element. Equation (3.45) can be used directly if we multiply it by V_0, and β_1 and β_2 are replaced by the eigenvalues of $A+B+M^{(ij)}/d_0^2$. Note that for each pairwise interaction, the matrix $M^{(ij)}$ changes and requires a new evaluation of the eigenvalues.

The third term we need to evaluate is the hyperangular kinetic term at fixed R. This kinetic term is proportional to the grand angular momentum operator Λ defined for the $N=3$ case as

$$\frac{\Lambda^2\hbar^2}{2\mu R^2} = -\sum_i \frac{\hbar^2\nabla_i^2}{2\mu} + \frac{\hbar^2}{2\mu}\frac{1}{R^5}\frac{\partial}{\partial R}R^5\frac{\partial}{\partial R}. \tag{3.47}$$

The expression can be formally written as

$$\mathcal{T}_\Omega = \mathcal{T}_T - \mathcal{T}_R, \tag{3.48}$$

where

$$\mathcal{T}_\Omega = \frac{\Lambda^2\hbar^2}{2\mu R^2}, \quad \mathcal{T}_T = -\sum_i \frac{\hbar^2\nabla_i^2}{2\mu}, \text{ and } \mathcal{T}_R = -\frac{\hbar^2}{2\mu}\frac{1}{R^5}\frac{\partial}{\partial R}R^5\frac{\partial}{\partial R}. \tag{3.49}$$

In typical calculations, $\mathcal{T}_\Omega$ is evaluated by directly applying the corresponding derivatives in the hyperangles Ω. However, in this case, it is convenient to evaluate $\mathcal{T}_T$ and $\mathcal{T}_R$ separately, and make use of (3.48).

The integrand of the total kinetic term $\mathcal{T}_T$ takes the form

$$B|\mathcal{T}_T|A = \exp(-\frac{x^T.B.x}{2}) \left(-\sum_i^2 \frac{\hbar^2}{2\mu} \nabla_i^2 \right) \exp(-\frac{x^T.A.x}{2}). \tag{3.50}$$

First, we diagonalize A and use the eigenvectors and eigenvalues of A, obtaining,

$$B|\mathcal{T}_T|A = -\frac{\hbar^2}{2\mu} \left(-\mathrm{Tr}[A] + x^T.A^2.x\right) \exp(-\frac{x^T.(A+B).x}{2}). \tag{3.51}$$

Here Tr is the trace function. We can use $\mathrm{Tr}[A] = (\alpha_1 + \alpha_2)$, where α_1 and α_2 are the eigenvalues of A. Now we diagonalize $A+B$. We call T the matrix with the orthonormal eigenstates in columns and β_1 and β_2 are the eigenvalues of $A+B$. We make a change of coordinates to the basis set that diagonalizes $A+B$. We obtain

$$B|\mathcal{T}_T|A = -\frac{\hbar^2}{2\mu} \left(-3(\alpha_1 + \alpha_2) + y.G.y\right) \exp(-\frac{\beta_1 y_1^2 + \beta_2 y_2^2}{2}), \tag{3.52}$$

where $G = T^T.A^2.T$, and $\mathbf{y}_1$ and $\mathbf{y}_2$ are the vectors in the new eigen basis. The integration over the angles of these vectors is trivial. After this integration, we fix the hyperradius and integrate over the hyperangle θ defined by $y_1 = R\cos\theta$ and $y_2 = R\sin\theta$,

$$\langle B|\mathcal{T}_T|A\rangle \Big|_R = -\frac{(4\pi)^2}{2} \int_0^{\pi/2} \Big\{ -3(\alpha_1 + \alpha_2) + g_{11}R^2\cos^2\theta + g_{22}R^2\sin^2\theta \Big\} \exp(-\frac{\beta_1 R^2\cos^2\theta + \beta_2 R^2\sin^2\theta}{2}) \cos^2\theta \sin^2\theta d\theta. \tag{3.53}$$

This integration can be done analytically and the results expressed in terms of the Bessel functions I_1 and I_0:

$$\langle B|\mathcal{T}_T|A\rangle \Big|_R = -\frac{e^{-\frac{(\beta_1+\beta_2)R^2}{2}}\pi^3}{4(\beta_1-\beta_2)} \Big\{ -8(g_{11}-g_{22}) I_0\left[\frac{1}{4}(\beta_1-\beta_2)R^2\right] + \frac{8}{(\beta_1-\beta_2)R^2} \Big\{ 8(g_{11}-g_{22}) + (\beta_1-\beta_2)\left(-6(\alpha_1+\alpha_2) + (g_{11}+g_{22})R^2\right) \Big\} I_1\left[\frac{1}{4}(\beta_1-\beta_2)R^2\right] \Big\}. \tag{3.54}$$

Now we will evaluate $\mathcal{T}_R$, the hyperradial kinetic term. It is written as

$$\mathcal{T}_R = -\frac{\hbar^2}{2\mu} \left(\frac{1}{R^{5/2}} \frac{\partial^2}{\partial R^2} R^{5/2} - \frac{15}{4R^2} \right). \tag{3.55}$$

Therefore, the integrand takes the form

$$B|\mathcal{T}_R|A = -\frac{\hbar^2}{2\mu} \exp(-\frac{x^T.B.x}{2}) \left(\frac{1}{R^{5/2}} \frac{\partial^2}{\partial R^2} R^{5/2} - \frac{15}{4R^2} \right) \exp\left(-\frac{x^T.A.x}{2}\right), \tag{3.56}$$

We use the property that $x^T.A.x = R^2 F_A(\Omega)$ to evaluate the derivatives with respect to R. This allows a simple application of the derivatives in Eq. (3.56), yielding

$$B|\mathcal{T}_R|A = \frac{\hbar^2}{2\mu R^2}\left[6x^T.A.x - (x^T.A.x)^2\right]\exp\left[-\frac{x^T.(A+B).x}{2}\right]. \tag{3.57}$$

We diagonalize $A+B$. Defining $D = T^T.A.T$, we obtain

$$B|\mathcal{T}_R|A = \frac{\hbar^2}{2\mu R^2}\left[6y.D.y - (y.D.y)^2\right]\exp\left(-\frac{\beta_1 y_1^2 + \beta_2 y_2^2}{2}\right) \tag{3.58}$$

The terms $y.D.y$ and $(y.D.y)^2$ depend on the polar angles of the vectors. The integration over the polar angles ($\Omega_1 = \{\phi_1, \theta_1\}$ and $\Omega_2 = \{\phi_2, \theta_2\}$) of these terms is

$$\int\left[6y.D.y - (y.D.y)^2\right]d\Omega_1 d\Omega_2 = (4\pi)^2\Big\{6d_{11}y_1^2 + 6d_{22}y_2^2 - \left[d_{11}^2 y_1^4 + (2d_{11}d_{22} + 4d_{12}^2/3)y_1^2 y_2^2 + d_{22}^2 y_2^4\right]\Big\}. \tag{3.59}$$

Now we carry out the integration over the hyperangle θ. Using $y_1 = R\cos\theta$ and $y_2 = R\sin\theta$, we obtain

$$\begin{aligned}\langle B|\mathcal{T}_R|A\rangle\Big|_R = \frac{(4\pi)^2\hbar^2}{2\mu R^2}\int_0^{\pi/2}\Big\{&6d_{11}R^2\cos^2\theta + 6d_{22}R^2\sin^2\theta - \\ &d_{11}^2R^4\cos^4\theta - (2d_{11}d_{22} + 4d_{12}^2/3)R^4\cos^2\theta\sin^2\theta - d_{22}^2R^4\sin^4\theta\Big\} \\ &\exp\left(-\frac{\beta_1R^2\cos^2\theta + \beta_2R^2\sin^2\theta}{2}\right)\cos^2\theta\sin^2\theta d\theta.\end{aligned} \tag{3.60}$$

This integration has the analytical form

$$\begin{aligned}\langle B|\mathcal{T}_R|A\rangle\Big|_R = -\frac{\hbar^2}{\mu}\frac{e^{-\frac{(\beta_1+\beta_2)R^2}{4}}\pi^3}{4R^2(\beta_1-\beta_2)^2}\Big\{&-8\Big[-8d_{12}^2 + (d_{11}-d_{22})\big(6(-\beta_1+\beta_2+d_{11}-d_{22}) + \\ &(\beta_1-\beta_2)(d_{11}+d_{22})R^2\big)\Big]I_0\left[\frac{1}{4}(\beta_1-\beta_2)R^2\right] + \frac{8}{(\beta_1-\beta_2)R^2}\Big[-64d_{12}^2 + \\ &48(d_{11}-d_{22})(-\beta_1+\beta_2+d_{11}-d_{22}) + 2(\beta_1-\beta_2)(-3\beta_1+3\beta_2+4d_{11}-4d_{22})(d_{11}+d_{22})R^2 \\ &+(\beta_1-\beta_2)^2(d_{11}^2+d_{22}^2)R^4\Big]I_1\left[\frac{1}{4}(\beta_1-\beta_2)R^2\right]\Big\}.\end{aligned} \tag{3.61}$$

Combining Eqs. (3.54, 3.61), we obtain $\mathcal{T}_\Omega$. The expression for $\mathcal{T}_\Omega$ can be simplified using the relation $G = D^2$ to write G matrix elements of Eq. (3.54) in terms of the ones of D.

A useful test to verify the functional form of the matrix elements is to integrate them with respect to R, with the corresponding volume element, and compare that result with the CG matrix elements presented in Appendix B. Another important test is to verify that $\mathcal{T}_\Omega$ is symmetric under the exchange of the basis functions A and B. This is not a trivial test since neither $\mathcal{T}_T$ nor $\mathcal{T}_R$ are symmetric. Both tests can be carried out numerically.

3.4.3 General considerations

Many of the procedures of the standard CG method can be easily extended to the CGHS. The selection, symmetrization, and optimization of a basis follow the same ideas of the standard CG method (see Appendices A, C, D, F and E). However, the evaluation of the unsymmetrized matrix elements at fixed R is clearly different. Furthermore, the hyperangular Hamiltonian [Eq. 3.23] need to solved at different hyperradius R.

There are several properties that makes this method particularly efficient. For the model potential used, the scattering length is tuned by varying the potential depths of the two-body interaction. Therefore, as in the CG case, the matrix elements need only be calculated once; then they can be used for a wide range of scattering lengths. Of course, the basis set should be complete enough to describe the relevant potential curves at all the desired scattering length values.

The selection of the basis function generally depends on R. To avoid numerical problems, the mean hyperradius of each basis function $\langle R \rangle_B$ should be of the same order of the hyperradius R in which the matrix elements are evaluated. We can ensure that $\langle R \rangle_B \sim R$ by selecting some (or all) the weights d_{ij} to be of the order of R.

We consider two different optimization procedures. The first possible optimization procedure is the following: First, we select a few basis functions and optimized them to describe the lowest hyperspherical harmonics. The widths of these basis functions are rescaled by R at each hyperradius so that they represent the hyperspherical harmonics

equally well. These basis functions are used at all R, while the remaining are optimized at each R. Starting from small R (of the order of the range of the potential), we optimize a set of basis functions. As R is increased, the basis set is increased and reoptimized. At every R step, only a fraction of the basis set is optimized, and those basis functions are selected randomly. After a several R-steps, the basis set is increased.

Instead of optimizing the basis set at each R, one can alternatively try to create a complete basis set at large R_{max}. In this case, the basis functions should be complete enough to describe the lowest channel functions with interparticle distances varying from interaction range r_0 up to the hyperradius R_{max}. Such a basis set can be rescaled to any $R < R_{max}$ and should efficiently describe the channel functions at that R. The rescaling procedure is simply $d_{ij}/R = d_{ij}^{max}/R_{max}$. This procedure avoids the optimization at each R. Furthermore, the kinetic, overlap, and couplings matrix elements at R are straightforwardly related with the ones at R_{max}. So, the interaction potential is the only matrix element that need to be recalculated at each R. This property can be understood by dimensional analysis. The kinetic, overlap and couplings matrix elements only depend on R, so a rescaling of the widths is straightforward related to a rescaling of the matrix elements. In contrast, the interaction potential introduces a new length scale, so the matrix elements depends on both R and d_0, and the rescaling does not work.

These two methods, the complete basis set or the small optimized basis set, can be appropriate in different circumstances. If a large number of channels are needed, probably the complete basis method is the best choice. But, if only a couple of particular channels are needed, then the optimization might be more efficient.

The most convenient way we have found to optimize the basis function in the four-boson and four-fermion problem is the following: First we select an hyperradius R_m that is $R_m \approx 300\, d_0$ where the basis function will be initially optimized. The basis set is increased and optimized until the relevant potential curves are converged and,

in that sense, the basis is complete. This basis is then rescaled, as proposed in the second optimization method, to all $R < R_m$. For $R > R_m$, it is too expensive to have a "complete" basis set. For that reason, we use the first optimization method that allow a reliable description of the lowest potential curves.

Note that for standard correlated Gaussian calculations, the matrices A and B need to be positive definite. This condition restricts the Hilbert space to exponentially decaying functions. In the hyperspherical treatment, this is not necessary since the matrix elements can be always calculated at fixed R, even for exponentially growing functions. This gives more flexibility in choosing the optimal basis functions.

Chapter 4

Renormalized Mean-Field Methods

4.1 Introduction

In this chapter, we analyze the behavior of a two-component Fermi gas in the negative-scattering-length or BCS region. In recent years, the BCS-BEC crossover problem has become experimentally accessible [82, 99, 195, 104], enabling tests of different many-body theories. The BCS theory has been successful in explaining superfluidity in Fermi gases, but this theory is incomplete because it neglects the Hartree term of the interaction, $4\pi a\rho/m$ (ρ is the density of one spin component). Comparatively little research has included the Hartree term in considering Fermi gases [76, 113, 33, 86, 54]. In the cases the Hartree term was included, it was primarily to study the perturbative regime where $\rho a_s^3 << 1$. These studies usually analyze the "normal state" of the gas, and contrasts with the superfluid state that is study with the BCS theory. Quantum Monte Carlo (QMC) simulations include (in a sense) both the Hartree term and pairing physics, but a complete theory that contains both ingredients is still required. A recent approach [54] started from the mean-field BCS theory and reproduced the Hartree term by including quantum fluctuations. Therefore, this theory succeeded in reproducing both normal and superfluid contributions. However, its validity in the strongly interacting regime and the importance of higher order corrections are still unclear. This chapter analyzes mean-field theories with zero-range interactions that reproduce the correct Hartree term in the perturbative limit.

The Hartree term can be easily incorporated using a mean field approach and effective zero-range interactions. When the range of interaction is much smaller than the interparticle distance, the potential can be replaced by a delta-function interaction. However, this replacement must be done with caution because the delta function interaction is too singular to be exactly solvable, even in principle. In the weakly-interacting limit, $\rho a_s^3 << 1$, the coupling parameter in the delta-function interaction is proportional to the two-body scattering length a_s; this interaction is known as the Fermi pseudopotential [73]. Here, we analyze the first-order corrections introduced by the Fermi pseudopotential. By including this approximation beyond first-order correction, mean-field theories have been applied to Fermi gases [33, 149]. However, the use of this approximation in strongly interacting regimes leads to an unphysical collapse of the Fermi gas. To go beyond the weakly interacting regime using a zero-range pseudopotential, it is crucial to renormalize the coupling constant. In this Chapter, we introduce a new and convenient way to achieve this renormalization.

The renormalization strategy presented here is based on a zero range interaction of the Fermi pseudopotential form but with a_s replaced by an effective scattering length a_{eff}. The a_{eff} is then calculated by using the exact energies of few particles in a trap. We compare many-particle predictions obtained by using the renormalized interaction potential with diffusion Monte Carlo simulations and alternative mean-field calculations. We find that our renormalization automatically gives the correct behavior in both the strong and weak interaction limits, for both positive- and negative-scattering lengths.

This Chapter is organized as follows. In Section 4.2, we review the noninteracting solutions of the trapped two-component Fermi gas and analyzes corrections introduced by the Fermi pseudopotential. Section 4.3 describes the general ideas of the density renormalization. Section 4.4 develops the renormalization procedure and shows that a simple two-parameter analytical formula can be utilized as an excellent approximation over the whole range from positive-to-negative–two-body scattering lengths. Section 4.5

applies the renormalization to many-particle–mean-field theory and presents some of its predictions. Section 4.6 compares the results obtained using our renormalized mean-field theory with quantum Monte Carlo calculations and with perturbative mean-field calculations. Finally, in Section 4.7, we present the conclusions.

4.2 Perturbative behavior of a trapped two-component Fermi gas

In this section, we analyze the weakly interacting Fermi gas in a harmonic trap. First, we review the solutions of noninteracting Hamiltonian with an arbitrary number of particles [N_1 in component one and N_2 in component two]. Then, we discuss the use of the Fermi pseudopotential to analyze first-order corrections. Finally, we apply degenerate perturbation theory to analyze open-shell systems.

4.2.1 The noninteracting two-component Fermi gas in a trap

Consider an N-particle system in a spherical trap. In the noninteracting limit, the Hamiltonian of the N-particle system can be expanded in single-particle Hamiltonians, e.g.,

$$\mathcal{H} = \sum_{i=1}^{N} h(\mathbf{r}_i), \tag{4.1}$$

where the single-particle Hamiltonians in spherical coordinates are

$$h(\mathbf{r}) = -\frac{\hbar^2}{2m}\nabla^2 + \frac{m\omega^2 r^2}{2}. \tag{4.2}$$

Here, ω is the frequency of the trap and m is the mass of the particles. The single-particle Hamiltonian is spherically symmetric and describes a particle in a trap. The single-particle Schrödinger equation is

$$h(\mathbf{r})\psi_{nlm} = \epsilon_{nl}\psi_{nlm}, \tag{4.3}$$

where the eigenfunctions ψ_{nlm} can be written as

$$\psi_{nlm}(\mathbf{r}) = \frac{u_{nl}(r)}{r} Y_{lm}(\Omega), \tag{4.4}$$

where $Y_{lm}(\Omega)$ are the standard spherical harmonics, and $\Omega = \{\theta, \phi\}$ are the angular coordinates. The radial orbitals are solutions of an effective one-dimensional Schrödinger equation given by

$$u_{nl}(r) = a_{ho}^{3/2}\sqrt{\frac{2n!}{\Gamma(n+l+3/2)}}\exp(-\frac{r^2}{2a_{ho}^2})(r/a_{ho})^{l+1}L_n^{l+1/2}(r^2/a_{ho}^2), \tag{4.5}$$

where $a_{ho} = \sqrt{\hbar/(m\omega)}$ is the trap length. The single particle energies are

$$\epsilon_{nl} = (2n + l + 3/2)\hbar\omega, \tag{4.6}$$

where $n = 0, 1...$ is the number of radial nodes, and $l = 0, 1, ...$ is the orbital angular momentum.

Up to this point, we have omitted the spin dependence in the orbitals. The different components of the Fermi gas can be treated as distinguishable particles which simplifies the calculation. In this case, the spin part of the many-body wave functions completely factors out. The spatial part of the many-body wave functions is now antisymmetric in each component but there is no symmetrization between particles of component one and two. Therefore, the spatial wavefunction of a system with N_1 particles in component 1 and N_2 particles in component 2, where $N_1 + N_2 = N$; the spatial wave function is given by

$$\Psi_{NI}^k = \mathcal{A}(\phi_{n_1^i l_1^i m_1^i}(\mathbf{r}_1), \cdots, \phi_{n_1 l_1 m_1}(\mathbf{r}_{N_1}))\ \mathcal{A}(\phi_{n_2^i l_2^i m_2^i}(\mathbf{r}_{1'}), \cdots, \phi_{n_2^f l_2^f m_2^f}(\mathbf{r}_{N_2'})) =$$
$$\det\begin{vmatrix} \phi_{n_1^i l_1^i m_1^i}(\mathbf{r}_1) & \cdots & \phi_{n_1^i l_1^i m_1^i}(\mathbf{r}_{N_1}) \\ \vdots & & \vdots \\ \phi_{n_1^f l_1^f m_1^f}(\mathbf{r}_1) & \cdots & \phi_{n_1^f l_1^f m_1^f}(\mathbf{r}_{N_1}) \end{vmatrix} \det\begin{vmatrix} \phi_{n_2^i l_2^i m_2^i}(\mathbf{r}_{1'}) & \cdots & \phi_{n_2^i l_2^i m_2^i}(\mathbf{r}_{N_2'}) \\ \vdots & & \vdots \\ \phi_{n_2^f l_2^f m_2^f}(\mathbf{r}_{1'}) & \cdots & \phi_{n_2^f l_2^f m_2^f}(\mathbf{r}_{N_2'}) \end{vmatrix}. \tag{4.7}$$

Here, unprimed coordinates refer to component 1 and primed coordinates to component 2. The quantum numbers $\{n_1^i l_1^i m_1^i\}$ and $\{n_1^f l_1^f m_1^f\}$ correspond to the first and last occupied orbitals of component 1. Similarly, the quantum numbers $\{n_2^i l_2^i m_2^i\}$ and $\{n_2^f l_2^f m_2^f\}$ correspond to the first and last occupied orbitals of component 2. These sets of orbitals characterize the wave function that is labeled by a general quantum number

k. $\mathcal{A}$ is the antisymmetrization operator that can be realized by constructing a Slater determinant [second line of Eq. (4.7)]. The Slater determinant vanishes if an orbital is doubly occupied. Thus, the wave function Ψ^i_{NI} will be nonzero only if all the orbitals in each Slater determinant are different. This is just a mathematical manifestation of the Pauli exclusion principle.

Any Ψ^i_{NI} constructed as in Eq. (4.7) is an eigenfunction of the Hamiltonian (4.1) with energy

$$E^k_{NI} = \sum_{nlm=n^i_1 l^i_1 m^i_1}^{n^f_1 l^f_1 m^f_1} \epsilon_{nl} + \sum_{nlm=n^i_2 l^i_2 m^i_2}^{n^f_2 l^f_2 m^f_2} \epsilon_{nl}. \tag{4.8}$$

Thus, to construct the ground state, we just need to minimize Eq. (4.8). This is achieved by simply selecting the N_1 and N_2 orbitals with the lowest energy.

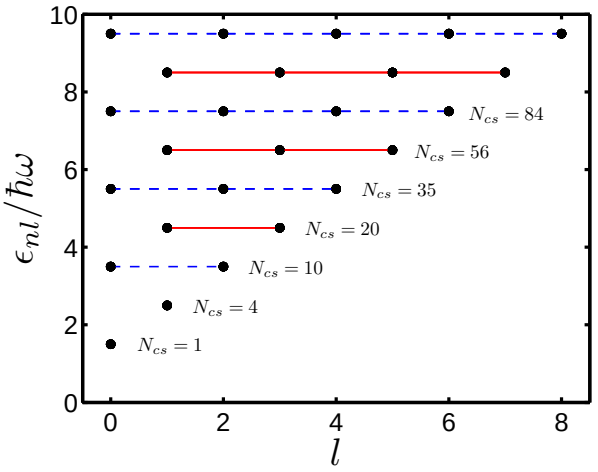

Figure 4.1: Orbital energies ϵ_{nl} as a function of the quantum number l. The number of particles in a closed shell N_{cs} is written next to each shell.

As in Eq. (4.8), the ground-state noninteracting energy E_{NI} can be evaluated as the sum of the noninteracting energies of polarized Fermi gases E^p_{NI} with N_1 and N_2 particles, i.e., $E_{NI}(N) = E^p_{NI}(N_1) + E^p_{NI}(N_2)$. To select the lowest N_i orbitals, we first consider Fig. 4.1. Here, the energies of the orbitals as functions of the angular quantum number l show a clear shell structure. In each shell, the energies of the orbitals are

$(n_s + 1/2)\hbar\omega$ and degeneracy of the orbitals is $n_s(n_s + 1)/2$. The shells are closed at the magic numbers

$$N_{cs} = \frac{n_s(n_s + 1)(n_s + 2)}{6}. \tag{4.9}$$

The ground-state energy of the polarized system in a closed shell has a simple closed form

$$\frac{E^{cs}_{NI}(n_s)}{\hbar\omega} = \frac{(n_s - 1)n_s(n_s + 1)(n_s + 2)}{8} + \frac{3N^{cs}}{2}. \tag{4.10}$$

The $E^{p}_{NI}(N_i)$ can be written in terms of the shell number n_s, the energy of the closed shell subsystem $E^{cs}_{NI}(n_s)$, and the corresponding magic number N^{cs}:

$$E^{p}_{NI}(N_i) = E^{cs}_{NI}(n_s) + \left(\frac{3}{2} + n_s\right)(N - N_{cs})\hbar\omega. \tag{4.11}$$

On the right hand side of Eq. (4.11), the first term is the contribution from the closed-shell fermions while the second term is the contribution from the fermions in the open shell. Here, the shell number n_s represents the number of closed shells. It can be written in terms of the number of particles N_i as

$$n_s = \text{Int}\left[\frac{1}{g[N_i]} + \frac{g[N_i]}{3} - 1\right], \tag{4.12}$$

where

$$g[N_i] = \sqrt[3]{3\left(27N_i - \sqrt{3(243N_i^2 - 1)}\right)}, \tag{4.13}$$

and Int$[x]$ is the integer part of x.

For most N values, the ground-state solutions are degenerate. Only if N_1 and N_2 correspond to the magic N_{cs} is the ground state system not degenerate. Such closed-shell systems are special cases in which all the orbitals couple to zero-angular momentum. The degeneracy for open-shell systems is generally broken by interactions.

4.2.2 Effective versus exact wave function

Here, we discuss first order corrections to the noninteracting energy and the use of zero-range potential instead of finite-range potential. Note that the zero-range potential

presented here provides a qualitatively different treatment of correlations in the system than the zero-range potential presented in Sect.2.2.

Consider the two-component Fermi gas interacting through a short-range potential V_{int}. Consider each component as a distinguishable particle such that the noninteracting wave functions can be written as a product of two Slater determinants, i.e., Eq. (4.7). If the system is dilute, the interaction only depends on the scattering length a_s. However, the first-order perturbation theory correction is

$$E_1 = \langle V_{int} \rangle = \int \int \rho_1(\mathbf{r}_1) V_{int}(\mathbf{r}_1 - \mathbf{r}_2) \rho_2(\mathbf{r}_2) d\mathbf{r}_1 d\mathbf{r}_2. \tag{4.14}$$

Here, ρ_1 and ρ_2 are the densities of components 1 and 2, respectively. Clearly, this correction depends on the shape of the two-body potential V_{int}. To obtain the scattering length a_s dependence we need to include many orders in perturbation theory. In other words, we have to be able to describe correlations of the order of the range of the interaction r_0. Such a description would imply a large configuration interaction (CI) expansion. This treatment is impossible in large systems.

An alternative option for describing the correction due to the scattering properties of V_{int} can be obtained using a Jastrow term to describe the correlations:

$$\Psi = J(r_{11'}, \cdots, r_{22'}) \Psi_{NI}(\mathbf{r}_1, \cdots, \mathbf{r}_N). \tag{4.15}$$

The Jastrow-Slater wave function was discussed in the fixed-node diffusion Monte Carlo (FN-DMC) section in chapter 3. In the Jastrow term, all the pair correlations are explicitly built from the two-body solutions and describe the correct scattering behavior. Thus, the energy correction depends mainly on a and not on the form of V_{int}. However, it is very difficult to work with Eq. (4.15), and its exact implementation is usually restricted to Monte Carlo methods. There are other methods like lowest-order constrained variational [41, 100] that use Eq. (4.15) as a starting point but require some approximations to obtain the energy of the system.

To avoid similarly complicated techniques that deal with real two-body potentials, Fermi proposed a zero-range pseudopotential that explicitly depends on the scattering length and not on the shape of the real potential. This pseudopotential is expressed as

$$V_F(\mathbf{r}) = \frac{4\pi\hbar^2 a_0}{m}\delta(\mathbf{r}). \tag{4.16}$$

Here a_s is the two-body scattering length, and m is the mass of the particles. The first-order correction of this potential is

$$E_1^F = \langle V_p \rangle = \frac{4\pi\hbar^2 a_0}{m}\int \rho_1(\mathbf{r})\rho_2(\mathbf{r})d\mathbf{r}. \tag{4.17}$$

This first-order correction depends on the scattering length and not on the shape of the potential. In the dilute limit, both the Jastrow correlations or the CI expansion for the realistic potential should lead to the same correction expressed in Eq. (4.17). With this pseudopotential, we are able to reproduce the correct energy correction without including the corresponding correlations. Thus, in the Fermi pseudopotential philosophy, the exact solution is replaced by a mean-field solution. In that way, the many-body problem is greatly simplified. All the information about the correlations is lost but the new problem reproduces mean-field properties.

4.2.3 Perturbative behavior of two-component Fermi gas

Here, we use the Fermi pseudopotential to analyze how the degeneracy in open shells is broken in first-order perturbation theory. The Fermi pseudopotential [Eq. (4.16)] can be used to describe the atomic ground state in weakly interacting regimes where $|a_s| \ll a_{ho}$. To obtain the correct first-order correction, we use degenerate perturbation theory. The wave function in a first order correction $\Psi^{(1)}$ is expanded in terms of all the degenerate noninteracting states as

$$\Psi^{(1)} = \sum_{k\,\{E^k = E_{NI}\}} c_k\,\Psi^k_{NI} \tag{4.18}$$

Here, the sum is over all the states Ψ_{NI}^k whose energy corresponds to the ground-state noninteracting energy E_{NI}. The coefficients c_k are obtained by diagonalizing the degenerate submatrix of the Hamiltonian in this basis. Different Ψ_{NI}^k states are coupled with each other through the Fermi pseudopotential.

We can use the fact that Eq. (4.18) resembles a CI expansion to evaluate the matrix elements. Since the noninteracting wave functions Ψ_{NI}^k are formed with single-particle orbitals, only states that differ by less than one orbital per component are coupled. Furthermore, the interaction matrix elements can be easily expanded in matrix elements of the occupied single-particle orbitals.

Since the potential and interactions are spherically symmetric, the total angular momentum is a good quantum number. Therefore, we could could couple states Ψ_{NI}^k to a given total angular momentum and diagonalize the Hamiltonian in that reduced representation. However, since we are only going to consider small N systems, we can diagonalize the "entire" Hamiltonian matrix and then analyze the angular momentum of the solutions.

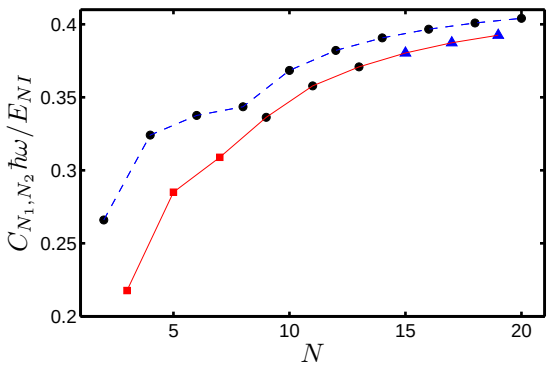

Figure 4.2: C_{N_1,N_2} coefficients divided by E_{NI} as a function of N. Circles correspond to $L = 0$ ground states, squares to $L = 1$ ground states and triangles to $L = 2$ ground states. A solid line connects the odd-N values, while a dashed line connects the even-N values. Figure from Ref. [185].

Degenerate perturbation theory predicts an energy

$$E \approx E_{NI} + \hbar\omega\, C_{N_1,N_2}\, \frac{a_s}{a_{ho}}, \tag{4.19}$$

where C_{N_1,N_2} is a dimensionless quantity obtained through diagonalization. When both N_1 and N_2 correspond to closed shells there is no degeneracy; then C_{N_1,N_2} can be straightforwardly calculated to be [184]

$$C_{N_1,N_2} = 4\pi a_{ho}^3 \int \rho_1^{NI}(\vec{r})\rho_2^{NI}(\vec{r})d\vec{r}. \tag{4.20}$$

Here, $\rho_i^{NI}(\vec{r})$ is the density of a one-component non-interacting gas with N_i fermions of mass m_i, normalized so that $\int \rho_i^{NI}(\vec{r})d\vec{r} = N_i$. Alternatively, one can approximate the ρ_i^{NI} with Thomas-Fermi density profiles. This approximation should be quite accurate in the large N limit but it cannot describe the splitting of the energies related to the angular momentum of the states.

To obtain the C_{N_1,N_2} for open-shell systems, we apply first-order degenerate perturbation theory. This calculation additionally allows us to obtain the angular momentum quantum number L of the ground state. Figure 4.2 and Table 4.1 present the results for $N \leq 20$. The coefficients C_{N_1,N_2} increase monotonically with increasing N and show a slight odd-even staggering. In general, the coefficients C_{N_1,N_2} for even N are comparatively higher than those for odd N, implying a smaller energy for even N than for odd N and suggesting that, even in the perturbative regime, the odd-even oscillations are already present. We note that the C_{N_1,N_2} coefficients for even N shown in Fig. 4.2 clearly reflect the shell closure at $N = 8$.

4.3 Density renormalization idea

The use of the Fermi pseudopotential has been extended beyond first-order perturbation theory [20]. This extension has to be done with caution because a full diagonalization of a Hamiltonian with an attractive delta-function interaction (in 3D) would

Table 4.1: Angular momentum L and coefficients C_{N_1,N_2} for the ground state of two-component Fermi gases in the weakly attractive regime. Here, we consider $N_2 = N_1$ for even N and $N_1 = N_2 + 1$ for odd N.

N	L	C_{N_1,N_2}	N	L	C_{N_1,N_2}
2	0	$\frac{2}{\sqrt{2\pi}}$	12	0	12.2274
3	1	$\frac{3}{\sqrt{2\pi}}$	13	0	13.1651
4	0	$\frac{13}{2\sqrt{2\pi}}$	14	0	15.2382
5	1	$\frac{15}{2\sqrt{2\pi}}$	15	2	16.1642
6	0	$\frac{11}{\sqrt{2\pi}}$	16	0	18.2445
7	1	$\frac{12}{\sqrt{2\pi}}$	17	2	19.1735
8	0	$\frac{31}{2\sqrt{2\pi}}$	18	0	21.2476
9	0	$\frac{145}{8\sqrt{2\pi}}$	19	2	$\frac{1779}{32\sqrt{2\pi}}$
10	0	9.21052	20	0	$\frac{1945}{32\sqrt{2\pi}}$
11	0	10.1980			

always lead to an infinitely bound state. This unphysical collapse can be avoided if the description of the system is restricted to a mean-field level of approximation.

For example, in Ref. [20], the Gross-Pitaevskii equation with Fermi-pseudopotential interactions is solved to describe a BEC. The Gross-Pitaevskii equation emerges from mean-field theory, and, for that reason, the solutions are well behaved. When the scattering length becomes large enough in magnitude and negative, the system collapses. However, this is not an artifact of the zero-range interaction, but a real physical effect that has been experimentally verified [151].

A similar approach can be used to analyze fermionic systems. For two-component Fermi gases, the use of the Fermi pseudopotential can also be extended beyond first-order perturbation theory. For this system, we would use the Hartree-Fock (HF) level of approximation, which produces well-behaved results for small a_s. However, for large and negative scattering lengths, the HF solutions collapses. This collapse occurs in a regime where the Fermi pseudopotential approximation is no longer justified. In this section, we propose a renormalization method to extend the validity of a zero-range pseudopotential to large scattering lengths.

For the remainder of the Chapter, we consider a system of fermions in a spherically symmetric harmonic oscillator trap at temperature $T = 0$. The Hamiltonian that we adopt is

$$\mathcal{H} = \sum_i \left(-\frac{\hbar^2}{2m}\nabla_i^2 + \frac{1}{2}m\omega^2\mathbf{r}_i^2 \right) + \sum_{i<i'} \frac{4\pi\hbar^2 a_{eff}}{m}\delta(\mathbf{r}_i - \mathbf{r}_{i'}). \tag{4.21}$$

This Hamiltonian cannot be diagonalized exactly, since the delta-function interaction is too singular and would produce divergent results [62]. Therefore, full diagonalization of a Hamiltonian with delta-function interactions requires a momentum cut-off renormalization even in the weakly interacting limit. This type of renormalization has been carried out, for example, in Refs.[107, 28, 114, 152, 98, 165, 156, 131, 108], to name a few such studies. However, such a renormalization is unnecessary at small or modest scattering lengths when the system is studied at a mean-field level with zero-range interactions. The mean-field theories are well behaved in this limit. To go beyond the weakly interacting limit of mean-field theory, we propose a density-dependent renormalization of the coupling parameter that is intended to apply even in the long-wavelength limit.

The idea is to extract a_{eff} from the calculation of a few-body system that can be solved exactly. The premise is that the renormalized scattering length extracted from few-body systems will be close to the a_{eff} that governs the large N limit. The level of approximation we adopt to solve the many-body Hamiltonian is the same one we use to solve the corresponding Schrödinger equation for a few-body system. For example, if we want to diagonalize this Hamiltonian in the random-phase approximation (RPA), we would use RPA for the few-body system and obtain the renormalization by matching exact and RPA observables.

However, it is important to carefully select the appropriate level of approximation. An explicitly correlated wave function or an extensive configuration interaction (CI) wave function can produce divergent results, and a momentum cutoff renormalization is necessary. Since we want to obtain and apply a density renormalization without

the necessity of introducing a momentum renormalization, we need to carefully select the level of approximation in the wave function. The HF approximation does not introduce explicit interparticle correlations, as the only correlations included are "exchange correlations" from the Pauli exclusion principle. This makes the HF wave function a suitable approximation to adopt in our renormalization technique, since it does not require a momentum renormalization.

Before proceeding with the extraction of a_{eff}, it is important to analyze its functional dependence. Since we want to extract a_{eff} valid in the large N limit, we consider the homogenous system. Dimensional analysis suggests that, in an infinite, dilute and uniform Fermi gas the only parameter that characterizes the behavior of the system is the dimensionless combination $k_f a_s$ of the Fermi momentum k_f and a_s [113]. Throughout this chapter the Fermi momentum is defined as $k_f \equiv (6\pi^2\rho)^{1/3}$ where the density is just the one-spin component density. If we were applying the renormalized scattering length a_{eff} to an infinite uniform system, the only relevant parameter would be $k_f a_{eff}$. This suggests that $k_f a_{eff}$ has to be a function of $k_f a_s$. So, we propose the following functional dependence for the effective scattering length:

$$a_{eff} \equiv \frac{\zeta(k_f a_s)}{k_f}. \tag{4.22}$$

We see below that the renormalization function, $\zeta(k_f a_s)$, will have the desired behavior in the limiting cases, becoming independent of $k_f a_s$ in the unitarity limit ($|a_s| \to \infty$) and reproducing the relation $a_{eff} = a_s$ in the weakly interacting limit ($k_f a_s \ll 1$). The unrenormalized Fermi pseudopotential can be obtained by setting the renormalization function to $\zeta^F(k_f a_s) = k_f a_s$. We consider that Eq.(4.22) holds even with the inclusion of a trapping potential. The renormalized scattering length a_{eff} can be viewed as accounting, to some extend, for the correlations neglected in the mean-field wave functions.

The renormalization function is intimately related with the equation of state,

as we will show in using the T-F approximation. Therefore, sophisticated many-body solutions of the energy per particle in the BCS-BEC crossover can be readily used to extract the renormalization function. For example, quantum Monte Carlo results from Ref. [7] provide probably the most reliable solutions to extract ζ. However, it is not in the spirit of the method presented here to use such a sophisticated method to extract ζ, but, rather to use simple few-body solution to obtain an approximate ζ.

4.4 Renormalization procedure for two trapped particles

The simplest system that can be used to extract the renormalization function is two particles in a trap. To obtain the renormalized scattering length we solve (4.21) for two opposite-spin fermions in the HF approximation. The ground state energies in this approximation are matched with the exact energies of the system for different values of the bare two-body scattering length a_s. From this procedure we extract the functional dependence of a_{eff} on a_s. The spectrum of two opposite-spin fermions in a trap having a specified scattering length a_s and zero-range interactions can be determined exactly [35, 17, 22, 21]. This solution represents the ideal case in which the spectrum only depends on a_s and the density (characterized by the trap length). Then, Eq. (4.21) can be solved numerically for two particles using a HF wave function.

In choosing to extract a_{eff} from a two-body system, we are implicitly assuming that two-body correlations are the most important in the many-body system. This assumption is reasonable for two-spin-component fermions with short-range interactions because the probability of finding more than two fermions close enough to interact is significantly reduced by Pauli repulsion.

4.4.1 Exact Energies

The zero-range pseudopotential proposed by Yang and Huang [95] and presented in Sec. 2.2 has the necessary ingredients to represent the exact solutions. The boundary

conditions imposed by this pseudopotential produce the correct energies and correlations of the system. The solutions of two particles in trap interacting through the Yang-Huang pseudopotential were presented in Sec. 2.3. Here, we select the appropriate energy branch to generate the renormalization function.

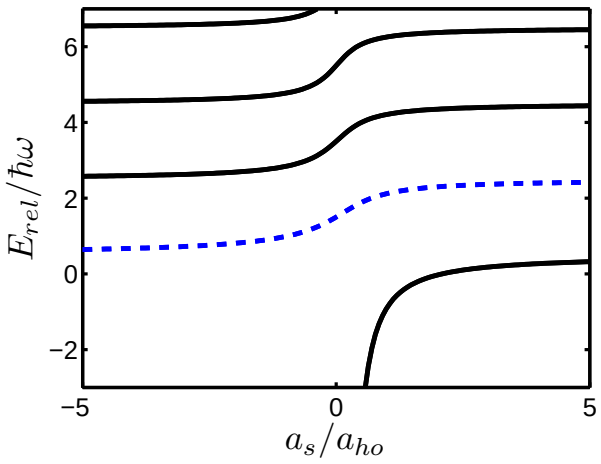

Figure 4.3: Spectrum E_{rel} as a function of a_s. The dashed blue line corresponds to the energy branch selected for the renormalization procedure developed in this study.

Figure 4.3 shows the spectrum of E_{rel} [Eq. (2.13)] as a function of the scattering length. Since we are interested in describing the ground state solution, we focus on the lowest energy curves. The lowest curve for $a > 0$ of the spectrum describes the formation of a molecule, where interparticle correlations are fundamental. One anticipates that a HF wave function would be a terrible approximation for such a state in which the two atoms are bound together to form a molecular eigenstate. However, because we do not consider molecule formation in this work, we will consider instead the second branch in Fig. 4.3 for the renormalization. The renormalization for the positive scattering length will only be valid when the two-body potential does not support a bound state or we are interested in describing the atomic ground state with no molecule formation. The energies used for the renormalization are $E_{CM} = 3/2\hbar\omega$ and the energy branch where $1/2\hbar\omega < E_{rel} < 5/2\hbar\omega$. This branch of solutions is a smooth curve that gives the correct

noninteracting energy at $a_s = 0$.

4.4.2 Mean-field solution

Next we determine a renormalization function $\zeta(k_f a_s)$ that, applied to the system of two particles in a trap and using the HF approximation, yields the exact results obtained in the previous section.

To obtain the HF solution of two opposite-spin particles in a trap, we utilize a product wave function having the same orbital for both particles. Thus, the two-body spatial wave function is

$$\Psi(\mathbf{r}_1, \mathbf{r}_2) = \psi(\mathbf{r}_1)\psi(\mathbf{r}_2), \tag{4.23}$$

and the spin part is antisymmetric. We introduce this trial wave function into the Hamiltonian and obtain the energy functional

$$\mathcal{E}(\psi) = \int \left(2\psi(\mathbf{r}) \left(-\frac{\hbar^2}{2m}\nabla^2 + \frac{1}{2}m\omega^2\mathbf{r}^2 \right) \psi(\mathbf{r}) + \frac{4\pi\hbar^2\zeta(k_f a_s)}{mk_f}\psi(\mathbf{r})^4 \right) d\mathbf{r}. \tag{4.24}$$

Minimization of this energy functional determines the ground-state energy and wave function. The minimization is done with respect to the orbital $\psi(\mathbf{r})$ as in a standard HF procedure [66]. But prior to carrying out this minimization of Eq. (4.24), we must choose how to evaluate k_f. Since its formal definition is $k_f \equiv (6\pi^2\rho)^{1/3}$, this means that k_f depends at each r-value on $\psi(\mathbf{r})$. For many-particle systems, we will use local density approximation to evaluate k_f. However, the application of a local density approximation for a system of two particles does not seem physically correct. Thus, for two particles, we consider the expectation value of $\overline{k}_f$ to be the more appropriate quantity

$$\overline{k}_f \equiv \int k_f(\mathbf{r})\psi(\mathbf{r})^2 d\mathbf{r} = \int (6\pi^2\psi(\mathbf{r})^2)^{1/3}\psi(\mathbf{r})^2 d\mathbf{r}. \tag{4.25}$$

The minimization procedure leads to a Schrödinger-type equation, where $\psi^2(\mathbf{r})$ is the

1-particle density:

$$\left(-\frac{\hbar^2}{2m}\nabla^2+\frac{1}{2}m\omega^2\mathbf{r}^2+\frac{4\pi\hbar^2\zeta(\overline{k}_f a_s)}{m\overline{k}_f}\psi(\mathbf{r})^2+\right.$$
$$\left.\frac{8\pi\hbar^2(6\pi^2)^{1/3}\overline{\rho}}{3m}\left(\frac{\zeta'(\overline{k}_f a_s)a_s}{\overline{k}_f}-\frac{\zeta(\overline{k}_f a_s)}{\overline{k}_f^2}\right)\psi(\mathbf{r})^{2/3}\right)\psi(\mathbf{r})=\epsilon\psi(\mathbf{r}), \quad (4.26)$$

where ϵ is a Lagrange multiplier that represents the chemical potential. The relation between ϵ and the energy is not as straightforward as in the HF case, primarily because of the appearance of $\zeta'(k_f a_0)$. Note that $\psi(r)^{2/3}$ is supposed to be evaluated on a branch for which it is real and positive everywhere. Here and in the following, $\zeta'(x)\equiv d\zeta(x)/dx$.

Equation (4.26) corresponds to the Gross-Pitaevskii equation for 2 particles with a renormalized scattering length $a_{eff}=\zeta(\overline{k}_f a_s)/\overline{k}_f$. After solving Eq. (4.26) we use Eq. (4.24) to evaluate the energy. The basic idea is that, for any chosen bare two-body scattering length a_s, we need to find $\zeta(\overline{k}_f a_0)$ such that the energy of the ground state of Eq. (4.24) matches exactly $E_0=E_{CM}+E_{rel}$ with $E_{CM}=3\hbar\omega/2$ and E_{rel} obtained from Eq. (2.13). From our numerical experience, the functional dependence of ζ on $\overline{k}_f a_s$ appears to be uniquely defined by the set of equations Eqs. (2.13), (4.24), (4.25), and (4.26).

There are two self-consistent procedures involved in this calculation. To solve Eq. (4.26), we follow the standard HF procedure, adopting noninteracting solutions as the initial guess for the orbitals. Then, we iterate Eq. (4.26) until convergence is achieved. For this procedure, we need the functional forms of $\zeta(\overline{k}_f a_s)$ and $\zeta'(\overline{k}_f a_s)$ over a range of $\overline{k}_f a_s$ values since $\overline{k}_f$ is changing in each iteration. This means that we cannot find the exact renormalization function $\zeta(\overline{k}_f a_s)$ at any fixed value of a_s without knowledge of the functional form of $\zeta(\overline{k}_f a_s)$ at nearby values. To solve this problem, we calculate $\zeta(\overline{k}_f a_s)$ self-consistently over the *entire* range in $\overline{k}_f a_s$ that is of interest. First, we select a set of scattering length (a_s) values that cover the entire range of interest. For an initial trial $\zeta^{(0)}(\overline{k}_f a_s)$, we solve Eqs. (4.26) and (4.24) at each a_s, obtaining the energy E, $\overline{k}_f$, the wave function and ϵ. Then, to obtain a new $\zeta^{(1)}(\overline{k}_f a_s)$, we look

for the value of the scattering length $\widetilde{a}_0$ for which $E_{exact}(\widetilde{a}_0) = E$, and we generate a new renormalization function that satisfies $\zeta^{(1)}(\overline{k}_f\widetilde{a}_0) = \zeta^{(0)}(\overline{k}_f a_s)$. The modification of the renormalization function is evidently in the abscissa rather than in the ordinate. This is a convenient way to approach this calculation. Once we have carried out the matching procedure with the whole set of scattering-length (a_s) values, we generate the next iteration for $\zeta^{(1)}(\overline{k}_f a_s)$ and its derivative by interpolation.

In the next iteration, $\zeta^{(0)}(\overline{k}_f a_s)$ is replaced by $\zeta^{(1)}(\overline{k}_f a_s)$, and we repeat the energy-matching step for the whole set of a_s values. This procedure is repeated a few times until it converges to give a single correct renormalization function $\zeta(\overline{k}_f a_s)$. Note that this iterative procedure determines a "numerically exact" renormalization function $\zeta(\overline{k}_f a_s)$. Because the iteration procedure is efficient, in five iterations we obtain nine digits of agreement between E_{exact} and E over the entire a_s range. However, it is important to introduce a sensible initial trial renormalization function $\zeta^{(0)}(\overline{k}_f a_s)$. Many trial $\zeta^{(0)}(\overline{k}_f a_s)$ functions, like $\zeta^{(0)}(\overline{k}_f a_s) = \overline{k}_f a_s$, would produce collapse of the two-fermion wave function for large and negative a_s. To avoid this collapse, we propose an initial trial $\zeta^{(0)}(\overline{k}_f a_s)$ which is close to the correct $\zeta(\overline{k}_f a_s)$. We do this by choosing a qualitatively correct functional form with a few free parameters, and we then find the set of parameters that best reproduce the exact two-body energies.

The final numerical results obtained for the renormalization function $\zeta(\overline{k}_f a_s)$ are accurately approximated by the monotonic functional form $\zeta_0(\overline{k}_f a_s) = A + B\arctan(C + D\overline{k}_f a_s)$, where A and B are chosen to have the corresponding maximum and minimum values at $a_s \to \pm\infty$, and C and D are chosen to obey $\zeta(\overline{k}_f a_s) \to \overline{k}_f a_s$ for $\overline{k}_f a_s << 1$. The maximum value is $\zeta^{max} = 2.182$, and minimum value is $\zeta^{min} = -1.392$. These values lead to $A = 0.395$ and $B = -1.138$. Getting the correct behavior for $\overline{k}_f a_s << 1$ requires $C \equiv \arctan(-A/B) \approx 0.362$ and $D \equiv -(1 + C^2)/B \approx -0.994$. Thus there are only two independent parameters A, and B specified at this level of approximation. Figure 4.4 compares our numerical results for $\zeta(\overline{k}_f a_s)$ with this arctangent approxima-

tion:

$$\zeta_0(\overline{k}_f a_s) = 0.395 - 1.138 \arctan(0.362 - 0.994\overline{k}_f a_s). \tag{4.27}$$

Figure 4.5 displays the fractional error in $\zeta_0(\overline{k}_f a_s)$ defined as $(\zeta(\overline{k}_f a_s) - \zeta_0(\overline{k}_f a_s))/\zeta(\overline{k}_f a_s)$ and shows a maximum error of approximately 5%.

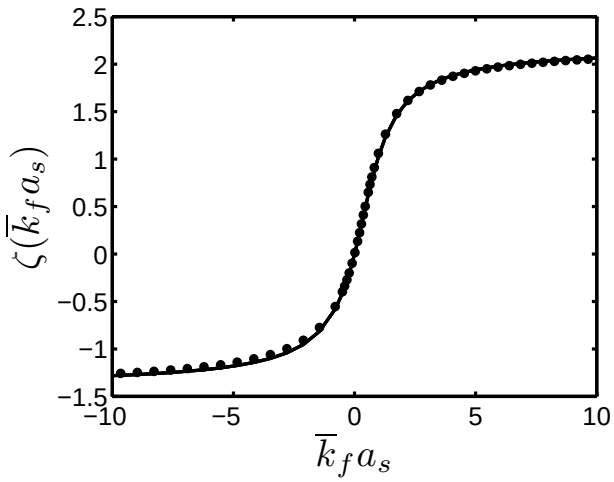

Figure 4.4: Effective scattering length $\zeta(\overline{k}_f a_s)$ (circles) and its analytical approximation $\zeta_0(\overline{k}_f a_s)$ (solid line). Figure from Ref. [183].

Now that the renormalization function has been determined, other observables can be tested for the two-particle system. Interestingly, there is a numerically exact agreement between the the trapping-potential-energy expectation values measured with the exact wave function and the mean-field-renormalized wave function.However, the one-particle density profiles calculated using the exact wave functions and the mean-field-renormalized wave function are only in qualitative agreement, i.e., for scattering lengths of large magnitude where $|\overline{k}_f a_s| >> 1$.

4.5 Application to many-particle systems

This section presents different many-particle approximations for which the renormalized scattering length can be used. The renormalization procedure is designed to be used in the HF approximation. However we will see that simpler approximations

Table 4.2: Exact numerical values of $\zeta(x)$.

x	$\zeta(x)$	x	$\zeta(x)$	x	$\zeta(x)$
$-\infty$	-1.392	-1.6582	-0.82404	4.9199	1.9248
-11.937	-1.2818	-1.3097	-0.73716	5.2872	1.9426
-11.394	-1.2767	-0.96693	-0.62355	5.6545	1.9581
-10.85	-1.2712	-0.63317	-0.47254	6.0219	1.9717
-10.306	-1.2651	-0.31351	-0.27173	6.3892	1.9838
-9.7626	-1.2584	-0.014329	-0.014242	6.7566	1.9946
-9.2193	-1.251	0.26087	0.2863	7.1239	2.0042
-8.6758	-1.2428	0.51684	0.59122	7.4913	2.0129
-8.1326	-1.2336	0.76339	0.86101	7.8586	2.0208
-7.5895	-1.2231	1.0072	1.0787	8.226	2.028
-7.0467	-1.2113	1.2507	1.2474	8.5933	2.0346
-6.504	-1.1977	1.6166	1.4309	8.9607	2.0406
-5.9617	-1.182	1.9829	1.5585	8.0056	2.0238
-5.4197	-1.1635	2.3497	1.6508	8.9117	2.0398
-4.8782	-1.1416	2.7166	1.7201	9.523	2.04896
-4.3373	-1.1153	3.0837	1.7737	9.8669	2.0536
-3.7973	-1.0829	3.4509	1.8164	10.895	2.0657
-3.2585	-1.0423	3.8181	1.8512	11.311	2.0699
-2.7216	-0.99004	4.1853	1.88	11.998	2.0763
-2.1875	-0.92043	4.5526	1.9042	$+\infty$	2.182

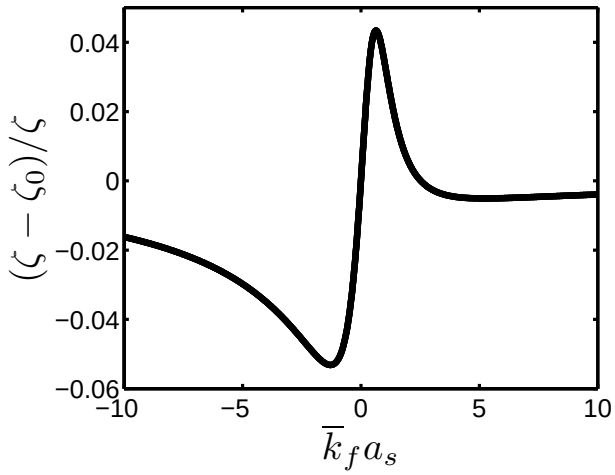

Figure 4.5: Fractional error in our analytical approximation to the numerical renormalization function, $\zeta_0(\overline{k}_f a_s)$. Figure from Ref. [183].

like TF or a variational trial wave function will yield equally effective results in the large N limit. The variational wave function we use is the noninteracting wave function rescaled in the radial direction by a factor λ [as in Eq. (4.28)], where λ is the variational parameter. For example, Figure 4.6 a comparison for the ground state energy of a two-component Fermi gas in an spherical trap in the large N limit. The result obtained with the approximate $\zeta_0(k_f a_s)$ in conjunction either with a variational trial-wave function or with the TF method are in good agreement with the full HF calculation with the exact $\zeta(k_f a_s)$. The difference between the results stems mainly from the replacement of the exact $\zeta(k_f a_s)$ with the approximate $\zeta_0(k_f a_s)$. If we use the exact $\zeta(k_f a_s)$ for all the methods, the energies agree to at least 3 digits. In systems having a small number of particles, the HF method is, of course, more reliable than the variational or the TF method.

4.5.1 Variational

The simplest approximation [148] utilizes a trial wave function that is a simple radial rescaling of the noninteracting wave function:

$$\Psi_\lambda(\mathbf{r}_1, \mathbf{r}_2, ..., \mathbf{r}_N) = \frac{1}{\lambda^{3N/2}} \Psi_{NI}(\mathbf{r}_1/\lambda, \mathbf{r}_2/\lambda, ..., \mathbf{r}_N/\lambda). \tag{4.28}$$

The expectation value of the renormalized Hamiltonian (4.21) can be separated into two terms, $E(\lambda) = E_{HO}(\lambda) + E_{int}(\lambda, a_s)$, where

$$\begin{aligned} E_{HO}(\lambda) &= \langle \Psi_\lambda | \sum_i \left(-\frac{\hbar^2}{2m} \nabla_i^2 + \frac{1}{2} m\omega^2 \mathbf{r}_i^2 \right) | \Psi_\lambda \rangle \,, \\ E_{int}(\lambda, a_s) &= \langle \Psi_\lambda | \sum_{i<i'} \frac{4\pi\hbar^2 a_{eff}}{m} \delta(\mathbf{r}_i - \mathbf{r}_{i'}) \, | \Psi_\lambda \rangle \,. \end{aligned} \tag{4.29}$$

The energy of this trial wave function is calculated as a function of the variational-scale parameter λ for the renormalized Hamiltonian (4.21). The noninteracting wave function is a Slater determinant formed with the occupied spin orbitals. The E_{HO} is simple to calculate, as it requires only a change of variables to determine the λ

dependence in Eq. (4.29) in conjunction with the known results of the noninteracting ground state, i.e.,

$$E_{HO}(\lambda) = E_{NI}\left(\frac{1}{2\lambda^2} + \frac{\lambda^2}{2}\right). \tag{4.30}$$

When we apply the renormalization locally as a function of the density, the interaction energy E_{int} can be written as

$$E_{int}(\lambda, a_s) = \frac{4\pi\hbar^2}{m}\int \frac{\zeta(k_f^\lambda(\mathbf{r})a_s)}{k_f^\lambda(\mathbf{r})}\rho_\lambda^2(\mathbf{r})d\mathbf{r}. \tag{4.31}$$

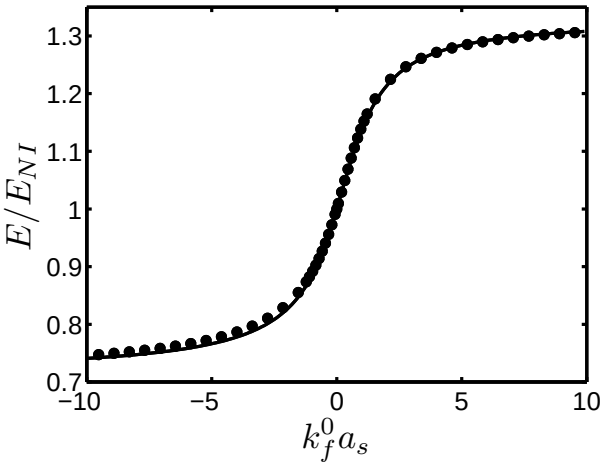

Figure 4.6: Ratio of the total energy to the noninteracting energy for a spherically trapped two-component degenerate Fermi gas in the large N limit. The circles correspond to HF calculations for 2280 particles using $\zeta(k_f a_s)$, while the solid line corresponds to either the variational solution, Eq. (4.33), or the TF solution, Eq. (4.45) using the approximate renormalization function $\zeta_0(k_f a_s)$; note that the curves are indistinguishable on the scale of the figure. Figure from Ref. [183].

In this equation, ρ is the density of one spin component, and $k_f^\lambda(\mathbf{r}) \equiv (6\pi^2\rho_\lambda(\mathbf{r}))^{1/3}$. In the large N limit, the density of the noninteracting wave function can be replaced by the TF density of the noninteracting system [148]. The density corresponding to our trial wave function is a simple radial rescaling in which the density in the high-N limit

becomes

$$\rho_\lambda(\mathbf{r}) = \begin{cases} \frac{\sqrt{6N}}{3\pi^2 a_{ho}^3 \lambda^3}\left(1 - \frac{r^2}{2a_{ho}^2\lambda^2(3N)^{1/3}}\right)^{3/2} & \text{if } r^2 < R_c^2, \\ 0 & , \quad \text{otherwise.} \end{cases} \tag{4.32}$$

Here N is the total number of particles, and $R_c = \sqrt{2}a_{ho}\lambda(3N)^{1/6}$ is the radius of the Fermi gas. In the large N limit, the total energy can be expressed in units of the noninteracting energy:

$$E/E_{NI} = \frac{1}{2\lambda^2} + \frac{\lambda^2}{2} + \frac{1}{\lambda^2}F\left(\frac{k_f^0 a_s}{\lambda}\right). \tag{4.33}$$

Here λ is the scaling parameter, $k_f^0 = \sqrt{2}(3N)^{1/6}/a_{ho}$ is the Fermi momentum of the noninteracting system at the trap center, and F is

$$F(\gamma) = \frac{4^4}{9\pi^2}\int_0^1 (1-x^2)^{5/2}x^2\zeta\left(\gamma\sqrt{1-x^2}\right)dx. \tag{4.34}$$

Equations (4.33)and (4.35) can be used to describe either the bare Fermi or the renormalized interaction. First, consider the bare Fermi pseudopotential prediction. To use the Fermi pseudopotential within our renormalization approach, we replace ζ with $\zeta^F(y) = y$. Then Eq. (4.35) can be easily solved, e.g.,

$$F(\gamma) = \frac{4^4}{9\pi^2}\int_0^1 (1-x^2)^{5/2}x^2\zeta^F\left(\gamma\sqrt{1-x^2}\right)dx = \frac{4096}{2835\pi^2}\frac{k_f^0 a_s}{\lambda}. \tag{4.35}$$

Therefore, the energy of the system is given by

$$E/E_{NI} = \frac{1}{2\lambda^2} + \frac{\lambda^2}{2} + \frac{4096}{2835\pi^2}\frac{k_f^0 a_s}{\lambda^3}. \tag{4.36}$$

Figure 4.7 (a) presents the energies [Eq. (4.36)] as functions of λ for some selected $k_f^0 a_s$. We can clearly see that the interaction term, which goes as $1/\lambda^3$, is the leading term for small λ. Therefore, for $a_s < 0$, the energy becomes infinitely negative. This is always true independent of the scattering-length strength. However, for small and negative $k_f^0 a_s$, there is a metastable state corresponding to a local minimum of E [cf. the red curve in Fig. 4.7 (a)]. This metastable state is considered the physical gaslike state. For some critical value of $k_f^0 a_s \approx -1.21$ the local minimum disappears, which produces a

collapse of the gaslike state (see, e.g., the green curve in Fig. 4.7 (a)). This reasoning is similar to the collapse picture of a trapped bosonic system presented in Ref. [20]. However, this analysis is incorrect in our case since the Fermi pseudopotential is only valid for $|k_f^0 a_s| \ll 1$. Now, we see how this behavior changes with the introduction of the renormalized interaction.

The evaluation of Eq. (4.35) for the renormalized ζ function obtained from the two-body problem must be calculated numerically unless further approximations are made. The energy results obtained using Eq. (4.33) are shown in Fig. 4.6. We observe that the energies remain finite for all scattering-length values, and no collapse occurs. In the unitarity limit, the behavior can be calculated exactly:

$$F(\gamma \to -\infty) = \frac{4^4 \zeta^{min}}{9\pi^2} \int_0^1 (1-x^2)^{5/2} x^2 dx = \frac{5\zeta^{min}}{9\pi}. \tag{4.37}$$

Therefore, at unitarity, the energy is:

$$E_U/E_{NI} = \frac{1}{2\lambda^2} + \frac{\lambda^2}{2} + \frac{5\zeta^{min}}{9\pi} \frac{k_f^0 a_s}{\lambda^2}. \tag{4.38}$$

To illustrate the behavior of the energies obtained with the renormalization, we show three curves predicted by Eq. (4.33) in Fig. 4.7 (b). For the entire range of interactions, the energy of the system (the minimum of the curve) remains finite, ranging from $0.713\, E_{NI}$ to $1.33\, E_{NI}$. Thus our renormalization circumvents the collapse that would occur for the bare Fermi pseudopotential.

Interestingly, the variational method presented here is similar to the K-harmonic hyperspherical method developed in Refs. [149, 150]. Furthermore, it was shown in Ref. [150] that the matrix elements calculated with the variational and K-harmonic hyperspherical method are identical in the large N limit if we replace λ by the hyperradius R. For that reason, Eqs. (4.36,4.38) are equivalent to Eq. (3.11) from Ref. [149] and Eq. (33) from Ref. [150], respectively. Therefore, the energy curves in Figs. 4.7 (a) and (b) can be seen as hyperspherical potential curves. This relationship is an informative new insight.

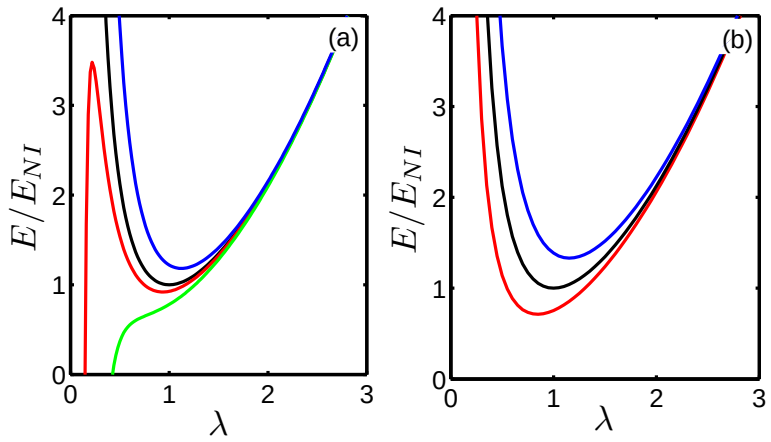

Figure 4.7: (a) Variational energy obtained with the Fermi pseudopotential prediction. Black curve is the noninteracting energy. Blue curve is the prediction for $k_f^0 a_s = 1.5$. The red and green curves correspond to the negative scattering length side with $k_f^0 a_s = 0.5$ and $k_f^0 a_s = -1.5$, respectively. (b)Variational energy as a function of λ for the renormalized interaction, in units of the noninteracting total energy. The solid curve corresponds to $k_f^0 a_s = 0$; the dashed curve corresponds to $k_f^0 a_s = -\infty$; the dotted-dashed curve corresponds to $k_f^0 a_s = \infty$. The minimum of the energy functional for $k_f^0 a_s = -\infty$ occurs at $\lambda = 0.844$, which represents the ratio between the cloud radius at unitarity and the noninteracting cloud radius.

4.5.2 Thomas-Fermi results

In this subsection we review the TF approximation using the renormalization function. The TF approximation was previously used to study a two-component Fermi gas with zero-range pseudopotentials [153], but in that study no renormalization was considered. As in the previous subsection, all the results presented here can be applied to the Fermi pseudopotential predictions by replacing the renormalized function by $\zeta^F(y) = y$ or a_{eff} by a_s.

TF is a local density approximation in which, at each position r inside the trap, the single particle orbitals are approximated by plane waves. Since we consider each component as a distinguishable particle, the wave function at each r is a product of two Slater determinants, one for each component. The orbitals are characterized by the vector momentum $\mathbf{k}$. The orbitals are filled uniformly up to a level $k_f(r)$, which is the same for spin-up and spin-down fermions. The value of $k_f(r)$ will depend on the distance r from the trap center, and on the number of particles in the system. For a uniform system, the value of k_f is a constant that characterizes the density of the system.

To calculate the local energy, we need to sum over all the states at that position. For example, the kinetic energy term K for the one-spin component is

$$K = \frac{1}{2m}\sum_{\mathbf{k}} \langle \mathbf{k}|\mathbf{p}^2|\mathbf{k}\rangle = \frac{\hbar^2}{2m}\sum_{\mathbf{k}} \mathbf{k}^2 \langle \mathbf{k}|\mathbf{k}\rangle = \frac{V\hbar^2}{2m(2\pi)^3}\int k^2 d^3k = \frac{V\hbar^2}{20\pi^2 m}k_f^5. \quad (4.39)$$

Here V is the volume of integration that will disappear when we consider the local energy. This volume is small in comparison with the external potential (in this case the trap) characteristic length but is big enough to contain many particles. Thus, k_f and V_{ext} can be considered constant during the integration. The calculation of the expectation value of an external-trapping potential is then straightforward. We obtain

$$\langle V_{ext}\rangle = \frac{V}{6\pi^2}V_{ext}k_f^3, \quad (4.40)$$

which is just the volume times the density of particles of one component $\rho_\uparrow = \rho_\downarrow = k_f^3/(6\pi^2)$ times the external potential at that position. Now we proceed to evaluate the interaction term,

$$\langle V_{int}\rangle = \sum_{\mathbf{kk'}} \langle \mathbf{kk'}|V_{int}|\mathbf{kk'}\rangle = \frac{1}{(2\pi)^6}\frac{4\pi a_{eff}\hbar^2}{m}\int_0^{k_f}\int_0^{k_f}\int\int \delta(\mathbf{x}-\mathbf{x}')d\mathbf{x}'d\mathbf{x}d^3k'd^3k$$
$$= V\frac{4\pi a_{eff}\hbar^2}{m}\frac{k_f^3}{6\pi^2}\frac{(k_f)^3}{6\pi^2} = V\frac{4\pi\hbar^2}{m}\frac{k_f^5\zeta(k_f a_s)}{(6\pi^2)^2} \quad (4.41)$$

The second to last equality is simply $4\pi a_{eff}\hbar^2/m\, V\rho_\uparrow\rho_\downarrow$, which is the Hartree term.

Combining the expectation value of the kinetic energy, the external potential energy, and the interaction energy, we obtain the total energy. For the case of two equally numerous spin components, the local energy (per unit volume) is

$$\mathcal{E}(k_f) = E(k_f)/V = \frac{\hbar^2}{2m}\frac{k_f^5}{5\pi^2} + V_{ext}\frac{k_f^3}{3\pi^2} + \frac{4\pi\hbar^2}{m}\frac{k_f^5\zeta(k_f a_s)}{(6\pi^2)^2}. \quad (4.42)$$

In an infinite uniform system, where $V_{ext} = 0$, the energy is

$$\mathcal{E}(k_f) = \frac{\hbar^2}{2m}\frac{k_f^5}{5\pi^2} + \frac{4\pi\hbar^2}{m}\frac{k_f^5\zeta(k_f a_s)}{36\pi^4}. \quad (4.43)$$

Equation (4.43) gives the equation of state for a uniform gas The ratio between the total energy and the noninteracting energy has a simple form that only depends on $k_f a_s$:

$$\mathcal{E}(k_f)/\mathcal{E}_{NI}(k_f) = 1 + \frac{10\zeta(k_f a_s)}{9\pi}. \quad (4.44)$$

Using Eq. (4.42), we construct an energy functional by integrating the local energy over all space.

$$E = \int d\mathbf{r}\left(\frac{\hbar^2}{2m}\frac{k_f(\mathbf{r})^5}{5\pi^2} + V_{ext}(\mathbf{r})\frac{k_f(\mathbf{r})^3}{3\pi^2} + \frac{4\pi\hbar^2}{m}\frac{k_f(\mathbf{r})^5\zeta(k_f a_s)}{36\pi^4}\right). \quad (4.45)$$

To find the ground state, we have to minimize the energy under the constraint that the total number of particles is fixed. This constraint can be implemented by introducing a Lagrange multiplier μ_0, which is usually called the chemical potential. Thus, the

minimization of Eq. (4.45) for a fixed number of particles is reduced to the minimization of

$$\Lambda \equiv E - \mu_0 N = E - \mu_0 \int d\mathbf{r} \frac{k_f(\mathbf{r})^3}{3\pi^2}, \tag{4.46}$$

where the variational parameter is $k_f(\mathbf{r})$. The necessary, but not sufficient, condition for $k_f(\mathbf{r})$ to minimize Λ is that

$$\frac{\partial \Lambda}{\partial k_f(\mathbf{r})} = 0. \tag{4.47}$$

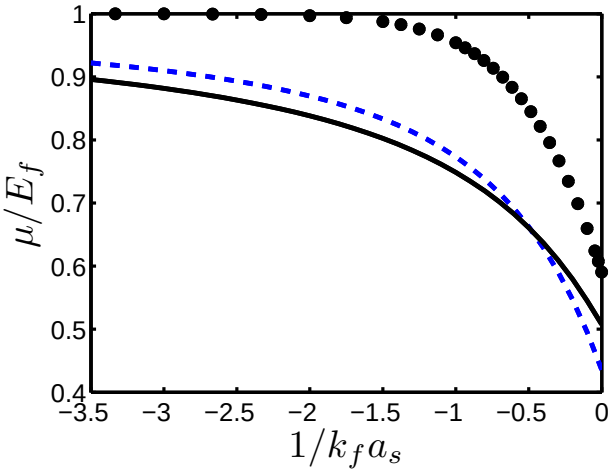

Figure 4.8: Chemical potential in units of the noninteracting Fermi energy. The black solid line is the prediction obtained via the renormalization function. The black circles represent the BCS prediction, and the blue dashed curve is the prediction obtained in Ref. [43]. Figure from Ref. [183].

This condition leads to a relationship between the local chemical potential, defined as $\mu(\mathbf{r}) \equiv \mu_0 - V_{ext}(\mathbf{r})$, and the local Fermi momentum $k_f(\mathbf{r})$:

$$\mu(\mathbf{r}) = \frac{\hbar^2 k_f^2(\mathbf{r})}{2m} \left(1 + \frac{10}{9\pi}\zeta(k_f(\mathbf{r})a_s) + \frac{k_f(\mathbf{r})a_s}{18\pi^2}\zeta'(k_f(\mathbf{r})a_s)\right). \tag{4.48}$$

The value of μ_0 fixes the number of particles, and with this relationship, we can calculate the density profile and the energy of the system. Figure 4.8 shows the chemical potential

dependence on $k_f a_s$ obtained with the renormalization function and other models. In Fig. 4.6, we see the energy obtained using Eqs. (4.45, 4.48) in the large N limit.

In the unitarity limit [$a_s \to -\infty$], we obtain

$$\mu = \frac{\hbar^2 k_f^2}{2m}\left(1 + \frac{10}{9\pi}\zeta^{min}\right). \tag{4.49}$$

At unitarity, when the scattering length is much larger than the interparticle distance, the only relevant parameter is the density [85, 130]. Dimensional analysis suggests that $\mu \propto \rho^{2/3} \propto k_f^2$. The expected relation between μ and k_f is usually written as

$$\mu = \frac{\hbar^2 k_f^2}{2m}(1+\beta). \tag{4.50}$$

From our calculations this relation appears naturally with a universal parameter $\beta = 10\zeta^{min}/9\pi = -0.492$. A more detailed discussion about the predictions of renormalization and the properties of a unitary Fermi gas will be presented in chapter 7.

It is well established [91, 130, 193] that an ultracold two-component Fermi system exhibits superfluidity. Even though our renormalization scheme does not explicitly consider superfluidity, it reproduces a number of properties of the Fermi gas sensibly, including the equation of state and the chemical potential. Consequently, these results can be used in a hydrodynamic theory to extract information about dynamics of the system such as the speed of sound or normal modes of excitation. For example, the speed of sound in a uniform two-component system is given by [85]

$$v^2 = \frac{\hbar}{m}\frac{\partial}{\partial\rho}\left(\rho^2\frac{\partial E/N}{\partial\rho}\right). \tag{4.51}$$

Using Eq. (4.44) we can thus evaluate the speed of sound, generating the results shown in Figure 4.9. The speed of sound results reproduce the expected limiting behaviors. In the noninteracting limit $v = v_f/\sqrt{3}$, while at unitarity $v = v_f\sqrt{(1+\beta)/3}$ [87]. This is one example of a nontrivial observable quantity for this system that can be predicted by the renormalization technique.

4.5.3 Hartree-Fock method

The HF method for a many-particle system is an extension of the two-particle calculation done in Section II. Consider a wave function written as the product of two Slater determinants, as in Eq. (4.7). The HF method looks for the best set of orbitals that minimize the energy of the system. The expectation value of the energy of the trial wave function for a Hamiltonian of Eq. (4.21) can be written as

$$\mathcal{E}(\psi) = \int \left(2\sum_{i}^{N/2} \psi_i(\mathbf{r}) \left(-\frac{\hbar^2}{2m}\nabla^2 + \frac{1}{2}m\omega^2\mathbf{r}^2 \right) \psi_i(\mathbf{r}) + \frac{4\pi\hbar^2\zeta(k_f(\mathbf{r})a_s)}{k_f(\mathbf{r})m}\rho(\mathbf{r})^2 \right) d\mathbf{r}. \quad (4.52)$$

Here, the orbitals $\psi_i(\mathbf{r})$ are the variational parameters, and Eq. (4.52) is the energy functional to minimize. The density $\rho(\mathbf{r})$ is the one-component density.

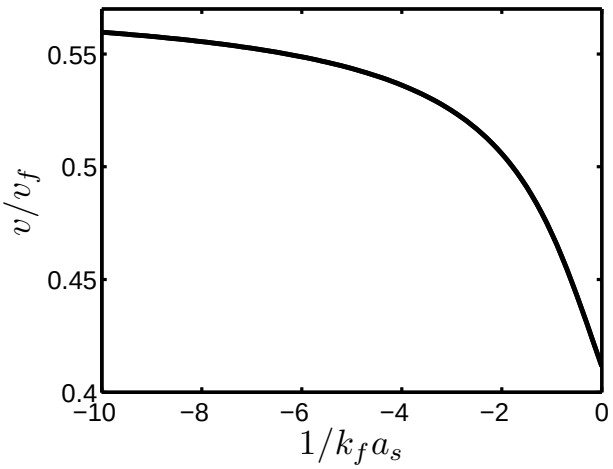

Figure 4.9: The speed of sound as a function of $k_f a_s$ shown in units of the Fermi velocity $v_f = \hbar k_f/m$ for a uniform two-component Fermi gas. Figure from Ref. [183].

In Eq. (4.52), we have considered restricted spin orbitals, which are constrained to have the same spatial function for spin-up and spin-down orbitals. Also, we focus on closed-shell systems, which have an even number N of particles, with all particles paired such that $n = N/2$ spatial orbitals are doubly occupied. In this situation, the density is

expected to be spherically symmetric, and the problem becomes spherically symmetric. Therefore, we can assume that the orbitals also have the spherical symmetry of Eq. 4.4, i.e.,

$$\psi_{nlm}(\mathbf{r}) = \frac{u_{nl}(r)}{r} Y_{lm}(\Omega) \tag{4.53}$$

Here, the $Y_{lm}(\Omega)$ are the spherical harmonics. The radial orbitals $u_{nl}(r)$ are not the noninteracting orbitals of Eq. (4.5) but are obtained from the minimization of the energy. Using the orbitals of Eq. (4.53), the density and the local Fermi momentum take the form

$$\rho(r) = \sum_{nl} \frac{(2l+1)}{4\pi} \frac{u_{nl}^2}{r^2}, \tag{4.54}$$

$$k_f(r) = (6\pi^2 \rho(r))^{1/3}. \tag{4.55}$$

The sum in Eq. (4.54) is over all the n and l of the occupied orbitals of a given shell.

Differentiating Eq. (4.52) over the orbitals, we find that the extreme condition is fulfilled when the orbitals obey the following set of nonlinear equations:

$$\begin{aligned} &\left\{ -\frac{\hbar^2}{2m}\frac{\partial^2}{\partial r^2} + \frac{l(l+1)\hbar^2}{2mr^2} + \frac{1}{2}m\omega^2 r^2 \right. \\ &\left. + \frac{4\pi\hbar^2}{m}\left[\frac{\zeta(k_f(r)a_s)}{k_f(r)}\rho(r) + \frac{k_f(r)}{6\rho(r)}\left(\frac{a_s\zeta'(k_f(r)a_s)}{k_f(r)} - \frac{\zeta'(k_f(r)a_s)}{k_f^2(r)} \right) \right] \right\} u_{nl}(r) = \epsilon_{nl} u_{nl}(r). \end{aligned} \tag{4.56}$$

Each of these equations can be seen as a Schrödinger equation of a particle immerse in a mean-field. The first line of the equation describes the kinetic and external potential terms. The term in the second line is the interaction with the mean field. The first term in the square brackets is the standard mean-field term that is proportional to the density. The second term in the square brackets comes from the density dependence of the effective scattering length.

Replacing the renormalization function by the Fermi pseudopotential prediction,

$zeta^F(y) = y$, we obtain the standard HF equation of a normal gas used in Ref. [33].

$$\left\{-\frac{\hbar^2}{2m}\frac{\partial^2}{\partial r^2} + \frac{l(l+1)\hbar^2}{2mr^2} + \frac{1}{2}m\omega^2 r^2 + \frac{4\pi\hbar^2 a}{m}\rho(r)\right\} u_{nl}(r) = \epsilon_{nl} u_{nl}(r). \tag{4.57}$$

The set of coupled equations for the orbitals, Eq. (4.56) or Eq. (4.57), are solved self consistently. Starting from the noninteracting solution, $k_f(r)$ and $\rho(r)$ are evaluated and introduced on the left hand side of Eq. (4.56) to obtain a new set of orbitals. The new set of orbitals are then used to obtain new estimates of $k_f(r)$ and $\rho(r)$. We repeat this iteration procedure until we reach convergence. During this procedure, we observe that the energy of system decreases verifying that equilibrium correspond to a minimum of energy.

Figure 4.6 shows results for the HF energy of 2280 particles. This approximation is particulary useful for systems with small numbers of particles, in which the TF approximation has limited applicability. In Sec. 4.6 below, this method is used to obtain the energies of eight fermions in a trap.

4.6 Comparison with other approaches

To compare the predictions based on our renormalized scattering length with other methods, we have carried out fixed-node diffusion Monte Carlo (FN-DMC) simulations for equal mixtures of different-spin fermions. Interactions are considered only between different-spin fermions, which are treated here as distinguishable particles. The interaction potential is a purely attractive Gaussian, and its width d is chosen so that $\rho d^3 \approx 10^{-4}$. The FN-DMC method was discussed in detail in Sec. 3.2. Since we focus on the BCS region, the results presented here correspond to the Jastrow-Slater wave function Eq. (3.7).

We have calculated FN-DMC energies for eight particles in the BCS side of the crossover. In Fig. 4.10, these energies are compared with HF calculations the include the first- and second-order corrections in the $k_f a_s$ expansion [95] and with full HF

calculations that use the renormalized scattering length directly,

$$E_{int}/N = \frac{\hbar^2 k_f^2}{m}\left(\frac{k_f a_s}{3\pi} + \frac{6(11-2\ln 2)}{105\pi^2}(k_f a_s)^2 + ...\right). \quad (4.58)$$

The idea of using this type of expansion to construct energy functionals has been applied for bosons [16, 28]. The expansion [Eq. (4.58)] can be introduced locally in variational treatments, yielding an energy functional

$$\mathcal{E}(\psi) = \int \left(2\sum_i^{N/2}\psi_i(\mathbf{r})\left(-\frac{\hbar^2}{2m}\nabla^2 + \frac{1}{2}m\omega^2\mathbf{r}^2\right)\psi_i(\mathbf{r}) + \frac{4\pi\hbar^2 a_0}{m}\rho(\mathbf{r})^2 + a_s^2\frac{12(11-2\log(2))}{105\pi^2}(6\pi^2)^{4/3}\rho(\mathbf{r})^{7/3}\right)d\mathbf{r}, \quad (4.59)$$

where $\rho = \rho_\uparrow = \rho_\downarrow$. If we only consider the first term in Eq. (4.58), we obtain the Fermi pseudopotential contribution.

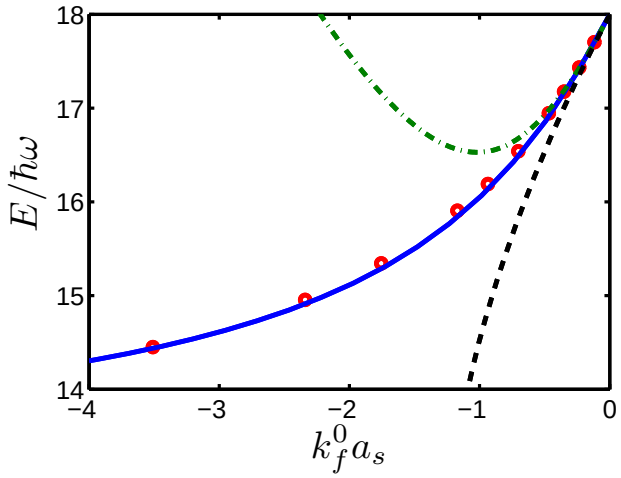

Figure 4.10: Total energy of eight fermions in a trap shown in oscillator units as a function of $k_f^0 a_s$. FN-DMC results are shown in open red circles, while the solid blue line corresponds to HF results using the effective renormalized scattering length. The dashed and dash-dotted curves correspond to solutions using first-order or first- and second-order terms in an expansion into powers of $k_f a_s$. See the discussion of Eqs. (4.58, 4.59). Figure from Ref. [183].

Previous authors [33, 153] have considered the Fermi pseudopotential approximation to study the weak interacting limit. This approximation corresponds to the

first term in the energy expansion (4.58). Applying Eq. (4.58) in the local density approximation is a convenient way to introduce higher-order corrections to mean-field theories. We obtain an expansion of the density-dependent renormalization function using Eq. (4.58);

$$\zeta(k_f a_s) = k_f a_s + \frac{6(11 - 2\ln 2)}{35\pi}(k_f a_s)^2 + \dots . \tag{4.60}$$

Insertion of this result into Eq. (4.21), with the local density approximation and a Slater determinant wave function, yields Eq. (4.59).

A power expansion of $\zeta(k_f a_s)$ obtained by the renormalization method should agree with this expansion. The first term is reproduced exactly but the second one is only in qualitative agreement. While the coefficient of the second-order expansion in Eq. (4.60) is approximately 0.525, in the density renormalization from Sec. 4.4, the coefficient is 0.422. This disagreement may be due to the level in approximation of the density renormalization procedure.

We find very good agreement between the mean-field results calculated using the renormalized interaction developed in this paper and the FN-DMC (Fig. 4.10). The variational methods including the perturbative corrections [Eq. 4.59] show good agreement in the small $k_f a_s$ region, but deviate from the FN-DNC results when the corrections to the expansion [Eq. (4.58)] become important.

It is also possible to compare our results with other quantum Monte Carlo calculations. For example, Astrakharchik and co-workers [7] have studied a homogenous doubly degenerate Fermi gas using FN-DMC methods. In their calculations, they considered up to 60 particles. We compare the energy of this system as obtained using the density renormalization procedure in Eq. (4.44). A comparison between the two calculations and a local density BCS result (see, discussion in Sec. 2.4 and Refs. [113, 123]) is shown in Fig. (4.11).

In this section, we compared the predictions of the renormalized interaction with

FN-DMC , mean-field BCS, and other local-density predictions. We showed that the renormalization approach is in generally good agreement with the FN-DMC results and provides a better description of the ground-state energy than the mean-field BCS results.

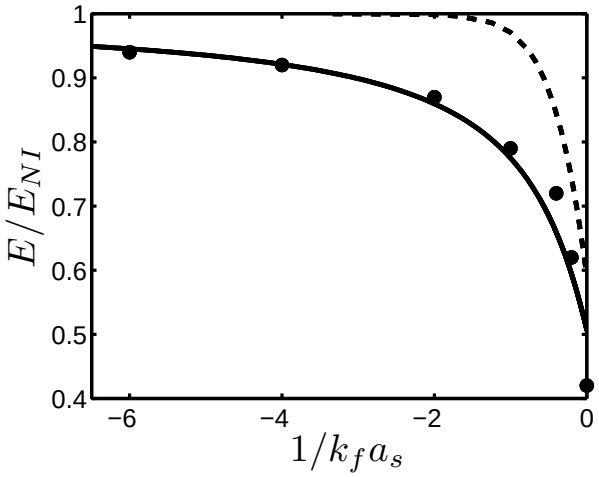

Figure 4.11: E/E_{NI} for an infinite homogeneous Fermi gas $k_f a_s$ in the mean-field approach (solid line). The dashed curve corresponds to the local density BCS solution, and the circles correspond to FN-DMC results obtained in Ref. [7]. Figure from Ref. [183].

4.7 Conclusions

In this chapter, we have presented different methods for analyzing the Hartree term correction. Starting with the Fermi pseudopotential, we have analyzed the first order correction in the weakly interacting BCS limit. Then we proposed a renormalization method to extend the use of zero-range interactions.

The density renormalization method applies the philosophy of many effective theories. It is the goal of most many-body theoretical studies to derive predictive power for numerous observables of interest, using simpler methods that bypass the actual calculation of this "true" ground-state wave function for the trapped atomic gas. At the heart of many such treatments are the following two steps: *(i)* replacement of the two-body potential energy by a zero-range Fermi pseudopotential, followed by *(ii)* a

mean-field wave function ansatz and the computation of observables. The basic level of description for a Bose gas incorporates no correlations whatsoever. For a Fermi gas, correlations are generally treated at either the bare minimalist level of exchange correlations alone, using Slater determinant wave function. A more sophisticated level is often considered for a system of mutually attractive fermions, which are frequently described with BCS-type correlations built into the description. One way of visualizing the value of a Fermi-type zero-range pseudopotential adopted in most such theories is to remember that it has been specifically designed to give a meaningful interaction energy for each pair of particles even when the wave function structure is too simplistic to incorporate any appreciable correlations.

The renormalization scheme presents an alternative implementation of this general philosophy. We developed a procedure for renormalizing the coefficient of a zero-range potential, based entirely on an analysis of the nonperturbative two-body system solved first with and then without wave-function correlations. When we applied this procedure to the many-body Fermi gas, we find agreement with the standard dilute gas limit, an important prerequisite for any realistic theory. But in addition, our procedure is able to treat higher densities ρ, including the regime $|\rho {a_s}^3| >> 1$. We studied a number of observables that have been explored both experimentally and theoretically in the BCS-BEC crossover regime, and found good agreement using our renormalized HF approach all the way to the unitarity limit, $a_s \to \infty$. Perhaps surprisingly, this good agreement is achieved without incorporating explicit BCS-type correlations into the many-body wave function. One result of this study is an approximate expression for the renormalization function in closed analytical form that may prove to be useful in other studies of the two-component degenerate Fermi gas. Another interesting result is that at unitarity, the chemical potential exhibits the expected density dependence characterized by the parameter $\beta = -0.492$, which, interestingly, is consistent with recent experiments [134, 25, 105, 167].

Unfortunately, the current implementation of the renormalization cannot describe the BEC side. An possible way to extend the renormalization method to the BEC side is to treat the dimers as bosonic particles and describe the system with the Gross-Pitaevskii equation. The renormalized dimer-dimer interaction would be obtained by matching the two-boson trapped system with the "exact" four fermions calculations from Chapter 6. This renormalization on the BEC side would complement the renormalization presented here for the BCS side. However, the combination of the BCS and BEC renormalization treatments would not predict a smooth transition in the crossover region. In order to achieve such smooth transition, we should use a more flexible many-body wave function which can represent a Fermi gas in the weak interacting region and a gas of Bose molecules in the BEC region as it is achieved by the BCS wave function. Such desired theory should also be able to include both Hartree and pairing corrections.

Chapter 5

Spectrum and Dynamics of few-body trapped systems

5.1 Introduction

In this chapter, we analyze the spectrum of fermionic few-body trapped systems in the BCS-BEC crossover. In particular, we focus on systems with $N = 2, 3, 4$. We will also analyze the dynamics of these systems when the scattering length is tuned in the BCS-BEC crossover.

Few-body systems can provide an alternative approach to the BCS-BEC crossover problem. A four-body system, made up of two spin-up and two spin-down fermions, is the smallest system that can describe the BCS-BEC crossover. Since a four-body system can describe the formation of two atom pairs or two bound molecules, we can analyze its evolution from an interacting atomic Fermi gas to an interacting molecular bosonic system.

The BCS-BEC crossover problem is usually studied by many-body theories that focus mainly on ground-state properties. In contrast, few-body calculations not only describe the ground state, but also the excitation spectrum. Furthermore, these calculations do not require the standard approximations applied to many-body systems. Thus, few-body systems allow exact numerical solutions that can be studied with many-body theories; they also allow us to test nontrivial behavior.

In this chapter, we first solve the time-independent Hamiltonian for different scattering length values a_s. Then we use these solutions to analyze the dynamics of the

system. The model Hamiltonian that describes a trapped two-component Fermi gas is given by

$$\mathcal{H} = \sum_{i}^{N_1} \left(-\frac{\hbar^2}{2m}\nabla_i^2 + \frac{1}{2}m\omega^2\mathbf{r}_i^2 \right) + \sum_{i'}^{N_2} \left(-\frac{\hbar^2}{2m}\nabla_{i'}^2 + \frac{1}{2}m\omega^2\mathbf{r}_{i'}^2 \right) + \sum_{i,i'}^{N_1,N_2} V(\mathbf{r}_{ii'}). \quad (5.1)$$

Here, unprimed indices label spin-up and spin-down particles. The interaction potential V has a purely attractive Gaussian form (see Eq. 3.20). The relevant length scale of the problem is the trap length $a_{ho} = \sqrt{\hbar/m\omega}$. In Eq. (5.1), the center-of-mass motion can be decoupled, reducing the dimensionality of the numerical calculations. All the solutions presented here have the center-of-mass wave function in its ground state.

To obtain the spectrum, we use a correlated-Gaussian (CG) basis-set expansion [157, 180], which allows a simple evaluation of the matrix elements. A diabatization procedure allows us to reduce the system to a tractable set of eigenfunctions. Then we solve the time-dependent Schrödinger equation using the adiabatic representation. The numerical results are then compared with a Landau-Zener model and with experimental results. Finally, we analyze temperature effects in the two-body system and compare them with experimental predictions for ultracold Fermi gases.

5.2 Spectrum in the BCS-BEC crossover

In this section we use the CG method to obtain the spectrum of $N = 2, 3, 4$ systems. All solutions have a relative angular momentum of $L_{ref} = 0$.

First, we consider the $N = 2$ system. Solutions for this system are very easy to find. In chapter 2 we presented semianalytical solutions for a zero-range pseudopotential. Using this model potential, the dynamics of the system have also been studied [22]. Here, we solve the $N = 2$ system with a short, but finite, two-body interaction using the CG method. These solutions help us to test both the CG method used to obtain the spectrum and the algorithm we use to solve the time-dependent Schrödinger equation. Our results are compared with the $N = 3, 4$ systems, yielding a general description of

few-body trapped systems.

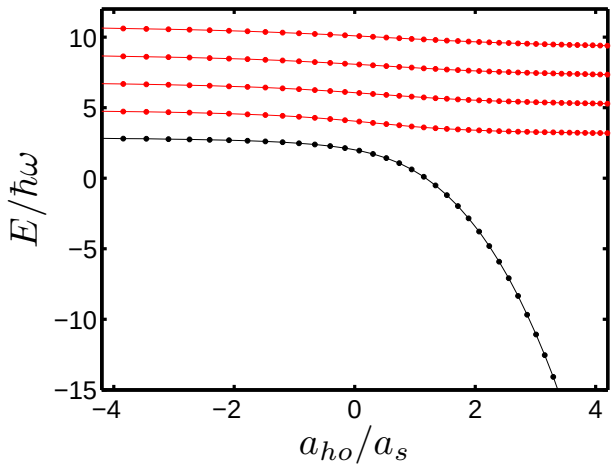

Figure 5.1: Spectrum of two particles with $J = 0$ in a trap obtained with CG method. The black curve corresponds to the ground state that evolves in a dimer configuration. Red curves correspond to excited states that evolve in a two free-atom configuration.

Figure 5.1 presents the $L = 0$ spectrum obtained with a CG of two particles in a trap. This spectrum resembles the zero-range spectrum presented in Fig. 2.2. Both finite and zero-range results are nearly indistinguishable because the range of the interacting potentials is much shorter than the scattering length a_s. In the system of two particles in a trap, we see a clear topology when the scattering length is tuned across a resonance. In the weakly interacting regime (small and negative a_s), the energies are approximately separated by $2\hbar\omega$. As a_s is tuned closer to the unitarity region, a set of avoided crossings appears that leads to the appearance of a two-body bound state in the $a_s > 0$ region. In free space, this state has a binding energy of $\hbar^2/(ma_s^2)$. The presence of a trap alters this result, leading to a trap energy given by Eq. 2.13. In the limit $a_s \ll a_{ho}$, the two particles form tightly bound dimers of size $\sim a_s/2$, and the trap energies given by Eq. 2.13 converge to their free-space value of $\hbar^2/(ma_s^2)$. Another interesting point is that the unbound spectrum on the weakly interacting BEC side reproduces the spectrum of the weakly interacting BCS side.

We are interested in understanding how this spectrum changes when we consider more particles. Here, we analyze the $L = 0$ spectra for $N = 3$ and $N = 4$ in the BCS-BEC crossover. To obtain the spectra, we use the CG method to solve the time-independent Schrödinger equation for different values of a_s. Like most numerical methods, this method provides an adiabatic spectrum, i.e., the energies of the spectrum are labeled according to their energy values as a_s changes. The $N = 3$ and $N = 4$ spectra present a series of crossings or narrow avoided crossings when the scattering length is tuned in the BCS-BEC crossover. For this reason, it is convenient to use a representation where these narrow avoided crossings are treated diabatically, and the spectrum smoothly evolves from the BCS to the BEC side. The diabatic representation is more relevant from the physical point of view since the diabatic states are usually associated with good or "approximately good" symmetries of the problem.

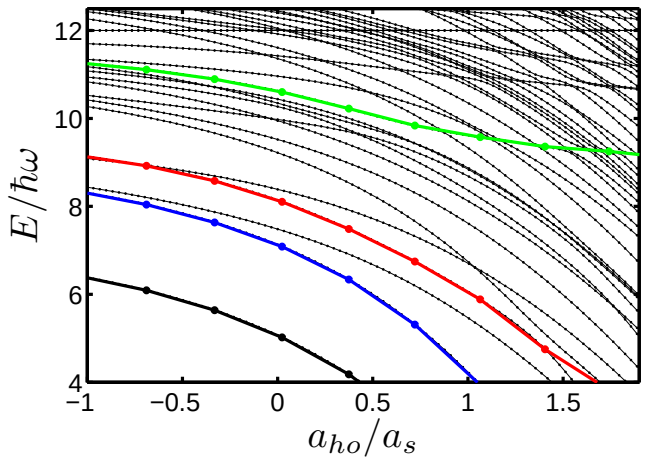

Figure 5.2: Energy spectrum as a function of λ in the unitarity region for $N = 4$ with $J = 0$. The thin solid black lines correspond to the adiabatic spectrum. The wide black line with circles is the diabatic ground state labeled Ψ_1. The blue curve with circles is the diabatic first-excited state labeled Ψ_2, the wide red curve with circles is the diabatic state Ψ_5, and the wide green curve with circles is the diabatic state Ψ_{13}.

To illustrate the diabatization procedure, we consider the spectrum of the $N = 4$ system in the strongly interacting region as shown in Fig. 5.2. We see a series of crossings

and avoided crossings when the adiabatic parameter $\lambda \equiv 1/a_s$ is tuned in the strongly interacting region. The avoided crossings can be roughly characterized by their width $\Delta\lambda$, which is the range where the two adiabatic energy curves are coupled. There are narrow crossings where $\Delta\lambda \ll 1/a_{ho}$ and there are wide crossings where $\Delta\lambda \gtrsim 1/a_{ho}$. To obtain smooth energy values, we use variation of the diabatization procedure presented in Ref. [88].

The objective of the diabatization algorithm is to make the one-to-one connection between states and energies in consecutive points of the λ grid that maximize the sum of the overlaps between connected states. The diabatization procedure starts from the BCS side of the resonance and connects the states (and their energies) between consecutive values of λ for which their overlap is maximum. When two initial energies connect to the same final energy, a refinement of the diabatization procedure is applied.

Diabatization is controlled by the spacing between consecutive values of λ given by $\Delta\lambda_g$. If the width of the avoided crossing is smaller than $\Delta\lambda_g$, then that crossing is diabatized. But if the width of the avoided crossing is larger than $\Delta\lambda_g$, then that crossing is not diabatized. Thus, $\Delta\lambda_g$ is selected so that narrow crossings are diabatized and wide crossings remain adiabatic. For example, in Fig. 5.2 we see how this procedure diabatizes the narrow crossings of Ψ_{13} of the $N = 4$ system. However, wide crossings such as the one between Ψ_5 and Ψ_{13}, are still adiabatic in this representation.

This structure of avoided crossings permits a global view of the manner in which states evolve from weakly interacting fermions at $a < 0$ to all the different configurations of a Fermi gas at $a > 0$, i.e., molecular bosonic states, fermionic states, and molecular boson-Fermi mixtures. Furthermore, it allow us to visualize concretely the possible pathways of the time-dependent sweep experiments. Here, we analyze the diabatic spectrum for $N = 3$ and $N = 4$.

The diabatic spectrum of the $N = 3$ system is presented in Fig. 5.3. The system of three particles in a trap presents a rich structure of avoided crossings related to the

appearance of a bound dimer state. There is a family of states with energies separated by approximately $2\hbar\omega$ that are attached with the two-body threshold. These states represent the ground state and excitations of a system formed with a dimer and a fermion in an $L = 0$ state. There are other states corresponding to the red energy curves in Fig. 5.3 that do not form dimer states. These three-atom states reproduce the three-particle noninteracting spectrum in the BEC limit, i.e., $a_s \to 0^+$. Finally, we note that no trimer formation occurs.

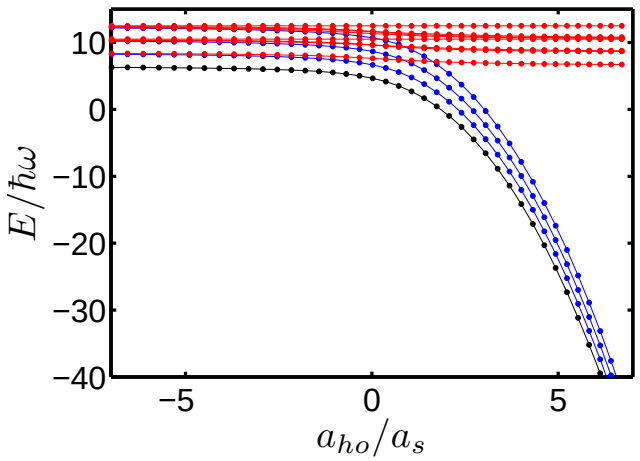

Figure 5.3: Energy spectrum of $L = 0$ three-particle states. The black line with circles shows the diabatic ground state. The blue curves with circles show the diabatic excited states, which represent a bound dimer plus an extra particle. The red curves with circles show the diabatic states where no bound dimer is formed.

We next consider the four-body diabatic spectrum presented in Fig. 5.4. The structure of avoided crossings is more complicated because of the appearance of two different thresholds for the dimer and dimer-dimer, respectively. We identify three different families of diabatic states in this spectrum. The dimer-dimer family, represented by the black and blue curves, describes the ground and excited dimer-dimer states. These states are approximately separated by $2\hbar\omega$ on the BEC side. The dimer–two-atom family, represented by the red energy curves, follows the dimer threshold. In the

BEC limit, the dimer–two-atom family reproduces the degeneracies of three distinguishable particles: a spin up, a spin down and a dimer. The third family describes four-atom systems. In this family, none of the atoms form dimers, and the energy remains positive in the crossover region. In the BEC limit, the four-atom family reproduces the spectrum of the noninteracting four-body system.

The evolution of the $N = 3$ and $N = 4$ spectra in the BCS-BEC crossover can be qualitatively understood by considering the important quantum numbers for the description of the dimer. In the $N = 3$ system, for each vibrational excitation of $2\hbar\omega$, there is one state in the noninteracting limit that diabatically becomes a atom-dimer state. This atom-dimer state corresponds qualitatively to a states where the relative angular momentum of a spin-up–spin-down pair is zero $[L_{rel}^{\uparrow\downarrow} = 0]$, and the relative angular momentum between the pair and the remaining atom is also zero. The spin-up–spin-down pair is in the lowest vibrational state $1s$, that evolves in a weakly bound dimer. In the weakly interacting BCS limit where the degeneracy of the vibrational states is broken, such pair-atom states correspond to the lowest states.

A similar effect occurs in the N=4 system. For each vibrational excitation of $2\hbar\omega$ in the noninteracting limit, there is one state that diabatically becomes a dimer-dimer state. These states correspond qualitatively to states where the relative angular momentum of two spin-up–spin-down pairs is zero $[L_{rel}^{\uparrow\downarrow} = 0]$, and the relative angular momentum between the pairs is also zero. The spin-up–spin-down pairs are in the lowest vibrational state. In the weakly interacting BCS limit, where the degeneracy of the the vibrational states is broken, pair-pair states correspond to the lowest states.

A direct and more concrete way to visualize the structure of the spectrum is to analyze the evolution of the adiabatic hyperspherical potential curves. Figure 5.5 presents the $N = 4$ hyperspherical potential curves $U_\nu(R)$ as functions of the hyperradius R obtained with the correlated Gaussian hyperspherical method (CGHS). Panel (a) presents the potential curves in the BCS regime. These potential curves are clearly grouped

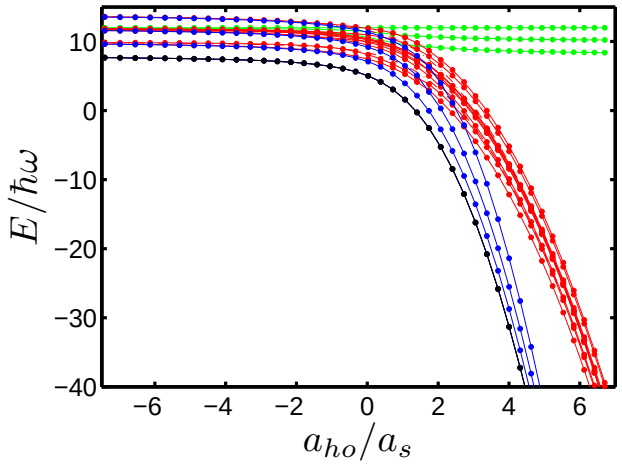

Figure 5.4: Energy spectrum for four particles with $J = 0$ in the crossover region (lowest 20 diabatic states). The black curve corresponds to the ground state. The blue curves are the states that go diabatically to excited dimer-dimer configurations. The red curves correspond to states that go diabatically to configurations of a dimer plus two free atoms, and the green curves correspond to states that go adiabatically to configurations of four free atoms. The lowest green curve is the *atomic ground state* on the BEC side of the resonance. Results from Ref. [182].

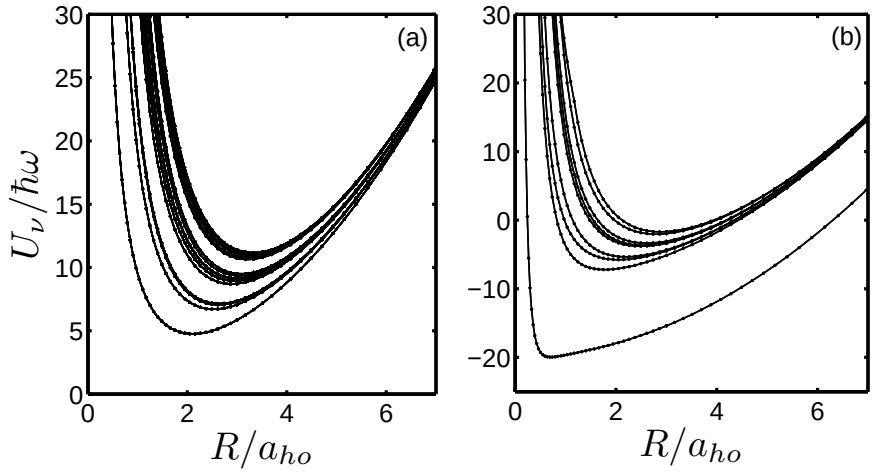

Figure 5.5: Hyperspherical potential curves in the BCS-BEC crossover for $N = 4$ with $J = 0$. (a) Potential curves in the BCS regime, $a_s \sim -0.3a_{ho}$. (b) Potential curves in the BEC regime, $a_s \sim 0.3a_{ho}$.

in families. The potential curves belonging to the same family are degenerate in the noninteracting limit. Thus, the weak interactions in the BCS break the degeneracies of the potential curves forming these families of potential curves. Panel (b) describes the system in the BEC regime. In this case, the description of the system is quite clear. The lowest potential curve is more than twice as deep as the rest of the curves and is associated with the dimer-dimer threshold. The family of dimer-dimer states lives mainly in the lowest potential curve. The rest of the potential curves are associated with the dimer–two-atom threshold. The dimer–two-atom states are mainly described by this family of potential curves. There is a third family of potential curves, not shown in Fig. 5.5 (b), that describes four-atom states. This family of potential curves has a different large R asymptotic behavior.

5.3 Time evolution

The diabatic representation can be used to ramp an initial configuration through the BCS-BEC crossover, mimicking experiments carried out at different laboratories at JILA and Rice University. The initial configuration is propagated using the time-dependent Schrödinger equation

$$i\hbar\frac{d\left|\Psi\right\rangle}{dt} = \mathcal{H}[\lambda(t)]\left|\Psi\right\rangle. \tag{5.2}$$

The time dependence of the Hamiltonian comes from the $\lambda(t)$ term. In our work, we focus on unidirectional ramps. Starting from the ground state on the BCS side, the parameter λ is ramped through the resonance to the BEC side at different speeds, $\nu = \frac{d\lambda}{dt}$. The relevant dimensionless speed quantity is $\xi = a_{ho}\nu/\omega$.

To propagate the initial configuration, we use the diabatic representation obtained previously. First, we divide the BCS-BEC crossover range into sectors. Starting from the BCS side at $\lambda \approx \lambda_{BCS}$ to the BEC side at $\lambda \approx \lambda_{BEC}$, the BCS-BEC crossover is divided in 40–80 sectors. At the middle of each sector, the time-independent Hamiltonian [Eq.

(5.1)] is solved using the CG method. For the $N = 3$ and $N = 4$ systems, thousands of CG basis functions are usually needed to describe the spectrum. We could use this basis set to solve Eq. (5.2) but this large basis would make the numerical propagation very slow. Instead, we use the diabatic representation obtained at the middle of the sector to expand the time-dependent wave function through the sector j, i.e.,

$$|\Psi(t)\rangle = \sum_{i}^{N_d} c_i^j(t)\,|\Psi_i^j\rangle\,. \tag{5.3}$$

Here, $|\Psi_i^j\rangle$ is the diabatic basis i of sector j, and N_d is the number of diabatic states considered. The time dependence only appears on the complex coefficients $c_i^j(t)$. Selecting only the lowest 20–100 diabatic states at that point, we reduce the size of the Hamiltonian matrix in Eq. (5.2). Since the inverse scattering length λ changes very little in each sector, the relevant diabatic states are well described by this reduced basis throughout the sector.

The time-dependent Schrödinger equation, Eq. (5.2), is propagated from one extreme of the sector to the other using an adaptive step Runge-Kutta method. When λ changes from a sector to the following one, the wave function in the basis set is projected onto the new basis set. It is important to test that no information is lost in this projection. To avoid this potential problem, the relevant states for the particular propagation must be well described in each sector. For example, in most of the time propagations considered here, the ground state at the BCS side, $|\Psi_1^{BCS}\rangle$, is propagated to the BEC side at different speeds. If the velocity is fast enough, the propagation is almost a projection of the initial states into states at different λ values. In other words, the propagation is so fast that the initial state does not have time to change, it is simply projected in the different basis sets as a function of λ. To accurately describe this fast propagation, the diabatic basis set in each sector should be able to accurately describe $|\Psi_1^{BCS}\rangle$. This state is well described in the BEC side by the lowest atomic state. However, in the strongly interacting unitarity region, there is no state that qualitatively

describes $|\Psi_1^{BCS}\rangle$.

For that reason, we do observe in the numerical propagations that some probability is lost during these fast ramps. Also, we observe that most probability is lost in the strongly interacting region. To avoid this problem, we introduce a new state in our diabatic basis set at each sector. This new state is orthogonal to the diabatic basis set and completes the description of the ground state in the BCS side. To obtain this new state, we apply a Gram-Smith orthogonalization of the ground state on the BCS side with respect to the diabatic basis set:

$$|\Psi_{N_d+1}^j\rangle = \mathcal{N}\left(|\Psi_1^{BCS}\rangle - \sum_i^{N_d} \langle\Psi_i^j|\Psi_1^{BCS}\rangle\,|\Psi_i^j\rangle\right). \tag{5.4}$$

Here $\mathcal{N}$ is a normalization factor. The new state $|\Psi_{N_d+1}^j\rangle$ ensures that the ground state in the BCS side is well described at any λ value.

To understand the time propagation of this system, we visualize how the probabilities evolve in the BCS-BEC crossover. At each point of the time propagation, the probability of being in state i is given by $p_i(t) = |c_i^j(t)|^2$. Here j denotes the sector that includes $\lambda(t)$. We can obtain the probabilities of evolving in a given family by summing the probabilities of all states belonging to the same family. For two particles, there are two families, the dimer family, which only includes the lowest state, and the two-atom family, which includes the rest of the states. In this case, we define $p_d(t) = |c_1^j(t)|^2$, and $P_{2a}(t) = \sum_{i=2}^{N_d} |c_i^j(t)|^2$.

Similarly, for the $N = 3$ system we can define three families: the ground state, the excited atom-dimer state, and the three-atom state. For each of these families we can define a probability: $p_g(t)$, $p_{ad}(t)$, $p_{3a}(t)$, respectively.

Finally, in the $N = 4$ system, we can define four families: the ground state, the excited dimer-dimer states, the dimer–two-atom states, and the four-atom states. These families are characterized by the probabilities $p_g(t)$, $p_{dd}(t)$, $p_{d2a}(t)$, and $p_{4a}(t)$, respectively.

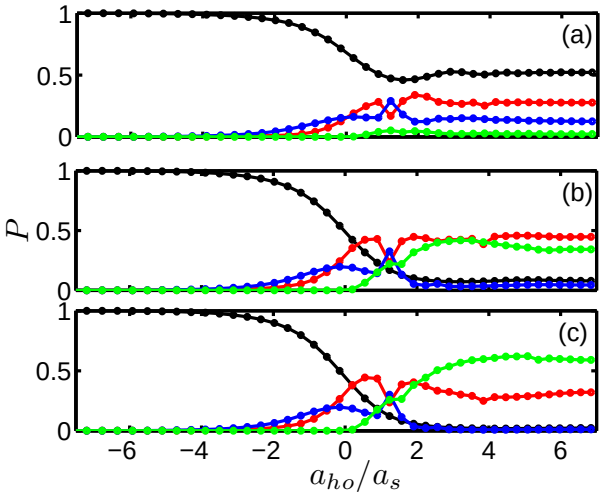

Figure 5.6: Probabilities of the $N = 4$ system during a unidirectional ramp at constant speed from the BCS to the BEC side. The initial configuration is $|\Psi_1^{BCS}\rangle$. The black curve corresponds to $p_g(t)$. The blue curve corresponds to $p_{dd}(t)$. The red curve corresponds to $p_{d2a}(t)$, and the green curve corresponds to $p_{4a}(t)$. (a) Probabilities in a ramping at a speed of $\chi \approx 13$. (b) Probabilities in a ramping at a speed of $\chi \approx 52$. (c) Probabilities in a ramping at a speed of $\chi \approx 128$

.

Figure 5.6 presents examples of the numerical time evolution of a $N = 4$ system during a unidirectional ramp at constant speed from the BCS to the BEC side. As expected, the probability of staying in the ground state decreases with speed. The probability of evolving in the four-atom configuration increases with speed, which is in agreement with the projection argument. The transfer of probability occurs mainly in the strongly interacting regime, $-2 \lesssim a_{ho}/a_s \lesssim 2$. In this region, the diabatic states are sometimes mixed, producing jumps in the probabilities. For example, around $a_{ho}/a_s \approx 1$, the red and blue curves have a kink due to an avoided crossing between an excited dimer-dimer state and a dimer–two-atom state.

We can also study the probabilities at the end of the time evolution as functions of the speed ξ. Before analyzing these numerical results, however, we must consider the simple Landau-Zener model that provides insights about our numerical calculations.

5.3.1 The Landau-Zener model and the P-matrix analysis

The Landau-Zener model provides a simple description of nonadiabatic transitions. We review this model and analyze the relationship between the P-matrix between adiabatic states and the Landau-Zener parameter, as derived in Ref. [45].

We first consider a two-channel model as a function of an adiabatic parameter λ that is changed at constant speed, i.e., $\lambda = \nu t$. The Landau-Zener model assumes the following Hamiltonian,

$$\mathcal{H} \begin{pmatrix} \psi_1 \\ \\ \psi_2 \end{pmatrix} = \begin{pmatrix} \epsilon_1 & \epsilon_{12} \\ \\ \epsilon_{12} & \epsilon_2 \end{pmatrix} \begin{pmatrix} \psi_1 \\ \\ \psi_2 \end{pmatrix}. \tag{5.5}$$

Following the Landau-Zener model, we set $\epsilon_1 - \epsilon_2 = \alpha\lambda$, and we consider ϵ_{12} independent of λ, i.e., $d\epsilon_{12}/dt = 0$. The time evolution of this model can be easily solved. We are particularly interested in the nonadiabatic transition probability T_{na}. T_{na} describes the probability of evolving to a final adiabatic state different from the initial adiabatic state after the parameter λ is tuned through an avoided crossing. To obtain this probability,

the time-dependent Schrödinger equation is propagated starting at $t = -\infty$ [with $\psi(t) = \psi_1$] to $t = +\infty$. The nonadiabatic probability is then given by $T_{na} = |\langle\psi(+\infty)|\psi_2\rangle|^2$. Landau and Zener solved this problem analytically and showed that

$$T_{na}(\nu) = e^{-\delta}, \tag{5.6}$$

where $\delta = 2\pi\epsilon_{12}/(\alpha\nu)$.

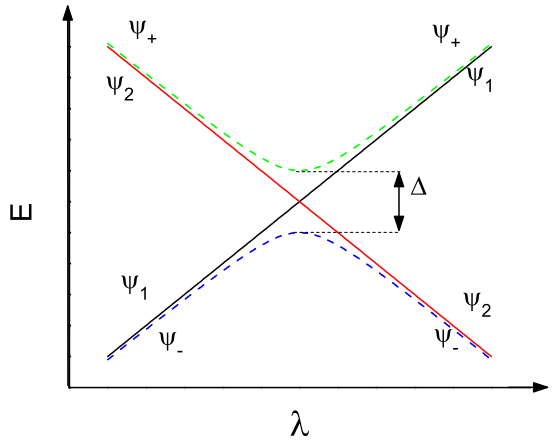

Figure 5.7: Schematic description of the Landau-Zener model. Solid black and red curves correspond to the nonadiabatic states ψ_1 and ψ_1, respectively. Dashed blue and green curves correspond to the adiabatic states ψ_- and ψ_+, respectively.

Unfortunately, Eq. (5.6) is not very useful in its current form when it comes to analyzing numerical results. In particular, it requires a knowledge of nonadiabatic quantities such as α and ϵ_{12}. In numerical calculations, in which the adiabatic spectrum is obtained, these quantities cannot be directly calculated. To obtain the coupling ϵ_{12}, we can calculate Δ, i.e., the difference between adiabatic energy curves at the closest approach. In the Landau-Zener model $\Delta = 2\epsilon_{12}$. However, the quantity α is difficult to estimate unless you have a very clean avoided crossing (like the one in Fig. 5.7).

Nevertheless, Clark [45] showed how α can be obtained from an analysis of the adiabatic P-matrix coupling. The P-matrix between two adiabatic states $|\psi_+\rangle$ and $|\psi_-\rangle$

is defined as

$$P_{+-}(\lambda) = \langle \psi_+ | \frac{d\psi_-}{d\lambda} \rangle \,. \tag{5.7}$$

As we show below, the properties of $P_{+-}(\lambda)$ depend on Δ and α. Therefore, by analyzing the P-matrices, we can extract the Landau-Zener parameters.

To show the relation between the $P_{+-}(\lambda)$ and Δ and α, we consider the time-independent solutions of the Hamiltonian [Eq. (5.5)] to be a function of the adiabatic parameter λ, where

$$\mathcal{H}(\lambda)\psi_\pm(\lambda) = \epsilon_\pm(\lambda)\psi_\pm(\lambda). \tag{5.8}$$

The eigenvalues are given by

$$\epsilon_\pm = \frac{1}{2}\left(\epsilon_1 + \epsilon_2 \pm \sqrt{(\epsilon_2 - \epsilon_2)^2 + 4\epsilon_{12}^2}\right) = \frac{1}{2}\left(\epsilon_1 + \epsilon_2 \pm \sqrt{\alpha^2\lambda^2 + \Delta^2}\right). \tag{5.9}$$

Here, we set $\epsilon_1 - \epsilon_2 = \alpha\lambda$, and $\Delta = 2\epsilon_{12}$. The adiabatic eigenvectors can be now written as

$$\begin{pmatrix} \psi_+ \\ \psi_- \end{pmatrix} = \begin{pmatrix} \cos\theta & \sin\theta \\ -\sin\theta & \cos\theta \end{pmatrix} \begin{pmatrix} \psi_1 \\ \psi_2 \end{pmatrix}. \tag{5.10}$$

Next, we consider the P-matrix for this system:

$$P_{+-}(\lambda) = \langle \psi_+ | \frac{d\psi_-}{d\lambda} \rangle = \frac{\langle \psi_+ | \frac{d\mathcal{H}}{d\lambda} | \psi_- \rangle}{\epsilon_+ - \epsilon_-}. \tag{5.11}$$

The second equality is a consequence of the Hellman-Feynman theorem, and we use it to extract $P_{+-}(\lambda)$. Using Eqs. (5.5) and (5.10), we obtain

$$\langle \psi_+ | \frac{d\mathcal{H}}{d\lambda} | \psi_- \rangle = -\alpha\cos(\theta)\sin(\theta) = -\alpha\frac{\tan(\theta)}{1+\tan^2(\theta)}. \tag{5.12}$$

Analyzing the eigenvectors and setting $\epsilon_1 - \epsilon_2 = \alpha\lambda$ and $\Delta = 2\epsilon_{12}$, we obtain that

$$\tan(\theta) = -\frac{\Delta}{\alpha\lambda + \sqrt{\alpha^2\lambda^2 + \Delta^2}}. \tag{5.13}$$

Finally, combining Eqs. (5.11-5.13), we obtain

$$P_{+-}^{LZ}(\lambda) = \frac{1}{2}\left(\frac{\alpha}{\Delta}\right)\frac{1}{1+(\frac{\alpha\lambda}{\Delta})^2}. \tag{5.14}$$

Thus, the P-matrix only depends on the ratio α/Δ. Since the Landau-Zener parameter depends on Δ^2/α, the P-matrix analysis is not enough to extract the Landau-Zener parameter δ. For that reason, Δ is extracted from the spectrum. Another interesting point is that the area under the P-matrix in entirely independent of both α and Δ.

5.4 Landau-Zener analysis of few-body trapped systems.

The $N = 2$ trapped system can be treated with the two-channel Landau-Zener model. However, the $N = 3$ and $N = 4$ systems are more complicated. Their spectra have several avoided crossings that are potentially important for the unidirectional ramps considered in this section. Thus, the dynamic of these systems cannot be described by a simple Landau-Zener transition. For that reason, we model the transition probabilities p_i of the $N = 3$ and $N = 4$ systems with a sequence of Landau-Zener transitions. Analyzing the spectra and the numerical P-matrices, we can extract the Landau-Zener parameters δ. Since the P-matrices peak at different λ values, we can use the positions of the peaks to understand the order in which the Landau-Zener transitions occur.

We begin by extending the definitions presented in the Sect. 5.3.1 for describing several Landau-Zener transitions. The Landau-Zener transition probability between the adiabatic Ψ_i and Ψ_j is

$$T_{ij}(\nu) = e^{-\delta_{ij}} = e^{-\frac{\eta_{ij}}{\xi}}. \tag{5.15}$$

The Landau-Zener parameter δ_{ij} characterizes the transition and has the form $\delta_{ij} = \frac{\pi\Delta_{ij}^2}{2\alpha_{ij}\nu}$, where $\Delta = E_i - E_j$ is evaluated in the transition region (at the peak of the P-matrix), and α_{ij} is obtained from P-matrix analysis. The transition probabilities T_{ij} can be conveniently described as functions of the dimensionless speed parameter ξ and dimensionless quantities η_{ij} that describe the specific transitions.

Similarly, we extend the definitions of the P-matrix to several states. The P-

matrix between two adiabatic states Ψ_i and Ψ_j is

$$P_{ij}(\lambda) = \langle \Psi_i | \frac{d\Psi_j}{d\lambda} \rangle = \frac{\langle \Psi_i | \frac{d\mathcal{H}}{d\lambda} | \Psi_j \rangle}{E_i - E_j}, \tag{5.16}$$

where λ is the adiabatic parameter, and E_i and E_j the energies of these states. To numerically evaluate $P_{ij}(\lambda)$, we use

$$\mathcal{H} = \mathcal{H}_0 + V_0(\lambda)\,\mathcal{H}_{int} \quad \text{and} \quad \frac{\mathcal{H}}{d\lambda} = V_0'(\lambda)\,\mathcal{H}_{int}. \tag{5.17}$$

In the CG basis set expansion, $\mathcal{H}_0$ and $\mathcal{H}_{int}$, are matrices and $V_0(\lambda)$ is the potential depth of the interaction whose derivative is $V_0'(\lambda)$. Using Eq. (5.17), the evaluation of a P-matrix takes the form

$$P_{ij}(\lambda) = \frac{V_0'(\lambda)}{E_i(\lambda) - E_j(\lambda)} \langle \Psi_i(\lambda) | \mathcal{H}_{int} | \Psi_j(\lambda) \rangle \,. \tag{5.18}$$

In Eq. (5.18), we include all the explicit dependence on λ. Note that $\mathcal{H}_{int}$ does not depend on λ and is only evaluated once before being used to describe the complete crossover region. For the Gaussian interaction used for these systems, $V_0(\lambda)$ is, to a good approximation, a linear function, and $V_0'(\lambda)$ is then constant. The energies $E_i(\lambda)$ and $E_j(\lambda)$ are extracted from the spectra presented in Figs. 5.1, 5.3, and 5.4. The term $\langle \Psi_i(\lambda) | \mathcal{H}_{int} | \Psi_j(\lambda) \rangle$ implies just a matrix multiplication of the eigenstates with the matrix $\mathcal{H}_{int}$.

Figure 5.8 presents some of the P-matrices we obtained numerically. We observe that all these P_{ij} have a Lorentzian-like form. The $P_{1,2}$ has a smooth behavior but the other P_{ij} are not very smooth. The series of crossings or narrow avoided crossings affect the P-matrices because the diabatization procedure cannot avoid a possible mixing of states when the energies are close to becoming degenerate. Nevertheless, as we show below, the analysis of these P-matrices is possible and provides good estimates of the Landau-Zener parameters.

According to the Landau-Zener theory presented above, for each transition be-

tween Ψ_i and Ψ_j has a Lorentzian form of

$$P_{ij}^{LZ}(\lambda) = \frac{\alpha_{ij}}{2\Delta_{ij}} \frac{1}{1 + \left[\frac{\alpha_{ij}(\lambda - \lambda_{ij})}{\Delta_{ij}}\right]^2}, \tag{5.19}$$

where Δ_{ij} and α_{ij} are the parameters that characterize the Landau-Zener parameter δ_{ij}. For Landau-Zener transitions, we can more rigorously define the width of the avoiding crossing as $\Delta\lambda_{ij} \equiv \Delta_{ij}/\alpha_{ij}$. The position of the $P_{ij}^{LZ}(\lambda)$ peaks are given by λ_{ij}. In the Landau-Zener formula, the height and width of the Lorentzian are characterized by a single parameter Δ_{ij}/α_{ij}. However, because most of numerical calculations cannot be described accurately by $P_{ij}^{LZ}(\lambda)$, a more flexible function is needed. To fit our numerical results we propose

$$P_{ij}^{fit}(\lambda) = \frac{a_{ij}}{2} \frac{1}{1 + \left[\frac{(\lambda - \lambda_{ij})}{b_{ij}}\right]^2}. \tag{5.20}$$

The height of the Lorenztian is given by a_{ij}, and the width is given by b_{ij}. In principle, we can use either a_{ij}, b_{ij}, or a combination of both quantities to estimate Δ_{ij}/α_{ij}. We observe that the extraction of Δ_{ij}/α_{ij} using the width of the Lorentzian, b_{ij}, usually gives results closer to the numerical predictions. For the $N = 2$ case, the Landau-Zener formula works well, and $a_{ij} \approx b_{ij}$, but in the $N = 4$ case, the width and height of the fitted Lorentzian can differ up to a factor of 2.

5.4.1 Numerical results

We first analyze the dynamics of the $N = 2$ system. Starting at $\lambda_{BEC} \approx -7/a_{ho}$, we ramp the interaction at different speeds ν to the BEC side, where $\lambda_{BEC} \approx 7/a_{ho}$. The probability of remaining in the ground state (dimer state) is then measured. The symbols in Fig. 5.9 (b) present the numerical results. The black circles correspond to the probability of evolving in the dimer state (red energy curves in Fig. 5.1), and the red circles correspond to the probability of evolving in two-atom states (red energy curves in Fig. 5.1).

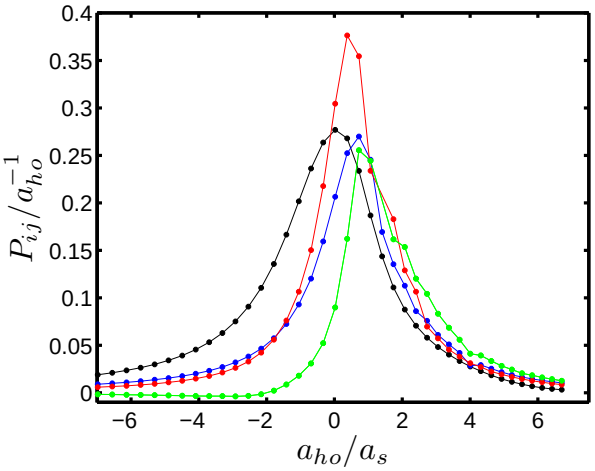

Figure 5.8: The most important P matrices involved in a ramping that starts at the BCS side with all the probability in the ground state. The black curve represents P_{1-2}, the blue P_{1-5}, the red P_{2-5}, and the green P_{5-13}.

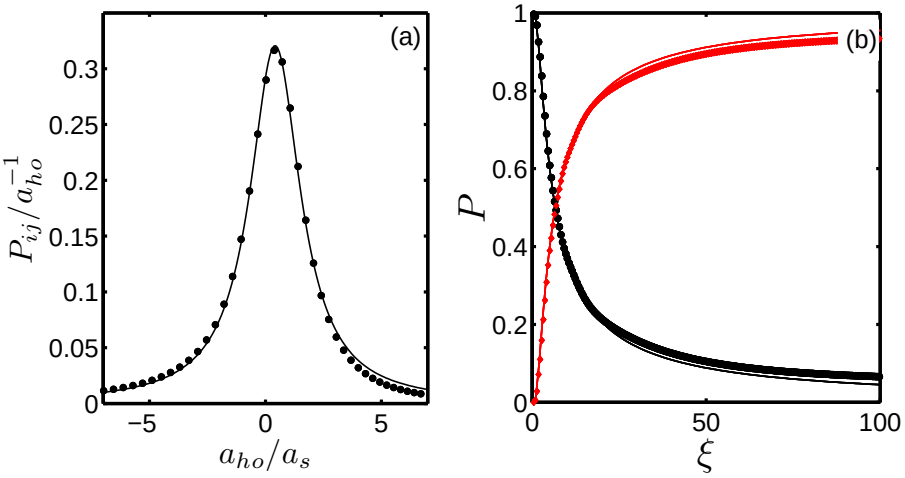

Figure 5.9: Numerical results and Landau-Zener model for $N = 2$.(a) circles correspond to P_{12} obtained numerically. The solid line corresponds to the best fit with P_{12}^{fit}. (b) Transition probabilities as a function of the speed ξ. Black symbols represents evolution in the dimer family (ground-state). Red symbols represents evolution in the two-atom family (red energy curves in Fig. 5.1). Black and red lines correspond to p_1 and p_2 obtained from the Landau-Zener model.

The simple form of the transition-probability numerical results and the spectrum suggest that the $N = 2$ system can be modeled by a single Landau-Zener transition between the ground state, labeled by 1, and the first-excited state, labeled by 2. We analyze the numerical P_{12} and find it has a clear Lorentzian shape [see Fig. 5.9 (a)]. For this P_{12}, the difference between a_{12} and b_{12} is less than 15%. Still, the b_{12} parameter provides a better Landau-Zener parameter η_{12}. The Landau-Zener model predicts probabilities p_1 to remain in the ground state and p_2 to evolve in the first excited state as given by

$$p_1 = (1 - T_{1,2}), \tag{5.21}$$

$$p_2 = T_{1,2}. \tag{5.22}$$

The Landau-Zener parameter corresponding to this transition is $\eta_{12} \approx 4.625$. For large speed parameters ξ, we note that the Landau-Zener prediction is slightly higher than the numerical results. This discrepancy might be due to limitations in the numerical calculation for predicting a full conversion efficiency. However, we note an excellent agreement between the numerical results and the Landau-Zener prediction.

Things get more complicated as we turn the discussion to a $N = 3$ system. Figure 5.10 presents the numerical results and the Landau-Zener prediction. In this case, we cannot describe the transition probabilities with a single Landau-Zener transition; instead we propose a sequence of Landau-Zener transitions. Even so, we want to restrict our model to the simplest possible case. Since in the $N = 3$ system there are three families of states, we consider only three states, one for each family, in describing this system in the Landau-Zener approximation. Analyzing the spectrum and the numerical P-matrices, we observe that the most important P-matrices describe transitions between the lowest energy states of each family. These states correspond to the ground state (labeled as 1), the first-excited state (labeled as 2), and the state corresponding to the lowest red energy curve in Fig. 5.3. This last state is the second-excited state in the

BCS regime, and we label it as 3. Analyzing the P-matrices, we note that the first transition is $1 \rightarrow 2$, the second transition is $1 \rightarrow 3$, and finally the third transition is $2 \rightarrow 3$. This order in the transitions implies probabilities

$$p_1 = (1 - T_{1,2})(1 - T_{1,3}), \tag{5.23}$$

$$p_2 = T_{1,2}(1 - T_{2,3}), \tag{5.24}$$

$$p_3 = T_{1,2}T_{2,3} + T_{1,3}(1 - T_{1,2}). \tag{5.25}$$

It is easy to test whether the total probability is conserved, i.e., $p_1 + p_2 + p_3 = 1$.

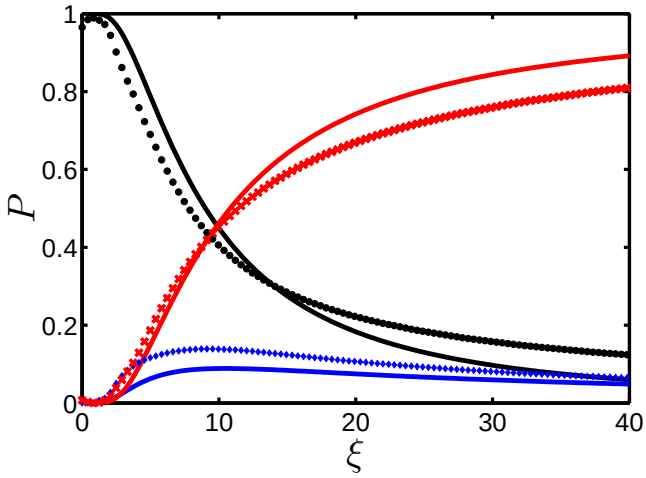

Figure 5.10: Probability of evolving in a given configuration as a function of the dimensionless speed parameter χ. The symbols correspond to the numerical evolution, while the curves correspond to the Landau-Zener theory. Black curve and symbols correspond to the ground state. Blue curve and symbols corresponds to the excited atom-dimer configuration, and red curve and symbols corresponds to the three-atom configuration.

Analyzing the spectrum and the P-matrices, we obtain Landau-Zener transitions of $\eta_{12} \approx 9.1$, $\eta_{13} \approx 13.4$, and $\eta_{12} \approx 2.5$. The probability p_i results from the Landau-Zener model are presented as solid lines in Fig. 5.10. From the figure we can see that the Landau-Zener model qualitatively describes the numerical results. However, we can also clearly see the limitations of this model, including important deviations between it and the numerical results. In particular at large ξ, the conversion efficiency for three-atom

states according to the Landau-Zener model is much higher than the numerical results. We carried out several tests of the numerical calculations that confirmed the results presented in Fig. 5.10. We observe that the P-matrices have large overlaps and their peaks are very close together. As a result, the approximation of a sequence of isolated Landau-Zener transitions fails. A theory that takes into account multiple simultaneous transitions will be needed. Such theory is beyond the scope of this dissertation.

Finally, we consider the $N = 4$ system. Figure 5.11 (b) displays our numerical results. The black symbols correspond to the dimer-dimer ground state. The blue symbols correspond to the excited dimer-dimer family, the red symbols to the dimer–two-atom family, and the green symbols to the four-atom family. For slow ramps (small ξ), the probability of forming a condensate, i.e., remaining in the ground state, is large. For intermediate ramps, the greatest probability is breaking one bond and ending up with a dimer plus two particles. For fast ramps (large ξ), the probability of staying in the *atomic ground state* on the BEC side is the most important. The probability of the system evolving in an excited dimer-dimer configuration remains small for all ramping speeds.

To analyze these transitions within the Landau-Zener approximation, we label the diabatic states according to their energies in the BCS regime. This labeling is arbitrary since many of the states are almost degenerate. To select the potentially important states, we consider the possible pathways according to the P-matrix couplings. Starting from the ground state, we note that $|\Psi_1\rangle$ has important couplings with states $|\Psi_2\rangle$ and $|\Psi_5\rangle$. Here, $|\Psi_2\rangle$ is the first excited dimer-dimer state, i.e., the lowest state of the excited dimer-dimer family. State $|\Psi_5\rangle$ is the first excited state of the dimer–two-atom configuration. Since an important probability is transferred to states $|\Psi_2\rangle$ and $|\Psi_5\rangle$, we analyze the couplings of these states to follow the flow of probability. State $|\Psi_2\rangle$ has an important coupling with $|\Psi_5\rangle$, and state $|\Psi_2\rangle$ has an important coupling with $|\Psi_{13}\rangle$. Here, $|\Psi_{13}\rangle$ is the lowest state of the four-atom configuration, i.e., the atomic ground

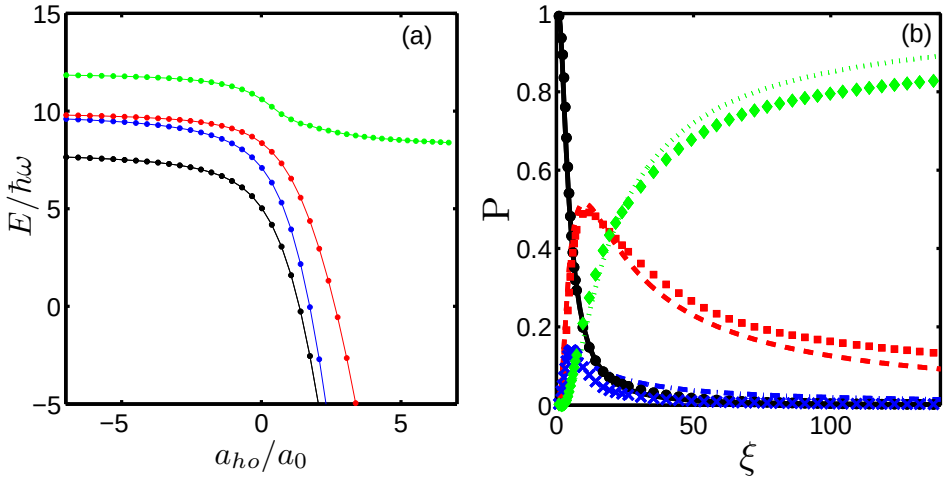

Figure 5.11: (a) Energy in the BCS-BEC crossover of the important states in the Landau-Zener approximation. The black curve corresponds to $|\Psi_1\rangle$ which represents the ground state configuration. The blue curve corresponds to $|\Psi_2\rangle$ which represents the excited dimer-dimer configuration. The red curve corresponds to $|\Psi_5\rangle$ which represents the configuration of a dimer plus two atoms. The green curve corresponds to $|\Psi_{13}\rangle$ which represents the four-atom configuration. (b) Probability of evolving in a given configuration as a function of the dimensionless speed parameter χ. The symbols correspond to the numerical evolution, while the curves correspond to the Landau-Zener theory. The colors follow the same convention of Figure (a). Results from Ref. [182].

state in the BEC side. Figure 5.11 (a) presents the energy curves of these four states. Conveniently, each of these states represents a different configuration. For that reason, this is the minimal set of states that can describe the numerical results. We could include more states in our analysis but we restrict ourselves to the simplest possible case.

Figure 5.8 presents the relevant numerical P-matrices. The order of the peaks reveals the following sequence: the first transition is $1 \rightarrow 2$, then $2 \rightarrow 5$, then $1 \rightarrow 5$, and finally $5 \rightarrow 13$. The Landau-Zener prediction for this sequence is

$$\begin{aligned} p_1 &= (1 - T_{1,2})(1 - T_{1,5}), \\ p_2 &= T_{1,2}(1 - T_{2,5}), \\ p_5 &= ((1 - T_{1,2})T_{1,5} + T_{2,5}T_{1,2})(1 - T_{5,13}), \\ p_{13} &= ((1 - T_{1,2})T_{1,5} + T_{2,5}T_{1,2})T_{5,13}. \end{aligned} \tag{5.26}$$

Again, the sum of all these probabilities is, by construction, 1. The Landau-Zener parameters obtained from the P-matrix analysis are $\eta_{12} \approx 5.4$, $\eta_{15} \approx 6.6$, $\eta_{25} \approx 2.1$ and $\eta_{5,14} \approx 13.8$. We note that the P-matrix P_{5-13} in Fig. 5.8 is only in qualitative agreement with the Lorentzian form, so the uncertainty in $\eta_{5,13}$ is large. However, the sequence of Landau-Zener transitions in the model shows very good agreement with the numerical results even though many possible transitions were neglected. In comparison with the $N = 3$ case, the sequence of transitions is better defined, suggesting a reason for the better agreement with the numerical results.

5.5 Comparison with experimental results.

In this section, we compare our few-body calculations with experimental results obtained with ultracold Fermi gases. First, we compare the molecule fraction as a function of the speed of the ramping. Then, we analyze atom-molecule coherence. Finally, we study conversion efficiency as a function of temperature.

5.5.1 Molecule fraction as a function of the speed

To compare our results with Fermi gas experiments, we have to find a way to relate few-body calculations with many-body calculations. We first consider a homogeneous system where λ is tuned from $\lambda = -\infty$ (BCS) to $\lambda = +\infty$ (BEC). The only relevant quantities of this system are the speed ν, the density ρ, and the mass of the particles m. Therefore, the dimensionless speed parameter that characterizes the ramp is $\chi = \frac{m}{\hbar\rho}\frac{d\lambda}{dt}$. This is the relevant parameter for comparing homogeneous systems at different densities, ramp speeds ν, or masses. We also consider χ to be the relevant parameter for comparing our calculations to larger, experimentally accessible systems.

Here, we consider that it is the density of the system (and not the trap length as in ξ) that characterizes both few- and many-body systems. The trap only plays a role in confining the gas to a given density. In other words, to relate a large Fermi gas with a few body calculation, we solve the few-body system in a trap tight enough so that the average density of this few-body system is the same as the average density of the Fermi gas in the experiment. This strategy is similar to the frequency-scaling method presented in Ref. [22].

This strategy allows us to write Eq. (5.27) in terms of the parameter χ, i.e.,

$$T_{ij}(\chi) = e^{-\frac{\varkappa_{ij}}{\chi}}, \tag{5.27}$$

where $\varkappa_{ij}$ are now dimensionless parameters. In the experiments carried out at JILA and Rice, the Landau-Zener parameter for atom-molecule transitions is usually written as $\delta_{exp} = \beta\left(\frac{dB}{dt}\right)^{-1}$ [143]. If the dependence of a_s on the magnetic field can be approximated by $a_s(B) = a_{bg}\left(1 + \frac{w}{B-B_0}\right)$, then β has been theoretically predicted [77] to be $\beta = c\rho w a_{bg}/m$, where c is a proportionality constant, w is the width of the resonance, and a_{bg} is the background scattering length.

The same results can be obtained from our dimensional analysis arguments. Using $a_s(B)$, we can write χ in terms of the experimental parameters. Then, the Landau-Zener

parameter $\varkappa_{exp}/\chi = \beta\left(\frac{dB}{dt}\right)^{-1}$, where $\beta = c\rho w a_{bg}/m$. Thus, by considering χ as the relevant dimensionless parameter, we obtain agreement in the functional dependence of the Landau-Zener parameter with Ref. [77]. The dependence of δ_{exp} on ρ has been experimentally verified [90]. Like in the experiments, we use the average density on the weakly interacting BCS side to evaluate χ. Using noninteracting wave functions, we obtain $\rho_2 = 2/(\sqrt{2\pi}a_{ho})^3 \approx 0.127/a_{ho}^3$ and $\rho_4 = 29/(12(\sqrt{2\pi}a_{ho})^3) \approx 0.153/a_{ho}^3$.

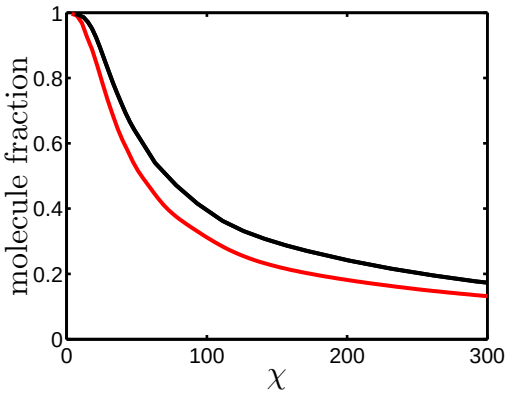

Figure 5.12: Molecular fraction as a function of χ. The dashed red curve is the $N = 2$ prediction, and the black solid line is the $N = 4$ prediction.

The molecule fraction, i.e., the fraction of particles that become molecules after the ramping procedure, is probably the most relevant quantity to compare with experiments. Only even-N systems can produce full conversion efficiency and, for that reason, are considered for molecule-fraction analysis. In the $N = 2$ system, the molecule fraction is just the probability of staying in the ground state. For $N = 4$ systems, the molecule fraction is defined as the probability of evolving in a dimer-dimer configuration plus one-half the probability of evolving in a dimer plus two-atom configuration. In Fig. 5.12, we compare the two-body prediction with four-body predictions.

In the experiments, the molecule fraction is fitted with a Landau-Zener function, $f_m(1 - e^{-\varkappa_{mol}/\chi})$, where f_m is is the conversion efficiency that depends on temperature. Whether a Landau-Zener function is the correct functional form to describe the

molecule-formation fraction in large systems remains a question that existing experiments have not resolved [136, 3, 189]. The Landau-Zener model presented in this work for four particles does not predict a single Landau-Zener function but rather a combination of different Landau-Zener terms. However, the final molecule fraction predicted by this model and the numerical results for the molecule-formation fraction can be approximately fitted by the Landau-Zener function, leading to $\varkappa_{mol4} \approx 59 \pm 6$; this value is higher than the two-body prediction of $\varkappa_{mol2} \approx 39$. This result is consistent with the experimental Landau-Zener parameter obtained of Ref. [145] for ^{40}K. The fit of the experimental data to a Landau-Zener formula predicted a $\beta = 20 \pm 6$ μs/G, which can be expressed in terms of the dimensionless form. For the experimental conditions, this result gives a value of $\varkappa_{exp} \approx 62 \pm 15$. Note that this experiment was carried out at $T/T_F = 0.33$ where a conversion efficiency of approximately $f_m = 0.6$ was observed. In contrast, our calculations are at $T = 0$ where the conversion efficiency is 100%. In addition, the experiments carried out at Rice measured the Landau-Zener parameter of $\beta = 1.3$ ms/G for ^{6}Li [170]. Taking into account the experimental conditions and properties of the ^{6}Li Feshbach resonance at $B \approx 543.8$, we estimate a $\varkappa_{exp} \sim 90$. In this second experiment, the conversion efficiency was of the order of $f_m = 0.5$, and the estimated temperature $T \approx 0.1\, T_F$. Both experiments are in qualitative agreement with the four-body predictions, suggesting that χ is the relevant quantity for comparing few-body results with many-body results.

Up to this point, we have only considered unidirectional ramps. However, more sophisticated ramp schemes can be implemented. Next, we consider ramps scheme that manifest the atom-molecule coherence in the system.

5.5.2 Atom-molecule coherence

Another interesting phenomenon studied experimentally is atom-molecule coherence. For bosonic condensates, atom-molecule oscillations [58], or quantum beats [22],

have previously been explored. Fermionic systems near a narrow Fano-Feshbach resonance have been also predicted to exhibit aatom-molecule coherence [6]. Here, we analyze atom-molecule oscillations in the $N = 4$ system.

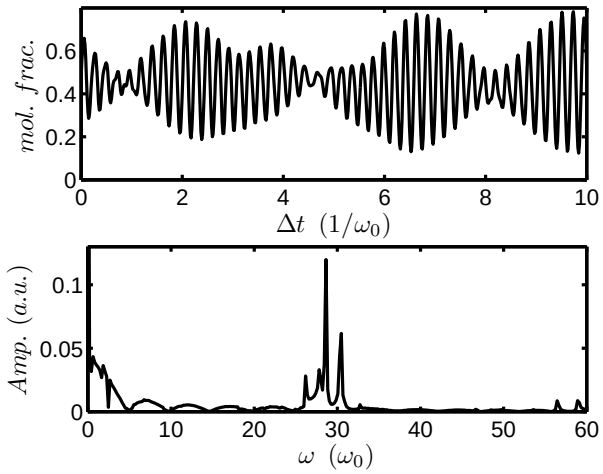

Figure 5.13: (upper panel) Molecule fraction as a function of the delay Δt in the ramp scheme. (lower panel) Fourier transform of the upper panel figure. The peaks of the spectrum correspond to the most important energy transitions. Figure from Ref. [182].

To study atom-molecule coherence in a Fermi gas, we proposed the following ramping scheme. Starting in the ground state on the BCS side, we ramp at medium speed ($\chi \approx 32$) to the BEC side. We stop at a value λ_{still}, we wait a time Δt, and then we go back with the same speed to the BCS side. Finally, we slowly ramp λ to the BEC ($\chi \approx 2$) side, and we measure the molecule fraction. The molecule fraction as a function of Δt is shown in Fig. 5.13 (upper panel). This ramping scheme produces a large molecule-fraction oscillation that varies from 0.2 to 0.8. To analyze the frequencies involved in the molecule-fraction oscillations, we Fourier transform the molecule fraction, as shown Fig. 5.13 (lower panel). The peaks in the Fourier transform can be easily related with the most important transition at λ_{still}. The peaks around $\omega \approx 28\,\omega_0$ correspond to transitions between configurations that have one extra or one fewer dimer. For example, the highest peak is a transition between Ψ_5 and Ψ_{13}, while the second

highest is a transition between Ψ_1 and Ψ_5. The peaks around $\omega \approx 57\omega_0$ correspond to a transition between Ψ_1 and Ψ_{13} as well as Ψ_2 and Ψ_{13}. In the real experiment, where the atom-molecule transitions are much larger than the trap frequency, this multipeak structure in the Fourier transform around the atom-molecule transition frequency will disappear, yielding only a single peak.

5.5.3 Conversion efficiency as a function of temperature.

In the experiments with Fermi gases carried out at JILA, the maximum molecule fraction was measured versus temperature [90]. To explore the dependence of the molecular-formation probability on the initial temperature, we have carried out a two-body calculation in the canonical ensemble.

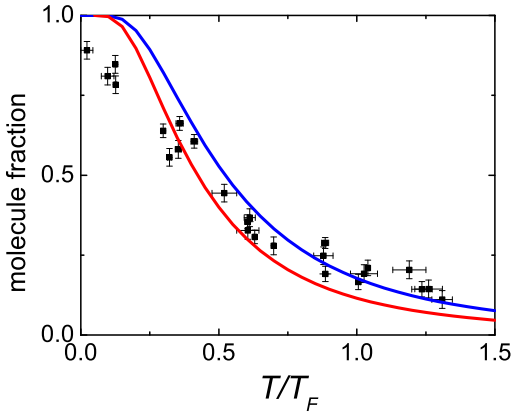

Figure 5.14: Molecule fraction as a function of T/T_F. The black circles are the experimental results showing the maximum molecule fraction as a function of the temperature [90]. The blue and curves are the theoretical predictions from two particles in a trap using T_F^{2b} and T_F^{TF}, respectively. Experimental data courtesy of Cindy Regal.

We assume there is complete adiabaticity during the ramping with regard to the molecular formation process. However, the ramps were not so slow as to allow thermal equilibrium to be reached at each moment during the ramp. Therefore, we can deduce the molecule fraction by simply "counting" the states that would form molecules in the

initial thermal distribution. The resulting molecular fraction is extracted as a function of initial temperature by starting from the initial thermal distribution and counting the states that, in a completely adiabatic ramp, would form molecules. For this study, we begin from thermal equilibrium in a weakly interacting gas on the BCS side. The two-body states under study are filled accordingly to Boltzmann factors, and the partition function is

$$Z(T) = \sum_q e^{-\frac{E_q}{k_B T}}. \tag{5.28}$$

Here, k_B is the Boltzmann constant, and E_q are the eigen energies of the $N = 2$ system labeled by the collective quantum number q. Separating in relative and center-of-mass coordinates and solving the noninteracting system in spherical coordinates, the energy of the $N = 2$ system can be written as

$$E_{n_{CM},l_{CM},n_r,l_r} = E_{CM} + E_r = (2n_{CM} + l_{CM} + 2n_r + l_{CM})\hbar\omega. \tag{5.29}$$

Only those atom pairs that are in the relative coordinate ground state will form molecules. This pairs have $n_r = l_r = 0$. Both the partition function, Eq. (5.28), and the sum over the pairs that form molecules can be solved analytically. These calculations lead to a molecule fraction given by

$$F(T) = e^{-3\hbar\omega/k_B T}\left(e^{\hbar\omega/k_B T} - 1\right)^3. \tag{5.30}$$

To compare this two-body prediction with experimental results, we plot the results as a function of T/T_F. Since T_F ultimately depends on the density, this technique involves a density scaling.

Considering the highest occupied orbital energy, $T_F^{2b} = E_F/k_B = 3\hbar\omega/(2k_B)$, where E_F is the Fermi energy. However, the Fermi energy E_F for small N systems depends strongly on the shell effects. For that reason, we propose to use a smooth semiclassical Fermi energy obtained from a Thomas-Fermi approximation, i.e., $E_F^{TF} \approx 1.211\hbar\omega$. Therefore, $T_F^{TF} \approx 1.211\hbar\omega/(k_B)$. Figure 5.14 presents the comparison between

the experimental results and the $N = 2$ prediction. The red curve is obtained using T_F^{2b}, and the blue curve is obtained using T_F^{TF}. Both predictions are in good agreement with the numerical results.

The experimental results presented in Fig. 5.14 were successfully described by a many-body model proposed by Cornell [90] in 2005. This model is based on similar arguments. As in our $N = 2$ calculation, the conversion efficiency only depends on the initial conditions before the adiabatic ramp. According to Cornell's model, two particles of the gas would form a molecule depending on their "distance" in phase space δ_{ps}. For distances δ_{ps} smaller than some cutoff δ_{ps}^c, the particles would form a molecule, and for $\delta_{ps} > \delta_{ps}^c$, the particles would not form a molecule. This simple idea was implemented using Monte Carlo methods and δ_{ps}^c as a fitting parameter to the experimental results. Excellent agreement was obtained between the theory and the experiment. In contrast, our theory does not have fitting parameters besides the uncertainty in defining the most relevant E_F.

5.6 Conclusions

In this chapter, we have presented an accurate description of few-body trapped systems. First, we showed how the $N = 2$, $N = 3$, and $N = 4$ spectra evolve in the BCS-BEC crossover. These results were used to propagate in time trapped atoms in the ground state from the BCS region through the crossover, while investigating the important nonadiabatic transitions. Even though the spectra present a rich structure of avoided crossings, we have shown that a simple Landau-Zener model approximately describes the dynamics of unidirectional ramps.

Finally, we compared our few-body results with experimental measurements. We find reasonable agreement in molecule-fraction predictions as functions of the speed of the ramping and temperature. We also investigated atom-molecule coherence using a novel ramping scheme. These results show that few-body calculations can successfully

describe an appreciable fraction of many-body experimental results.

Chapter 6

BCS-BEC Crossover of few-body trapped Systems

6.1 Introduction

In this chapter, we analyze the energetics and structural properties of fermionic few-body trapped systems in the BCS-BEC crossover. In particular, we focus on systems with $N = 3, 4$.

The systems considered here are relevant for experiments in optical lattices. In a deep three-dimensional optical lattice, the tunneling probability between lattice sites is negligible, and each lattice site can be considered an harmonic trap. Therefore, the optical lattice becomes an ensemble of microscopic harmonic traps in which the few-body properties can be probed.

Interestingly, in some cases few-body physics controls the many-body phenomena in an optical lattice. A clear example is an optical lattice with $N = 3$ particles in each site. The ground state changes its angular momentum from $L = 1$ for small and negative scattering lengths to $L = 0$ for small and positive scattering lengths. This change produces a quantum-phase transition in the optical lattice as the scattering length is tuned in the BCS-BEC crossover [103]. In addition, if the optical lattice is not that deep and the tunneling probability is small but not negligible, then few-body trapped solutions can be used as starting point in perturbative treatments of many-body theories.

Solving the Schrdinger equation for more than a few fermions by first-principles

methods is, despite the increasing available computer power, still a challenging task. Monte Carlo methods are one of the most suitable methods for such studies. Unfortunately, however, assessing the accuracy of the assumptions going into Monte Carlo calculations, such as the nodal surface employed in the FN-DMC approach, remains a challenge. Our calculations for $N = 3, 4$, which use the CG and FN-DMC approaches in parallel, benchmark the strengths and limitations of the nodal surface employed in the FN-DMC calculations and validates, to some extent, the FN-DMC for $N > 4$.

The calculations for trapped systems can also be used to extract properties of the free systems. If the range of the interactions and the scattering length are much smaller than the trapped size, then the trapping potential provides confinement without significantly affecting the few-body physics. Consequently, the trapped results can be related with those of the free systems. When the magnitude of scattering length is similar to the trapping potential, then the confinement plays a major role affecting the energies and the correlations.

The main objective of this chapter is to obtain and interpret solutions of few-body trapped systems. The model Hamiltonian that describes these systems is given by

$$H = \sum_{i=1}^{N_1} \left(\frac{-\hbar^2}{2m_1} \nabla_i^2 + \frac{1}{2} m_1 \omega^2 \vec{r}_i^{\,2} \right) + \sum_{i'=1}^{N_2} \left(\frac{-\hbar^2}{2m_2} \nabla_{i'}^2 + \frac{1}{2} m_2 \omega^2 \vec{r}_{i'}^{\,2} \right) + \sum_{i=1}^{N_1} \sum_{i'=1}^{N_2} V(r_{ii'}). \quad (6.1)$$

Here, unprimed indices label mass m_1 and primed indices mass m_2 fermions, and N is assumed to be even, ω denotes angular trapping frequency, and $\vec{r}_i$ the position vector of the ith fermion. The interaction potential V has a purely attractive Gaussian form (see Eq. 3.20). The mass ratio κ is defined by m_1/m_2, and throughout the analysis we assume $m_1 \geq m_2$. For each specie or component, there is a trap length associated $a_{ho}^{(i)} = \sqrt{\hbar/m_i\omega}$. We also define a trap length associated with the pair $a_{ho} = \sqrt{\hbar/2\mu\omega}$, where $\mu = m_1 m_2/(m_1 + m_2)$. For equal mass systems, $a_{ho} = a_{ho}^{(1)} = a_{ho}^{(2)}$.

For $N = 3$ systems, there are two types of systems: the two heavy and one light particle system [$N_1 = 2$ and $N_2 = 1$] and the two light and one heavy particle system

$[N_1 = 1$ and $N_2 = 2]$. For $N = 4$ systems, $N_1 = 2$ and $N_2 = 2$.

In the following section, we first analyze the spectrum of Eq. (6.1) as the scattering is tuned in the BCS-BEC crossover. Then, we compare the correlated Gaussian (CG) lowest energy results with both the fixed-node diffusion Monte Carlo (FN-DMC) predictions and the theoretical predictions in the limiting behaviors. Next we study the lowest state in the BEC side and extract collisional properties of these systems. Then we show how a simple two-channel model can describe qualitatively the BCS-BEC crossover. Finally, we analyze the structural properties of these few-body trapped systems. Most of the work in this chapter was done in collaboration with D. Blume and presented in Refs. [184, 185].

6.2 Energy crossover curves for $N = 3$ and $N = 4$

This section analyzes in detail the ground-state energy of $N = 3$ and $N = 4$ systems. The calculations are extended to unequal mass systems, and comparisons between CG results and FN-DMC results are presented.

Consider initially the $N = 4$ system. From the ground-state energy, we construct the energy crossover curve $\Lambda_4^{(\kappa)}$, defined in Refs. [184, 185] as

$$\Lambda_4^{(\kappa)} = \frac{E(2,2) - 2E(1,1)}{2\hbar\omega}. \tag{6.2}$$

Here $E(2,2)$ is the ground-state energy of the four-particle system and, $E(1,1)$ is the ground-state energy of the two-particle system. Both energies depend on the mass ratio κ and the scattering length. The energy crossover curve is convenient for comparisons because any effects of finite-range interactions on the two-body binding energy are significantly reduced by the subtraction in Eq. (6.2). Therefore, even though both $E(4)$ and $E(2)$ are not completely universal, $\Lambda_4^{(\kappa)}$ is universal.

The energy crossover curve $\Lambda_4^{(\kappa)}$ is shown in Figure 6.2 for four fermions as a function of $a_{ho}^{(2\mu)}/a_s$ calculated by the CG and FN-DMC approaches for (a) $\kappa = 1$ and

(b) $\kappa = 8$. Here, the oscillator length $a_{ho}^{(2\mu)}$ is defined in terms of the reduced mass $\mu = m_1 m_2/(m_1 + m_2)$, i.e., $a_{ho}^{(2\mu)} = \sqrt{\hbar/(2\mu\omega)}$. The solid lines in Fig. 6.2 are obtained using $E(4)$ calculated by the CG approach, while the circles and crosses are obtained using $E(4)$ calculated by the FN-DMC approach using $\Psi_{N=4}$ and Ψ_P, respectively. The ranges r_0 of the two-body potentials used in Fig. 6.2 are much smaller than the oscillator lengths, i.e., $r_0 \approx 0.01 a_{ho}^{(2\mu)}$. From our CG energies for different r_0, we estimate that the $\Lambda_N^{(\kappa)}$ curves shown in Fig. 6.2 deviate by at most 1% from the corresponding curves for zero-range interactions. For $m_1 = m_2$, e.g., the energy at unitarity calculated by the CG approach for the Gaussian interaction potential is $E = 5.027\hbar\omega$ for $r_0 = 0.01 a_{ho}^{(2\mu)}$ and $E = 5.099\hbar\omega$ for $r_0 = 0.05 a_{ho}^{(2\mu)}$. For comparison, the FN-DMC energy for the square well potential with $r_0 = 0.01 a_{ho}^{(2\mu)}$ is $E = 5.069(9)$, which is in good agreement with the energies calculated by the CG approach.

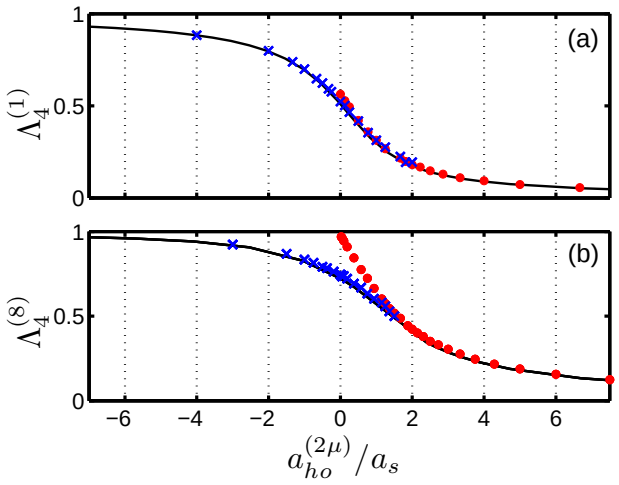

Figure 6.1: Energy crossover curve $\Lambda_4^{(\kappa)}$ as a function of $a_{ho}^{(2\mu)}/a_s$ for (a) $\kappa = 1$ and (b) $\kappa = 8$. Solid lines are calculated by the CG approach, and circles and crosses by the FN-DMC method using $\psi_{N=4}$ and ψ_P, respectively. Figure from Ref. [184].

As expected, the energy-crossover curve smoothly connects the limiting values of one on the BCS side and zero on the BEC side. Importantly, the lowest FN-DMC energies and the CG energies agree well, implying that the functional forms of $\Psi_{(N=4)}$

and Ψ_P are adequate. For equal masses [panel (a)], the FN-DMC energies at unitarity calculated using the two different trial wave functions agree approximately. In contrast, for unequal masses [panel (b)], the nodal surface of $\psi_{(N=4)}$ leads to a lower energy at unitarity than that of ψ_P, and the crossing point between the energies calculated using $\Psi_{(N=4)}$ and Ψ_P moves to the BEC side. The normal $\Psi_{(N=4)}$ describes the system in a wider region which can be understood by realizing that the densities of the heavy and light particles do not overlap fully, leading to a reduced pairing.

The good agreement between both numerical methods suggests two things. First, $\Lambda_4^{(\kappa)}$ is indeed universal. Second, numerical methods accurately described the BCS-BEC crossover of the four-body system.

We continue our analysis by studying the crossover curve for $N = 3$ for different mass ratios κ. Here, the behavior of odd N systems is rich and, in many cases, qualitatively different from that of even N systems. One characteristic of odd N systems is a possible change of the angular momentum of the ground state as the scattering length is tuned through the BEC-BCS crossover region [103, 166, 185]. The ground state in the BCS region can have nonzero angular momentum (see Sec. 4.2), but in the BEC limit, the ground state has always $L = 0$. Therefore, to obtain the ground-state energy for odd N systems, we need to consider $L > 0$. This is a problem since CG only describes $L = 0$ states. This problem was overcome in Refs. [19, 185]) by introducing a spectator particle that couples to $L = 0$ in the N particle system. This method allows one, in principle, to obtain the spectrum of the N particle system with an arbitrary L. We will explore this method in more detail in chapter 7.

As in the the $N = 4$ system, we can define an energy-crossover curve. The energy crossover curve for the $N = 3$ systems takes the form

$$\Lambda_3^{(\kappa)} = \frac{E(3) - E(1,1) - 3\hbar\omega/2}{\hbar\omega}, \tag{6.3}$$

where $E(3)$ is the ground state energy of the $N = 3$ system and corresponds to $E(2,1)$ for

two heavy and one light atoms and $E(1,2)$ for two light and one heavy atoms. For equal masses $E(3) = E(2,1) = E(1,2)$. The definition of $\Lambda_3^{(\kappa)}$ is sometimes convenient because it depends on the ground state $E(3)$ regardless of its angular momentum. However, to see the energy crossings between states, it is more convenient to analyze the lowest states for each angular momentum L. Figure 6.2 shows the three-particle energy E, with the energy $E(1,1)+3\hbar\omega/2$ subtracted for $L = 0$ (solid lines) and $L = 1$ (dashed lines). The upper panel shows results for $\kappa = 1$, and the two lower panels for $\kappa = 4$ [panels (b) and (c) consider the three-particle system with a spare heavy and a spare light particle, respectively]. The ground state has $L = 1$ for $a_{ho}/a_s \to -\infty$ and $L = 0$ for $a_{ho}/a_s \to \infty$. These limiting behaviors are independent of κ and independent of whether the spare particle is heavy or light. For equal masses, the change of symmetry occurs at $a_s \approx a_{ho}$. In contrast, for $\kappa = 4$ it occurs at $a_s \approx 0.3a_{ho}$ if the extra particle is a heavy atom [panel (b)] and at $a_s \approx 3a_{ho}$ if the extra particle is a light atom [panel (c)]. The dashed and solid lines shown in Fig. 6.2 coincide with the normalized crossover curve $\Lambda_3^{(\kappa)}$, Eq. (6.3), in the region where the ground state of the three-particle system has $L = 1$ and 0, respectively. The normalized crossover curve $\Lambda_3^{(\kappa)}$ changes from 1 in the weakly interacting molecular BEC regime to 0 in the weakly interacting BCS regime.

We find that the normalized $L = 1$ energy curve for two heavy atoms and one light atom [Fig. 6.2(b)] depends on the range of the underlying two-body potential if the scattering length a_s is positive. For example, the normalized energy curve changes by as much as 20% if the r_0 of the two-body potential changes from $0.01a_{ho}$ to $0.02a_{ho}$. This comparatively large dependence on r_0 indicates that the properties of the system with two heavy atoms and one light atom are not fully determined by the s-wave scattering length for the ranges considered. In the $r_0 \to 0$ limit, the $\kappa = 4$ system is expected to behave universally [140, 102]. We speculate that the comparatively strong dependence of the normalized energy curve on the range for $a_s > 0$ is related to the fact that the three-particle system supports weakly bound states for sufficiently large κ.

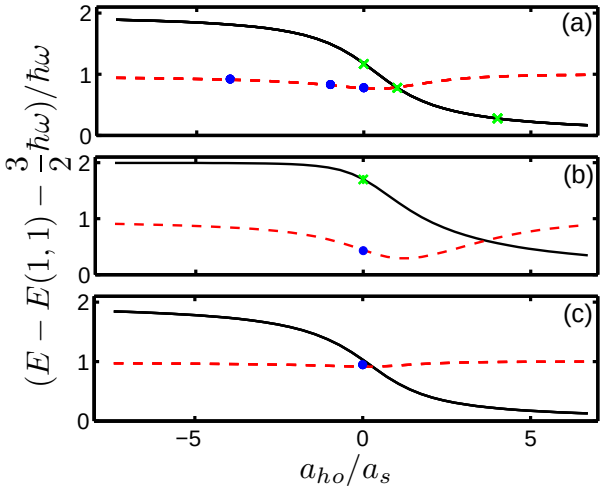

Figure 6.2: Normalized energy $(E - E(1,1) - 3\hbar\omega/2)/\hbar\omega$ for $N = 3$ as a function of a_{ho}/a_s calculated by the CG approach (lines). E denotes the three-body energy for $L = 0$ (solid lines) and for $L = 1$ (dashed lines). (a) Equal-mass atoms [$\kappa = 1$, $E = E(2,1) = E(1,2)$]. (b) Two heavy atoms and one light atom [$\kappa = 4$, $E = E(2,1)$]. (c) Two light atoms and one heavy atom [$\kappa = 4$, $E = E(1,2)$]. The normalized energy crossover curve $\Lambda_3^{(\kappa)}$, Eq. (6.3), coincides with the dashed and solid lines, respectively, depending on whether the three-particle ground state has $L = 1$ or 0. In the CG calculations, the range r_0 of the two-body potential is fixed at $0.01a_{ho}$. For comparison, crosses and circles show selected FN-DMC energies for $L = 0$ and $L = 1$, respectively. Figure from Ref. [185].

For comparison, circles and crosses in Fig. 6.2 show selected three-particle energies calculated by the FN-DMC method for $L = 0$ and $L = 1$, respectively. The good agreement with the CG results (lines) indicates that the FN-DMC method can be used to accurately describe different symmetry states.

Our CG energies for equal-mass systems interacting through short-range potentials presented in Fig. 6.2(a) can be compared with those of Kestner and Duan [103] obtained for zero-range interactions. Our $L = 1$ energy curve agrees with that of Kestner and Duan for all scattering lengths a_s considered. The $L = 0$ energy curve, however, only agrees for $a_s < 0$. For $a_s > 0$, our results are noticeably lower than those of Kestner and Duan. As shown below, our $a_s > 0$ results for $L = 0$ predict the correct atom-dimer scattering length, suggesting that our energies should be very close to those for $r_0 = 0$ and that the disagreement is not due to finite-range effects. We speculate that the results of Kestner and Duan might not be fully converged for $a_s > 0$ although other possibilities cannot be excluded.

Now, we compare our numerical results with the theoretical predicted limiting behaviors. As presented in Sec. 4.2, the first order corrections in the BCS- and BEC-limiting behaviors can be obtained using the Fermi pseudopotential. In general, we find good agreement between the numerical results and these theoretical predictions. Furthermore, the numerical results can be used to extract information about the collisional aspect of these systems. As an example, consider the equal mass $N = 3$ system. On the weakly interacting BCS side,

$$E(3) \approx E_{NI} + \hbar\omega \frac{3}{\sqrt{2\pi}} \frac{a_s}{a_{ho}}. \tag{6.4}$$

The first term corresponds to a zero order correction, the noninteracting energy. The second term is a first-order correction corresponding to the Hartree term of the Fermi pseudopotential.

In the weakly interacting molecular BEC side, the $N = 3$ system behaves as a

dimer and an atom interacting with a short-range potential characterized by a scattering length a_{ad}. Therefore,

$$E(3) \approx E(1,1) + \frac{3\hbar\omega}{2} + \hbar\omega\sqrt{\frac{2}{\pi}}\frac{a_{ad}}{a_{ho}^{(ad)}}. \tag{6.5}$$

The first two terms correspond to the energy of the dimer and the atom, respectively, and the third term corresponds to the first-order correction proportional to a_{ad}.

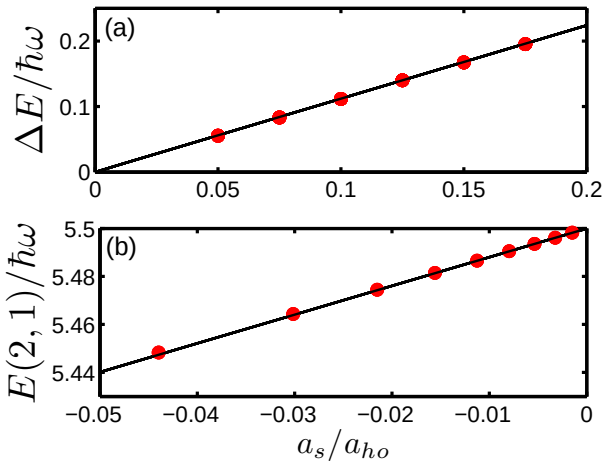

Figure 6.3: Limiting behavior of the ground-state energy for $N = 3$ equal mass fermions. (a) Energy correction $\Delta E = E(2,1) - E(1,1) - 3\hbar\omega/2$ on the BEC side. Circles show the CG results, while the solid line shows the first order correction for $a_{ad} \approx 1.2a_s$. (b) Energy $E(2,1)$ on the BCS side. Circles show the CG results while the solid line shows the first-order correction on the BCS side. Figure from Ref. [185].

Figures 6.3(a) and (b) present the BCS- and BEC-limiting behaviors for an equal mass system with $N = 3$. The perturbative expression, Eq. (6.5), on the BEC side is expected to be applicable if $r_0 \ll a_s \ll a_{ho}$; thus, we choose a small r_0, i.e., $r_0 = 0.005a_{ho}$, in the CG calculations. The energy in this region is determined by the atom-dimer scattering length a_{ad}. The CG energies change linearly with a_s, showing that a_{ad} is proportional to a_s, i.e., $a_{ad} = c_{ad}a_s$. A simple linear fit to the CG results predicts $c_{ad} \approx 1.21$, in good agreement with previous studies [158, 138], which found $a_{ad} \approx 1.2a_s$. A solid line in Fig. 6.3(a) shows the resulting linear expression. (A more

sophisticated analysis accounting for the energy-dependence is presented presented in the next section.) On the BCS side, the first-order correction varies also linearly with a_s. Circles in Fig. 6.3(b) show the CG results, while the solid line shows the prediction from Eq. (6.4). Good agreement is observed in both limiting behaviors. We perform a similar analysis of the BCS- and BEC-limiting behaviors for the $N = 4$ system. Again, good agreement is obtained between the numerical results and the theoretical predictions.

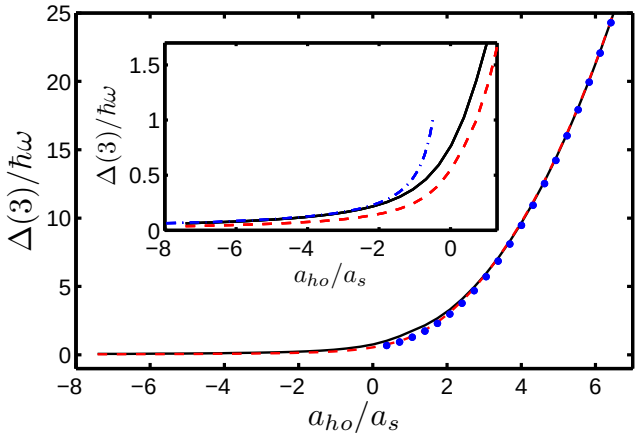

Figure 6.4: Excitation gap $\Delta(N)$ for $N = 3$ as a function of a_{ho}/a_s calculated by the CG approach for $\kappa = 1$ (solid line) and $\kappa = 4$ (dashed line). Circles present the BEC limiting behavior $3\hbar\omega/2 - E(1,1)/2$ which is independent of κ. The inset shows a blow-up of the region where $\Delta(3)$ is smallest; in this region, the dependence of $\Delta(3)$ on κ is most pronounced. The dash-dotted line shows the limiting behavior for $\kappa = 1$ obtained by approximating the $E(N)$ in Eq. (6.6) by their perturbative values, Eq. (6.4). Figure from Ref. [185].

Finally, we turn the discussion to analyze the odd-even staggering in the $N = 2, 3, 4$ systems. Our CG energies for $N = 2$, 3 and 4 can be readily combined to determine the excitation gap,

$$\Delta(3) = \frac{E(2,1) + E(1,2) - E(2,2) - E(1,1)}{2}. \tag{6.6}$$

Figure 6.4 shows the excitation gap $\Delta(3)$ as a function of a_{ho}/a_s for two different mass ratios, i.e., $\kappa = 1$ and 4. In the weakly-interacting molecular BEC regime, the excitation gap approaches $3\hbar\omega/2 - E(1,1)/2$ (circles), independent of the mass ratio. In the weakly-

interacting BCS regime, however, the excitation gap depends on the mass ratio (see inset of Fig. 6.4). For equal masses, $\Delta(3)$ is very well described by the perturbative expression for $a_s \lesssim -0.5a_{ho}$ (dash-dotted line in the inset). Figure 6.4 shows that $\Delta(3)$ is smaller for $\kappa = 4$ than for $\kappa = 1$. Intuitively, this might be expected since the radial densities of the two species do not fully overlap for unequal masses (recall, we consider the case where species one and two experience the same trapping frequency). Thus, the pairing mechanism is expected to be less efficient in the unequal-mass system, especially on the BCS side, than in the equal-mass system. The next chapter discusses the behavior of the excitation gap at unitarity in more detail.

In this section, we showed that the CG and FN-DMC numerical results agree and behave universally, describing a smooth crossover for the $N = 4$ system. For $N = 3$, we showed that the ground state of the systems changes its angular momentum in BCS-BEC crossover. Finally, we verified that the theoretical BCS- and BEC-limiting behaviors are reproduced.

6.3 Extraction of dimer-dimer collisional properties

The four-body problem of two-component Fermi system in the BEC side was first considered by Petrov *et al.* 2004 [139]. Their solution showed that the system of bosonic dimers is stable and that the interaction between dimers is characterized by an effective scattering length of $a_d d = 0.6a_s$. This value was later derived using diagrammatic techniques [115, 31]. Here, we extract the dimer-dimer scattering length and its first energy correction, the effective range from the four-body spectrum. These calculations are extended to two fermionic species with unequal mass ratio.

In the BEC limit, the lowest $N = 3$ states behave as a dimer and an atom. Similarly, the lowest $N = 4$ states describe different vibrational states of a dimer-dimer configuration. Therefore, both the $N = 3$ and $N = 4$ systems can be treated effectively as two-particle systems. A comparison between the two particle solutions with the

$N = 3$ or $N = 4$ solutions allows us to extract information on the effective atom-dimer or dimer-dimer interactions.

The two-particle system is much simpler to solve than the corresponding $N = 3$ or $N = 4$ systems. However, we do not know the form of the dimer-dimer or atom-dimer effective potentials. A simple way to deal with this problem is to approximate the effective potentials with zero-range pseudopotentials. Since the size of the dimers are of the order of a, we expect that the range of the effective potentials should also be of order of a. Thus, we consider including effective range effects using an energy dependent scattering length. We recognize that the inclusion of the energy dependence of the scattering length notably extends the validity regime of the zero-range pseudopotential when applied to the description of the scattering of two atoms with finite-range potentials under external confinement [17, 21].

Therefore, we opt to use the zero-range pseudopotential two-particles solutions found in Sec. 2.2 to describe these effective two-body systems. In the zero-range solutions, we include the energy dependence of the scattering length by using the effective range expansion

$$-\frac{1}{a_{E_{rel}}} \approx -\frac{1}{a_f} + \frac{1}{2}k^2 r_{eff}. \tag{6.7}$$

Here, $a_{E_{rel}}$ is the energy-dependent scattering length parameterized by the (zero-energy) scattering length a_f and the effective range r_{eff}. The momentum k is associated with the relative kinetic energy of the dimer. Thus, $k^2/2\mu = E_{rel}$ where $E_{rel} = E_{3b} - E_{2b}$ for $N = 3$ and $E_{rel} = E_{4b} - 2E_{2b}$ for $N = 4$. For $N = 4$, relative mass μ is $\mu_{dd} = M/2$, where M is the mass of the bosonic molecules, $M = m_1 + m_2$. For $N = 3$ we only consider the equal mass case $[m_1 = m_2]$, thus relative mass μ is $\mu_{ad} = Mm/(M + m) = 2m/3$, where $M = 2m$.

Using the effective range expansion [Eq. (6.7)], the regularized zero-range potential $V(r)$ [95] takes the form $V(r) = g(E)\delta(\vec{r})(\partial/\partial r)r$. The scattering strength g is

parameterized by the scattering length a_0 and the effective range r_{eff}, i.e.,

$$g(E) = \frac{2\pi\hbar^2\, a_f}{\mu}\left[1 - \frac{\mu E_{rel} r_{eff} a_f}{\hbar^2}\right]^{-1}. \tag{6.8}$$

As presented in Sec. 2.3, the $L = 0$ spectrum of the two particle system is then given by

$$\sqrt{2}\frac{\Gamma\left(-\frac{E_{rel}}{2\hbar\omega} + \frac{3}{4}\right)}{\Gamma\left(-\frac{E_{rel}}{2\hbar\omega} + \frac{1}{4}\right)} = \frac{a_{ho}^{(\mu)}}{a_{E_{rel}}}. \tag{6.9}$$

Equation (6.9) is a transcendental equation that can be easily solved numerically. The solutions of Eq. (6.9) are obtained as functions of the a_f and r_{eff} parameters and fitted to the numerical results. The calculation can be carried out at different values of the two-body scattering length a_s and, in this way, one can obtain a more reliable estimation of a_f and r_{eff}. To compare calculations at different values of a_s, we have to first understand the dependence of a_f and r_{eff} on a_s.

To relate a_f and r_{eff} with the two-body scattering length a_s we can use dimensional analysis considerations. If the particles interact through short-range interactions characterized by a scattering length a_s, both the size of the dimers and the atom-atom interaction only depend on a_s. For this reason, we expect that the effective dimer-atom or dimer-dimer interactions only depends on a_s and not on the details of the short-range interactions. This implies that a_{ad}, a_{dd}, r_{ad}, and r_{dd} should be proportional to the two-body scattering length a_s. Therefore, we propose $a_{ad} = c_{ad}a_s$, $a_{dd} = c_{dd}a_s$, $r_{ad} = d_{ad}a_s$, and $r_{dd} = d_{dd}a_s$. The parameters c_{ad} and d_{ad} are obtained by fitting the zero-range two-particle solution to the atom-dimer states of the $N = 3$ system. Similarly, the parameters c_{dd} and d_{dd} are obtained by fitting the zero-range–two-particle solution to the dimer-dimer states of the $N = 4$ system.

First, we analyze the equal-mass atom-dimer system. Considering the three lowest energy levels on the BEC side, we obtain $a_{ad} \approx 1.18(1)a_s$ and $r_{ad} \approx 0.08(1)a_s$. The atom-dimer scattering length agrees with that of Refs. [158, 138, 154]. As discussed earlier [141], the atom-dimer system can be characterized by a soft-core repulsion with

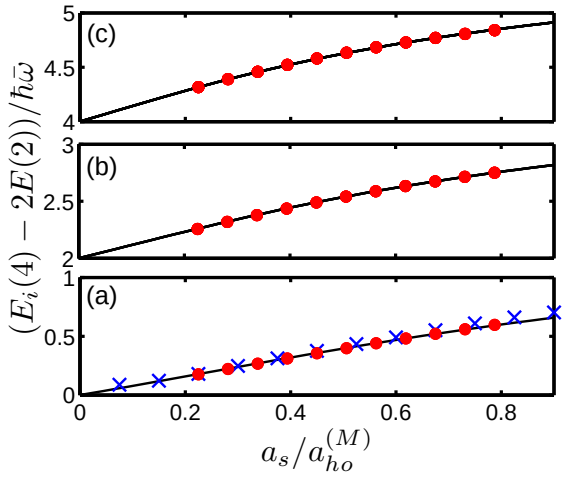

Figure 6.5: Four-body energies of the three energetically lowest-lying dimer-dimer states as a function of $a_s/a_{ho}^{(M)}$ for $\kappa = 8$. Panel (a) shows the energetically lowest lying energy level ($i = 0$), panel (b) the energetically second lowest ($i = 1$) and panel (c) the energetically third lowest state ($i = 2$). Circles and crosses show our CG and FN-DMC results, respectively. Solid lines show the zero-range model results. Figure from Ref. [184].

range of the order of a_s; our calculations support this general picture but predict a range about 10 times smaller than a_s.

Second, we analyze the dimer-dimer states of the $N = 4$ systems. To illustrate the fitting procedure, the circles in Figs. 6.5(a)–(c) show three energetically lowest-lying dimer-dimer energy levels, referred to as $E_i(4)$, where $i = 0$–2 with the center-of-mass energy and the dimer-binding energy subtracted. The results of Figs. 6.5(a)–(c) correspond to $\kappa = 8$ and where obtained by the CG approach Solid lines show the energy levels obtained by fitting these four-body energies to the two-boson energies obtained using the energy-dependent zero-range pseudopotential. We find that inclusion of the effective range r_{dd} extends the validity regime over which the four-fermion system can be described by the two-boson model and additionally allows for a more reliable determination of a_{dd}. Figure 6.5 illustrates that the two-boson spectrum reproduces the dimer-dimer states of the four-fermion spectrum well over a fairly large range of atom-atom scattering lengths, a_s.

For comparison, crosses in Fig. 6.5(a) show the corresponding FN-DMC energies for the energetically lowest-lying dimer-dimer state. In the application of Blume's FN-DMC, we do not attempt to construct a guiding function that would allow for the determination of excited dimer-dimer states. We find that the FN-DMC energies are slightly larger than the CG energies and that the deviation increases with increasing a_s. Presumably, this increasing deviation can be attributed to the functional form of the nodal surface used in the FN-DMC calculations, which should be best in the very deep BEC regime. The increasing deviation between the FN-DMC and CG energies with increasing a_s explains why the effective range predicted by the analysis of the FN-DMC energies is somewhat larger than that predicted by the analysis of the CG approach (see discussion of Fig. 6.6 below).

Formation of trimers or tetramers can affect this dimer-dimer analysis. If we use short-range Gaussian two-body potentials that support no two-body–s-wave-bound

state for negative a_s and one two-body–s-wave-bound state for positive a_s, the four-body energy that enters the calculation of the energy crossover curves shown in Fig. 6.2 is the true ground state of the system, i.e., no energetically lower-lying bound trimer or tetramer states with $L^P = 0^+$ symmetry exist. For larger mass ratios, bound trimer states exist. The mass ratio at which these nonuniversal trimer states appear depends on the range r_0 of the two-body potential employed. In the regime where three-body bound states exist, the four-body spectrum calculated by the CG approach also contains universal states that are separated by approximately $2\hbar\omega$; they can be best described as two weakly interacting composite bosons. For fixed a_s ($a_s > 0$), the energy of these "dimer-dimer states" changes smoothly as a function of κ even in the regime where bound trimer states appear. In the following, we use these dimer-dimer states to extract the dimer-dimer scattering length as a function of κ up to $\kappa = 20$.

Our analysis of the dimer-dimer states is carried out for selected values of the mass ratio κ. Table 6.1 summarizes the results. Circles and crosses in Fig. 6.6 show the resulting dimer-dimer scattering lengths, a_{dd}, extracted from the energies calculated by

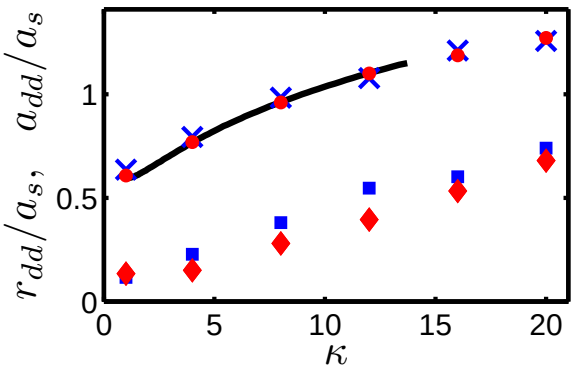

Figure 6.6: Circles and crosses show a_{dd}/a_s as a function of κ extracted from the four-fermion CG and FN-DMC energies, respectively. For comparison, a solid line shows the results from Fig. 3 of Ref. [140]. Diamonds and squares show r_{dd}/a_s extracted from the four-fermion CG and FN-DMC energies, respectively. Figure from Ref. [184].

the CG and the FN-DMC approach, respectively, as a function of κ. For all mass ratios

Table 6.1: Dimer-dimer scattering length, a_{dd}, and dimer-dimer effective range, r_{dd}, obtained using (a) the CG spectrum and (b) the FN-DMC energies. The reported uncertainties reflect the uncertainties due to the fitting procedure; the potential limitations of the FN-DMC method to accurately describe the energetically lowest-lying gaslike state, e.g., are not included here (see Sec. IIIB of Ref. [184]).

κ	a_{dd}/a_s (a)	a_{dd}/a_s (b)	r_{dd}/a_s (a)	r_{dd}/a_s (b)
1	0.608(2)	0.64(1)	0.13(2)	0.12(4)
4	0.77(1)	0.79(1)	0.15(1)	0.23(1)
8	0.96(1)	0.98(1)	0.28(1)	0.38(2)
12	1.10(1)	1.08(2)	0.39(2)	0.55(2)
16	1.20(1)	1.21(3)	0.55(2)	0.60(5)
20	1.27(2)	1.26(5)	0.68(2)	0.74(5)

considered in Fig. 6.6, we include up to three dimer-dimer energy levels in our analysis of the CG results and only the lowest dimer-dimer level in our analysis of the FN-DMC results. Our dimer-dimer scattering lengths agree well with those calculated by Petrov **et al.** within a zero-range framework [140] (solid line in Fig. 6.6). The calculations by Petrov **et al.**, performed for the free and not the trapped four-fermion system, terminate at $\kappa \approx 13.6$, beyond which a three-body parameter is needed to solve the four-body equations within the applied framework. Our calculations show the existence of deeply-bound "plunging" states, that consist of a trimer plus a free atom. These states signal a qualitative change of the energy spectrum, in agreement with Petrov **et al.** [140]. At the same time, our calculations for finite-range potentials predict that a_{dd} continues to increase smoothly when the mass ratio κ exceeds 13.6. This can possibly be explained by the fact that the presence of the external confining potential may "wash out" some of the features present in the free-space system. As already mentioned, the study of the stability of the four-fermion system, consisting of two dimers, with large mass ratios is beyond the scope of this work. Nevertheless, a recent theoretical study found good agreement with our predictions beyond 13.6 [122].

We now turn to an analysis of the effective range results. Diamonds and squares in Fig. 6.6 show the effective range, r_{dd}, extracted from our CG and FN-DMC energies,

respectively. We estimate the uncertainty of r_{dd} obtained from the CG approach to be about 10%; this uncertainty is quite a bit larger for that extracted from the FN-DMC energies. Figure 6.6 shows that the ratio r_{dd}/a_{dd} increases from about 0.2 for $\kappa = 1$ to about 0.5 for $\kappa = 20$. While earlier work already suggested that the dimer-dimer potential may be best characterized as a broad soft-core potential [140], implying a non-negligible value for the effective range of r_{dd}, our work makes the first quantitative predictions for r_{dd} as a function of κ. The large value of r_{dd} suggests that effective-range corrections may need to be considered in analyzing the physics of molecular Fermi gases.

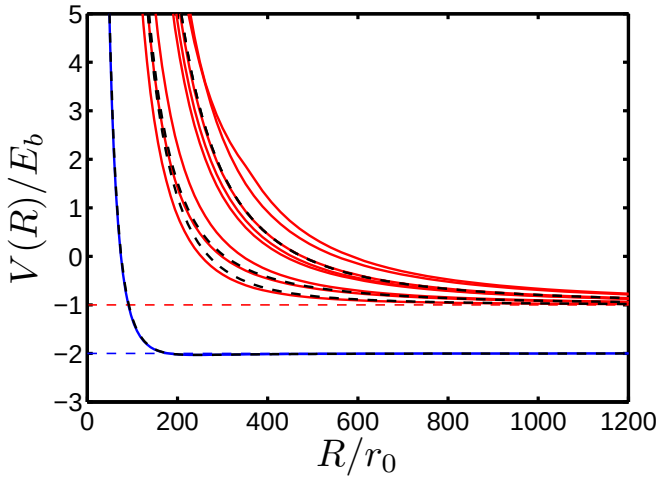

Figure 6.7: Hyperspherical potential curves U_ν for a scattering length $a_s = 100r_0$. The dashed red curve is the dimer threshold and the dashed blue curve is the dimer-dimer threshold. Therefore, the blue curve is a dimer-dimer potential curve and the red curves are dimer–two-atom potential curves. Dashed-black curves are predictions from Ref. [56].

The development of four-body hyperspherical methods allows an analysis of the full energy dependence of the dimer-dimer scattering length. Figure 6.7 presents the four-fermion potential curves obtained with correlated Gaussian hyperspherical (CGHS). The lowest curve represents the dimer-dimer channel and the rest represent different dimer–two-atom channels. Standard multichannel scattering techniques, like the R-matrix method, can be applied to solve the hyperspherical coupled differential equa-

tions. This analysis was performed in a recent study by D'Incao **et. al.** [56] where energy dependence of the dimer-dimer scattering length for equal mass systems was obtained. Black dashed curves in Figure 6.7 represent the potential curves of Ref. [56]. As we can see, the CGHS method presented in this dissertation predicts very similar potential curves. The dimer-dimer potential curves obtained with the different methods are almost indistinguishable. For dimer–two-atom potential curves, the CGHS predicts lower potential curves suggesting that the CGHS calculation is slightly better. At large R, the asymptotic behavior of both methods agree. This is very encouraging since in D'Incao **et. al.** method, the asymptotic behavior of the channels is correct by construction but in the CGHS implies an important nontrivial test. Preliminary calculations with the CGHS potential curves predict a similar energy dependence of the dimer-dimer scattering length. Therefore, we consider that the CGHS opens the possibility for accurately analyzing four-body scattering events, as we will see in the four-boson problem presented in chapter 8.

To conclude, we have shown that few-body trapped systems can be used to extract information on the collisional properties of free systems. Atom-dimer and dimer-dimer scattering lengths can be extracted by analyzing the trapped few-body spectrum for different two-body scattering length values. Furthermore, energy-dependent corrections to a_{ad} and a_{dd} can also be obtained with this method.

6.4 A two-channel model for the BEC-BCS crossover.

We observed in Sec. 3.2, that the BCS- and BEC-limiting behaviors can be described by completely different wave functions. The BCS-limiting behavior is described by a Jastrow-Slater type of wave function, while the BEC behavior is described by a paired wave function. These type of wave functions where discussed from a technical point of view in the FN-DMC section of chapter 3 to construct the appropriate trial wave function. Here, we use these two trial wave functions to propose a simple interpretation

of the BCS-BEC crossover problem.

Since the BCS and BEC regimes are described by qualitatively different wave functions, it is natural to suspect that the BCS-BEC crossover can be understood as an avoided crossing between these two limiting cases. This interpretation suggests a crossover from a normal to a superfluid state. The paired wave function is consistent with superfluidity because of its long-range correlations, while the Jastrow-Slater wave function only contains short-range correlations that are characteristic of a normal state. Therefore, the crossover would imply an avoided crossing between a normal and a superfluid state.

Here, we propose a two-channel model to qualitatively describe the BCS-BEC crossover. In this model, the trial wave function ansatz is a linear combination of the Jastrow-Slater wave function and the paired wave function. We apply it to the four-fermion system and compare our model to the full CG results.

To implement this model, we have to construct the paired and Jastrow-Slater states and evaluate the matrix elements in this reduced two-state Hilbert space. Next, we solve the Schrödinger equation for this two-channel system. The paired wave function for four particles takes the form,

$$\begin{aligned}\Psi_P(\mathbf{r}_1,\mathbf{r}_2,\mathbf{r}_{1'},\mathbf{r}_{2'}) &= \mathcal{A}\{\psi_{2p}(\mathbf{r}_1,\mathbf{r}_{1'}),\psi_{2p}(\mathbf{r}_2,\mathbf{r}_{2'})\} \\ &= N_p\left(\psi_{2p}(\mathbf{r}_1,\mathbf{r}_{1'})\psi_{2p}(\mathbf{r}_2\mathbf{r}_{2'}) - \psi_{2p}(\mathbf{r}_1,\mathbf{r}_{2'})\psi_{2p}(\mathbf{r}_2,\mathbf{r}_{1'})\right). \quad (6.10)\end{aligned}$$

Here N_p is a normalization constant, and ψ_{2p} is the two-body solution of the trapped system. The Jastrow-Slater wave function is

$$\Psi_J(\mathbf{r}_1,\mathbf{r}_2,\mathbf{r}_{1'},\mathbf{r}_{2'}) = \prod_{i,i'} J(r_{ii'})\Psi_{NI}(\mathbf{r}_1,\mathbf{r}_2,\mathbf{r}_{1'},\mathbf{r}_{2'}). \quad (6.11)$$

The correlations in the Jastrow-Slater term are usually obtained by using the small-r region of the zero-energy solution matched to a fast-decaying function (for example with an exponential decay). In the negative scattering length, the Jastrow-Slater term

does not have nodes, but in the positive scattering length region, each Jastrow-Slater correlation has a node that describes the zero-energy correlations of the excited atomic state, but not the weakly bound molecular ground state. Thus, the total wave function describes the atomic ground state in both the BCS- and BEC-limiting cases.

We use the two-body solutions of two particles in a trap to construct ψ_{2p}. These solutions can be separated in center-of-mass and relative coordinates, R_{CM} and r, as

$$\psi_{2p}(\mathbf{r}_1, \mathbf{r}_2) = e^{-2R_{CM}^2/a_{ho}^2}\phi(r). \tag{6.12}$$

The evaluation the matrix elements requires the evaluation of multidimensional integrals. Thus, it is convenient to use a correlated-Gaussian expansion that allows an analytical computation of the matrix elements. To obtain the paired wave function, we first solve the two-body Schrödinger equation in the relative coordinate using CG, then we use the ground-state–two-body solution to expand Eq. (6.10) in a CG basis functions.

To construct the Jastrow-Slater wave function, we use a different approach. In practical terms, it is not very convenient to construct the Jastrow-Slater wave function from the two-body solution and the noninteracting wave function. This solution would produce an unnecessarily large CG basis-function expansion. Instead, it is easier to solve the exact Hamiltonian in the perturbative regime where we know that the exact solution has the form of Eq. (6.11) and then use that solution in the two-channel model. Here, it is assumed that the Jastrow term does not depend strongly on a and that we can use a solution at one a value for a wide region of the crossover. This assumption is considered valid in the BCS and BEC regimes but not in the strongly interacting region where an extra node appears in the correlations. Thus, Jastrow terms in the BCS and BEC side are significantly different because the appearance of that extra node. Therefore, we use the perturbative solution on the BCS side to describe the BCS-unitarity region and we use the peturbative solution on the BEC side to describe the BEC-unitarity region.

This approximation seems to be sensible for our qualitative two-channel model.

Figure 6.8 present the results of the two-channel model. The black solid lines correspond to the noninteracting energy [$E = 8\hbar\omega$] and the energy of the paired wave function. The blue dashed lines correspond to the solutions of the two-channel model. The red lines with circles corresponds to the exact ground state obtained with the CG method, and green lines with circles corresponds to the state that diabatically becomes the "atomic ground state" in the BEC. First, we note that the paired state represents a diabatic state that crosses the trapped states in the BCS regime and correctly describes the dimer-dimer states in the BEC regime. The lowest dashed curve, which is the ground state of the two-channel model, follows closely the true ground state. As expected, the deviations of the two-channel model solution to the exact solution are maximal in the strongly interacting unitarity regime. Another important result is that the excited solution of the two-channel model describes the atomic ground state in the BEC side.

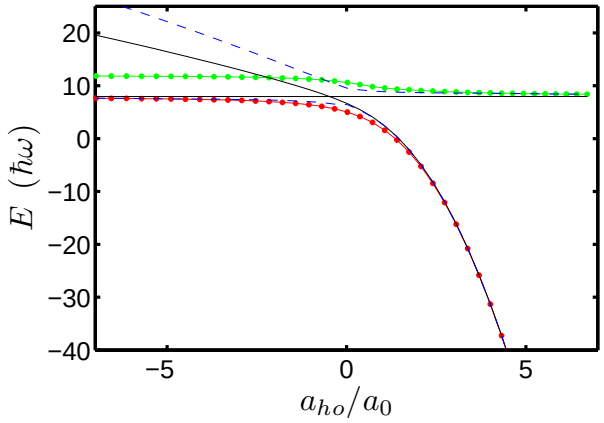

Figure 6.8: Comparison of exact calculations with the two-channel model. Solid black lines correspond to the noninteracting energy and the pair-state energy, respectively. Blue dashed curves correspond to the two-channel model solutions. Red and green lines with circles correspond to the exact CG results for the ground state and the lowest atomic state in the BEC side, respectively.

Finally, we have shown that the two-channel model qualitatively describes the BCS-BEC crossover providing, an alternative interpretation to the crossover physics.

6.5 Structural properties

The analysis of the spectrum in the BCS-BEC crossover can be complemented with the analysis of the wave functions and their structural properties. Here, we obtain the one-body densities and pair-distribution functions of two-component Fermi systems in the crossover regime for different κ. We determine the averaged radial densities, $\rho_i(r)$, normalized so that $4\pi \int \rho_i(r) r^2 dr = N_i$; $4\pi r^2 \rho_i(r)/N_i$ tells one the probability of finding a particle with mass m_i at a distance r from the center of the trap. If $N_1 = N_2$ and $m_1 = m_2$, the radial one-body densities $\rho_1(r)$ and $\rho_2(r)$ coincide. If m_1 and m_2 or N_1 and N_2 differ, however, the radial one-body densities $\rho_1(r)$ and $\rho_2(r)$ are, in general, different. We also determine the averaged radial pair distribution functions $P_{ij}(r)$, normalized so that $4\pi \int P_{ij}(r) r^2 dr = 1$; $4\pi r^2 P_{ij}(r)$ tells one the probability of finding a particle of mass m_i and a particle of mass m_j at a distance r from each other. For notational simplicity, we refer to the radial one-body densities as one-body densities and to the radial-pair distribution functions as pair-distribution functions in from now on.

To compute these structural properties we use CG. Since the CG method only calculates $L = 0$ states, all the structural properties extracted from CG are spherically symmetric. When $N + 1$ systems are studied to obtain solutions for the N system with $L > 0$, the N-particle system and the spectator particle are coupled to $L = 0$. Therefore, even though the structural properties of the N-system are not spherically symmetric, the structural properties obtained from the $N+1$ calculation are spherically symmetric. We can recover the corresponding angular dependence by multiplying the CG result by the corresponding spherical harmonic. However, for plotting purposes, it is convenient to present the spherically symmetric CG results, which is equivalent to averaging over the angular degrees of freedom.

To evaluate the structural properties, we calculate

$$4\pi r^2 F(r) = \langle \Psi_n | \delta(x-r) | \Psi_n \rangle = \int d\mathbf{r}_1 ... d\mathbf{r}_N \delta(x-r) |\Psi_n(\mathbf{r}_1, \mathbf{r}_{1'}, ..., \mathbf{r}_{N_1}, \mathbf{r}_{N_2})|^2. \quad (6.13)$$

Here, $F(r)$ is a generic structural property, i.e., the density profiles ρ_1 or ρ_2, the inter-species pair-correlation function P_{12}, or the intraspecies pair-correlation functions P_{11} or P_{22}. x is the length of the coordinate vector that describes the structural property. For ρ_1 and ρ_2, $x = r_1$ and $x = r_{1'}$, respectively. For P_{12}, x is the interparticle distance between opposite-spin or different species, $x = r_{11'}$. For P_{11} and P_{22}, x is the same-spin or same species interparticle distance, with $x = r_{12}$ and $x = r_{1'2'}$, respectively. To evaluate $4\pi r^2 F(r)$, we expand Ψ_n in the CG basis set. The integral in Eq. (6.14) can be carried out analytically for the CG basis functions (see Appendix G).

6.5.1 Analysis of the validity of the numerical structural properties

The first question that we want to answer is how reliable are our structural properties. To answer this question, we first compare structural properties obtained by CG and FN-DMC methods. Then, we analyze how well these structural properties reproduce the expected behavior from a zero-range pseudopotential.

Figures 6.9 (a) and (b) compare the pair distribution functions $P_{12}(r)$ for the three-particle system with $L = 1$ and the four-particle system with $L = 0$, respectively, calculated by the CG and the FN-DMC methods. The pair correlation functions $P_{12}(r)$ at unitarity allow the most stringent comparisons between the CG and FN-DMC predictions. The correlations between opposite spins or different species describe a non-trivial behavior controlled by the properties of the short-range interactions. Therefore, these correlations depend strongly on the scattering length a_s, and the shape and range of the interaction r_0. Since we use different short-range potentials in CG and FN-DMC, the good agreement in Figs. 6.9(a) and (b) suggest that these correlations are mainly described by the scattering length. Another important point is that we make

the comparison at unitarity in the strongly interacting regime where the correlations are nontrivial.

The agreement between the pair-distribution functions calculated by the CG method (solid lines) and the FN-DMC method (circles) is very good, supporting both numerical results. This is particularly important for the FN-DMC results since it suggests that the construction of the nodal surface of the trial wave function ψ_T is close to the exact one. Furthermore, the good agreement suggests that the technique used to extract the FN-DMC results, i.e., the evaluation of the mixed estimator, provides structural properties very close exact ones estimator (see discussion on the mixed estimator in Chapter 3). This agreement is very encouraging. In particular, it suggest that the $N > 4$ structural properties obtained in Ref. [185] with FN-DMC are reliable.

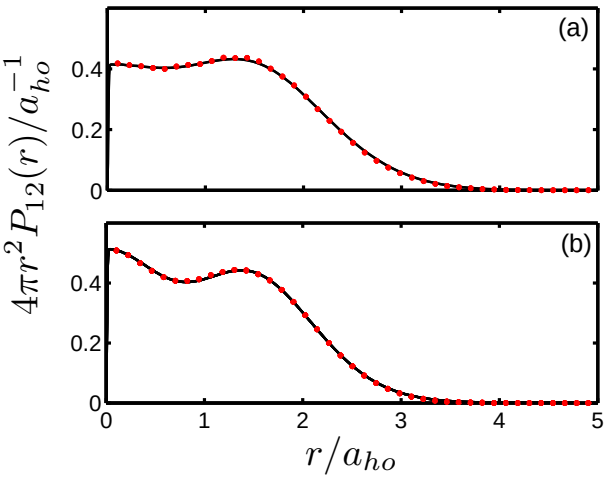

Figure 6.9: Pair-distribution functions $P_{12}(r)$, multiplied by r^2, at unitarity for equal mass Fermi systems with (a) $N = 3$ ($L = 1$) and (b) $N = 4$ ($L = 0$) atoms calculated by the CG method (solid lines) and by the FN-DMC method (circles). The agreement is excellent. Figure from Ref. [185].

The second question we want to answer is how these numerical results compare to the zero-range pseudopotential predictions. The comparison presented in Figures. 6.9(a) and (b) made the first step in this direction by showing that the numerical solutions

are, to a good approximation, independent of the model potential used. To further investigate the universal behavior of the structural properties we analyze zero-range predictions. For zero-range pseudopotential, the opposite-spin pair-correlation function obeys a boundary condition [118, 76]

$$\frac{[rP_{12}(r)]'_{r=0}}{[rP_{12}(r)]_{r=0}} = -\frac{2}{a_s}. \tag{6.14}$$

This boundary condition is a consequence of the Bethe-Peierls boundary condition. Equation (6.14) can be derived by taking into account that the wave functions obey the boundary condition $[r_{12}\Psi(r_{12})]'_{r_{12}=0}/[r_{12}\Psi(r_{12})]_{r_{12}=0} = -1/a_s$. The factor of 2 in Eq. (6.14) can be understood by noticing that the pair correlation is proportional to the square of the wave function, i.e., $P_{12}(r) \propto \Psi(r_{12})^2$. A direct consequence of Eq. (6.14) is that at unitarity, i.e., when $|a| = \infty$, $r^2 P_{12}(r)$ has zero slope as $r \to 0$. This condition is qualitatively fulfilled in the numerical results presented in Figs. 6.9 (a) and (b).

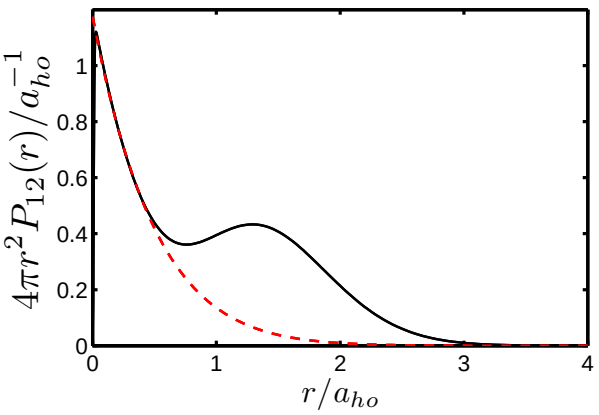

Figure 6.10: Pair-distribution functions $P_{12}(r)$, multiplied by r^2, for equal-mass–two-component Fermi systems with $N = 2$ (dashed lines) and $N = 4$ (solid lines). The $N = 2$ pair-correlation function has an arbitrary norm selected to match the $N = 4$ pair correlation in the small r regime.

The numerical verification of Eq. (6.14) is very difficult. For systems with finite range interactions, Eq. (6.14) is valid in a narrow regime of r values. For $a_s < 0$, Eq. (6.14) is valid when r is much larger than the range of the potential and much

smaller than the mean interparticle distance, i.e., the $r_0 \ll r \ll a_{ho}$ regime. For $a_s > 0$, Eq. (6.14) is valid when r is much larger than the range of the potential and much smaller than the size of the dimer (given by a) and the mean interparticle distance, i.e., the $r_0 \ll r \ll \min[a_s, a_{ho}]$ regime. This regime is almost nonexistent for our numerical calculations, which consider only the $a_ho/r_0 = 100$ case.

An alternative procedure is to compare the numerical results with the two-body analytical results of the zero-range pseudopotential presented in Sec. 2.3. This comparison is more convenient because the two-body analytical results include corrections to Eq. (6.14) for trapping effects and finite r. Figure 6.10 presents the $N = 2$ and $N = 4$ pair correlation $r^2 P_{12}(r)$. The calculations are done on the BEC side [$a_s = a_{ho}$], where both the $N = 2$ and $N = 4$ pair correlations in the small r region are controlled by molecule formation (see discussion below). The good agreement between the $N = 2$ and $N = 4$ pair correlations in the small r region suggests that the $N = 4$ numerical results correctly describe the zero-range pseudopotential limit.

6.5.2 Structural properties along the BEC-BCS crossover

Here, we analyze how structural properties change in the BCS-BEC crossover. We focus in particular on the structural properties of the ground state for $N = 4$ and the lowest $N = 3$ state with $L = 0, 1$.

Figure 6.11 shows the pair distribution function $P_{12}(r)$ for $N = 3$ (dash and dash-dotted lines correspond to $L = 0$ and 1, respectively) and $N = 4$ (solid lines) along the crossover for equal mass systems [$\kappa = 1$]. Panel (a) shows results for $a_s = -a_{ho}$, panel (b) for $1/a_s = 0$ and panel (c) for $a_s = 0.1a_{ho}$. Interestingly, the pair distribution functions for $N = 3$ and $N = 4$ show a similar overall behavior. In the BCS regime [Fig. 6.11(a)], the quantity $P_{12}(r)r^2$ shows a minimum at small r (for very small r, $P_{12}(r)r^2$ goes smoothly, but steeply, to zero; this rapid change of $P_{12}(r)r^2$ is hardly visible on the scale shown in Fig. 6.11). At unitarity [Fig. 6.11(b)], $P_{12}(r)r^2$ shows a

maximum at small r and a second peak at larger r. In the BEC regime [Fig. 6.11(c)], the two-peak structure is noticeably more pronounced. The peak at small r indicates the formation of weakly bound dimers (one dimer for $N = 3$ and two dimers for $N = 4$), while the peak between $1\,a_{ho}$ and $2\,a_{ho}$ is related to the presence of larger atom-atom distances set approximately by the atom-dimer distance for the three-body system and the dimer-dimer distance for the four-body system. This interpretation suggests that the three-particle system has one small and one large interspecies distance, and the four-particle system has two small and two large interspecies distances. Indeed, integrating $P_{12}(r)$ for $N = 3$ and $N = 4$ from 0 to the r value at which $P_{12}(r)r^2$ exhibits the minimum, we find that the likelihood of being at small distances (forming a molecule) and being at large distances is the same. Finally, we note that in the BCS-BEC crossover the slope of $r^2 P_{12}(r)$ at small r changes from positive to zero to negative as predicted by Eq. (6.14).

We now analyze the pair distribution function $P_{12}(r)$ for $N = 4$ more quantitatively. Dash-dotted lines in Figs. 6.12 (a) and (b) show the pair-distribution function, $P_{12}(r)$, multiplied by r^2, for two trapped atoms with $a_s = 0.1a_{ho}$ (normalized to 1/2). This dimer curve is essentially indistinguishable from the small r part of the four-particle pair distribution function (circles). To describe the large r part of the four-particle pair-distribution function, we consider two bosonic molecules of mass $2m$, which interact through an effective repulsive potential with dimer-dimer scattering length $a_{dd} \approx 0.6a_s$ [140, 184]. The dashed line in Fig. 6.12 (a) shows the pair-distribution function for this system under external confinement. This dashed curve is essentially indistinguishable from the large r part of the pair-distribution function for the four-particle system. For comparison, a dotted line shows the pair-distribution function for two noninteracting trapped bosons of mass $2\,m$. Figure 6.12 indicates that the effective repulsive interaction between the two dimers is crucial for accurately reproducing the structural properties of the four-body system. Our analysis shows that the entire pair

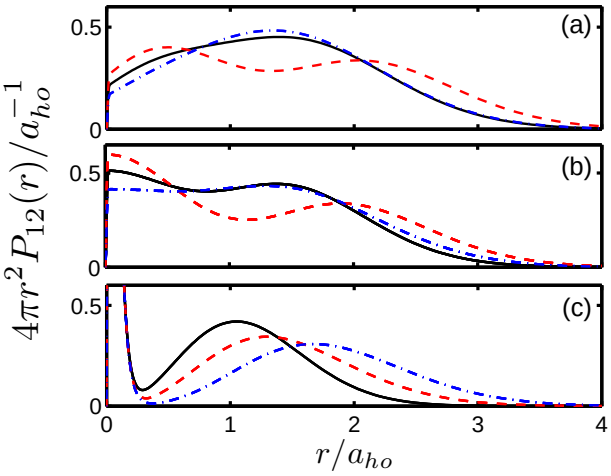

Figure 6.11: Pair-distribution functions $P_{12}(r)$, multiplied by r^2, for equal-mass–two-component Fermi systems with $N = 3$ and $L = 0$ (dashed lines), $N = 3$ and $L = 1$ (dash-dotted lines), and $N = 4$ and $L = 0$ (solid lines) obtained by the CG approach for three different scattering lengths, a_s: (a) $a_s = -a_{ho}$ (BCS regime), (b) $1/a_s = 0$ (unitarity), and (c) $a_s = 0.1a_{ho}$ (BEC regime). The pair distribution function for $N = 4$ and $a_s = 0.1a_{ho}$ [solid line in panel (c)] is shown in more detail in Fig. 6.12. Figure from Ref. [185].

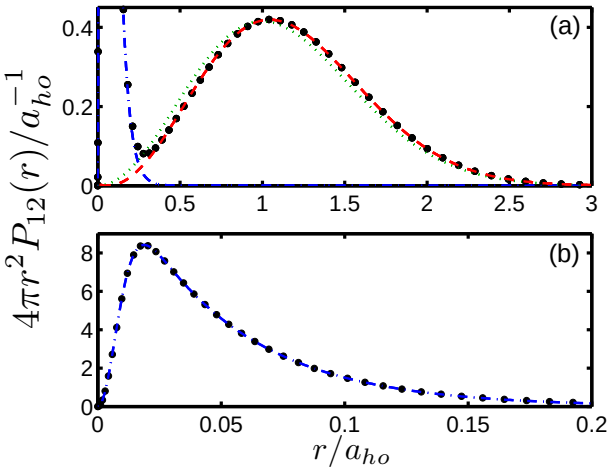

Figure 6.12: (a) Circles show the pair-distribution function, $P_{12}(r)$, multiplied by r^2, for $a_s = 0.1a_{ho}$ (BEC regime) calculated by the CG approach for $N = 4$ and $\kappa = 1$ [note, this quantity is also shown by a solid line in Fig. 6.11(c)]. For comparison, the blue dash-dotted line shows $P_{12}(r)r^2$ for two atoms of mass m with the same scattering length but normalized to 1/2, the red dashed line shows $P_{12}(r)r^2$ for two trapped bosonic molecules of mass $2\,m$ interacting through a repulsive effective potential with $a_{dd} = 0.6a_s$, and the green dotted line shows $P_{12}(r)r^2$ for two trapped noninteracting bosonic molecules of mass $2\,m$. Panel (b) shows a blow-up of the small r region. Figure from Ref. [185].

distribution function, $P_{12}(r)$, of the four-body system in the weaklyinteracting molecular BEC regime can be described quantitatively in terms of a "dimer picture."

The pair-correlation function $P_{12}(r)$ also reflects the ground-state symmetry inversion of the $N = 3$ system (see Sec. 6.2). In the BCS regime and at unitarity [Figs. 6.11 (a) and (b)], $P_{12}(r)$ shows less structure for $L = 1$ than for $L = 0$. In the weakly-interacting molecular BEC regime [Fig. 6.11(c)], the pair-distribution function for $L = 0$ nearly coincides with that for $L = 1$ at small r, but is more compact than that for $L = 1$ at large r.

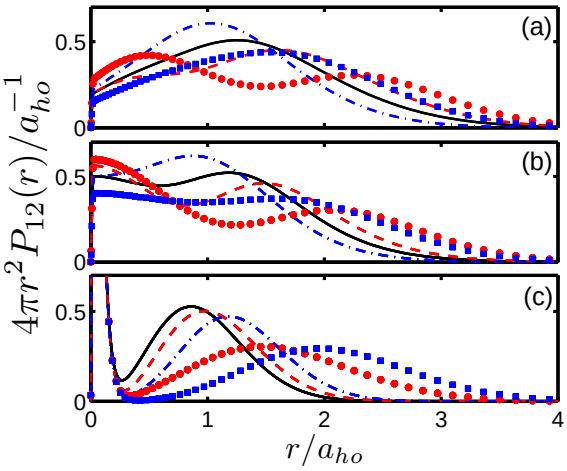

Figure 6.13: Pair-distribution function $P_{12}(r)$, multiplied by r^2, for two-component Fermi gases with $\kappa = 4$ for different scattering lengths a_s: (a) $a_s = -a_{ho}$ (BCS regime), (b) $1/a_s = 0$ (unitarity), and (c) $a_s = 0.1a_{ho}$ (BEC regime). Dashed and dash-dotted lines show $P_{12}(r)r^2$ for $N = 3$ (two heavy particles) with $L = 0$ and 1, respectively. Circles and squares show $P_{12}(r)r^2$ for $N = 3$ (two light particles) with $L = 0$ and 1, respectively. Solid lines show $P_{12}(r)r^2$ for $N = 4$ with $L = 0$. Figure from Ref. [185].

Next, we analyze how the behaviors of the pair distribution functions $P_{12}(r)$ for $N = 3$ and 4 change along the crossover if the mass ratio is changed from $\kappa = 1$ to 4. Figure 6.13 shows the pair distribution functions for $\kappa = 4$. For $N = 3$, we consider three-particle systems with either a spare light particle or a spare heavy particle. The pair distributions for the three-particle system with two light particles and one heavy

particle are notably broader than those for the three-particle system with one light particle and two heavy particles. We attribute this behavior to the fact that $a_{ho}^{(1)} > a_{ho}^{(2)}$. Besides this, a comparison of the pair-distribution functions shown in Fig. 6.13 for $\kappa = 4$ and those shown in Fig. 6.11 for $\kappa = 1$ reveals that the overall behavior of the $P_{12}(r)$ is similar.

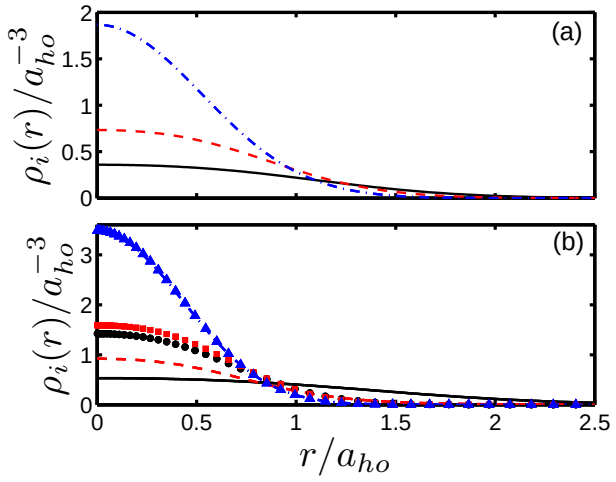

Figure 6.14: One-body densities $\rho_1(r)$ and $\rho_2(r)$ for $N = 4$ and (a) $\kappa = 1$ and (b) $\kappa = 4$ for different scattering lengths a_s [for $\kappa = 1$, $\rho_1(r)$ and $\rho_2(r)$ coincide and only $\rho_2(r)$ is shown]: Circles and solid lines show $\rho_1(r)$ and $\rho_2(r)$ for $a_s = 0$, squares and dashed lines show $\rho_1(r)$ and $\rho_2(r)$ for $1/a_s = 0$, and triangles and dash-dotted lines show $\rho_1(r)$ and $\rho_2(r)$ for $a_s = 0.1a_{ho}$. Note, $\rho_2(r)$ for $\kappa = 4$ and $a_s = 0$ [solid line in panel (b)] is multiplied by a factor of three to enhance the visibility. Figure from Ref. [185].

The analysis of the pair correlation function is complemented with the analysis of the one-body densities. Figures 6.14(a) and (b) show the one-body densities for $\kappa = 1$ and 4, respectively. In the noninteracting limit [the solid lines show $\rho_1(r)$ and the circles show $\rho_2(r)$], the sizes of $\rho_1(r)$ and $\rho_2(r)$ are determined by $a_{ho}^{(1)}$ and $a_{ho}^{(2)}$, respectively. As is evident in Fig. 6.14, the density of the light particles extends to larger r than the density of the heavy particles. The density mismatch for $\kappa = 4$ between the two one-body densities decreases as a_s is tuned through the strongly-interacting regime to the weakly-interacting molecular BEC side. In the weakly-interacting molecular BEC

regime, two molecules consisting each of a heavy and a light particle form. In this regime, the size of the system is determined by the molecular trap length and the densities $\rho_1(r)$ and $\rho_2(r)$ [triangles and dash-dotted line in Fig. 6.14(b)] nearly coincide. Furthermore, the densities are to a very good approximation described by the one-body density for two bosonic molecules of mass $m_1 + m_2$ interacting through an effective repulsive interaction characterized by the dimer-dimer scattering length ($a_{dd} \approx 0.77 a_s$ for $\kappa = 4$ [140, 184]).

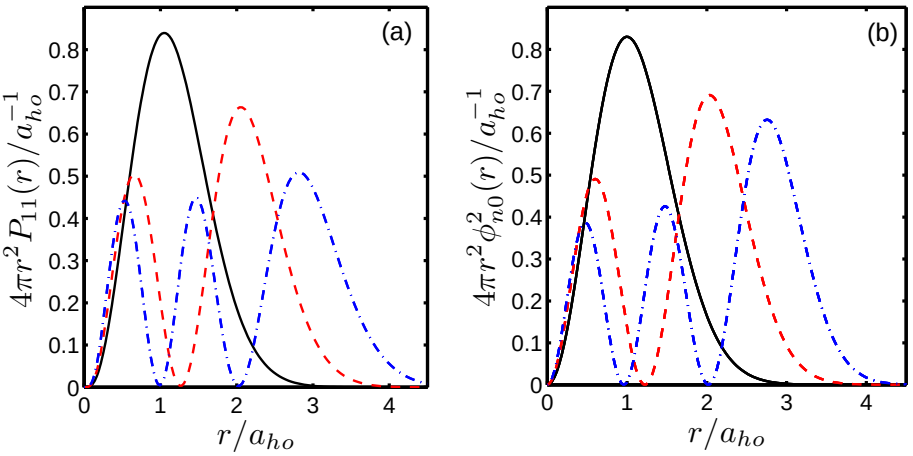

Figure 6.15: Ground and excited dimer-dimer states for $a_s = 0.1 a_{ho}$.(a) Pair-distribution function $4\pi r^2 P_1 1(r)$ for the lowest dimer-dimer states (b) Lowest two-body solutions, $4\pi r^2 \phi_{n0}(r)$, of a noninteracting trapped system of bosonic particles of mass $2\,m$.

On the weakly interacting molecular BEC side, where the size of the molecules is much smaller than the trap length, a_{ho}, P_{11} of the dimer-dimer states describes, to a good approximation, the molecule-molecule pair-correlation function. To understand why, consider the molecule-molecule pair-correlation function. If we treat the dimers as point particles, the molecule-molecule pair correlation function would measure the density probability as a function of the distance between the center of mass of two different dimers. But since the dimers are very small in comparison with the dimer-dimer distance, measuring the dimer-dimer distance from the center of masses or from each

of the spin up particles yields almost identical results. For this reason, on the weakly interacting molecular BEC side, P_{11} describes the molecule-molecule pair-correlation function.

As an example, consider the $P_{11}(r)$ for $a_s = 0.1a_{ho}$. Figure 6.15(a) shows $P_{11}(r)$ of the ground and excited dimer-dimer states. For comparison, Fig. 6.15(b) presents the square of the relative-coordinate wave functions ϕ_{nl} of two noninteracting particles of mass $M = 2\,m$ in a trap. The pair-correlation function of the $N = 2$ system is simply the square of relative-coordinate wave functions. Since the dimer-dimer states of the $N = 4$ system describe vibrational states with dimer-dimer angular momentum $l = 0$, Fig. 6.15(b) presents the $l = 0$ two-body solutions. The number of nodes in the $P_{11}(r)$ and ϕ^2_{nl} correspond to the number of vibrational excitations. The good agreement between panels (a) and (b) in Fig. 6.15 confirms that the dimer-dimer $P_{11}(r)$ in the BEC side describes the molecule-molecule pair-distribution function.

6.6 Conclusions

In this chapter, we have presented an accurate description of few-body trapped systems. First, we showed how the $N = 3$ and $N = 4$ spectrum evolves in the BCS-BEC crossover. Then, we analyzed more quantitatively the ground state energies and compared them both theoretical predictions and FN-DMC numerical results.

We also showed that the spectrum in the BEC regime reveals atom-dimer and dimer-dimer collisional properties such as scattering lengths and effective-range corrections. We have also presented calculations of the hyperspherical potential curves for $N = 4$. The analysis of the hyperspherical potential curves for free systems allows a direct measurement of the collisional properties. For this reason, the development the CGHS for four-body systems opens the possibility to deeper understanding of dimer-dimer collisional properties.

Finally, we analyzed the structural properties of $N = 3$ and $N = 4$ systems. We

showed how the qualitative change in the behavior of the systems in the BCS-BEC crossover is reflected in the structural properties.

Chapter 7

Unitary Gas

7.1 Introduction

In many-body systems, the strongly-interacting region is characterized by $k_F|a| \gtrsim 1$. In this region, the scattering length becomes larger than the interparticle distance, which, in turn, is much larger than the range of the two-body potential. Thus, the gas is both dilute and strongly interacting. This unusual situation is difficult to study physically since there is no small parameter for perturbation analysis. Even understanding the stability of such systems is challenging. Bosonic systems in such conditions are known to collapse, and fermionic systems, even though they are expected to be more stable because of Pauli repulsion, are not guaranteed to be stable. Sophisticated numerical simulations and experimental observations are required to show that fermionic systems are indeed stable.

Similarly for few-body trapped systems, the strongly-interacting region is also characterized by $k_F|a| \gtrsim 1$, which is equivalent to $|a| \gtrsim a_{ho}$. In the few-body case, difficulties similar to those of the many-body problem arise. There is no small parameter for perturbative treatments and there exist semianalytical solutions only for some cases of $N \leq 3$ [35, 187]. For $N > 3$, computationally demanding numerical techniques, like the ones presented in this chapter, have been used to analyze such systems.

A particular point in the strongly-interacting region, where the s-wave interaction strength reaches its maximal value, is usually called unitarity. Therefore, this regime is

characterized by a universal behavior of the scattering amplitude:

$$f_0(k) = \frac{i}{k}. \tag{7.1}$$

Unitarity is alternatively characterized by a divergent s-wave scattering length, $|a| = \infty$. In this situation, if the range of the interaction is much smaller than the typical interparticle distance and the scattering length is divergent, then there is no relevant length scale that characterizes the interaction. This situation is similar to the noninteracting limit, where the absence of interactions implies, of course, the absence of a length scale that describes the interaction. The absence of a length scale that describes the interaction allows us to extract the functional form of different quantities via dimensional analysis. Furthermore, it allows us to relate quantities at unitarity to those in the noninteracting limit.

For example, in the homogenous system at unitarity, the only relevant length scale is the interparticle distance of the noninteracting system, or, equivalently, k_F^{-1}. Therefore, the energy and the chemical potential of the system at unitarity should be proportional to those of the noninteracting system. In general, this relation is written as

$$\mu_U = (1+\beta)\mu_{NI}, \tag{7.2}$$

$$\mathcal{E}_U = (1+\beta)\mathcal{E}_{NI}. \tag{7.3}$$

Here, the subscripts U and NI refer to the unitary and noninteracting limits, respectively, and $\mathcal{E}$ is the energy per unit volume. The relation between these unitary and noninteracting quantities is characterized by the parameter β. This parameter is universal, i.e., it is the same for any equally populated two-component Fermi gas and is independent of the nature of the interaction. An equivalent parameter, defined as $\xi = 1 + \beta$, has been extensively used in the literature. The same proportionality constant, $(1 + \beta)$, relates the noninteracting and unitarity pressures of the system. Also,

other quantities are related by powers of this constant. For example, the speed of sound (c) and the size of a trapped cloud $R^{(s)}$ are related as [75, 87]

$$c_U = \sqrt{1+\beta}c_{NI}, \tag{7.4}$$

$$R_U^{(s)} = (1+\beta)^{1/4}R_{NI}^{(s)}. \tag{7.5}$$

Because of these relationships, much effort has been expended to obtain the parameter β. The value of β has been calculated by, among other methods, numerical simulations using quantum Monte Carlo techniques [7]. Section presents a table with many different theoretical and experimental values for β. Other properties of unitary homogenous systems have been determined using dimensional analysis arguments [89].

The same dimensional analysis arguments used in homogeneous systems can be extended to few- and many- body systems using the hyperspherical framework. Dimensional analysis becomes particularly interesting in the hyperspherical framework of a free system, where the hyperradius is the only coordinate with units of length. Since the potential curves have units of energy and the only length scale is given by R, then it follows that $V_U(R) \propto 1/R^2$. This is equivalent of saying that $V_U(R) \propto V_{NI}(R)$, since the noninteracting potential curves have the form $1/R^2$(see Sec. 2.5). The inclusion of a trapping potential discretizes the spectrum and introduces similar scaling properties which influence the topology of the spectrum. We will analyze such universal properties of the trapped system in Sec. 7.2, where we will also explore their consequences.

However, not every system at unitarity obeys these universal properties. There are some cases where the short-range physics needs to be included to obtain converged results. A typical example is the three boson system. In this case, the lowest potential curve has an attractive $1/R^2$ form. This type of dipole interaction is too divergent as $R \to 0$. Therefore, the zero-range model predicts an unphysical Thomas collapse [176], i.e., there is no lower bound to the ground state, and there is an infinite number of bound states with divergent binding energies. The introduction of more-realistic short-

range physics is crucial for remedying this unphysical situation, because realistic short-range physics introduces a lower bound to the series of weakly bound states known as Efimov states [60, 61]. Thus, a new length scale that describes the short-range physics is necessary for describing the system. Consequently, the properties obtained by dimensional analysis are no longer valid for the all the solutions, but, they remain valid for some of the solutions.

The universal behavior of a system and its stability are closely related. The collapse of a trapped system is a many-body effect. Nevertheless, the existence or absence of weakly bound few-body systems clearly influence the stability of a system. For example, a clusterization process, i.e., formation of continuously enlarging bound systems, would also lead to a collapse. On the other hand, if, there is no weakly bound state for $N < N_c$ but there exists a weakly bound N_c-body state, then it is required that $N_c + 1$ particles get close together to form a N_c-body state. Therefore, the larger N_c is the more unlikely the clusterization process will occur [1] .

The need for a short-range physics length scale, the appearance of an attractive $1/R^2$ potential, and the formation of weakly bound states appear to be related. Verification of these scaling properties can tell us if a system behaves universally or if the formation of weakly bound molecules occurs. As we said before, formation of weakly bound molecules has consequences for the stability of the system.

7.2 Universal properties in trapped systems

In this section, we review the universal properties of trapped systems at unitarity. These properties, and the derivation presented in this Section, were obtained by Werner and Castin [38, 186].

As presented in the Introduction, short range interactions with large scattering

[1] In this discussion we are omitting the possible formation of tightly bound molecules which are also unlikely.

lengths can, in some cases, be replaced by a zero-range pseudopotential as in Eq. (2.9). The pseudopotential is equivalent to the Bethe-Peierls boundary condition [15] that, at unitarity, takes the form

$$\lim_{r_{ij}\to 0} \Psi \approx \frac{F}{r_{ij}} + \mathcal{O}(r_{ij}). \tag{7.6}$$

Here r_{ij} is any of the distances between interacting particles, and F is a smooth function of all coordinates except the interparticle distance r_{ij}. This unitary condition implies that when two particles get very close together, the wave function should behave as the scattering solution at unitarity, i.e., $\Psi \propto 1/r_{ij}$.

Except for these boundary conditions in the vicinity of coalescent points, i.e., r_{ij} is much smaller than the typical interparticle spacing, the wavefunction obeys the noninteracting Schrodinger equation $H_0\Psi = E\Psi$. The Hamiltonian is

$$H_0 = \sum_i -\frac{\hbar^2}{2m_i}\nabla_i^2 + \frac{1}{2}m_i\omega^2\mathbf{r}_i^2. \tag{7.7}$$

This Hamiltonian is identical to that of an ideal gas. The effects of interactions are included in the above boundary conditions, Eq. (7.6), which introduces a great mathematical difficulty to the problem.

To analyze this problem we use hyperspherical coordinates. We define the hyperspherical vector $\mathbf{R} = \{\mathbf{r_1}, ..., \mathbf{r_N}\}$. $\mathbf{R}$ describes all the coordinates of the system and can be divided into the hyperradius $R = |\mathbf{R}|$ and a set of angles encapsulated in a single coordinate called Ω. The contact conditions at unitarity do not have a length scale associated with them, since $a \to \infty$. Thus, they become invariant under the rescaling of the spatial coordinates. This behavior implies that for any wave function ψ that obeys the contact conditions, Eq. (7.6), we can define a rescaled wave function $\psi_\lambda(\mathbf{R}) = \psi(\mathbf{R}/\lambda)$ that also obeys the contact conditions. Here $\lambda > 0$ is the scaling factor.

In free space, this scale invariance implies that if ψ is an eigenstate of energy E, then there is an eigenstate of energy E/λ^2 for any λ. This relationship implies the absence of bound states in free space which otherwise would be an unphysical continuum

of states. In the trapped system, the appearance of a length scale, the trap length a_{ho}, breaks down the scale invariance properties of the eigenstates. However, as we will see in the following, a similar scale invariance analysis can be applied to trapped systems to extract unique universal properties.

To analyze the properties of a trapped system, consider the evolution of an initial stationary state Ψ_0 when the frequency of the external potential becomes time dependent, i.e., $\omega = \omega(t)$. Castin proposed the following ansatz for the time-dependent wavefunction,

$$\Psi(\mathbf{R}, t) = N(t) e^{imR_j^2 \lambda'(t)/2\hbar\lambda(t)} \Psi_0(\mathbf{R}/\lambda(t)) \tag{7.8}$$

where the scaling factor $\lambda(t)$ and the normalization $N(t)$ need to be determined. To verify to the validity of Castin's ansatz, we first note that Eq. (7.8) obeys the boundary condition, Eq.(7.6). Eq. (7.8) also obeys the time-dependent Schrödinger equation governed by the Hamiltonian of Eq. (7.7) provided that the time evolution of λ is described by

$$\lambda'' = \frac{\omega^2(0)}{\lambda^3} - \omega^2(0)\lambda. \tag{7.9}$$

In analyzing the perturbative time-dependent behavior of a stationary state of energy E, Castin showed that there exist states with energies $E \pm 2\hbar\omega$ [38]. Furthermore, in this time-dependent analysis, the operators responsible for $\pm 2\hbar\omega$ are obtained, and can be associated with raising and lowering operators [186]:

$$L_+ = \frac{3N}{2} + R\partial_R + \frac{H}{\hbar\omega} - \frac{m\omega R^2}{\hbar}, \tag{7.10}$$

$$L_- = -\frac{3N}{2} - R\partial_R + \frac{H}{\hbar\omega} - \frac{m\omega R^2}{\hbar}. \tag{7.11}$$

The commutations relations of H, L_+ and L_- have the structure of the SO(2,1) Lie

algebra;

$$[H, L_+] = 2\hbar\omega L_+, \tag{7.12}$$

$$[H, L_-] = -2\hbar\omega L_-, \tag{7.13}$$

$$[L_+, L_-] = -4H/\hbar\omega. \tag{7.14}$$

From this point on, all the machinery for raising and lowering operators can be applied. By successively applying the lowering operator to any eigenstate, we obtain a new eigenstate with arbitrary negative energy. To avoid this unphysical scenario, we have to impose the condition that for some eigenstate ψ_0,

$$L_- |\psi_0\rangle = 0. \tag{7.15}$$

Without a loss of generality, we assume that the energy of ψ_0 takes the form

$$E_{\nu,0} = (s_\nu + 3/2)\hbar\omega. \tag{7.16}$$

Here, ν is a general quantum number that labels the state and its energy. In addition, Eq. (7.15) can be easily solved in hyperspherical coordinates. We obtain,

$$\psi_{\nu,0}(\vec{R}) = R^{s_\nu+3(N-1)/2} e^{-R^2/2a_{ho}^2} \Phi_\nu(\Omega). \tag{7.17}$$

The state ψ_0 is the lowest of a ladder of eigenstates $|\psi_q\rangle = L_+^m |\psi_0\rangle$ with energies

$$E_{\nu,m} = (s_\nu + 3/2 + 2m)\hbar\omega, \tag{7.18}$$

where m is a positive integer. The coefficients s_ν dictate the beginning of the ladder, and to obtain them, we have to solve the complete many-body Schrodinger equation. Even though we do not know where these ladder of state begin, we showed that the structure of the spectrum consists of families of eigenstates, labeled by ν, with energies separated by $2\hbar\omega$.

The functional form of the unnormalized states obtained by successive applications of L_+ to the lowest state are

$$\psi_{\nu,m}(\vec{R}) = R^{s_\nu+3(N-1)/2} e^{-R^2/2a_{ho}^2} L_m^{s_\nu+1/2}(R^2/a_{ho}^2)\Phi_\nu(\Omega). \tag{7.19}$$

These eigentates are separable in the hyperspherical coordinates (R, Ω). In the hyperspherical framework, the separability of the eigenstates implies that the adiabatic approximation is exact [119]. Furthermore, the channel functions Φ_ν do not depend on the hyperradius. Since the L_+ only acts on the collective coordinate R, the $2\hbar\omega$ spacing is associated with collective or breathing mode excitations.

From the functional form of the eigenstates [Eq. (7.19)], we can infer the effective hyperradial potentials. We define the hyperradius wave function $F_{\nu,m}$ with the correct normalization, $\psi_{\nu,m}(\vec{R}) = R^{1-3N/2} F_{\nu,m}(R)\Phi_\nu(\Omega)$. The hyperradial wave functions have the same functional form as the noninteracting system, so we expect that the functional form of the hyperradial potentials should also agree. This agreement can be verified by inserting the wavefunction solutions of Eq. (7.19) into the hyperspherical Schrodinger equation [Eq. (2.32)]. This procedure leads,

$$\left(-\frac{\hbar^2}{2m}\frac{\partial^2}{\partial R^2} + \frac{m\omega^2 R^2}{2} + \frac{\hbar^2 s_\nu(s_\nu+1)}{2mR^2}\right) F_{\nu,m} = E_{\nu,m} F_{\nu,m}. \tag{7.20}$$

The effective potential curves include a trapping term and a term proportional to $1/R^2$ that includes the kinetic energy and the effects of the two-body interactions. By taking the limit $\omega \to 0$ in Eqs. (7.19,7.20) we can verify that the $1/R^2$ term remains unchanged in the absence of a trap. In this limit, the trapping potential disappears and all the trapping states from Eq. (7.19) tend to the zero energy eigenstate of the free system.

We can now easily show that these state obey a virial theorem [175, 186]. Consider the expectation value of the external potential $V_{trap} = \frac{m\omega^2}{2}\sum_i r_i^2$ over an eigenstate,

$$\langle\psi_{\nu,m}|V_{trap}|\psi_{\nu,m}\rangle = \frac{m\omega^2}{2}\langle\psi_{\nu,m}|\sum_i r_i^2|\psi_{\nu,m}\rangle = \frac{m\omega^2}{2}\langle\psi_{\nu,m}|R^2|\psi_{\nu,m}\rangle\,. \tag{7.21}$$

Equation 7.21 can be evaluated analytically in hyperspherical coordinates. The integration over the hyperangles is trivial since the eigenstates are separable in this coordinates and V_{trap} does not depend on Ω. We are then left with a one dimensional integration over R, using the properties of the Laguerre polinomials we obtain the virial theorem

relation

$$\langle \psi_{\nu,m} | V_{trap} | \psi_{\nu,m} \rangle = \frac{E_{\nu,m}}{2}. \tag{7.22}$$

Since all the eigenstates obey the virial theorem, a thermal distribution would also obey the same virial theorem.

All the properties presented above are valid for both few- and many-body systems. For large N systems, it is convenient to introduce variables rescaled by the noninteracting quantities. If one defines $x = R'/R'_{NI}$ and $\epsilon_{\nu n} = E_{\nu n}/E_{NI}$, the hyperradial Schrödinger equation can be rewritten as

$$\left(-\frac{1}{2\mu_{eff}} \frac{d^2}{dx^2} + \frac{s_\nu(s_\nu+1)}{2\mu_{eff}x^2} + \frac{1}{2}x^2 \right) \bar{F}_{\nu n}(x) = \epsilon_{\nu n} \bar{F}_{\nu n}(x), \tag{7.23}$$

where $\mu_{eff} = E_{NI}^2/(\hbar\omega)^2$. R_{NI} in the above definition of x denotes the rms radius of the non interacting system. The virial theorem [Eq. 7.22] implies that R_{NI} can be expressed in terms of the energy E_{NI} of the non-interacting two-component Fermi gas,

$$R_{NI} = \sqrt{\langle R^2 \rangle_{NI}} = \sqrt{\frac{\hbar}{M\omega}} \sqrt{\frac{E_{NI}}{\hbar\omega}}. \tag{7.24}$$

The dimensionless coefficient C_N is defined by

$$C_N = \frac{s_0(s_0+1)}{\mu_{eff}} = \frac{s_0(s_0+1)\hbar^2\omega^2}{E_{NI}^2} \tag{7.25}$$

and it characterizes the ground state of the system at unitarity. The scaled hyperradius x and the scaled energies $\epsilon_{\nu n}$ remain finite in the large N limit. For example, in the limit $N \to \infty$,

$$\epsilon_{00} \approx \sqrt{C_\infty} \quad \text{or} \quad E_{00} \approx \sqrt{C_\infty} E_{NI}. \tag{7.26}$$

Here, we have used that C_N converges to a finite value C_∞ in the large N limit. Thus, the scaled quantities are particularly well suited to discussing the large N limit. For small systems, in contrast, some properties of the system can be highlighted more naturally using the unscaled hyperradius R.

Finally, all the properties explained in this section remain valid if the center-of-mass motion is removed and the particles have different masses. Both for a system with the center of mass decoupled and for an unequal mass system, there exists a set of Jacobi vectors which obey the boundary condition of Eq. (7.6) and transform the Hamiltonian to that of the form Eq. (7.7), reproducing the problem considered above.

The coefficients s_ν describe both the trapped and free systems and are related to the universal parameter ξ of the homogeneous system [19, 174]. Thus, the hyperspherical framework connects few- and many-body quantities and allows one to bridge the gap between atomic and condensed matter physics.

7.3 Numerical verification of universal properties for trapped systems

It cannot be known *a priori* in which cases the theory presented in the previous section is valid. The theory can only say that, if the system behaves universally, then it has the mentioned properties. To verify that a particular system is universal we need to solve the complete problem, i.e., we have to obtain solutions of the spectrum and wavefunctions and test whether the universal properties are fulfilled.

For example, a two-component Fermi gas is expected to behave universally. Pauli repulsion is considered responsible for stabilizing the system against collapse and avoiding clustering. On the other hand, bosonic systems with attractive interactions are known to collapse and form cluster systems. Therefore, it is clear that bosonic systems are not universal. However, there can be part of the bosonic spectrum that follows these universal properties.

The stability of two-component Fermi gases is supported by experimental results and numerical simulations. The most relevant numerical results are obtained by FN-DMC, which shows that the energy of a homogenous Fermi gas at unitarity is positive [36, 7]. However, these results do not constitute proof that the two-component Fermi

gas is universal. Furthermore, FN-DMC calculations have important limitations due to the nodal constraint, so we cannot know for sure that the $E = (1 + \beta)E_{NI}$ is the true ground state (for a zero-range pseudopotential) or just the lowest "gas-like" state. In addition, unphysical purely attractive potentials, used in these FN-DMC calculations, produce many-body bound states for large N systems. It is not completely clear what would happen with these many-body bound states if the potentials would get replaced by realistic potential or by zero-range pseudopotentials.

In this section, we analyze the few-body two-component Fermi gas at unitarity by solving the many-body Schrodinger equation with the CG method. The universal properties described in the previous section are valid with and without the inclusion of the center-of-mass motion [186]. In the numerical calculations, we removed the center-of-mass motion to reduce the computational demands. The center-of-mass motion is described by a simple one-particle harmonic oscillator wave function and can be trivially included after the numerical calculations.

For even systems, we consider $N_1 = N_2 = N/2$, while for odd systems we consider $N_1 = N_2+1$. As we noted in the Introduction, the perturvative BEC and BCS behaviors of the even N systems predict an $L = 0$ ground state while for odd N systems L can be different from zero. This is consistent with the pairing arguments that suggest that an even N system should have all the pairs couple to $L = 0$. Therefore, we expect that even at unitarity the even-N systems should have $L = 0$. However, to analyze odd N systems we have to consider $L > 0$ solutions. The CG method as implemented above only describes $L = 0$ states [182].

To obtain $L > 0$ states, we introduce a spectator particle. Specifically, we solve an $(N + 1)$-atom system. This spectator particle does not interact with the rest of the particles but couples to them to form an $L = 0$ state. Through this introduction of an extra particle to an N particle system, the wave function will now describe "solutions of the N-particle"+ "solutions of the extra particle" coupled to zero angular momentum.

Even though the extra particle does not interact at all with the N-particle system, the constraints of the wave function force it to be coupled with the N-particle system to zero angular momentum. Thus, if the extra particle has angular momentum L, then the N-particle system has also angular momentum L so they couple to zero angular momentum. To know the angular momentum of the N system, we measure the energy of the spectator particle, which should agree with the energy of one particle in a trap. From the energy of the spectator particle, we can deduce the angular momentum of the system. For example, consider that we want to extract the spectrum of the N-particle system with $L = 1$ from the $L = 0$ spectrum of the $N + 1$-particle system. In such case, we know that the $L = 1$ ground-state energy of the extra particle in a trap is $5/2\hbar\omega$. Therefore, by measuring the energy of the extra particle, we can know the angular momentum of the N-particle system, and we can predict its energy, via $E_N = E_{N+1} - 5/2\hbar\omega$. Table 7.1 summarizes a few selected results for $N = 3 - 6$.

A property of the even-N systems that is important for numerical calculations is the symmetry under the exchange of spin-up and spin-down particles. In the equal-mass case, the different spin components are treated as distinguishable, particles and there is only interaction between spin-up and spin-down particles. Therefore, both the Hamiltonian and the symmetry of the wave function remain unchanged if we replace all the spin-up particles with spin-down particles and vice versa. This exchange operation reveals a symmetry of the problem that we call "spin exchange" symmetry. The eigenfunctions have to be even or odd under this symmetry transformation. The ground state of an even-N system is expected to be even under spin exchange, since the "odd spin" wave function is forced to have an extra node. In the $N = 4$ system, we test this property. First, we calculate the complete $L = 0$ spectrum, and then we calculate the even-spin spectrum imposing the even-spin symmetry in the wave function. The even-spin spectrum accurate reproduces the ground state and part of the excitation spectrum. For the $N = 6$ calculations presented in Table 7.1, we use this property to

enforce the even-spin symmetry to the wave function. This significantly reduces the Hilbert space and allows an accurate description of several states.

Table 7.1: CG energies $E_{\nu n}$ for $N = 3 - 6$ (the range r_0 of the Gaussian potential is $0.01a_{ho}$ for $N = 3$ and 4, and $0.05a_{ho}$ for $N = 5$ and 6). Finite range effects are expected to be $\approx 0.02\hbar\omega$ and $0.1\hbar\omega$ for $r_0 = 0.01\hbar\omega$ and $0.05\hbar\omega$, respectively. Results from Ref. [19].

N	L_{rel}	$E_{00}/(\hbar\omega)$	$E_{01}/(\hbar\omega)$	$E_{02}/(\hbar\omega)$	$E_{10}/(\hbar\omega)$	$E_{20}/(\hbar\omega)$
3	0	4.682	6.685	8.688	7.637	9.628
3	1	4.275	6.276	8.279	6.868	8.229
4	0	5.028	7.032	9.039	7.464	8.051
4	0	7.11			7.19	7.74
5	0	8.03	10.04	12.06	8.83	10.38
5	1	7.53			9.13	
6	0	8.48	10.50	12.52	10.44	11.00

The $2\hbar\omega$ spacing reported in Table 7.1 strongly suggests the validity of the universal properties. However, as the energy increases, there is a large quasi-degeneracy of states and the states separated by $2\hbar\omega$ are hard to identify. The difficulty to identify the $2\hbar\omega$ spacing occurs even more if we consider the numerical uncertainty of the energies and the finite range effects. Therefore, it would be convenient to compute an independent observable that would also reveal the universal properties and complement the spectrum analysis. Hence, we analyze the behavior of the hyperradial density $F^2_{\nu,n}(R)$. The numbers of nodes tell us the number of $2\hbar\omega$ excitations and the analytical forms of the hyperradial densities are known, see Eq. (7.19). The analytical solutions can be directly compared with the numerical results. The combination of the analysis of the spectrum with the verification of the functional forms of the hyperradial densities provides strong numerical evidence of the universal nature of the spectrum.

To obtain the hyperradial densities, we integrate the square of the wave function over all the hyperangles. This multidimensional integration would be computationally difficult using standard integration techniques. Accordingly, we use two unconventional numerical techniques that work remarkably well for this specific problem. We use the

first technique for $N \leq 4$ and take advantage of the properties found in correlated Gaussian hyperspherical method (CGHS). As explained in Sec. 3.4, the overlap matrix element of two basis functions can be reduced to an analytical expression for $N = 3$ or to a one-dimensional numerical integration for $N = 4$. Thus, by using the basis expansion of the wave function we can significantly reduce the computational demands of the integration. As the number of particles N increases, the dimension of the numerical integration goes as $N-3$, so this method becomes very computationally demanding for $N > 4$.

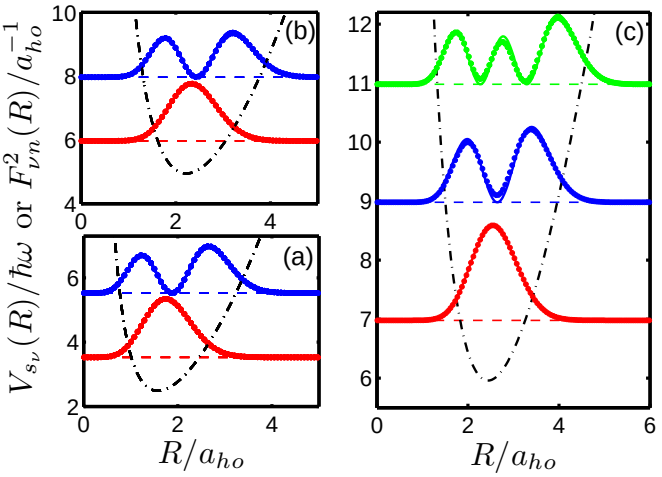

Figure 7.1: Dash-dotted lines show $V(R)$ as a function of R/a_{ho} for (a) $N = 4$ with $\nu = 0$, (b) $N = 4$ with $\nu = 1$, and (c) $N = 6$ and $\nu = 0$. Circles and solid lines show the corresponding $F^2_{\nu n}$ determined numerically and analytically, respectively. Dashed horizontal lines show the energies $E^{rel}_{\nu n}$. Results are from Refs. [185, 19].

The second method uses Monte Carlo techniques to carry out the integration. The universal wavefunctions [see Eq. (7.19)] are separable in hyperradius and hyperangles. Therefore, if the numerical solutions are of the form of Eq. (7.19), we could simply fix the hyperangles Ω to some value, and evaluate the square of the wavefunction as a function of the hyperradius. That procedure should give us a function proportional to $F^2_{\nu,n}(R)$. However, our numerical solutions are not exactly separable in hyperspherical

coordinates because of the finite range of the interaction. Also, numerical limitations can affect the separability in hyperspherical coordinates. Therefore, instead of selecting a single set of hyperangles and extracting the square of the wave function, we can repeat this process for many different sets of hyperangles and average over them. The different sets of hyperangles are selected randomly, and this process is equivalent to a Monte Carlo integration. Since the numerical solutions are approximately separable in hyperspherical coordinates, we do not need a large number of randomly selected sets of hyperangles to converge the solution. In other words, the standard deviation of the numerical integration goes to zero as the separability becomes exact.

Figure 7.1 presents numerical results for $N = 4$ and $N = 6$ hyperradial densities and compares them to the analytical solutions. The analytical solutions are obtained by extracting the s_ν values from the numerical energies shown in Table 7.1. The $N = 4$ solutions were obtained with the basis set expansion technique while the $N = 6$ method is obtained with the Monte Carlo technique. In both cases, good agreement is obtained between the numerical and the analytical solutions.

The analysis of the universal properties can be extended to unequal mass systems. The universal properties predicted in Sec. 7.2 are also valid for universal systems of two fermionic species with arbitrary mass ratio so long as all the particles feel the same trapping frequency. Here, we analyze the spectrum of four trapped fermions, two for each fermionic species, characterized by a mass ratio κ. In Fig. 7.2, the spectrum is analyzed as a function of the mass ratio. The circles correspond to the numerical spectrum. We can clearly identify families of solutions separated by $2\hbar\omega$. To identify these families, we generate a series of solid lines that correspond to $E_{00} + 2n\hbar\omega$, a series of dashed lines that correspond to $E_{10} + 2n\hbar\omega$, and a series of dash-dotted lines that correspond to $E_{20} + 2n\hbar\omega$. The energies (circles) that agree with the lines correspond to the same family. The energies $E_{\nu 0}$ determine the coefficients s_ν of the hyperradial potential curves $V_{s_\nu}(R)$. Table 7.2 summarizes the three smallest coefficients for various

κ.

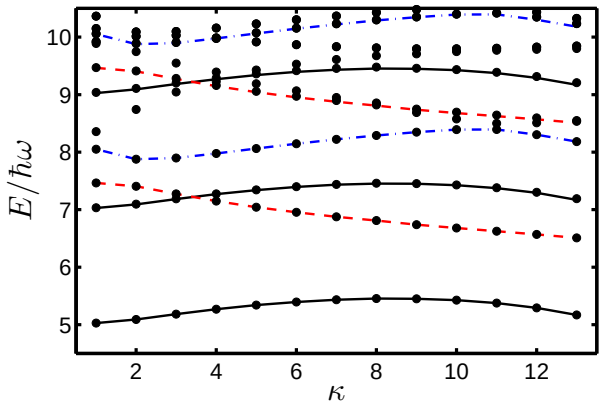

Figure 7.2: Four-body energy spectrum for $L = 0$ at unitarity as a function of κ. Circles correspond to the numerical results obtained by the CG approach. Solid, dashed and dash-dotted lines show the energies $E_{\nu 0} + 2n\hbar\omega$ for $\nu = 0$, 1 and 2, respectively ($n = 0, 1, \cdots$). Results are from Ref. [185].

From the numerical results presented in this section, we have indirectly verified the form of the hyperspherical potential curves. The $2\hbar\omega$ spacing clearly suggests the universality of the potential curves and the $1/R^2$ free-space hyperspherical potential. The development of the CGHS method allows us to carry out a hyperspherical calculation for the four-fermion problem and to directly verify the form of the hyperspherical potentials. Also, it allows us to analyze deviations from the zero-range solutions due to finite-range effects.

The 20 lowest four-body potential curves $2\mu R^2 U_\nu(R)/\hbar^2$ for the equal-mass system are presented in Figure 7.3. We can identify three regimes in these potential curves. The region $R \lesssim r_0$ is controlled by the kinetic energy. The kinetic energy effects are more important than the interaction energy and the potential curves are well approximated by the non-interacting potential curves. In other words, $2\mu R^2 U_\nu(R)/\hbar^2 \approx \Lambda^2 + 12$ and the eigenchannels are well approximated by the hyperspherical harmonics (see Sec. 2.5). For that reason, there is a large degeneracy in the $R \lesssim r_0$ region which corresponds to

Table 7.2: Coefficients s_ν of the hyperradial potential curves $V_{s_\nu}(R)$, Eq. (7.18), for the $N = 4$ system with $L = 0$ for various mass ratios κ. Results are from Refs. [185].

κ	s_0	s_1	s_2	κ	s_0	s_1	s_2
1	2.03	4.46	5.05	8	2.45	3.81	5.29
2	2.09	4.41	4.88	9	2.45	3.74	5.35
3	2.18	4.27	4.90	10	2.42	3.68	5.39
4	2.27	4.15	4.98	11	2.37	3.62	5.39
5	2.34	4.04	5.06	12	2.29	3.57	5.30
6	2.40	3.95	5.15	13	2.17	3.51	5.18
7	2.43	3.88	5.22				

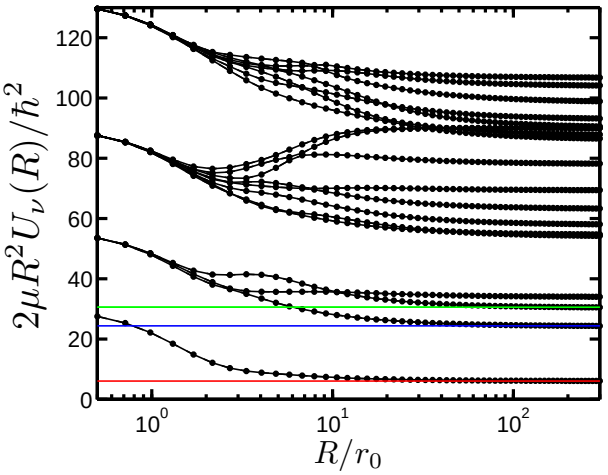

Figure 7.3: Hyperspherical potential curves for the 4-fermion system multiplied by $2\mu R^2/\hbar^2$. The solid lines represent the predictions from analyzing the spectrum obtained with the CG method. The symbols correspond to direct evaluation of the potential curves with the CGHS method. Unpublished results.

the degeneracy of the Λ^2 operator. Furthermore, the potential curves are, to a good approximation, proportional to $1/R^2$. The second region is $r_0 \lesssim R \lesssim 20r_0$. In this region both the kinetic and the interaction terms are important and finite range effects are important. In the third region, $R \gtrsim 20r_0$, the potential curves recover their universal behavior. The potential curves are, again, approximately proportional to $1/R^2$. As R/r_0 increases, finite range effects tend to zero and we obtain the zero-range potential curves at unitarity. Therefore, in this region, the eigenvalues of $2\mu R^2 U_\nu(R)/\hbar^2$ are approximately $s_\nu(s_\nu+1)$. Thus we can compare these results with the ones deduced from trapped calculations for $r_0/a_{ho} = 0.01$ presented in Table 7.2. The red, blue and green solid lines correspond to $s_0(s_0+1)$, $s_1(s_1+1)$ and $s_2(s_2+1)$ respectively. There is good agreement between the predictions from the trapped system and the direct computation of the potential curves.

To quantify this last statement, we analyze the value of s_0. Several groups [182, 40, 184, 2, 166] have tried to benchmark the four-body value of E_{00}, which is straightforwardly related with s_0. The calculations from Ref. [2] use zero-range interactions explicitly.and they report a value of $E_{00} \approx (5.045 \pm 0.003)\hbar\omega$. To extract the s_0 value in the zero-range limit, we carry out two different calculations. First, we study the E_{00} energy obtained with CG as a function of the range of the two-body interaction and then we extrapolate to zero-range limit. This method was previously applied for the three-body system and the numerical results agreed with the analytical predictions up to 7 digits [185]. The same procedure applied to the four-body system, leads to $s_0 \approx 2.0096$. The second calculation analyzes the long-range behavior of the potential curves. To eliminate finite-range effects, we extrapolate the potential curve $U_0(R)$ to $R/r_0 \to \infty$. In this limit, $U_0(R)$ is characterized by a value $s_0 \approx 2.0092$. These two different methods provide a value of s_0 which agrees in four digits. These values are slightly lower than $s_0 \approx 2.045 \pm 0.003$ predicted in Ref. [2]. Therefore, we consider that the uncertainty in Ref. [2] is underestimated.

7.4 Renormalization and unitarity

The dimensional arguments of the unitary system have been taken into account in functional form of the effective scattering length. The effective scattering length is assumed to take the following functional form [183],

$$k_f a_{eff} = \zeta(k_f a_s). \tag{7.27}$$

If the renormalization ζ function remains finite in the $a_s \to \infty$ limit, the interaction at unitarity is only characterized by the Fermi momentum,

$$a_{eff} = \zeta^{min}/k_f. \tag{7.28}$$

In the Thomas-Fermi approximation, the renormalization technique leads to

$$\mu_U = \frac{\hbar^2 k_f^2}{2m}\left(1 + \frac{10}{9\pi}\zeta^{min}\right), \tag{7.29}$$

$$\mathcal{E}_U/\mathcal{E}_{NI} = \left(1 + \frac{10}{9\pi}\zeta^{min}\right). \tag{7.30}$$

Here, ζ^{min} is the asymptotic behavior for $a_s \to \infty$. In this renormalization approach, the β parameter is intimately related with the value of the renormalization at unitarity. Comparing Eq. (7.2) to Eq. 7.29 we obtain $\beta = 10\zeta^{min}/9\pi$. The renormalization procedure described in Sec. 4.4 leads to a $\beta \approx -0.492$. Table 7.3 shows different experimental and theoretical values of β. Experimental groups, like Thomas and Hulet groups, measure the ratio of the size of the Fermi cloud at unitarity, R_U, and in the noninteracting limit, R_{NI} [134, 105]. In the Thomas-Fermi approximation, the ratio is $R_U/R_{NI} = (1+\beta)^{1/4}$ [75]. This relation was obtained previously using dimensional arguments [75] and appears naturally using the renormalization approach.

The renormalization applied to the hyperspherical method has predicting power also. Rittenhouse and Greene [150] showed that a renormalization of the form of Eq. (7.27) applied in the K-harmonic approximation leads to a hyperspherical potential

Table 7.3: Experimental and theoretical predictions of β.

	β		
Experiments	$-0.54(5)$[1]	$-0.64(15)$[2]	$-0.49(4)$[4]
Experiments	$-0.68^{+0.13}_{-0.10}$ [3]	$-0.54^{+0.05}_{-0.12}$ [5]	
QMC	$-0.58(1)$[6]	$-0.56(1)$[7]	
Padé asymptotes	-0.674[8]	-0.432[9]	
Green's function	-0.545[10]	-0.599[11]	
BCS*——ϵ Expansion†	-0.41[12] *	-0.525[13] †	
Other methods	-0.3[14]	-0.564[15]	-0.492[16]

[1]Ref. [134] [2]Ref. [25] [3]Ref. [13] [4]Ref. [105] [5]Ref.[167] [6]Ref. [7] [7]Ref. [41] [8]Refs. [9, 85] [9]Ref. [9] [10]Ref. [137] [11]Ref. [92] [12]This is a well known result, see for example Ref. [137] [13]Ref. [128] [14]Ref. [32] [15]Ref. [43] [16]Result obtained using the renormalization function of this thesis (and from Ref. [183])

at unitarity of the form,

$$V(R) = \frac{\hbar^2(1+\beta)}{2MR^2}, \tag{7.31}$$

where $\beta = 10\zeta^{min}/9\pi$. Here, the hyperradius can be understood as a measure of the global size of the cloud and breathing mode oscillations can be understood as small oscillations at the bottom of this potential curve. Therefore, oscillations in R are collective oscillations. For a spherically symmetric trap, the functional form of the potential [Eq. (7.31)] predicts $\omega_0 = 2\hbar\omega$, in agreement with the universal properties presented in Sec. 7.2 and several other many-body predictions.

The renormalization function is applied at the mean-field level of approximation, which does not take into account pair correlations. The pair correlations are essential for the description of the superfluid nature of the system. For that reason, this renormalization approach cannot predict whether the system is superfluid or not; it cannot describe superfluid observables. However, it does predict the correct relation between chemical potential μ and the density ρ that control the collective excitations in the hydrodynamic theory [49, 93]. These collective excitations have been measured experimentally and are in good agreement with theory.

7.5 Monte Carlo calculations for trapped systems: β parameter and the gap

For systems with a large number of particles, the calculation of the complete spectrum using a method such as the CG becomes computationally prohibitive. In contrast, quantum Monte Carlo simulations can be extended to larger systems and allow a reliable determination of the β parameter and the excitation gap for a two-component Fermi gas. For example, the first calculations, carried out in 2003, considered a homogenous system and used both variational and fixed-node diffusion Monte Carlo techniques (VMC and FN-DMC). The universal parameter was determined to be $\beta = -0.56(1)$ [36]. These calculations were followed in 2004 by the authors of Ref. [7] in which the BCS-BEC crossover was considered; a similar parameter was obtained, with $\beta = -0.58(1)$. Another important parameter calculated with FN-DMC is the excitation gap. The excitation gap Δ of the homogenous system was calculated by Carlson and Reddy [37] to the $\Delta = 0.84(5)E_{FG}$, where E_{FG} denotes the energy per particle of noninteracting homogeneous Fermi gas.

Initial calculations of the energy of trapped two-component Fermi gases were reported in Ref.[183]. These calculations were significantly improved and extended to larger systems by Chang and Bertsch [40] and D. Blume who performed the FN-DMC calculations in Refs. [184, 19]. I participated in the implementation FN-DMC simulations for different trial wave functions and in the analysis of the results. Using my own implementation of FN-DMC method and considering more flexible trial wave functions, I was able to reproduce some of D. Blume results. In some cases, more flexible trial wave functions predict lower energies than those of Ref. [184, 19]. However, the improvement was usually less than 2%, very small considering the computational demands of my calculations. For detailed discussion of Monte Carlo methods in general and the trial wave functions considered in the trapped two-component Fermi gas, please

see Sec. 3.2. Here, we analyze the numerical results.

Figure 7.5 presents the total energy at unitarity as a function of the number of particles N. We can clearly see an odd-even behavior in the energies as a function of N that is related, as we will see later, to the excitation gap.

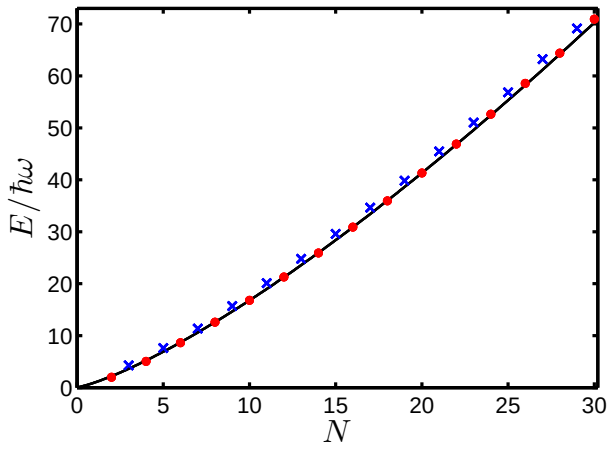

Figure 7.4: Circles and crosses show the fixed-node diffusion Monte Carlo (FN-DMC) energies $E(N)$ in units of $\hbar\omega$ as a function of N at unitarity. Circles correspond to even-N systems and crosses correspond to odd-N systems. Solid lines show a fit of the even FN-DMC energies to Eq. (7.34). Numerical results are from Refs. [184, 19].

For sufficiently large N, the energy of the trapped system at unitarity can be calculated using the homogeneous result of Eq. (7.2) in a local density approximation (LDA). As with Eq. (7.2), we obtain an equation that relates the noninteracting energy of the trapped system $E_{NI}^{(T)}$ with the energy at unitarity of the trapped system $E_{U}^{(T)}$:

$$E_{U}^{(T)}(N) = \sqrt{1+\beta}E_{NI}^{(T)}(N). \tag{7.32}$$

Equation (7.32) allows us to extract β from the energy of trapped system at unitarity. The noninteracting energies $E_{NI}^{(T)}$ present a shell structure. However, the energies at unitarity up to $N = 30$ show little shell structure and can be described to a very good approximation by a smooth function. Therefore, for Eq. (7.32) to actually work in the small N ($N < 30$) region, we have to approximate $E_{NI}^{(T)}$ by a smooth function. Such

an approximation can be accomplished by applying the extended Thomas-Fermi (ETF) model [29] to $E_{NI}^{(T)}$ so that

$$E_{NI,ETF}^{(T)} \approx \hbar\omega \frac{(3N)^{4/3}}{4}\left(1 + \frac{(3N)^{-2/3}}{2} + \cdots\right). \tag{7.33}$$

Using ETF in Eq. (7.32), we obtain

$$E_U^{(T)} \approx \sqrt{1+\beta} E_{NI,ETF}^{(T)}. \tag{7.34}$$

Fitting our energies to Eq. (7.34) and treating β as a variational parameter, we find $\beta = -0.535$. Our β extracted from the trapped system is about 10% larger than that determined for the bulk system, i.e., $\xi_1 = 0.58(1)$ [7, 37], suggesting that one has to go to somewhat larger trapped systems to extrapolate to the bulk β with high accuracy within the LDA. Although the β obtained from the fit to the energies of the trapped system is larger than the corresponding bulk value, it is worthwhile to note that the simple functional form given in Eq. (7.34) provides an excellent description of the energies of the trapped system even for small N-particle systems.

The Monte Carlo calculations for odd and even systems can be combined to obtain the excitation gap $\Delta(N)$ for the trapped unitary Fermi gas as a function of N. The definition of the excitation gap for the homogeneous system [36], which equals half the energy it takes to break a pair, can be readily extended to the trapped system [40, 34] where

$$\Delta(N) = E(N) - [E(N-1) + E(N+1)]/2. \tag{7.35}$$

The excitation gap $\Delta(N)$ obtained from our FN-DMC energies is shown in Fig. 7.6 (circles). $\Delta(N)$ increases from $\approx 0.75\hbar\omega$ for $N = 3$ to $\approx 1.5\hbar\omega$ for $N = 29$. For comparison, we show the excitation gap $\Delta(N)$ calculated using the DFT energies (triangles) obtained recently by Bulgac [34]. The agreement between Bulgac's $\Delta(N)$ and our results is quite good.

Alternatively, the excitation gap can be deduced from the excitation spectrum. According with pairing theories, the ground state of even N systems has all the particles paired up and it is separated of the excited states by the energy necessary to break the pair. In contrast, odd N system have one unpaired particle and the spectrum does not reveal the excitation gap. In nuclear systems, the excitation gap is observed by comparing the excitation spectrum from odd and even nucleon systems (see e.g. Ref. [147]). In two-component trapped systems, the gap for small N-system is of the same order of the trapping excitation energy $\hbar\omega$. Therefore, it is more difficult to identify the effects of the excitation gap in the excitation spectrum. Despite these difficulties, we analyze the behavior of the excitation spectrum for $N = 3, 4$ and 5.

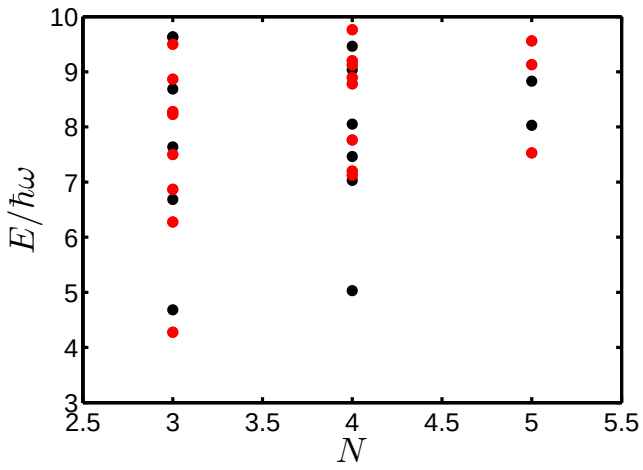

Figure 7.5: Excitation spectrum for $N = 3, 4$ and 5 at unitarity. Black circles correspond to $L = 0$ states and red circles correspond to $L = 1$ states.

Figure 7.5 presents the $L = 0$ and $L = 1$ excitation spectrum for $N = 3, 4, 5$. The states corresponding to the same hyperspherical potential curve are separated by $2\hbar\omega$. Clearly, these excitations are not associated with the excitation gap. To see the effects of the excitation gap, we consider the energy difference between the lowest $L = 0$ and $L = 1$ states for odd and even N systems. Here, we assume that the

change of angular momentum ensures the breaking of the pair in the even N system. Considering Table 7.1, we see that the $N = 4$ has an energy difference much larger than the $N = 3$ and $N = 5$ systems. To estimate the excitation gap we consider that the energy difference $|E_{L=0}^{N=4} - E_{L=1}^{N=4}|$ has two contributions: the energy for breaking the pair and the energy for the change of symmetry. In this picture, the odd systems have only the contribution from the change of symmetry. Therefore, we can estimate the gap, i.e., half the energy for breaking the pair, as

$$\Delta(4) = \frac{1}{2}\left(|E_{L=0}^{N=4} - E_{L=1}^{N=4}| - \frac{1}{2}[|E_{L=0}^{N=3} - E_{L=1}^{N=3}| + |E_{L=0}^{N=5} - E_{L=1}^{N=5}|]\right). \tag{7.36}$$

The second term correspond to the energy due to the change of symmetry for $N = 4$ which is estimated averaging over the $N = 3$ and $N = 5$ values. Using the energies from Table 7.1, we estimate $\Delta(4) \approx 0.81\hbar\omega$ which is close to $\Delta(3) \approx \Delta(5) \approx 0.75\hbar\omega$ obtained with Eq. (7.35). This qualitative agreement support the assumption that the odd-even behavior is a consequence of pairing physics. Unfortunately, the analysis of the spectrum can only be done for $N \leq 5$. For larger systems, only the ground state is known and we need to use Eq. (7.35). Next, we consider the dependence of the gap on N and its large N limit behavior.

To analyze the large N limit behavior of the excitation gap, we use LDA and obtain

$$\Delta_{LDA}(N) = 3\alpha_{hom}\,(3N)^{1/3}\,\hbar\omega/(8\sqrt{1+\beta}). \tag{7.37}$$

The universal parameter α describes the even-odd oscillations and α_{hom} equals 0.85 for the bulk system [37]. Using α as a fitting parameter we find $\alpha_{tr} = 0.60$ for the trapped system. The $\Delta_{LDA}(N)$ with the ξ_{tr} and α_{tr} parameters, shown in Fig. 7.6 by a solid line, provides a good description of our FN-DMC results. It is the fact that α_{tr} is noticeably smaller than α_{hom} which suggests that the extra particle is not distributed uniformly throughout the cloud; rather it has a greater probability of residing at the surface of the cloud where the gap is smaller. Indeed, our density profiles for $N \gtrsim 11$

(not shown) indicate that the extra particle sits near the surface of the cloud [185]. The unpaired particle location is verified by comparing the density profiles of the spin-up and spin-down particles. In general, the LDA is expected to describe the center region of the trap well, but to fail in the surface region, raising questions about the validity of our LDA treatment [Eq. (7.37)]. Recently, Son reached similar conclusions [160]. In his analysis, the gap increases with $N^{1/9}$ as $N \to \infty$. A fit of our results for $\Delta(N)$ for $N \geq 9$ shows consistency with the $N^{1/9}$ dependence but does not conclusively confirm it.

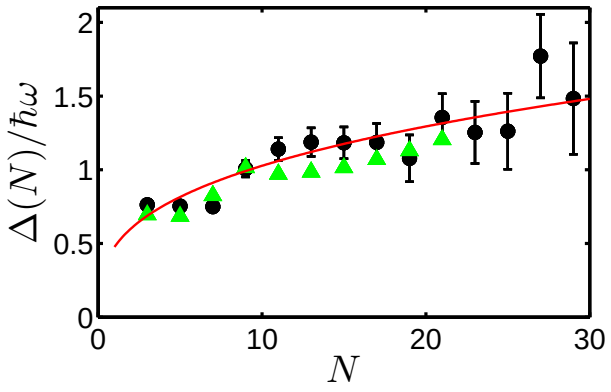

Figure 7.6: Circles show the excitation gap $\Delta(N)$ determined from our FN-DMC energies. A solid line shows $\Delta_{LDA}(N)$. For comparison, triangles show $\Delta(N)$ determined from the DFT energies [34]. Figure taken from Ref. [19].

The FN-DMC energies provide interesting insights on the evolution from few- to many-body systems. Such evolution can be studied in the hyperspherical framework. We can use the FN-DMC energies to extract the lowest hyperspherical potential curves that describe these systems. The ground-state energies $E(N)$ determine the coefficients s_0 [see Eq. (7.16)] of the hyperradial potential $V_{s_0}(R)$ [see Eq. (7.20)]. Figures 7.7 (a) and (b) show the lowest hyperradial potential curves $V(R)$ [$V(R) = V_{s_0}(R) + V_{trap}(R)$, where $V_{trap}(R) = \frac{1}{2}\mu_N\omega^2R^2$ and $\mu_N = m$] for $N = 3-20$ in the noninteracting limit and at unitarity, respectively. The small R behavior of $V(R)$ is dominated by $V_{s_0}(R)$, while

the large R behavior of $V(R)$ is dominated by $V_{trap}(R)$. Comparison of Figs. 7.7 (a) and (b) shows that the attractive interactions lead to a lowering of the potential curves at unitarity compared to those of noninteracting system. Furthermore, the $V(R)$ at unitarity appear to be "staggered," i.e., odd-even oscillations are visible, reflecting the finite excitation gap at unitarity. In the noninteracting limit, in contrast, the excitation gap [Eq. 7.35] is zero and no odd-even staggering of the hyperradial potential curves is visible.

Another important aspect of these potential curves is their relation to the parameter β. As was pointed out previously by Tan [174] and was shown using the renormalized hyperspherical approach [150], the small R behavior of the wavefunction and the hyperspherical potential curves in the large N limit are intrinsically related to the universal parameter β. To analyze the large N limit, we use the rescaled coefficients $\bar{C}_N$ presented at the end of Section 7.2. Figure 7.5 shows the normalized coefficients $\bar{C}_N$. As in our analysis of the energies E_U, we find it useful to smooth the energies E_{NI}). Therefore $\bar{C}_N$ stands for C_N from Eq. (7.25) with E_{NI} replaced by $E_{NI,ETF}$, as a function of N. The coefficients $\bar{C}_N$ oscillate between two smooth curves, a curve for even N (circles) and a curve for odd N (crosses), reflecting the odd-even staggering. As N increases, the difference between the two curves decreases. In the large N-limit, the value of $\bar{C}_N$ for two-component Fermi gases at unitarity should approach the universal parameter $\xi = 1 + \beta$ [19]. This relationship can be shown by comparing the ground-state energy obtained within the hyperspherical framework, Eq. (7.26), to the LDA prediction, or by applying renormalized zero-range interactions within the hyperspherical framework [150]. The dash-dotted and dashed lines in Fig. 7.5 show the ξ value obtained by FN-DMC calculations for the homogeneous system ($\xi = 0.42$) [7, 37] and the ξ value obtained with a renormalization procedure ($\xi = 0.508$) [183], respectively. For comparison, our energies for the trapped system predict $\xi_{tr} = 0.467$. The circles in Fig. 7.5 approach this value. The fact that ξ_{tr} is larger than the corresponding value

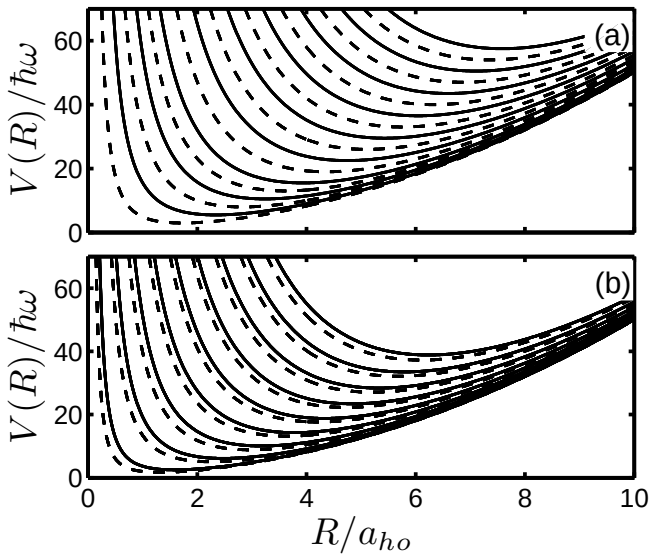

Figure 7.7: Hyperradial potential curves $V(R)$ for equal-mass two-component Fermi systems with (a) vanishing interactions and (b) infinitely strong interactions as a function of R. The hyperradial potential curves naturally appear ordered as N increases: Solid lines correspond, from bottom to top, to $N = 4 - 20$ (N even), while dashed lines correspond, from bottom to top, to $N = 3 - 19$ (N odd). Figure taken from Ref. [185].

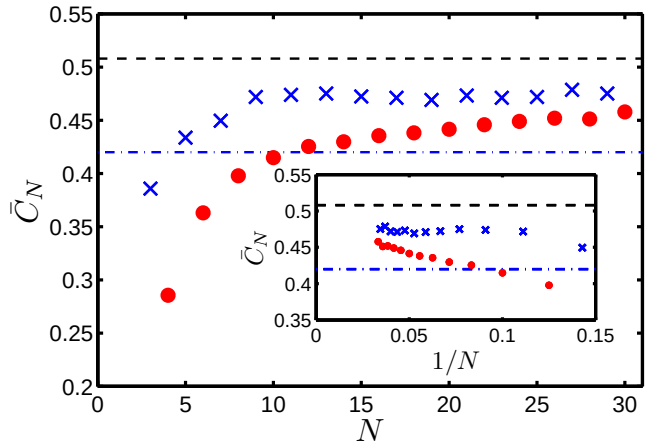

Figure 7.8: Normalized coefficients $\bar{C}_N$, Eq. (7.25) with E_{NI} replaced by $E_{NI,ETF}$, as a function of N; values for even N are shown by circles and values for odd N by crosses. The dash-dotted line shows the value $\xi = 0.42$ obtained by FN-DMC calculations for the homogeneous system [7, 37], while a dashed curve shows the value $\xi = 0.508$ obtained with a renormalization procedure [183]. The inset shows the same quantities as a function of $1/N$ instead of N. Figure taken from Ref. [185].

of the bulk system, i.e., $\xi = 0.42$, might be attributable to the fact that comparatively small system sizes ($N \leq 30$) are considered in our analysis. If finite size effects are responsible for such disagreement, we would expect the circles in the main part of Fig. 7.5 to turn around at larger N values approaching to the homogeneous prediction $\xi = 0.42$ (dashed-dotted curve). Nevertheless, we cannot rule out that the nodal surface entering our FN-DMC calculations might not be optimal. Even though the trial wave functions for the trapped system are analogous to the wave functions of the homogenous case [7], trapping effects and the shell structure might affect differently the trapped calculations and more sophisticated trial wave functions might be required.

7.6 Conclusions

The verification of the universal properties of few-body systems has important consequences in the understanding of the unitary regime. In the two-component Fermi gas, we show quantitatively that the system behaves universally up to $N = 6$. This result implies that there are no weakly bound states for $N \leq 6$ which explains, from a few-body perspective, the stability of two-component Fermi gases. The FN-DMC calculations do not exclude the presence of negative energy states; but, we do not find evidence of such states. The stability of the FN-DMC calculations reveals, to some extent, the stability of the system [18]. If the system is unstable, the walkers evolve into cluster configurations with very large and negative energies which produces an instability of the simulation. This effect does not occur in the two-component Fermi gas. The FN-DMC simulations are remarkably stable, suggesting that the state described is also quite stable.

Chapter 8

Four Bosons with large scattering length

8.1 Introduction

The behavior of few-body bosonic systems with finite range interaction potentials and large scattering lengths is quite different from fermionic systems. A remarkable prediction by Efimov [60] in 1970 stated that a system of three bosonic particles with resonant interactions, but without a two-body bound state, has an infinite family of weakly bound three-body states. The existence of weakly bound Efimov states implies a completely different topology of the spectrum as compared to fermionic systems. In bosonic systems, for example, a "three-body parameter" is required to describe these weakly bound states. Therefore, two parameters are needed to describe the system: the scattering length a_s and the three-body parameter. When the scattering length diverges, the three-body bound states obey interesting scaling properties. The energies and sizes of two consecutive states are related to each other by a scaling factor that is independent of the nature of the interaction.

Fundamental questions arise when another particle is added to such a system. Does the four-boson system have an equivalent to the three-body Efimov effect? Does the system requires a new parameter, i.e., a "four-body" parameter? Unfortunately, only limited or approximate solutions to the four-boson problem exist [1, 163, 142, 83] because of the complexity of such systems and these questions have not yet been resolved. Here, we present solutions to the four-boson system obtained by using the correlated-

Gaussian (CG) and correlated-Gaussian-hyperspherical (CGHS) methods. In contrast with previous calculations, these methods essentially do not rely on any approximation; thus limited only by numerical convergence.

We show that when a three-body Efimov state is at the zero-energy threshold, there is only a finite number of four-body states. From this perspective, we conclude that there is no four-body Efimov effect. However, when two-body interactions are resonant, i.e., when the two-body bound state is at threshold, there is a family of four-body bound states that are intercalated in energy with the family of three-body Efimov states and this four-body family follows the same scaling properties. These results are consistent with the prediction from Ref. [83] that no four-body parameter is needed.

Other important phenomena concern the effects of Efimov physics on the collisional properties of four-boson systems. We know that Efimov physics significantly affects the collisional aspects of identical bosons with tunable interactions producing striking features in the three-body recombination [63, 27]. These features were experimentally observed for the first time in 2006 in an ultracold gas of cesium atoms [67, 109]. Here, we use our solutions to the four-boson problem to predict the consequences of Efimov physics in dimer-dimer collisions. We show that for particular scattering length values, an atom-trimer mixture can be obtained with high efficiency by colliding dimers. We have also been able to study atom-trimers collisions which will help deduce the lifetime of the atom-trimer mixture.

In this chapter, we first review the three-body Efimov effect from the hyperspherical point of view. This solution will help us understand the four-boson system. Next, we use the CG method to extract information about the spectrum and structural properties of the four-boson system. We then apply the CGHS method and extract the four-body hyperspherical potential curves. We use these results to confirm the topology of the spectrum and study dimer-dimer and atom-trimer collisions. The results presented in this chapter are preliminary, and the research on the four-boson system is still underway.

8.2 Efimov physics in a three-body system.

In this section we analyze the Efimov effect from the hyperspherical perspective. This perspective reduces the description of the Efimov effect to an analysis of the functional form of the relevant hyperspherical potential curve.

In the hyperspherical representation, the Efimov effect is revealed in the form of the adiabatic hyperspherical potential curve $W_0(R)$. In the region where $r_0 \ll R \ll |a_s|$, the lowest potential curve behaves like

$$W_0(R) \approx -\frac{s_0^2 - 1/4}{2\mu R^2}, \tag{8.1}$$

where $s_0 = 1.0062378$ [55, 127]. This attractive $1/R^2$ potential resembles that of a charge-dipolar interaction [80, 79, 78, 65, 71, 191]. At unitarity, when the scattering length diverges, the $1/R^2$ behavior of the potential extends all the way up to $R \to \infty$. This long-range behavior is known to have an infinite series of bound states [61]. This infinite series of states becomes finite on both sides of the unitarity point, where the $1/R^2$ behavior is only valid up to approximately $|a_s|$. Beyond that point, the potential becomes repulsive [for $a_s < 0$] or converges quickly to the dimer-binding energy [for $a_s > 0$]. The bound states whose sizes are much greater than r_0 are mainly controlled by $1/R^2$ behavior and are therefore considered universal, i.e., independent of the nature of the interaction. Note that this universality is slightly different from the universal behavior of fermions discussed previously. Here, two parameters are necessary to characterize the Efimov states: the scattering length a_s and a three-body parameter. The three-body parameter is related to the range of the two-body potential (not to be confused with the two-body effective range), and it controls the size and energy of the "first" Efimov state.

The form of the potential curve at unitarity is responsible of certain scaling properties. The energy ratio between consecutive states is given by $E_n/E_{n-1} = e^{-2\pi s_0} \approx 1/515$, while the ratio of the mean sizes $r_n/r_{n-1} = e^{\pi s_0} \approx 22.7$. These scaling laws only

depend on s_0 which is a universal quantity. The value of s_0 only depends on the nature of the particles and their corresponding symmetry. The value of $s_0 = 1.0062378$ is only valid for three identical bosons.

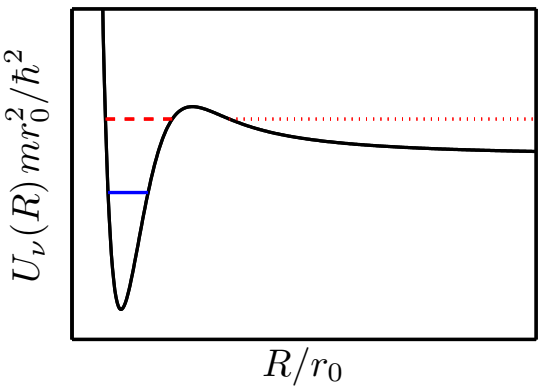

Figure 8.1: Schematic hyperradial potential curve for three identical bosons having $a_s < 0$. The dashed red line corresponds to a quasi-bound Efimov state above threshold. As the attraction increases, the state becomes bound. The blue line corresponds to a bound Efimov state.

An interesting phenomenon, called "Efimov-like shape resonance" [63], occurs in the negative scattering length region when an Efimov state is about to appear. The attractive $1/R^2$ is valid up to $R \sim |a_s|$. Beyond that point the interaction diminishes, and the effective potential is controlled mainly by the kinetic energy which produces a repulsive $1/R^2$. This change of behavior produces a potential curve of the form in Fig. 8.1. In the outer region, there is a potential barrier. This potential barrier appears ar $R \sim a_s$ and controls the size of the trimer. Therefore, even at threshold, the size of the trimer remains finite. As the attraction increases, this state becomes bound.

8.3 Analysis of the four-boson system with the correlated Gaussian method

In this section, we present the analysis of the four-boson spectrum using the CG method. We also analyze the pair-correlation functions and extract information on the

structure of the four-body states.

The study of the four-boson systems is significantly more challenging than the four-fermion system. The scaling laws of the three-boson subsystem should appear in some form in the four-boson system. Thus, to describe a few Efimov states, we have to be able to accurately represent states whose sizes varies by couple order of magnitudes. For example, to produce three bound Efimov states in a trap, we have to make weak enough so that the trap length at least $10^3 r_0$, where r_0 is the range of the two-body interaction. Even for such a weak trapping potential, the size of the 4^{th} Efimov state is too big to fit in the trap.

To analyze the spectrum, we introduce an external trapping. We are interested in understanding not only the bound states in the four-boson system but also the quasi-bound states above the continuum described by three-body Efimov states and the extra particle. Thus, the inclusion of a trapping potential is convenient for the numerical analysis with CG since it allows us to discretize the continuum. However, numerical limitations do not allow us to converge the complete spectrum. For example, for a trap size of $10^4 r_0$, the binding energy of the lowest Efimov state is of the order of $10^7 \hbar\omega$. The 3+1 states formed by an Efimov state and an extra particle can be treated as two particles in trap; they are spaced in energy by approximately $2\hbar\omega$. So, between the lowest three-body threshold and the zero of energy there would be about 10^7 states. Of course, we cannot describe accurately all these states. As the numbers of nodes increases, the wave function becomes more difficult to describe. Numerically, we observe that only a few of these $3+1$ states at each three-body threshold are accurately described while the rest remain unconverged. Intercalated with these unconverged states, there are quasi-bound four-body states. In general, these quasi-bound four-body states are easier to converge than the 3+1 states.

To extract the quasi-bound four-body states from the complete spectrum, we have to be able to distinguish them from the 3+1 states. To do that, we first analyze

the convergence of the spectrum as an optimization procedure is applied. In a standard optimization procedure, the states converge according to their energy. The lowest states converge faster than the highly excited states. However, in trapped four-body systems, the quasi-bound four-body states converge much faster than any 3+1 state of the same energy. As we increase and optimize the basis, we can observe how unconverged 3+1 states plunge down, crossing the quasi bound-body states that remain remarkably stable. By analyzing the convergence of the spectrum, we can distinguish unconverged states from stable states that are good candidates for describing quasi-bound four-body states.

Next, we analyze the pair-correlation function of the states. The 3+1 pair correlation function presents two peaks. The first peak describes the trimer, while the second peak describes the trimer-extra particle correlation. Unconverged states produce unphysical pair correlation functions, while stable quasi-bound states have smooth and well-behaved pair correlation functions.

The combination of these analyses allows us to identify the quasi-bound four-body states. Of course, this semiempirical method does not guarantee the extraction of all the quasi-bound four-body states. Unconverged four-body states cannot be detected by this method.

Figure 8.2 presents the four-boson energy spectrum as a function of the inverse scattering length. Here, we introduce a function $F(x) = \mathrm{sgn}(x)\ln(1+|x|)$ that allows us to deal with the logarithmic nature of the Efimov scaling. The blue lines are the four-body states; the black lines correspond to three-body thresholds; the red lines correspond to dimer and dimer-dimer thresholds.

The first thing we notice is that there are two four-body states below the lowest Efimov threshold across the entire range of scattering length values considered. At unitarity, the deeper 4-body state has an energy $E_1^{4b} \approx 5.88 E_1^{3b}$, while the second has an energy $E_2^{4b} \approx 1.10 E_1^{3b}$. These ratios were also calculated by Platter *et al.*, who obtained 5 and 1.01, respectively [83]. Note that even though the our values differ

quantitatively from those of Platter *et al.*, the structure of the bound four-body system is similar, with one "tight" bound state and another state very close to the three-body threshold.

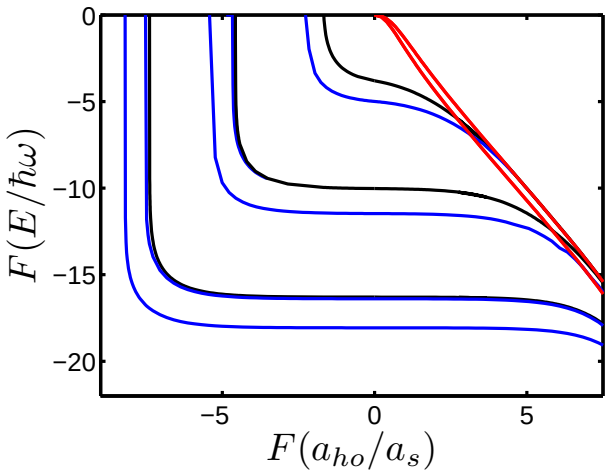

Figure 8.2: Spectrum of the four-boson system in a trap. The use of the function $F(x) = \mathrm{sgn}(x)\ln(1+|x|)$ allows to visualize effects at different orders of magnitude in a single graph. Blue lines correspond to four-body states. Black lines correspond to trimer+atom thresholds, and red lines correspond to dimer+atom+atom (upper) and dimer+dimer (lower) thresholds.

To understand the form of these states, we analyze the pair-correlation function. The pair correlation function for the lowest four-body and 3+1 states are presented in Fig. 8.3. The sizes of these three- and four-body states are of similar order to the range of the interaction; thus they are mainly nonuniversal. The mean interparticle distance in the lowest four-body state is $1.76r_0$ clearly showing that this has a size too small to be a universal state. The lowest three-body state has a mean interparticle distance of $2.55r_0$.

The second four-body state has an energy very close to the first three-body state. Analyzing the pair correlation functions of these three- and four-body states we observe that the four-body state can be understood as a three-body Efimov state with the 4^{th} particle weakly bound to it. The four-body pair correlation function presents a peak

at around $2\,r_0$ with a fairly long tail that extends out to approximately $10\,r_0$. The small-r region of the four-body–pair-correlation function describes the 3-body Efimov state, while the long tail describes the correlation between the three-body state and the 4^{th} particle. The mean distance between the three-body state and the 4t^{th} particle is $\sim 8\,r_0$.

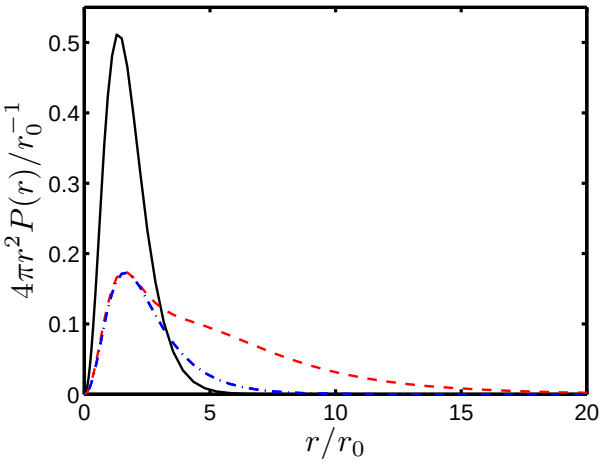

Figure 8.3: Lowest pair-correlation functions of the four-boson system at unitarity. The black solid line corresponds to the lowest four-body state; the dashed red curve is the second four-body state, and the dash-dotted curve is the lowest 3+1 state. The lowest 3+1 state has a double-peak structure with a second peak around $a_{ho} = 10^4 r_0$ that does not appear in the figure.

The rest of the four-body states are more weakly bound and behave universally. Since they are above the lowest three-body threshold, these four-body states are quasi-bound. There is one quasi-bound four-body state below each Efimov threshold. These states are universal and follow the same scaling law of the three-body Efimov physics; they are characterized by a scaling factor of $e^{\pi/s_0} \approx 22.7$. The binding energy of this series of four-body states (E_i^{4b}) are proportional to the three-body states (E_i^{3b}) and follows the relation $E_{i+1}^{4b} \approx 4.4 E_i^{3b}$ for $i > 1$ at unitarity.

We have numerically shown that pair-correlation functions follow the same Efimov-scaling law. Figure 8.4 compares the rescaled pair-correlation functions of the 3^{rd} and

4^{th} four-body states at unitarity. Within the accuracy of the CG calculations, we note that pair-correlation functions of four-body states follow the same scaling law as the three-body pair-correlation functions of the Efimov states.

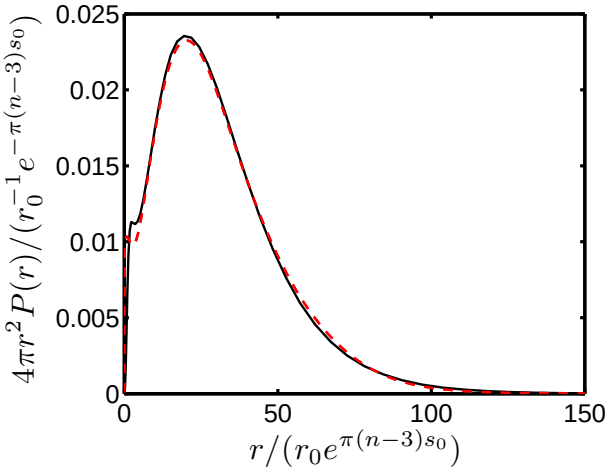

Figure 8.4: Rescaled pair-correlation functions of the 3^{rd} and 4^{th} four-body states. The pair correlation for $|\Psi_3\rangle$ has not been rescaled, but the $|\Psi_4\rangle$ pair-correlation function is rescaled by $e^{\pi/s_0} \approx 22.7$.

8.4 Analysis of the four-boson system in the hyperspherical representation

In this section, we analyze the four-boson system within the hyperspherical representation. Here, we consider an untrapped system. Using the correlated-Gaussian hyperspherical method (CGHS), we obtain channel functions and hyperspherical potential curves.

Figure 8.6 presents the hyperspherical potential curves in the a_s region where the first three-body Efimov states appear. It is useful to consider the situation in the three-body system (depicted in Fig. 8.1) in order to understand the qualitative behavior of the four-body potential curves. Figure 8.6 (a) corresponds to the case where the three-body system does not support a bound or quasi-bound state. Figure 8.6 (b) corresponds

to the case where the three-body system supports a quasi-bound state (schematically described by the dashed red line in Fig. 8.1). This quasi-bound state produces a series of avoided crossings in the four-body potential curves that describe an effective potential curve converging to the quasi-bound threshold. Finally, Fig. 8.6 (c) describes the case where the bound state lies below zero-energy threshold[1] (schematically described by the solid blue line in Fig. 8.1). The series of avoided crossings disappears, and the lowest potential curve is now seen to converge to the three-body bound-state threshold.

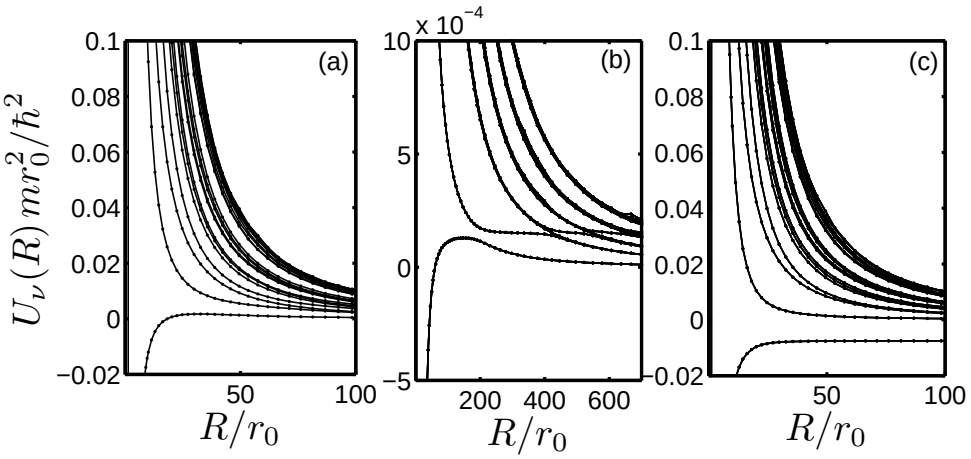

Figure 8.5: Potential curves in the scattering-length region near $a_{1f} \sim -6r_0$, where the first Efimov state appears. (a) Potential curves at $a_s > a_{1f}$ $[a_s \approx -5.31]$. The three-body bound state has not appear yet. (b) Potential curves at $a_s \gtrsim a_{1f}$ $[a_s \approx -6.16]$. For these scattering length values a quasi-bound state appears. (c) Potential curves at $a_s < a_{1f}$ $[a_s \approx -7.29]$. For these scattering length values the attraction increases and the three-body state becomes bound.

In this region of scattering lengths, the lowest four-body potential curve supports a bound state. In fact, as the magnitude of scattering length is being increased, two bound states are formed before the first three-body state appears. This finding is in agreement with the results obtained with the CG method (see Fig. 8.2). Therefore, when the three-body state is right at threshold, the number of four-body states is finite. In this sense, there is no "four-body" Efimov effect.

[1] In the energy scale used here, the zero is selected at the four-body breakup threshold

The absence of a four-body Efimov effect can be understood by considering the qualitative differences between the three- and four-body systems. The three-body Efimov effect occurs when the weakly-bound dimer is right at threshold. The size of the dimers is very large, with their wave functions decaying as $1/r$, where r is the interparticle distance. These long-range correlations are responsible in part for the long-range $1/R^2$ behavior of the lowest hyperspherical potential curve that produces the Efimov effect.

In contrast, in the four-body system, the size of the three-body state remains finite at threshold. The potential barrier schematically presented in Fig. 8.1 constrains the state to have a finite size. Therefore, for R much greater than the size of the trimer, the channel function describes an atom-trimer two-body system that decays much faster than $1/R^2$. This situation is qualitatively different than the three-body case in that no attractive $1/R^2$ potential occurs. However, in an intermediate region, we observe numerically that the potential takes the form

$$W_0(R) \approx \frac{A \ln(R/a_s) + B}{2\mu R^2}. \tag{8.2}$$

Here, A is a positive constant, and B is a negative constant such that $W_0(R)$ is negative in that region. This behavior is observed for ranges from $R \approx 6r_0$ to $R \approx 36r_0$ for the three-body first Efimov state and over the range from $R \approx 230r_0$ to $R \approx 1000r_0$ for the second Efimov state. In both cases, the long-range behavior changes after this intermediate region, converging fast to the asymptotic threshold. Equation (8.2) is only valid when the trimer energy is very close to threshold. Once the three-body Efimov state becomes more tightly bound, this intermediate behavior [Eq. (8.2)] is no longer valid.

As the magnitude of a_s increases, a second three-body bound state appears. In this a_s region, the energy of the first three-body bound state is quite deep. Therefore, the lowest potential curve has a deep threshold in comparison with the rest of the

potential curves. The remaining potential curves behave qualitatively as in Fig. 8.6. The behavior of the second potential curve in this a_s region is qualitatively described by the lowest potential curve of Fig. 8.6.

As in the lowest potential curve, the second potential curve supports two bound states when the second three-body bound state is at the zero-energy threshold. The second of the four-body bound states belonging to the second potential curve was not identified in the CG calculation because of the limitations of the method. This second bound state (included in Fig. 8.2) appears before the second Efimov state and becomes very shallow as the scattering length approaches unitarity. In the adiabatic approximation this state disappears. However, a coupled-channel calculation suggests that the state may reappear if these couplings are included. The binding energy of such a state would be less than 1% lower than the three-body threshold. The existence of this state very close to the trimer threshold should greatly influence the atom-trimer scattering length.

The second potential curve in the a_s region is quantitatively different from the lowest potential curve of Fig. 8.6. The lowest potential curve of Fig. 8.6 is more attractive, and the bound states are comparatively deeper than the levels in of the second potential curve. Furthermore, the second state in the second potential curve seems to disappear as a_s is tuned closer to unitarity while the second state continues to exist at unitarity and in the ranges where $1/a_s > 0$. These differences can be understood by considering finite attractive interaction effects. The lowest potential curve has a minimum around $R \approx 2r_0$ where the effects of the two-body attractive interaction are still visible. The second potential curve has a minimum around $R \approx 16r_0$, and it is not significantly affected by the two-body interaction. For this reason, we expect the second and higher potential curves to be universal in the $R \gg r_0$. To verify this statement, we now analyze the potential curves right at unitarity.

Figure 8.7 presents the lowest three potential curves rescaled by the length and

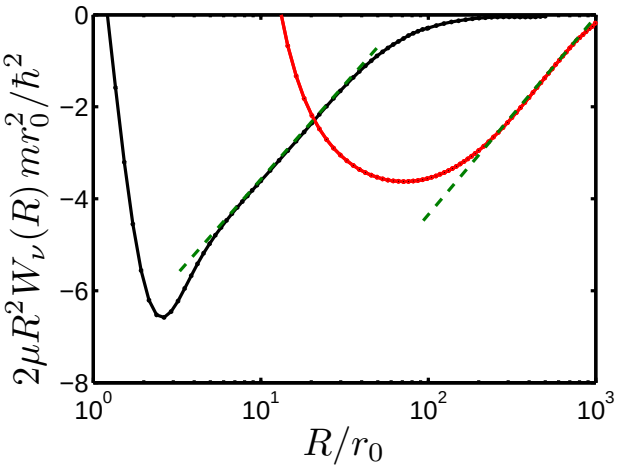

Figure 8.6: Lowest potential curves when three-body states are at threshold. Black curve correspond to the lowest potential curve at the scattering length value for which the first Efimov state is at threshold. The red curve is the second potential curve at the scattering length value for which the second potential Efimov state is at threshold. Green dashed lines present the linear behavior of the curves (note that the potential curves are multiplied by $2\mu R^2$ and that the x-axis is in logarithmic scale). The linear behavior of the curves in logarithmic scale is evidence of Eq. (8.2).

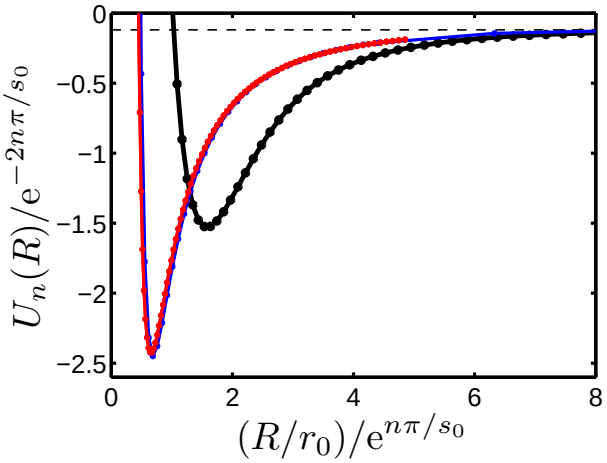

Figure 8.7: Lowest three rescaled potential curves U_ν are shown as functions of the four-body hyperradius. The black curve corresponds to the lowest curve. The blue curve is the second potential curve and the red curve is the third potential curve. The agreement between the rescaled second and third potential curves is numerical evidence for the universal behavior of the four-boson system, as is discussed.

energy scaling factors e^{π/s_0} and $e^{-2\pi/s_0}$, respectively. We can clearly see that the lowest potential curve (black symbols) is different from the second and third potential curves. However, the second and third rescaled potential curves (blue and red symbols) agree very well. Therefore, they are considered universal. This agreement strongly suggest that the three-body scaling factor appears in the four body problem as an scaling factor of the potential curves. This universal behavior of the four-body system is consistent with the speculations of Platter *et. al* [83]. Our results are also consistent with Platter *et. al* prediction that no four-body parameter is needed to renormalize the four-body system.

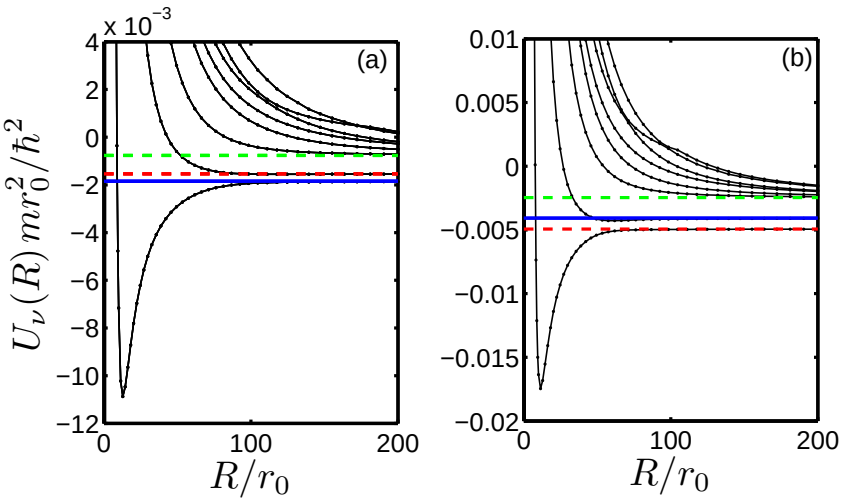

Figure 8.8: Potential curves at positive scattering-length values. (a) Potential curves at $a_s \sim 37r_0$. (b) Potential curves at $a_s \sim 21r_0$. Solid blue line corresponds to the atom-trimer threshold. Dashed-red line corresponds to the dimer-dimer threshold, and dashed-green line corresponds to the dimer–two-atom threshold.

Using the adiabatic hyperspherical approximation [Eq. (2.32)], we obtain the four-body energies. Since each potential curve supports one bound state, there is a family of quasi-bound four-body states which follow the same scaling relations of the potential curves. Therefore, the energies of the four-body bound state obey $E^{4b}_{n-1}/E^{4b}_n = e^{2\pi/s_0}$, which is the same relation between the energies of the three-body Efimov states.

Table 8.1: Lowest three- and four-body energies at unitarity. All the energies are in units of $\hbar^2/(mr_0^2)$. The three-body energies (left column) where calculated with CG without a trapping potential. The $N = 4$ energies were calculated with CG (center column) and CGHS in the adiabatic approximation (right column). The CG provides exact results for true bound state (E_1^{3b}, E_2^{3b}, E_3^{3b}, E_1^{4b}, and E_2^{4b}) but it is only approximated for quasi-bound states (E_3^{4b} and E_4^{4b}). The adiabatic approximation provides a rigorous upper bound of the exact energies. Therefore, the most reliable E_3^{4b} and E_4^{4b} are obtained with the CGHS in the adiabatic approximation.

$N = 3$ (CG)	$N = 4$ (CG)	$N = 4$ (CGHS)
$E_1^{3b} = -0.11922$	$E_1^{4b} = -0.7014$	$E_1^{4b} = -0.69998$
$E_2^{3b} = -0.2257\,10^{-3}$	$E_2^{4b} = -0.1311$	$E_2^{4b} = -0.1285$
$E_3^{3b} = -0.438\,10^{-6}$	$E_3^{4b} = -0.99\,10^{-3}$	$E_3^{4b} = -0.1035\,10^{-2}$
	$E_4^{4b} = -0.17\,10^{-5}$	$E_4^{4b} = -0.205\,10^{-5}$

However, the three-body system hyperspherical scenario is quite different since all the states belong to the same hyperspherical potential curve. A comparison of the energies of the three- and four-body systems leads to the relation $E_{i+1}^{4b} \approx 4.6 E_i^{3b}$. This relation is slightly different than the one obtained with CG. Since both calculations are variational and the adiabatic calculation predicts lower energies, we consider this second relation more accurate. Table 8.1 summarizes CG and CGHS results.

Finally, we consider the positive scattering length region. In Fig. 8.2, we observed how different two- and three-body thresholds crossed each other as the scattering length was tuned. Figure 8.8 shows the potential curves for two different scattering-length values. The blue line corresponds to the energy of the second Efimov trimer (trimer+atom threshold), the dashed-red line corresponds to the dimer-dimer threshold, and the dashed-green line corresponds to the dimer threshold. There is a also deeper potential curve that converges to the deep atom-trimer threshold that is not shown in the figure. Figure 8.8 (a) presents the case where the trimer threshold is below the dimer-dimer threshold. As the scattering length is decreased, the dimer-dimer threshold and the atom-trimer threshold cross each other. Figure 8.8 (b) shows the case where the dimer-dimer threshold lies energetically below the trimer+atom threshold. In both

figures, a four-body bound state is contained in the attractive region of the lowest potential curve. If we continue decreasing the scattering length, the dimer+atom+atom and trimer thresholds approach each other, and the atom-trimer potential curve smoothly becomes a dimer+atom+atom potential curves.

The crossing of thresholds and formation or destruction of a four-body bound state have important consequences in the collisional properties of the four-boson system. These consequences will be explored in the next section.

8.5 Scattering properties

From the potential curves obtained in the previous section, we can analyze the scattering properties of the four-boson system. In particular, we focus on the dimer-dimer and atom-trimer collisions.

Sharp features in ultracold collisional observables are expected when a bound or quasi-bound state crosses a fragmentation threshold or when two different fragmentation thresholds coincide. By analyzing the two-, three- and four-body spectrum (Fig. 8.2), we can deduce important scattering-length values in which sharp features would occur in collisional observables. There is one value of the two-body scattering length where the dimer energy equals one of the trimer energies. At this scattering-length value, we expect a pole in the atom-dimer scattering length. Similarly, when a four-body-state energy equals twice the dimer energy, we expect a pole in the dimer-dimer zero energy scattering length. Another sharp feature in the dimer-dimer scattering length should occur when the trimer energy equals twice the dimer energy and the thresholds of the atom-trimer and dimer-dimer potential curves coincide.

We define a_{trim-d} as the two-body scattering-length value where the trimer and dimer energies are equal. We also define $a_{trim-dd}$ as the two-body scattering-length value where the trimer energy equals twice the dimer energy. Similarly, we define a_{tet-dd} as the two-body scattering-length value where the tetramer (four-body) energy equals twice

the dimer energy. These three scattering lengths depend on the three-body parameter that controls three- and four-body state energies. Using the semi-analytical solutions from the three-body system [27], it can be shown that the ratio $a_{trim-d}/a_{trim-dd}$ is independent of the three-body parameter. Similarly, since the four-body state has the same universal properties of the three-body system, the ratios $a_{trim-dd}/a_{tet-dd}$ and a_{tet-dd}/a_{trim-d} should also be independent of the three-body parameter.

These ratios can be used to identify these sharp features experimentally. If the position of one of the scattering length values is known, then the other two can be deduced. An observation of these three sharp features in the atom-dimer and dimer-dimer collisions that obey the ratios predicted for a_{trim-d}, $a_{trim-dd}$,and a_{tet-dd} would be experimental verification that these features are a consequence of three and four-body states. Such experimental verification of Efimov physics would be much simpler than directly verifying the $e^{\pi/s_0} \approx 22.7$ scaling law, which would require control of the scattering length over a couple orders of magnitude.

From an experimental point of view, it is also important to find a_{tet-dd}. In the vicinity of a_{tet-dd}, there is a pole in the dimer-dimer scattering length that can be used to tune dimer-dimer interactions. These bosonic dimers can have both positive and negative scattering lengths. Therefore, the wide tunability of the dimer-dimer interaction opens the door to studying new phenomena of bosonic dimers with attractive interactions.

To obtain a_{trim-d}, $a_{trim-dd}$ and a_{tet-dd}, we analyze the bound states associated with the third Efimov state. We select these three- and four-body states because they are much larger than the range of the interaction and are expected to behave universally at all scattering length values.

Our analysis of the two-, three- and four-body spectrum determines the following

values:

$$a_{trim-dd} \approx 720 r_0, \tag{8.3}$$

$$a_{trim-d} \approx 105 r_0, \tag{8.4}$$

$$a_{tet-dd} \approx 254 r_0. \tag{8.5}$$

These scattering lengths lead to the ratios

$$\frac{a_{trim-dd}}{a_{tet-dd}} \approx 2.84, \qquad \frac{a_{tet-dd}}{a_{trim-d}} \approx 2.41. \tag{8.6}$$

To obtain a_{tet-dd}, we calculate the four-body energy using the hyperspherical adiabatic approximation. These energies are more accurate than the ones obtained by the CG (see Sec. 8.3).

The $a_{trim-dd}$ and a_{trim-d} only depend on two- and three-body physics. Therefore, we can use all the machinery that has been built to obtain an independent verification of the $a_{trim-dd}$ and a_{trim-d} values. In particular, we use the semi-analytical formulas from Ref. [27]. From the three-body energy of our third Efimov state at unitarity we extract the three-body parameter that characterizes the system. With this single parameter, we calculate $a_{trim-dd}$ and a_{trim-d} to be

$$a_{trim-dd} \approx 720 r_0, \tag{8.7}$$

$$a_{trim-d} \approx 107 r_0. \tag{8.8}$$

We find very nice agreement, with corrections of less than 2% in a_{trim-d}. This results show that our numerical calculations behave universally to a good approximation. Also, they give us confidence in our numerical procedure.

These scattering length ratios can be used to identify the sharp features but we do not know the shape of these features. To directly observe the sharp features in the dimer-dimer scattering length, we carry out scattering calculations using the hyperspherical representation and the R-matrix method [8] (these calculations were carried

out by Jose P. D'Incao). The third Efimov state is quite large and scattering calculations would be very difficult. Instead we analyze the two-body scattering-length region where the second Efimov and its four-body state crosses the dimer-dimer threshold. These states are affected by finite range corrections. For example, the trimer energy never crosses the dimer threshold [2] , and the ratio $a_{trim-dd}/a_{tet-dd} \approx 3.47$ instead of 2.84. Nevertheless, we consider that the behavior of the dimer-dimer scattering length qualitatively describes universal behavior.

Figure 8.5 shows the real and imaginary part of the dimer-dimer scattering length a_{dd} as a function of the two-body scattering length. The real part of the scattering length describes elastic scattering, while the imaginary part describes losses. The units are selected such that $r_0 = 100(a.u.)$, which is close to the Cs van der Waals length. The red lines and symbols correspond to the numerical results. The dashed vertical lines correspond to $a_{trim-dd}$ and a_{tet-dd}. At a_{tet-dd}, we observe a pole in the real-part of scattering length, and at $a_{trim-dd}$ we observe a discontinuity in the real part. For $a_s > a_{trim-dd}$, the dimer-dimer scattering length converges to approximately $a_{dd} \approx 1.3a_s$. However, it is not clear if this behavior is universal.

The imaginary part of the scattering length [right panel of Fig. 8.5] represents inelastic scattering processes. The peak around $a_{trim-dd} \sim 2900$ a.u. describes the conversion of two dimers into trimer and an atom. The second peak around 800 a.u. represents important losses close to the a_{tet-dd}.

Finally, we focus on atom-trimer collisions. Figure 8.10 presents the real and imaginary part of the atom-trimer scattering length. The main feature is the pole in the real part of the scattering length at $a_s \sim 6r_0$. The pole is due to the appearance of a four-body state in the atom-trimer channel. This four-body state occurs at small scattering-length values, and it is not universal. Also, a sharp feature occurs at $a_{trim-dd}$

[2] According to the $a_{trim-dd}$ value and the universal ratios [Eq. 8.6], a_{trim-d} should be approximately $4r_0$. Clearly, scattering lengths around this value are not large and the behavior of the system is not universal.

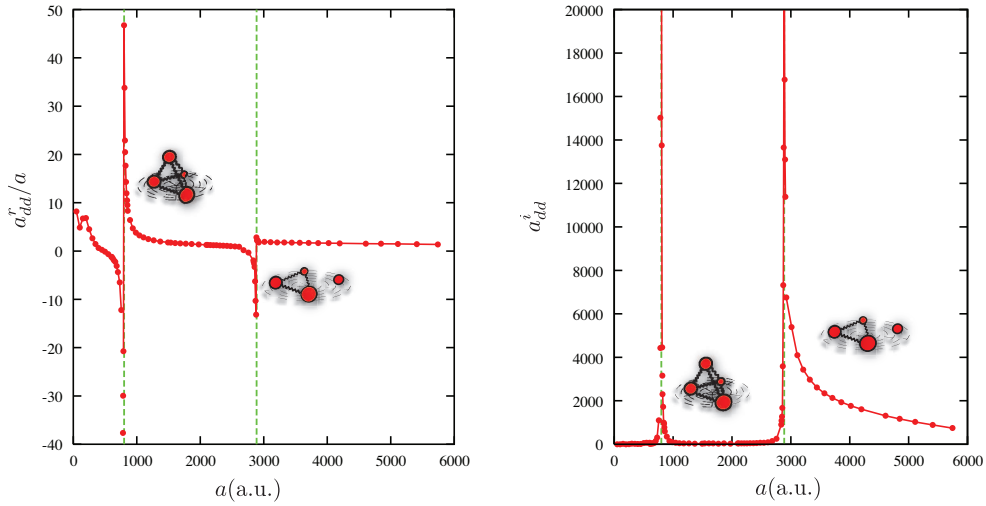

Figure 8.9: Real and imaginary parts of the dimer-trimer scattering length. Left and right panels present the real and imaginary parts of the dimer-trimer scattering length: a^r_{dd} and a^i_{dd}, respectively. The vertical dashed lines correspond to $a_{trim-dd}$ and a_{tet-dd}. Figure courtesy of Jose P. D'Incao.

where an atom and a trimer can decay into two dimers. An understanding of this feature will require a deeper analysis of the atom-trimer collisional properties.

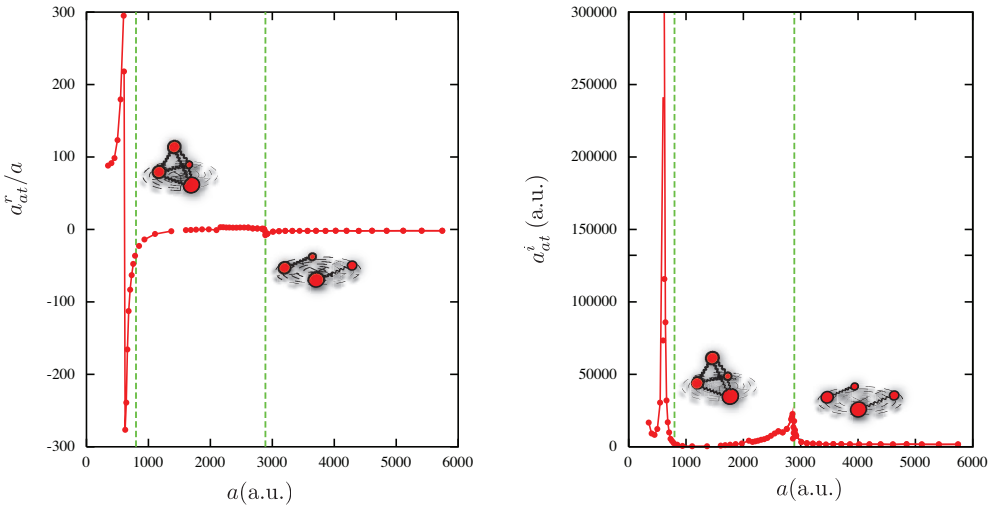

Figure 8.10: Real and imaginary parts of the atom-trimer scattering length. Left and right panels present the real and imaginary parts of the atom-trimer scattering length: a^r_{at} and a^i_{at}, respectively. The vertical dashed lines correspond to $a_{trim-dd}$ and a_{tet-dd}. Figure courtesy of Jose P. D'Incao.

8.6 Conclusions

We have presented a preliminary analysis of the four-boson problem using the CG method and the hyperspherical representation. The system at unitarity is described by a set of potential curves that are related via the Efimov scaling factor. Each of these potential curves contains a four-body state that follows the same scaling laws of the three-body system.

At positive scattering lengths, Efimov physics can be probed with dimer-dimer collisions. The four-body states produce poles in the scattering length that can be used to tune dimer-dimer interactions. Also, for scattering lengths slightly above $a_{trim-dd}$, dimer-dimer collisions can be used to obtain a trimer-atom mixture without significant losses.

Chapter 9

Summary and Outlook

The first objective of this dissertation was to develop a renormalized interaction that would eliminate the artificial instabilities that produce the Fermi pseudopotential in mean-field theories. The density renormalization obtained from two-particle solutions succeeds in this objective. It provides a simple model that both reproduces the Hartree term in the weakly attractive Fermi gas system and the expected functional form in the strongly interacting unitarity regime. This model has proven to be useful in Hartree-Fock, Thomas-Fermi, and hyperspherical calculations. However, the description of the system is limited. Pair correlations are not included, and the excitation gap is not reproduced. Also, the energy of the system at unitarity is slightly high in comparison with more sophisticated calculations such as fixed-node diffusion Monte Carlo (FN-DMC). In addition, the model presented here cannot be extended to Bose-Binstein condensation (BEC) because it does not incorporate the necessary pair correlations to describe molecule formation. Incorporating pair correlations would be the logical next step but this would require a completely new approach, one closer to standard BCS theory.

The second and primary objective of this dissertation was to obtain an appropriate solution to the four-body fermionic system in the BCS-BEC crossover. To this end, we developed and implemented a variant of the correlated-Gaussian (CG) method. The solutions obtained with CG accurately describe four trapped fermions. These solutions,

extended to $N = 2$ and 3, are described in chapter 5. They were first used to analyze the behavior of the spectrum as the interaction was tuned in the BCS-BEC crossover. Later, we solved the dynamics of few-body systems as the scattering length was tuned to produce different types of ramping schemes.

A nice extension to the calculations presented in chapter 5 would be the generalization to arbitrary angular momentum. Even though few-body solutions with $L = 1$ were obtained in chapters 6 and 7, the method used to obtain these solutions is limited and would not be appropriate for calculating the complete spectrum for arbitrary angular momentum. There are ways to extend the CG method to treat systems with arbitrary angular momentum [173]. Such extensions of the CG method could be useful in obtaining few-body solutions with arbitrary angular momentum.

The calculation of the spectrum and dynamics of a few-body system with different angular momenta would allow the study of temperature effects. At a finite temperature, states with any angular momentum can be populated. Therefore, to describe the dynamics of systems at any temperature, we need to consider all angular momentum cases.

In chapters 6 and 7, we quantitatively analyzed the spectrum and the structural properties of such a system. We extracted the dimer-dimer scattering length and effective range for different mass ratios. We verified universal properties of unitarity systems. We also showed that no weakly bound state exists for two-component Fermi systems with $L \leq 6$. These calculations were extended to larger systems using FN-DMC, which connected few- and many-body perspectives. All solutions obtained with CG and FN-DMC were restricted to describing bound systems. This restriction allowed us to extract collisional properties only in an indirect way, as was done in chapter 6. The correlated Gaussian hyperspherical (CGHS) method introduced a more suitable way of analyzing collisional properties.

The development of the CGHS method was a major numerical accomplishment

of this dissertation. This method opens up the possibility of studying the continuum and collisional properties of four-body systems using hyperspherical coordinates. Furthermore, it provides results more accurate than the standard CG method. We present examples of four-body fermionic potential curves obtained with CGHS in chapters 5, 6, and 7. In chapter 8, we also solve the four-boson system using CGHS. In addition to its great success, this method can be improved and extended.

The creation of the CGHS basis set can be improved upon by using the CG solutions of subsystems. These CG solutions can be selected to construct a particular channel function. For example, if we want to describe an atom-trimer channel, we can obtain the trimer state with CG and use it to construct the basis functions of the atom-trimer form. With a few of those solutions, we might be able to accurately describe the atom-trimer channel. Similarly, the dimer-atom-atom and dimer-dimer channels can be generated using the CG two-body solutions. These solutions would have several advantages. By construction, they would describe correctly the asymptotic behavior of the channels. And, we can introduce the channels in a controllable way, identifying the importance of each channel and obtaining a deeper understanding of the system.

Another major improvement would be the extension of CGHS method to describe $L > 0$ solutions. We might be able to use the ideas applied to standard CG to extend CGHS calculations to $L > 0$.

In chapter 8, we used both CG and CGHS methods to solve the four-boson system with tunable interactions. We showed that potential curves and energies follow Efimov-scaling relationships. We found that three- and four-body energies at unitarity also follow a scaling relationship. We then analyzed the effect of these four-body states in atom-dimer and dimer-dimer collisional properties. Finally, we showed that abrupt changes in the atom-dimer and dimer-dimer scattering properties occur at two-body scattering-length values whose ratios are independent of the three-body parameter. These scattering ratios can be useful in experimentally identifying poles in the

dimer-dimer scattering length.

The four-boson scaling relationships suggest that the system behaves universally. To verify universality, we could introduce a different short-range potential. If the system's behavior follows the same scaling relationships, then we would have demonstrated universality in the four-boson system.

Other studies would complement the results from chapter 8. The analysis of the collisional properties for $a_s < 0$ has not been carried out yet. We expect that sharp features in the four-body recombination would appear at two-body scattering-length values where the four-body states are at zero-energy threshold. The ratio of these scattering-length values would be independent of the three-body parameter. In addition, we could analyze atom-trimer collisions at unitarity to better understand the expected lifetime of atom-trimer mixtures.

Finally, it would be interesting to analyze collisional properties of other four-body systems. In particular, we could use the CGHS method to study a Bose-Fermi mixture. In this system, Efimov states can be formed with two bosons and one fermion. Therefore, we expect that Efimov physics would have important consequences in a Bose-Fermi mixture. Boson-trimer and fermion-trimer collisions could be analyzed by considering three bosons and a fermion or a two-boson-two-fermion system. Also, fermionic dimers could be formed with one boson and one fermion. The analysis of dimer-dimer collisions would require the extension of CGHS method to treat $L = 1$ systems.

Bibliography

[1] S. K. Adhikari and A. C. Fonseca. Four-body Efimov effect in a Born-Oppenheimer model. Phys. Rev. D, 24(2):416–425, 1981.

[2] Y. Alhassid, G. F. Bertsch, and L. Fang. New effective interaction for the trapped fermi gas. Phys. Rev. Lett., 100(23):230401, 2008.

[3] E. Altman and A. Vishwanath. Dynamic Projection on Feshbach Molecules: A Probe of Pairing and Phase Fluctuations. Phys. Rev. Lett., 95(11):110404, 2005.

[4] J. B. Anderson. Quantum chemistry by random walk. H 2 P, H+ 3 D 3h 1 A'1, H 2 3 Sigma+ u, H 4 1 Sigma+ g, be 1 S. J. Chem. Phys., 65(10):4121–4127, 1976.

[5] M. H. Anderson, J. R. Ensher, M. R. Matthews, C. E. Wieman, and E. A. Cornell. Observation of Bose-Einstein Condensation in a Dilute Atomic Vapor. Science, 269(5221):198–201, 1995.

[6] A. V. Andreev, V. Gurarie, and L. Radzihovsky. Nonequilibrium Dynamics and Thermodynamics of a Degenerate Fermi Gas Across a Feshbach Resonance. Phys. Rev. Lett., 93(13):130402, 2004.

[7] G. E. Astrakharchik, J. Boronat, J. D. Casulleras, and S. Giorgini. Equation of state of a Fermi gas in the BEC-BCS crossover: A quantum Monte Carlo study. Phys. Rev. Lett., 93(20):200404, 2004.

[8] M. Aymar, C. H. Greene, and E. Luc-Koenig. Multichannel Rydberg spectroscopy of complex atoms. Rev. Mod. Phys., 68(4):1015–1123, 1996.

[9] G. A. Baker, Jr. Neutron matter model. Phys. Rev. C, 60(5):054311, 1999.

[10] J. Bardeen, L. N. Cooper, and J. R. Schrieffer. Microscopic Theory of Superconductivity. Phys. Rev., 106(1):162–164, 1957.

[11] J. Bardeen, L. N. Cooper, and J. R. Schrieffer. Theory of Superconductivity. Phys. Rev., 108(5):1175–1204, 1957.

[12] M. Bartenstein, A. Altmeyer, S. Riedl, S. Jochim, C. Chin, J. H. Denschlag, and R. Grimm. Collective Excitations of a Degenerate Gas at the BEC-BCS Crossover. Phys. Rev. Lett., 92(20):203201, 2004.

[13] M. Bartenstein, A. Altmeyer, S. Riedl, S. Jochim, C. Chin, J. Hecker Denschlag, and R. Grimm. Crossover from a molecular bose-einstein condensate to a degenerate fermi gas. Phys. Rev. Lett., 92(12):120401, 2004.

[14] P. F. Bedaque and U. van Kolck. Nucleon-deuteron scattering from an effective field theory. Phys. Lett. B, 428(3-4):221–226, 1998.

[15] H. Bethe and R. Peierls. Quantum Theory of the Diplon. Proc. R. Soc. London, Ser. A, 148:146, 1935.

[16] D. Blume and C. H. Greene. Quantum corrections to the ground-state energy of a trapped Bose-Einstein condensate: A diffusion Monte Carlo calculation. Phys. Rev. A, 63(6):63601, 2001.

[17] D. Blume and C. H. Greene. Fermi pseudopotential approximation: Two particles under external confinement. Phys. Rev. A, 65(4):043613, 2002.

[18] D. Blume, S. T. Rittenhouse, J. von Stecher, and C. H. Greene. Stability of inhomogeneous multicomponent Fermi gases. Phys. Rev. A, 77(3):33627, 2008.

[19] D. Blume, J. von Stecher, and Chris H. Greene. Universal Properties of a Trapped Two-Component Fermi Gas at Unitarity. Phys. Rev. Lett., 99(23):233201, 2007.

[20] J. L. Bohn, B. D. Esry, and C. H. Greene. Effective potentials for dilute bose-einstein condensates. Phys. Rev. A, 58:584, 1998.

[21] E. L. Bolda, E. Tiesinga, and P. S. Julienne. Effective-scattering-length model of ultracold atomic collisions and Feshbach resonances in tight harmonic traps. Phys. Rev. A, 66(1):13403, 2002.

[22] B. Borca, D. Blume, and C. H. Greene. A two-atom picture of coherent atom–molecule quantum beats. New J. Phys., 5(1):111, 2003.

[23] J. P. Bouchaud, A. Georges, and C. Lhuillier. Pair wave functions for strongly correlated fermions and their determinantal representation. J. Phys. (Paris), 49(4):553, 1988.

[24] T. Bourdel, J. Cubizolles, L. Khaykovich, K. M. F Magalhães, S. Kokkelmans, G. V. Shlyapnikov, and C. Salomon. Measurement of the Interaction Energy near a Feshbach Resonance in a^{6} Li Fermi Gas. Phys. Rev. Lett., 91(2):20402, 2003.

[25] T. Bourdel, L Khaykovich, J. Cubizolles, J. Zhang, F. Chevy, M. Teichmann, L. Tarreell, S. J. J. M. F. Kokkelmans, and C. Salomon. Experimental Study of the BEC-BCS Crossover Region in ^{6}Li. Phys. Rev. Lett., 93(5):050401, 2004.

[26] S. F. Boys. The Integral Formulae for the Variational Solution of the Molecular Many-Electron Wave Equations in Terms of Gaussian Functions with Direct Electronic Correlation. Proc. R. Soc. London, Ser. A, 258(1294):402–411, 1960.

[27] E. Braaten and H. W. Hammer. Universality in few-body systems with large scattering length. Phys. Rep., 428(5-6):259–390, 2006.

[28] E. Braaten and A. Nieto. Quantum corrections to the ground state of a trapped Bose-Einstein condensate. Phys. Rev. B, 56(22):14745–14765, 1997.

[29] M. Brack and R. K. Bhaduri. Semiclassical Physics. Addison-Wesley, Reading, MA, 1997.

[30] C. C. Bradley, C. A. Sackett, J. J. Tollett, and R. G. Hulet. Evidence of Bose-Einstein Condensation in an Atomic Gas with Attractive Interactions. Phys. Rev. Lett., 75(9):1687–1690, 1995.

[31] I. V. Brodsky, M. Y. Kagan, A. V. Klaptsov, R. Combescot, and X. Leyronas. Exact diagrammatic approach for dimer-dimer scattering and bound states of three and four resonantly interacting particles. Phys. Rev. A, 73(3):32724, 2006.

[32] G. M. Bruun. Universality of a two-component Fermi gas with a resonant interaction. Phys. Rev. A, 70(5):53602, 2004.

[33] G. M. Bruun and K. Burnett. Interacting Fermi gas in a harmonic trap. Phys. Rev. A, 58(3):2427–2434, 1998.

[34] A. Bulgac. Local-density-functional theory for superfluid fermionic systems: The unitary gas. Phys. Rev. A, 76(4):040502(R), 2007.

[35] T. Busch, B.-G. Englert, K. Rzążewski, and M. Wilkens. Two cold atoms in a harmonic trap. Foundations of Phys., 28(4):549, 1998.

[36] J. Carlson, S. Y. Chang, V. R. Pandharipande, and K. E. Schmidt. Superfluid Fermi gases with large scattering length. Phys. Rev. Lett., 91:050401, 2003.

[37] J. Carlson and S. Reddy. Asymmetric two-component fermion systems in strong coupling. Phys. Rev. Lett., 95(6):060401, 2005.

[38] Y. Castin. Exact scaling transform for a unitary quantum gas in a time dependent harmonic potential. C. R. Phys., 5(3):407, 2004.

[39] D. M Ceperley and B. J. Alder. Quantum Monte Carlo for molecules: Greens function and nodal release. J. Chem. Phys., 81:5833, 1984.

[40] S. Y. Chang and G. F. Bertsch. Local-density-functional theory for superfluid fermionic systems: The unitary gas. Phys. Rev. A, 76(4):021603 (R), 2007.

[41] S. Y. Chang, V. R. Pandharipande, J. Carlson, and K. E. Schmidt. Quantum monte carlo studies of superfluid fermi gases. Phys. Rev. A, 70:043602, 2004.

[42] X. Chapuisat. Principal-axis hyperspherical description of N-particle systems: Quantum-mechanical treatment. Phys. Rev. A, 45(7):4277, 1992.

[43] C. Chin. Simple mean-field model for condensates in the BEC-BCS crossover regime. Phys. Rev. A, 72(4):41601, 2005.

[44] C. Chin, M. Bartenstein, A. Altmeyer, S. Riedl, S. Jochim, J. H. Denschlag, and R. Grimm. Observation of the Pairing Gap in a Strongly Interacting Fermi Gas. Science, 305(5687):1128–1130, 2004.

[45] C. W. Clark. Resonant Photodetachment of the Positronium Negative Ion. Phys. Lett., 70A(13):295, 1979.

[46] H. T. Coelho and J. E. Hornos. Proof of basic inequalities in the hyperspherical formalism for the n-body problem. Phys. Rev. A, 43(11):6379–6381, Jun 1991.

[47] L. N. Cooper. Bound Electron Pairs in a Degenerate Fermi Gas. Phys. Rev., 104(4):1189–1190, 1956.

[48] P. Courteille, R. S. Freeland, D. J. Heinzen, F. A. van Abeelen, and B. J. Verhaar. Observation of a Feshbach Resonance in Cold Atom Scattering. Phys. Rev. Lett., 81(1):69–72, 1998.

[49] Marco Cozzini and Sandro Stringari. Fermi gases in slowly rotating traps: Superfluid versus collisional hydrodynamics. Phys. Rev. Lett., 91(7):070401, Aug 2003.

[50] K. B. Davis, M. O. Mewes, M. R. Andrews, N. J. van Druten, D. S. Durfee, D. M. Kurn, and W. Ketterle. Bose-Einstein Condensation in a Gas of Sodium Atoms. Phys. Rev. Lett., 75(22):3969–3973, 1995.

[51] L. M. Delves. Tertiary and general-order collisions. Nucl. Phys., 9:391, 1959.

[52] L. M. Delves. Tertiary and general-order collisions. Part II. Nucl. Phys., 20:275, 1960.

[53] B. DeMarco and D. S. Jin. Onset of Fermi Degeneracy in a Trapped Atomic Gas. Science, 285(5434):1703, 1999.

[54] Roberto B. Diener, Rajdeep Sensarma, and Mohit Randeria. Quantum fluctuations in the superfluid state of the bcs-bec crossover. Phys. Rev. A, 77(2):023626, 2008.

[55] J. P. DIncao and B. D. Esry. Scattering Length Scaling Laws for Ultracold Three-Body Collisions. Phys. Rev. Lett., 94(21):213201, 2005.

[56] J. P. D'Incao, Seth T. Rittenhouse, N. P. Mehta, and Chris H. Greene. Dimer-dimer collisions at finite energies in two-component Fermi gases. arXiv:0806.3062, 2008.

[57] J. Dobaczewski, P. Magierski, W. Nazarewicz, W. Satuła, and Z. Szymański. Odd-even staggering of binding energies as a consequence of pairing and mean-field effects. Phys. Rev. C, 63(2):024308, 2001.

[58] E. A. Donley, N. R. Claussen, S. T. Thompson, and C. E. Wieman. Atom-molecule coherence in a Bose-Einstein condensate. Nature, 417(6888):529–33, 2002.

[59] D. M. Eagles. Possible Pairing without Superconductivity at Low Carrier Concentrations in Bulk and Thin-Film Superconducting Semiconductors. Phys. Rev., 186(2):456–463, 1969.

[60] V. Efimov. Weakly Bound States of Three Resonantly Interacting Particles. Yad. Fiz., 12:1080, 1970 [Sov. J. Nucl. Phys. 12, 589 (1971)].

[61] V. N. Efimov. Energy levels of three resonantly interacting particles. Nucl. Phys. A, 210(1):157, 1973.

[62] B. D. Esry and C. H. Greene. Validity of the shape-independent approximation for Bose-Einstein condensates. Phys. Rev. A, 60(2):1451–1462, 1999.

[63] B. D. Esry, C. H. Greene, and J. P. Burke Jr. Recombination of Three Atoms in the Ultracold Limit. Phys. Rev. Lett., 83(9):1751–1754, 1999.

[64] B. D. Esry, C. H. Greene, Y. Zhou, and C. D. Lin. Role of the scattering length in three-boson dynamics and Bose-Einstein condensation. J. Phys. B, 29(2):L51–L57, 1996.

[65] B. D. Esry, C. D. Lin, and C. H. Greene. Adiabatic hyperspherical study of the helium trimer. Phys. Rev. A, 54(1):394–401, 1996.

[66] B.D. Esry. Many-Boson Effects in Bose-Einsten Condensates of Dilute Atomic Gases. PhD thesis, University of Colorado at Boulder, 1997.

[67] B.D. Esry and C.H. Greene. Quantum physics: A ménage à trois laid bare. Nature, 440:289–290, 2006.

[68] L. D. Faddeev. Mathematical Aspects of the Three-Body Problem in Quantum Scattering Theory (Davey, New York, 1965). Zh. Eksp. Teor. Fiz, 39:1459, 1960.

[69] U. Fano. Sullo spettro di assorbimento dei gas nobili presso il limite dello spettro darco. Nuovo Cimento, 12:154–161, 1935.

[70] U. Fano. Effects of Configuration Interaction on Intensities and Phase Shifts. Phys. Rev., 124(6):1866–1878, 1961.

[71] D. V. Fedorov and A. S. Jensen. Efimov effect in coordinate space Faddeev equations. Phys. Rev. Lett., 71(25):4103–4106, 1993.

[72] E. Fermi. Sopra lo spostamento per pressione delle righe elevate delle serie spettrali. Nuovo Cimento, 11:157, 1934.

[73] E. Fermi. Sul moto dei neutroni nelle sostanze idrogenate. Ric. Sci., 7(2):13–52, 1936.

[74] H. Feshbach. A Unified Theory of Nuclear Reactions. II. Ann. Phys. (N.Y.), 19:287, 1962.

[75] M. E. Gehm, S. L. Hemmer, S. R. Granade, K. M. OHara, and J. E. Thomas. Mechanical stability of a strongly interacting Fermi gas of atoms. Phys. Rev. A, 68(1):11401, 2003.

[76] S. Giorgini, L. P. Pitaevskii, and S. Stringari. Theory of ultracold Fermi gases. cond-mat/0706.3360, 2007.

[77] K. Goral, T. Koehler, S. A. Gardiner, E. Tiesinga, and P. S. Julienne. Adiabatic association of ultracold molecules via magnetic-field tunable interactions. J. Phys. B, 37(17):3457–3500, 2004.

[78] C. H. Greene. Interpretation of Feshbach resonances in H-photodetachment. J. Phys. B, 13(2):L39–L44, 1980.

[79] C. H. Greene, U. Fano, and G. Strinati. General form of the quantum-defect theory. Phys. Rev. A, 19(4):1485–1509, 1979.

[80] C. H. Greene, A. R. P. Rau, and U. Fano. General form of the quantum-defect theory. II. Phys. Rev. A, 26(5):2441–2459, 1982.

[81] M. Greiner, O. Mandel, T. Esslinger, T. W. Hänsch, and I. Bloch. Quantum phase transition from a superfluid to a Mott insulator in a gas of ultracold atoms. Nature, 415:39–44, 2002.

[82] M. Greiner, C. A. Regal, and D. S. Jin. Emergence of a molecular Bose-Einstein condensate from a Fermi gas. Nature, 426(6966):537–540, 2003.

[83] H. W. Hammer and L. Platter. Universal properties of the four-body system with large scattering length. Eur. Phys. J. A, 32(1):113–120, 2007.

[84] B. L. Hammond, W. A. Lester, Jr., and P. J. Reynolds. Monte Carlo Methods in Ab Initio Quantum Chemistry. World Scientific, Singapore, 1994.

[85] H. Heiselberg. Fermi systems with long scattering lengths. Phys. Rev. A, 63(4):43606, 2001.

[86] H. Heiselberg. Pairing of fermions in atomic traps and nuclei. Phys. Rev. A, 68(5):53616, 2003.

[87] H. Heiselberg. Sound modes at the BCS-BEC crossover. Phys. Rev. A, 73(1):13607, 2006.

[88] M. Hesse, A. T. Le, and C. D. Lin. Protonium formation in the collision at low energies by a diabatic approach. Phys. Rev. A, 69(5):052712, 2004.

[89] T.-L. Ho. Universal thermodynamics of degenerate quantum gases in the unitary limit. Phys. Rev. Lett., 92:090402, 2004.

[90] E. Hodby, S. T. Thompson, C. A. Regal, M. Greiner, A. C. Wilson, D. S. Jin, E. A. Cornell, and C. E. Wieman. Production Efficiency of Ultracold Feshbach Molecules in Bosonic and Fermionic Systems. Phys. Rev. Lett., 94(12):120402, 2005.

[91] M. Houbiers, R. Ferwerda, H. T. C Stoof, W. I. McAlexander, C. A. Sackett, and R. G. Hulet. Superfluid state of atomic ^{6}Li in a magnetic trap. Phys. Rev. A, 56(6):4864–4878, 1997.

[92] H. Hu, X. J. Liu, and P. D. Drummond. Equation of state of a superfluid Fermi gas in the BCS-BEC crossover. Europhys. Lett., 74(4):574, 2006.

[93] Hui Hu, A. Minguzzi, Xia-Ji Liu, and M. P. Tosi. Collective modes and ballistic expansion of a fermi gas in the bcs-bec crossover. Phys. Rev. Lett., 93(19):190403, 2004.

[94] K. Huang and C. N. Yang. Phys. Rev., 105:767, 1957.

[95] K. Huang and C. N. Yang. Quantum-mechanical many-body problem with hard-sphere interaction. Phys. Rev., 105:767, 1957.

[96] S. Inouye, M. R. Andrews, J. Stenger, H. J. Miesner, D. M. Stamper-Kurn, and W. Ketterle. Observation of Feshbach resonances in a Bose–Einstein condensate. Nature, 392:151–154, 1998.

[97] R. Jáuregui, R. Paredes, and G. Toledo Sánchez. BEC-BCS crossover of a trapped Fermi gas without using the local density approximation. Phys. Rev. A, 76(1):011604, 2007.

[98] J. Javanainen, M. Koštrun, M. Mackie, and A. Carmichael. Simple Mean-Field Theory for a Zero-Temperature Fermionic Gas at a Feshbach Resonance. Phys. Rev. Lett., 95(11):110408, 2005.

[99] S. Jochim, M. Bartenstein, A. Altmeyer, G. Hendl, S. Riedl, C. Chin, J. Hecker Denschlag, and R. Grimm. Bose-Einstein Condensation of Molecules. Science, 302(5653):2101–2104, 2003.

[100] Ryan M. Kalas and D. Blume. Equation of state of cold atoms: A lowest-order-constrained variational study of systems with large non-s-wave scattering lengths. Phys. Rev. A, 76(1):013617, 2007.

[101] M. H. Kalos, D. Levesque, and L. Verlet. Helium at zero temperature with hard-sphere and other forces. Phys. Rev. A, 9(5):2178–2195, 1974.

[102] O. I. Kartavtsev and A. V. Malykh. Low-energy three-body dynamics in binary quantum gases. J. Phys. B, 40(7):1429, 2007.

[103] J. P. Kestner and L.-M. Duan. Level crossing in the three-body problem for strongly interacting fermions in a harmonic trap. Phys. Rev. A, 76(3):033611, 2007.

[104] J. Kinast, S. L. Hemmer, M. E. Gehm, A. Turlapov, and J. E. Thomas. Evidence for Superfluidity in a Resonantly Interacting Fermi Gas. Phys. Rev. Lett., 92(15):150402, 2004.

[105] J. Kinast, A. Turlapov, J. E. Thomas, Q. Chen, J. Stajic, and K. Levin. Heat Capacity of a Strongly Interacting Fermi Gas. Science, 307(5713):1296, 2005.

[106] T. Köhler, K. Góral, and P. S. Julienne. Production of cold molecules via magnetically tunable Feshbach resonances. Rev. Mod. Phys., 78(4):1311–1361, 2006.

[107] S. Kokkelmans and M. J. Holland. Ramsey Fringes in a Bose-Einstein Condensate between Atoms and Molecules. Phys. Rev. Lett., 89(18):180401, 2002.

[108] S. Kokkelmans, G. V. Shlyapnikov, and C. Salomon. Degenerate atom-molecule mixture in a cold Fermi gas. Phys. Rev. A, 69(3):31602, 2004.

[109] T. Kraemer, M. Mark, P. Waldburger, J. G. Danzl, C. Chin, B. Engeser, A. D. Lange, K. Pilch, A. Jaakkola, H. C. Naegerl, et al. Evidence for Efimov quantum states in an ultracold gas of caesium atoms. Nature, 440(7082):315–318, 2006.

[110] V. I. Kukulin and VM Krasnopol'sky. A stochastic variational method for few-body systems. J. Phys. G, 3(6):795–811, 1977.

[111] Y. Kwon, D. M. Ceperley, and R.M. Martin. Quantum Monte Carlo calculation of the Fermi-liquid parameters in the two-dimensional electron gas. Phys. Rev. B, 50(3):1684–1694, 1994.

[112] L. D. Landau and V. L. Ginzburg. On the theory of superconductivity. Zh. Eksp. Teor. Fiz, 20(1064):546–68, 1950.

[113] A. J. Leggett. in "Modern Trends in the Theory of Condensed Matter", ed. by A. Pekalski J. Przystawa, Springer, Berlin, 1980.

[114] G. P. Lepage. How to Renormalize the Schroedinger Equation. Arxiv preprint nucl-th/9706029, 1997.

[115] J. Levinsen and V. Gurarie. Properties of strongly paired fermionic condensates. Phys. Rev. A, 73(5):53607, 2006.

[116] C. D. Lin. Hyperspherical coordinate approach to atomic and other coulombic three-body systems. Phys. Rep., 257(1):1–83, 1995.

[117] G.-D. Lin, W. Yi, and L.-M. Duan. Superfluid shells for trapped fermions with mass and population imbalance. Phys. Rev. A, 74(3):031604(R), 2006.

[118] C. Lobo, I. Carusotto, S. Giorgini, A. Recati, and S. Stringari. Pair Correlations of an Expanding Superfluid Fermi Gas. Phys. Rev. Lett., 97(10), 2006.

[119] J. Macek. Properties of autoionizing states of He. J. Phys. B, 1:831, 1968.

[120] J. Macek. Loosely bound states of three particles. Z. Phys. D, 3(1):31, 1986.

[121] R. A. Malfliet and J. A. Tjon. Solution of the Faddeev Equations for the Triton Problem using Local Two-Body Interactions. Nucl. Phys. A, 127:161, 1969.

[122] B. Marcelis, S. J. J. M. F. Kokkelmans, G. V. Shlyapnikov, and D. S. Petrov. Collisional properties of weakly bound heteronuclear dimers. Phys. Rev. A, 77(3):032707, 2008.

[123] M. Marini, F. Pistolesi, and G. C. Strinati. Evolution from BCS superconductivity to Bose condensation: analytic results for the crossover in three dimensions. Eur. Phys. J. B, 1(2):151–159, 1998.

[124] N. P. Mehta, S. T. Rittenhouse, J. P. D'Incao, and C. H. Greene. Hyperspherical approach to the four-body problem. Arxiv preprint arXiv:0706.1296, 2007.

[125] N. Metropolis, A. W. Rosenbluth, M. N. Rosenbluth, A. H. Teller, and E. Teller. Equation of state calculations by fast computing machines. J. Chem. Phys, 21(6):1087–1092, 1953.

[126] N. Metropolis and S. Ulam. The Monte Carlo Method. J. Amer. Stat. Assoc., 44(247):335–341, 1949.

[127] E. Nielsen, D. V. Fedorov, A. S. Jensen, and E. Garrido. The three-body problem with short-range interactions. Phys. Rep., 347(5):373–459, 2001.

[128] Y. Nishida and D. T. Son. Epsilon Expansion for a Fermi Gas at Infinite Scattering Length. Phys. Rev. Lett., 97(5):50403, 2006.

[129] P. Nozières and S. Schmitt-Rink. Bose condensation in an attractive fermion gas: From weak to strong coupling superconductivity. J. Low Temp. Phys., 59(3):195–211, 1985.

[130] K. M. O'Hara, S. L. Hemmer, M. E. Gehm, S. R. Granade, and J. E. Thomas. Observation of a Strongly Interacting Degenerate Fermi Gas of Atoms. Science, 298(5601):2179, 2002.

[131] Y. Ohashi and A. Griffin. BCS-BEC Crossover in a Gas of Fermi Atoms with a Feshbach Resonance. Phys. Rev. Lett., 89(13):130402, 2002.

[132] H. K. Onnes. The resistance of pure mercury at helium temperatures. Comm. Phys. Lab. Univ. Leiden, pages 3–5, 1911.

[133] R. T. Pack and G. A. Parker. Quantum reactive scattering in three dimensions using hyperspherical (APH) coordinates. Theory. J. Chem. Phys., 87:3888, 1987.

[134] G. B. Partridge, W. Li, R. I. Kamar, Y. Liao, and R. G. Hulet. Pairing and Phase Separation in a Polarized Fermi Gas. Science, 311(5760):503–505, 2006.

[135] G. B. Partridge, K. E. Strecker, R. I. Kamar, M. W. Jack, and R. G. Hulet. Molecular Probe of Pairing in the BEC-BCS Crossover. Phys. Rev. Lett., 95(2):20404, 2005.

[136] E. Pazy, I. Tikhonenkov, Y. B. Band, M. Fleischhauer, and A. Vardi. Nonlinear Adiabatic Passage from Fermion Atoms to Boson Molecules. Phys. Rev. Lett., 95(17):170403, 2005.

[137] A. Perali, P. Pieri, and G. C. Strinati. Quantitative Comparison between Theoretical Predictions and Experimental Results for the BCS-BEC Crossover. Phys. Rev. Lett., 93(10):100404, 2004.

[138] D. S. Petrov. Three-body problem in Fermi gases with short-range interparticle interaction. Phys. Rev. A, 67(1):10703, 2003.

[139] D. S. Petrov, C. Salomon, and G. V. Shlyapnikov. Weakly Bound Dimers of Fermionic Atoms. Phys. Rev. Lett., 93(9):90404, 2004.

[140] D. S. Petrov, C. Salomon, and G. V. Shlyapnikov. Diatomic molecules in ultracold fermi gases- novel composite bosons. J. Phys. B, 38:S645, 2005.

[141] D. S. Petrov, C. Salomon, and G. V. Shlyapnikov. Scattering properties of weakly bound dimers of fermionic atoms. Physical Review A, 71(1):12708, 2005.

[142] L. Platter, H.W. Hammer, and U.G. Meißner. Four-boson system with short-range interactions. Phys. Rev. A, 70(5):52101, 2004.

[143] C. Regal and D. S. Jin. Experimental realization of BCS-BEC crossover physics with a Fermi gas of atoms. Arxiv preprint cond-mat/0601054, 2006.

[144] C. A. Regal, M. Greiner, and D. S. Jin. Observation of Resonance Condensation of Fermionic Atom Pairs. Phys. Rev. Lett., 92(4):40403, 2004.

[145] C. A. Regal, C. Ticknor, J. L. Bohn, and D. S. Jin. Creation of ultracold molecules from a Fermi gas of atoms. Nature, 424(6944):47–50, 2003.

[146] P. J. Reynolds, D. M. Ceperley, B. J. Alder, W. A. Lester Jr, et al. Fixed-node quantum Monte Carlo for molecules. J. Chem. Phys., 77:5593, 1982.

[147] P. Ring and P. Schuck. The Nuclear Many-Body Problem. Springer, New York, 1980.

[148] S. T. Rittenhouse, M. J. Cavagnero, J. von Stecher, and C. H. Greene. A Hyperspherical Variational Approach to the N-Fermion Problem. Few Body Syst., 38(2):85–90, 2006.

[149] S. T. Rittenhouse, M. J. Cavagnero, J. von Stecher, and C. H. Greene. Collective Behavior of the Closed-Shell Fermi Gas. Phys. Rev. A, 74:053624, 2006.

[150] S. T. Rittenhouse and C. H. Greene. The degenerate Fermi gas with renormalized density-dependent interactions in the K harmonic approximation. cond-mat/0702161, 2007.

[151] J. L. Roberts, N. R. Claussen, S. L. Cornish, E. A. Donley, E. A. Cornell, and C. E. Wieman. Controlled collapse of a bose-einstein condensate. Phys. Rev. Lett., 86(19):4211–4214, May 2001.

[152] M. W. J. Romans and H. T. C. Stoof. Bogoliubov theory of Feshbach molecules in the BEC-BCS crossover. Phys. Rev. A, 74(5), 2006.

[153] R. Roth and H. Feldmeier. Effective s-and p-wave contact interactions in trapped degenerate Fermi gases. Phys. Rev. A, 64(4):43603, 2001.

[154] G. Rupak. Dimer scattering in the epsilon expansion. Arxiv preprint nucl-th/0605074, 2006.

[155] C. A. R. Sá de Melo, M. Randeria, and J. R. Engelbrecht. Crossover from BCS to Bose superconductivity: Transition temperature and time-dependent Ginzburg-Landau theory. Phys. Rev. Lett., 71(19):3202–3205, 1993.

[156] D. E. Sheehy and L. Radzihovsky. BEC-BCS Crossover in Magnetized Feshbach-Resonantly Paired Superfluids. Phys. Rev. Lett., 96(6):60401, 2006.

[157] K. Singer. The Use of Gaussian (Exponential Quadratic) Wave Functions in Molecular Problems. I. General Formulae for the Evaluation of Integrals. Proc. R. Soc. London, Ser. A, 258(1294):412, 1960.

[158] G. V. Skorniakov and K. A. Ter-Martirosian. Three body problem for short range forces 1. Scattering of low energy neutrons by deuterons. Zh. Eksp. Teor. Fiz., 31:775, 1956 [Sov. Phys. JETP **4**, 648 (1957)].

[159] Y. F. Smirnov and K. V. Shitikova. Method of K harmonics and the shell model. Sov. J. Part. Nucl., 8:44, 1977.

[160] T. D. Son. Three comments on the Fermi gas at unitarity in a harmonic trap. cond-mat/0707.1851, 2007.

[161] H. H. Sørensen. Correlations in many-body systems with the Stochastic Variational Method. Arxiv preprint cond-mat/0502126 (Master Thesis), 2005.

[162] H. H. Sørensen, D. V. Fedorov, and A. S. Jensen. Correlated Gaussian method for dilute bosonic systems. Workshop on Nuclei and Mesoscopic Physics: WNMP 2004. AIP Conference Proceedings,, 777:12–20, 2005.

[163] O. Sørensen, D. V. Fedorov, and A. S. Jensen. Correlated Trapped Bosons and the Many-Body Efimov Effect. Phys. Rev. Lett., 89(17):173002, 2002.

[164] O. Sørensen, D. V. Fedorov, and A. S. Jensen. Two-body correlations in N-body boson systems. Phys. Rev. A, 66(3):32507, 2002.

[165] J. Stajic, J. N. Milstein, Q. Chen, M. L. Chiofalo, M. J. Holland, and K. Levin. Nature of superfluidity in ultracold Fermi gases near Feshbach resonances. Phys. Rev. A, 69(6):63610, 2004.

[166] I. Stetcu, B. R. Barrett, U. van Kolck, and J. P. Vary. Effective theory for trapped few-fermion systems. Phys. Rev. A, 76(6):063613, 2007.

[167] J. T. Stewart, J. P. Gaebler, C. A. Regal, and D. S. Jin. Potential energy of a [sup 40]k fermi gas in the bcs-bec crossover. Phys. Rev. Lett., 97(22):220406, 2006.

[168] T. Stöferle, H. Moritz, K. Günter, M. Köhl, and T. Esslinger. Molecules of Fermionic Atoms in an Optical Lattice. Phys. Rev. Lett., 96(3):30401, 2006.

[169] H. T. C. Stoof, M. Houbiers, C. A. Sackett, and R. G. Hulet. Superfluidity of Spin-Polarized ^{6}Li. Phys. Rev. Lett., 76(1):10–13, 1996.

[170] K. E. Strecker, G. B. Partridge, and R. G. Hulet. Conversion of an Atomic Fermi Gas to a Long-Lived Molecular Bose Gas. Phys. Rev. Lett., 91(8):80406, 2003.

[171] S. Stringari. Collective excitations of a trapped bose-condensed gas. Phys. Rev. Lett., 77(12):2360–2363, Sep 1996.

[172] H. Suno, B. D. Esry, C. H. Greene, and J. P. Burke Jr. Three-body recombination of cold helium atoms. Phys. Rev. A, 65(4):42725, 2002.

[173] Y. Suzuki and K. Varga. Stochastic Variational Approach to Quantum-Mechanical Few-Body Problems. Springer-Verlag, Berlin, 1998.

[174] S. Tan. Short Range Scaling Laws of Quantum Gases With Contact Interactions. Arxiv preprint cond-mat/0412764, 2004.

[175] J. E. Thomas, J. Kinast, and A. Turlapov. Virial theorem and universality in a unitary fermi gas. Phys. Rev. Lett., 95:120402, 2005.

[176] L. H. Thomas. The Interaction Between a Neutron and a Proton and the Structure of H^3. Phys. Rev., 47(12):903–909, 1935.

[177] A. G. Truscott, K. E. Strecker, W. I. McAlexander, G. B. Partridge, and R. G. Hulet. Observation of Fermi Pressure in a Gas of Trapped Atoms. Science, 291(5513):2570–2572, 2001.

[178] K. Varga and Y. Suzuki. Precise solution of few-body problems with the stochastic variational method on a correlated Gaussian basis. Phys. Rev. C, 52(6):2885–2905, 1995.

[179] K. Varga and Y. Suzuki. Stochastic variational method with a correlated Gaussian basis. Phys. Rev. A, 53(3):1907–1910, 1996.

[180] K. Varga and Y. Suzuki. Solution of few-body problems with the stochastic variational method I. Central forces with zero orbital momentum. Comp. Phys. Comm., 106(1-2):157–168, 1997.

[181] K. Varga, Y. Suzuki, and R. G. Lovas. Microscopic multicluster description of neutron-halo nuclei with a stochastic variational method. Nucl. Phys. A, 571(3):447–466, 1994.

[182] J. von Stecher and C. H. Greene. Spectrum and Dynamics of the BCS-BEC Crossover from a Few-Body Perspective. Phys. Rev. Lett., 99(9):090402, 2007.

[183] J. von Stecher and C.H. Greene. Renormalized mean-field theory for a two-component Fermi gas with s-wave interactions. Phys. Rev. A, 75(2):22716, 2007.

[184] J. von Stecher, Chris H. Greene, and D. Blume. BEC-BCS crossover of a trapped two-component Fermi gas with unequal masses. Phys. Rev. A, 76(5):053613, 2007.

[185] J. von Stecher, Chris H. Greene, and D. Blume. Energetics and structural properties of trapped two-component Fermi gases. Phys. Rev. A, 77(4):043619, 2008.

[186] F. Werner and Y. Castin. Unitarity gas in an isotropic harmonic trap: Symmetry properties and applications. Phys. Rev. A, 74:053604, 2006.

[187] F. Werner and Y. Castin. Unitary Quantum Three-Body Problem in a Harmonic Trap. Phys. Rev. Lett., 97(15):150401, 2006.

[188] P. A. Whitlock, D. M. Ceperley, G. V. Chester, and M. H. Kalos. Properties of liquid and solid^{4} He. Phys. Rev. B, 19(11):5598–5633, 1979.

[189] J. E. Williams, N. Nygaard, and C. W. Clark. Theory of Feshbach molecule formation in a dilute gas during a magnetic field ramp. New J. Phys., 8:150, 2006.

[190] O. A. Yakubovsky. Yad. Fiz., 5:1312, 1967 [Sov. J. Nucl. Phys. 5 937 (1967)].

[191] Z. Zhen and J. Macek. Loosely bound states of three particles. Phys. Rev. A, 38(3):1193–1201, 1988.

[192] Y. Zhou, C. D. Lin, and J. Shertzer. Hyperspherical approach to Coulombic three-body systems with different masses. J. Phys. B, 26:3937–3949, 1993.

[193] M. W. Zwierlein, J. R. Abo-Shaeer, A. Schirotzek, C. H. Schunck, and W. Ketterle. Vortices and superfluidity in a strongly interacting Fermi gas. Nature, 435:1047–1051, 2005.

[194] M. W. Zwierlein, C. A. Stan, C. H. Schunck, S. M. F Raupach, S. Gupta, Z. Hadzibabic, and W. Ketterle. Observation of Bose-Einstein Condensation of Molecules. Phys. Rev. Lett., 91(25):250401, 2003.

[195] M. W. Zwierlein, C. A. Stan, C. H. Schunck, S. M. F. Raupach, A. J. Kerman, and W. Ketterle. Condensation of Pairs of Fermionic Atoms near a Feshbach Resonance. Phys. Rev. Lett., 92(12):120403, 2004.

Appendix A

Symmetrization of the basis functions and evaluation of the matrix elements

The CG basis functions take the form

$$\Phi_A(\mathbf{x}_1, \mathbf{x}_2, ..., \mathbf{x}_N) = \mathcal{S}\left\{\exp(-\frac{1}{2}\mathbf{x}^T.A.\mathbf{x})\right\}. \tag{A.1}$$

The symmetrization operator $\mathcal{S}$ can be expanded in a set of simple particle permutations,

$$|\mathcal{S}(A)\rangle = \sum_{i=1}^{N_p} \mathrm{sgn}(P_i)\,|P_i(A)\rangle\,. \tag{A.2}$$

Here, N_p is the number of permutations that characterize the symmetry $\mathcal{S}$. Each of these permutations, P_i, has a sign associated, $\mathrm{sgn}(P_i)$, and is a given rearrangement of the spatial coordinates

$$P_i(\Phi_A(\mathbf{x}_1, ..., \mathbf{x}_N) = \Phi_A(\mathbf{x}_{P_i(1)}, ..., \mathbf{x}_{P_i(N)}) \tag{A.3}$$

The label i characterizes the rearrangement. This rearrangement of the spatial coordinates is equivalent to a rearrangement of the interparticle widths $\{d_{ij}\}$ (or the $\{\alpha_{ij}\}$),

$$P_k(\{d_{ij}\}) = \{d_{P_k(ij)}\}. \tag{A.4}$$

Therefore, permutation operations can be easily applied and become transformations of the matrix A.

In general the evaluation of the symmetrized matrix elements of an operator O is,

$$\langle\mathcal{S}(A)|O|\mathcal{S}(B)\rangle = \sum_{i=1}^{N_p}\sum_{i'=1}^{N_p} \mathrm{sgn}(P_i)\mathrm{sgn}(P_{i'})\,\langle P_{i'}(A)|O|P_i(A)\rangle\,, \tag{A.5}$$

which implies an N_p^2 evaluation of unsymmetrized matrix elements. Fortunately, if $\mathcal{S}(O) = O$ then,

$$\langle \mathcal{S}(A)|O|\mathcal{S}(B)\rangle = N_p \langle A|O|\mathcal{S}(B)\rangle = N_p \langle \mathcal{S}(A)|O|B\rangle . \tag{A.6}$$

This property significantly reduces the numerical demands since the left hand side of Eq.(A.6) implies N_p^2 permutations, while the right-hand side only implies N_p permutations. All operators of the Hamiltonian are invariant under the $\mathcal{S}$, operator and their matrix elements obey Eq.(A.6).

To obtain density profiles and pair-correlation functions, we use the delta function operator. A single delta function operator in a given coordinate is not invariant under this transformation; for this reason, the computational evaluation is more expensive. Alternatively, we can create a similar operator as a sum of delta functions. If the sum of delta functions reflects the symmetry of the problem, the this new operator would be invariant under $\mathcal{S}$.

The permutation operator clearly depends on the problem under consideration. In this work, we consider bosons and two-component fermions. For identical bosons and fermions,

$$\mathcal{S} = \sum_{i=1}^{N_p} \alpha_i P_i, \tag{A.7}$$

where $N_p = N!$ and $\alpha_i = 1$ for bosons and $\alpha_i = (-1)^p$; $p = 0, 1$ is the parity of the operator P_i. For two-component systems (boson-boson, fermion-fermion, or a Bose-Fermi mixture),

$$\mathcal{S} = \sum_{i_1=1}^{N_{p_1}} \sum_{i_2=1}^{N_{p_2}} \alpha_{i_1}\alpha_{i_2} P_{i_1} P_{i_2}, \tag{A.8}$$

where $N_{p_1} = N_1!$, $N_{p_2} = N_2!$, and N_1 and N_2 are the number of particles in component 1 and 2, respectively.

The symmetrization operation, if it involves a permutation with a negative sign, can significantly reduce the accuracy of matrix elements. In certain cases, the unsymmetrized matrix elements can be almost identical. Because of the negative sign

of the permutation, the symmetrized matrix elements can become a subtraction of very similar numbers. Therefore, accuracy is reduced. These basis functions are usually unphysical, so it is convenient to eliminate them. To do this, we evaluate $|\langle \mathcal{S}(A)|\mathcal{S}(A)\rangle|/\max(|\langle P_i(A)|P_i(A)\rangle|)$. If this is a small number, then the accuracy of the matrix elements is reduced. So, in general, we introduce a tolerance of the order of 10^{-3} to determine whether to keep or discard the basis functions.

Appendix B

Evaluation of unsymmetrized basis functions

For convenience, we introduce the following simplify notation,

$$|A\rangle = \exp(-\frac{1}{2}\mathbf{x}^T.A.\mathbf{x}). \tag{B.1}$$

As a simple example, consider the overlap matrix element

$$\langle A|B\rangle = \int d\mathbf{x}_1..d\mathbf{x}_N \exp(-\frac{1}{2}\mathbf{x}^T.(A+B).\mathbf{x}). \tag{B.2}$$

Since the matrix $A+B$ is real and symmetric, there exists a set of eigenvectors $\mathbf{y} = \{\mathbf{y}_1, ..., \mathbf{y}_N\}$ with eigenvalues $\{\beta_1, ..., \beta_N\}$ that diagonalize the matrix. In this set of coordinates, Eq. (B.2) takes the simple form,

$$\langle A|B\rangle = (4\pi)^N \int_0^\infty dy_1 y_1^2 e^{-\beta_1 y_1^2/2} ... \int_0^\infty dy_N y_N^2 e^{-\beta_N y_N^2/2} = \left(\frac{(2\pi)^N}{\det(A+B)}\right)^{3/2}. \tag{B.3}$$

Here, we used the product $\beta_1.\beta_2...\beta_N = \det(A+B)$. These basics steps can be followed to evaluate the remaining matrix elements.

To evaluate the kinetic energy, we use the following property,

$$\langle A| - \frac{\hbar^2}{2m}\nabla^2_{\mathbf{x}_i}|B\rangle = \frac{\hbar^2}{2m}\langle \nabla_{\mathbf{x}_i} A|\nabla_{\mathbf{x}_i} B\rangle . \tag{B.4}$$

This property can be simply proven by applying an integration by parts. Also, it simplifies the matrix element evaluation and provides an expression which is symmetric in A and B. Then, the matrix element takes the form,

$$\langle A| - \frac{\hbar^2}{2m}\sum_i^N \nabla^2_{\mathbf{x}_i}|B\rangle = \frac{\hbar 2}{2m} 3\,\mathrm{Tr}((A+B)^{-1}A.B)\,\langle A|B\rangle \tag{B.5}$$

Another important matrix element, which is similar to Eq.(B.5), is

$$\langle A|\mathbf{x}^T C\mathbf{x}|B\rangle = \frac{\hbar^2}{2m} 3\,\mathrm{Tr}((A+B)^{-1}C)\,\langle A|B\rangle\,. \tag{B.6}$$

Here, C is an arbitrary matrix. This matrix element is used to calculate the trapping potential energy. In such case, $C = m\omega^2 I/2$, where I is the identity matrix.

Finally, we calculate the matrix element for a two-body central force:

$$\langle A|V(\mathbf{r}_i - \mathbf{r}_j)|B\rangle = \int d^3r V(\mathbf{r})\,\langle A|\delta(b_{ij}^T\mathbf{x} - r)|B\rangle = G_{c_{ij}}[V]\,\langle A|B\rangle\,, \tag{B.7}$$

where $\mathbf{r}_i - \mathbf{r}_j = b_{ij}^T\mathbf{x}$, $c_{ij}^1 = b_{ij}^T(A+B)^{-1}b_{ij}$, and $G_c[V]$ is the Gaussian transform of the potential

$$G_c[V] = \left(\frac{c}{2\pi}\right)^{3/2} \int d^3r V(\mathbf{r}) e^{-cr^2/2}. \tag{B.8}$$

These matrix elements are enough to describe few-body systems.

Appendix C

Jacobi vectors and CG matrices

In this Appendix, we present the construction of the matrices that characterize the basis functions in terms of the widths d_{ij}. In the following $\mathbf{r} = \{\mathbf{r}_1, ..., \mathbf{r}_N\}$ correspond to Cartesian coordinates, while $\boldsymbol{\rho} = \{\boldsymbol{\rho}_1, ..., \boldsymbol{\rho}_{N-1}\}$ correspond to mass-scaled Jacobi coordinates. First, consider the basis function with the center of mass included

$$|A\rangle = \Psi_0(R_{CM}) \exp\left(-\sum_{j\geq i} \frac{(\mathbf{r}_1 - \mathbf{r}_2)^2}{2d_{ij}^2}\right) = \exp(-\frac{1}{2}\mathbf{r}^T.A.\mathbf{r}). \tag{C.1}$$

In the equal-mass case for N particles, it is more convenient to simply use Cartesian coordinates. The ground-state–center-of-mass wave function of particles in a harmonic trap takes, conveniently, a Gaussian form $\Psi_0(R_{CM}) = e^{-NR_{CM}^2/2a_{ho}^2}$. Thus, $\Psi_0(R_{CM})$ can be written as $\Psi_0(R_{CM}) = e^{-\mathbf{r}^T.M^{CM}.\mathbf{r}/2}$, where M^{CM} is the center-of-mass matrix whose matrix elements are $M_{kl}^{CM} = 1/(Na_{ho}^2)$ for all k and l. Then, for each interparticle distance r_{ij}, there exists a matrix $M^{(ij)}$ so that $r_{ij}^2 = \mathbf{r}^T.M^{(ij)}.\mathbf{r}$. The matrix elements of the $M^{(ij)}$ matrices are $M_{ii}^{(ij)} = M_{jj}^{(ij)} = 1$, $M_{ij}^{(ij)} = M_{ji}^{(ij)} = -1$; the rest are zero, yielding

$$A = M^{CM} + \sum_{j\geq i} \frac{1}{d_{ij}^2} M^{(ij)}. \tag{C.2}$$

In some cases it is important to include the center-of-mass motion. For example, this allows one to extract single-particle observables such as density profiles.

If the center of mass is not included, then Eq. (C.2) can be written as,

$$A = \sum_{j>i} \frac{1}{d_{ij}^2} M^{(ij)}. \tag{C.3}$$

In the next subsections we present the mass-scaled Jacobi vectors (see Fig. C.1) and the corresponding form of the matrices $M^{(ij)}$.

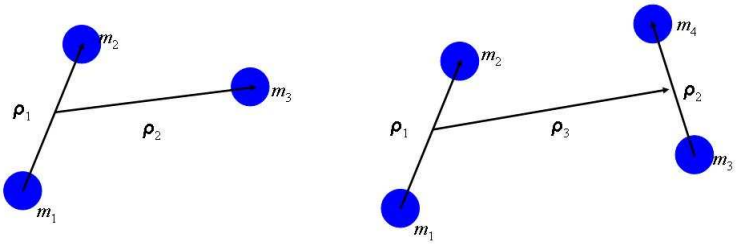

Figure C.1: Mass-scaled Jacobi vector for three and four particles.

C.1 Mass-scaled Jacobi vectors for three particles

A three-particle system can be described by the set of vectors [52]

$$\boldsymbol{\rho}_1 = (\mathbf{r}_1 - \mathbf{r}_2)/d, \tag{C.4}$$

$$\boldsymbol{\rho}_2 = d\left(\mathbf{r}_3 - \frac{m_1\mathbf{r}_1 + m_2\mathbf{r}_2}{m_1 + m2}\right), \tag{C.5}$$

$$\mathbf{R}_{CM} = \frac{m_1\mathbf{r}_1 + m_2\mathbf{r}_2 + m_3\mathbf{r}_3}{m_1 + m2 + m_3}, \tag{C.6}$$

where

$$\mu = \left(\frac{m_1 m_2 m_3}{m_1 + m_2 + m_3}\right)^{1/2}, \tag{C.7}$$

$$d = \sqrt{\frac{m_3}{\mu}}\left(\frac{m_1 + m_2}{m_1 + m_2 + m_3}\right)^{1/2}. \tag{C.8}$$

In Eq. (C.4) $\boldsymbol{\rho}_1$ and $\boldsymbol{\rho}_2$ are mass-scaled Jacobi vectors and $\mathbf{R}_{CM}$ is the center-of-mass vector.

All the interparticle vectors can be written in terms of the Jacobi vectors $\boldsymbol{\rho}_1$ and $\boldsymbol{\rho}_2$:

$$\mathbf{r}_2 - \mathbf{r}_1 = d\,\boldsymbol{\rho}_1, \tag{C.9}$$

$$\mathbf{r}_3 - \mathbf{r}_1 = \frac{dm_2}{m_1 + m_2}\,\boldsymbol{\rho}_1 + \frac{1}{d}\,\boldsymbol{\rho}_2, \tag{C.10}$$

$$\mathbf{r}_3 - \mathbf{r}_2 = -\frac{dm_2}{m_1 + m_2}\,\boldsymbol{\rho}_1 + \frac{1}{d}\,\boldsymbol{\rho}_2. \tag{C.11}$$

As is presented in the next subsection, all the $M^{(ij)}$ matrices can be obtained from Eqs. (C.9,C.10,C.11).

C.2 Mass-scaled Jacobi vectors for four particles

To present the mass-scaled Jacobi vectors for four particles we introduce the following definitions,

$$\mu = \left(\frac{m_1 m_2 m_3 m_4}{m_1 + m_2 + m_3 + m_4} \right)^{1/3}, \tag{C.12}$$

$$\mu_1 = \frac{m_1 m_2}{m_1 + m_2}, \tag{C.13}$$

$$\mu_2 = \frac{m_3 m_4}{m_3 + m_4}, \tag{C.14}$$

$$\mu_3 = \frac{(m_1 + m_2)(m_3 + m_4)}{m_1 + m_2 + m_3 + m_4}, \tag{C.15}$$

$$d_1 = \sqrt{\mu_1/\mu},\ d_2 = \sqrt{\mu_2/\mu},\ d_3 = \sqrt{\mu_3/\mu}. \tag{C.16}$$

Here, the value of μ is just selected by convention. Actually, μ can be left as an arbitrary mass factor.

This is usually called the H tree for the form of the Jacobi vectors,

$$\boldsymbol{\rho}_1 = d_1(\mathbf{r}_1 - \mathbf{r}_2) \tag{C.17}$$

$$\boldsymbol{\rho}_2 = d_2(\mathbf{r}_3 - \mathbf{r}_4) \tag{C.18}$$

$$\boldsymbol{\rho}_3 = d_3 \left(\frac{m_1 \mathbf{r}_1 + m_2 \mathbf{r}_2}{m_1 + m_2} - \frac{m_3 \mathbf{r}_3 + m_4 \mathbf{r}_4}{m_3 + m_4} \right) \tag{C.19}$$

$$\mathbf{R}_{CM} = \frac{m_1 \mathbf{r}_1 + m_2 \mathbf{r}_2 + m_3 \mathbf{r}_3 + m_4 \mathbf{r}_4}{m_1 + m2 + m_3 + m_4} \tag{C.20}$$

Here, $\boldsymbol{\rho}_1$, $\boldsymbol{\rho}_2$ and $\boldsymbol{\rho}_3$ are the mass-scaled Jacobi vectors and $\mathbf{R}_{CM}$ is the center-of-mass vector

The interparticle distances can be written in terms of transformations of the three

Jacobi vectors:

$$\mathbf{r}_1 - \mathbf{r}_2 = \boldsymbol{\rho}_1/d_1, \tag{C.21}$$

$$\mathbf{r}_1 - \mathbf{r}_3 = \sqrt{\frac{\mu_3}{\mu}}\left(\boldsymbol{\rho}_3 + \frac{\mu_1 d_3}{m_1 d_1}\boldsymbol{\rho}_1 - \frac{\mu_2 d_3}{m_3 d_2}\boldsymbol{\rho}_2\right), \tag{C.22}$$

$$\mathbf{r}_1 - \mathbf{r}_4 = \sqrt{\frac{\mu_3}{\mu}}\left(\boldsymbol{\rho}_3 + \frac{\mu_1 d_3}{m_1 d_1}\boldsymbol{\rho}_1 + \frac{\mu_2 d_3}{m_4 d_2}\boldsymbol{\rho}_2\right), \tag{C.23}$$

$$\mathbf{r}_2 - \mathbf{r}_3 = \sqrt{\frac{\mu_3}{\mu}}\left(\boldsymbol{\rho}_3 - \frac{\mu_1 d_3}{m_2 d_1}\boldsymbol{\rho}_1 + \frac{\mu_2 d_3}{m_3 d_2}\boldsymbol{\rho}_2\right), \tag{C.24}$$

$$\mathbf{r}_2 - \mathbf{r}_4 = \sqrt{\frac{\mu_3}{\mu}}\left(\boldsymbol{\rho}_3 - \frac{\mu_1 d_3}{m_2 d_1}\boldsymbol{\rho}_1 + \frac{\mu_2 d_3}{m_4 d_2}\boldsymbol{\rho}_2\right), \tag{C.25}$$

$$\mathbf{r}_3 - \mathbf{r}_4 = \boldsymbol{\rho}_2/d_2. \tag{C.26}$$

For both the $N = 3$ and $N = 4$ systems, the interparticle distances can be written in terms of the Jacobi vectors

$$\mathbf{r}_i - \mathbf{r}_j = \sum_k c_k^{(ij)} \boldsymbol{\rho}_k. \tag{C.27}$$

Now we can write the matrices $M^{(ij)}$ in these Jacobi vectors that describe an interparticle distance. The matrix elements of these matrices are simply $M_{kl}^{(ij)} = c_k^{(ij)} c_l^{(ij)}$.

Appendix D

Selection of the basis set

There are different strategies for selecting a basis set. If the numbers of dimensions of the system we are studying is not that large, then we can try to generate a large basis set that is complete enough to describe several eigenstates at different interaction strengths.

The Gaussian widths d_{ij} are selected randomly and cover a range of values from d_0 to the trap length a_{ho}. Specifically, the d_{ij} are selected randomly using a Gaussian distribution of range 1 and then scaled to three different distances: d_0, an intermediate distance $\sqrt{d_0 a_{ho}}$, and a_{ho}. These three distances are fixed once the interparticle potential range d_0 is fixed.

The basis set selection depends on the correlation we want to describe. So, the selection process changes depending whether the particles are bosons or fermions. For fermions, when there is no trimer formation, basis functions with more than two particles close together are not important.

For example, the algorithm for the selection of the basis functions for a two-component four-fermion system divides the basis into three parts: the first subbasis generates d_{ij}, which are all of the order of a_{ho}; they are useful for describing weakly interacting states. The second subbasis generates two d_{ij} of the order of d_0 or $\sqrt{d_0 a_{ho}}$ and the rest of the order of a_{ho}; they are useful to describe dimer-dimer states. The third subbasis has one d_{ij} of the order of d_0 or $\sqrt{d_0 a_{ho}}$ and the rest of the order of a_{ho}.

They are useful to describe dimer–two-free-atom states.

Appendix E

Controlling Linear dependence

The CG basis set is over complete. This, and the fact that the basis functions are chosen semi-randomly can introduce linear dependence problems in the basis set. There are several ways to control or eliminate these linear dependence of the basis set.

The first way is to simply eliminate the linear dependence. After wselecting the basis set and evaluating the matrix elements, we reduce the linear dependent basis set to a smaller basis set without linear dependence.

To do this, we first diagonalize the overlap matrix and then eliminate the eigenstates with negative or low eigenvalues. The remaining eigenstates form an orthonormal basis set. Finally, we transform the Hamiltonian to the new orthonormal basis set.

The threshold for the elimination can be selected automatically taking into account the lowest eigenvalue. If the lowest eigenvalue O_1 is small and positive, the tolerance can be selected as, for example, $10^3 O_1$. If O_1 is negative and the magnitude is large, then the basis set has a lot of linear dependence, and it is more convenient to change the initial basis set.

Appendix F

Stochastical variational method

The SVM has been developed in the context of nuclear physics to solve few-body problems [178, 179, 180]. It allows a systematically improvement of the basis set. A detailed discussion of the implementation of the SVM will not be presented here but can be found in Refs. [161, 173]. In the following, we present the main concepts of the SVM.

The SVM is based on the variational nature of the spectrum obtained by a basis set expansion. Consider a basis set of size D with eigenvalues $\{\epsilon_1, ..., \epsilon_D\}$, if we add a new basis function then the new eigenvalues $\{\lambda_1, ..., \lambda_{D+1}\}$ obey $\lambda_1 \leq \epsilon_1 \leq \lambda_2 ... \epsilon_D \leq \lambda_{D+1}$. Here, we assume that both set of eigenvalues are arranged in increasing order. Thus, by adding a new basis, all the D eigenvalues should decrease or remain the same. Therefore, the lower the new eigenvalues are the better the improvement of the basis set. Thus we can test the utility of the added basis function by considering the improvement in the eigenvalues.

In most cases, we are not interested in improving the complete spectrum. To select which states or energies we want to improve, we can construct an appropriate minimization function. This function would depend only on the energies we want to improve and is minimized by the SVM.

In order to optimize the basis set, the SVM utilizes a trial an error procedure. Starting from an initial basis set of size D, several basis functions are selected stochas-

tically and added, one at a time, to the basis set. For each $D+1$ basis set, the new eigenvalues are evaluated. The basis function that produces the best improvement of the selected energies is kept while the remaining basis functions are discarded. The initial basis function is then increased by one and the trial an error procedure is repeated.

If this procedure is continued indefinitely the size of the basis set has become large and the calculations become forbiddingly slow. Therefore, it is convenient to increase the basis up to a reasonable size and then continue the optimization process without increasing the basis size. This optimization can be carried out by a refinement process. Instead of adding a new basis function, we test the importance of the basis functions of the basis set. The trial and error procedure is then applied to each of the functions of the basis set.

For the SVM procedure to be efficient, the evaluation of both the matrix elements and the eigenvalues need to be fast and accurate. It is particularly important to obtain very accurate matrix elements because the improvement due to a single basis function is usually very small and can only be evaluated reliably if the matrix element are very accurate. The matrix element evaluation in the CG and CGHS is both fast and accurate making these methods particularly suitable for SVM optimization.

Also, the evaluation of the eigenvalues can be significantly speeded up in the trial and error procedure. The basis functions are added or replaced one by one which allowing us to reduce the evaluation of the eigenvalues to a root finding procedure. This root finding procedure is much faster than any diagonalization procedure.

The SVM automatically takes care of the selection of the basis function. Also, it tries to avoid linear dependence in the basis set by constraining the normalized overlap between any two basis function, i.e., $O_{12}/\sqrt{O_{11}O_{22}}$, to be below some tolerance O_{max}. The tolerance O_{max} is usually selected between 0.95 and 0.99. For example, the size of the basis set of $N=3$ and 4 can be increased up to 700 and 8000 respectively without introducing significant linear dependence.

Appendix G

CGHS unsymmetrized matrix elements for four particles

The same strategy for evaluating the matrix elements in the $N = 3$ case can be extended to the $N = 4$ system. The $N = 4$ system can be described by three Jacobi vectors, $\mathbf{x} \equiv \{\mathbf{x}_1, \mathbf{x}_2, \mathbf{x}_3\}$, once the center-of-mass motion is decoupled.

To evaluate the overlap matrix element, we change to the coordinate basis set that diagonalizes $A + B$. We call β_1, β_2 and β_3 the eigenvalues and $y \equiv \{\mathbf{y}_1, \mathbf{y}_2, \mathbf{y}_3\}$ are the eigenvectors. In this new coordinate basis set the overlap integrand takes the form

$$B.A = \exp\left(-\frac{\beta_1 y_1^2 + \beta_2 y_2^2 + \beta_3 y_3^2}{2}\right). \tag{G.1}$$

We integrate over the polar angles of $\mathbf{y}_1$, $\mathbf{y}_2$, $\mathbf{y}_3$, obtaining

$$\langle B|A\rangle \Big|_R = \frac{(4\pi)^3}{R^8} \int \exp\left(-\frac{\beta_1 y_1^2 + \beta_2 y_2^2 + \beta_3 y_3^2}{2}\right) y_1^2 y_2^2 y_3^2 dy_1 dy_2 dy_3 \Big|_R. \tag{G.2}$$

To integrate over the remaining hyperangles, we fix the hyperradius such that $y_1 = R\sin\theta\cos\phi$, $y_2 = R\sin\theta\sin(\phi)$ and $y_3 = R\cos\theta$; yielding

$$\langle B|A\rangle \Big|_R = (4\pi)^3 \int \exp\left(-\frac{R^2(\beta_1 \sin^2\theta\cos^2\phi + \beta_2 \sin^2\theta\sin^2\phi + \beta_3\cos^2\theta)}{2}\right) \sin^5\theta\cos^2\theta\cos^2\phi\sin^2\phi d\theta d\phi. \tag{G.3}$$

The integration over one of the angles can be carried out analytically. Introducing a

variable dummy y, the overap matrix element takes the form

$$\langle B|A\rangle\Big|_R = \frac{(4\pi)^3\pi}{2R^2(\beta_1-\beta_2)}\int_0^1 \exp\left(-\frac{R^2}{4}[(\beta_1+\beta_2)(1-y^2)+2\beta_3 y^2]\right) I_1\left[R^2\frac{(\beta_1-\beta_2)(1-y^2)}{4}\right] y^2(1-y^2)dy. \quad \text{(G.4)}$$

Next we calculate the angular kinetic energy. To do this, we calculate the total kinetic energy and the hyperradial kinetic energy. These two matrix elements are not symmetric, but the angular kinetic energy, i.e., the total kinetic energy minus the hyperradial kinetic energy, is symmetric. To obtain an explicitly symmetric operator, we symmetrize the operation $\langle B|\mathcal{T}_\Omega|A\rangle|_R = (\langle B|\mathcal{T}_T-\mathcal{T}_R|A\rangle|_R + \langle A|\mathcal{T}_T-\mathcal{T}_R|B\rangle|_R)/2$ and obtain

$$\langle B|\mathcal{T}_\Omega|A\rangle\Big|_R = \frac{(4\pi)^3}{R^8}\int \exp\left(-\frac{\beta_1 y_1^2+\beta_2 y_2^2+\beta_3 y_3^2}{2}\right) TAF(y_1,y_2,y_3) y_1^2 y_2^2 y_3^2 dy_1 dy_2 dy_3\Big|_R, \quad \text{(G.5)}$$

where

$$TAF(y_1,y_2,y_3) = \frac{1}{2}\left\{\sum_{i=1}^3\left[-3\beta_i+\left(\beta_i^2-2(A.B)_{ii}+\frac{d\beta_i}{R^2}\right)y_i^2\right] - \left(\sum_{i=1}^3\frac{\beta_i y_i^2}{R^2}\right)^2 + \frac{\overline{(\vec{y}.A.\vec{y})(\vec{y}.B.\vec{y})}}{R^2}\right\}. \quad \text{(G.6)}$$

It is easy to show that $(A.B)_{ii} = \sum_{j=1}^3 a_{ij}b_{ij}$ since A and B are symmetric matrices. Here the bar sign indicates the integration over the angular degrees of freedom of $\mathbf{y}_1$, $\mathbf{y}_2$, and $\mathbf{y}_3$. We then divide the total result by $(4\pi)^3$. Making these integrations analytically we obtain

$$\overline{(\vec{y}.A.\vec{y})(\vec{y}.B.\vec{y})} = \sum_{i=1}^3 a_{ii}b_{ii}y_i^4 + \sum_{i>j}^3\left(a_{ii}b_{jj}+b_{ii}a_{jj}+\frac{4}{3}a_{ij}b_{ij}\right)y_i^2y_j^2. \quad \text{(G.7)}$$

Using spherical coordinates for y_1, y_2, and y_3. We observe that one of the integrations in Eq. (G.5) can be done analytically. To simplify the notation, we introduce the following

variables,

$$xx = R^2 \frac{1}{4}(\beta_1 - \beta_2)(-1 + y^2), \tag{G.8}$$

$$c_1 = -9(\beta_1 - \beta_2)^2 - 12(-4a_{12}b_{12} + 3(a_{11} - a_{22})(b_{11} - b_{22})), \tag{G.9}$$

$$c_2 = -6a_{13}b_{13} + 6a_{23}b_{23}, \tag{G.10}$$

$$c_3 = (3\beta_1^2 - 3\beta_2^2 - 6\beta_1\beta_3 + 6\beta_2\beta_3 - 6a_{11}b_{11} + 6a_{33}b_{11}$$

$$+8a_{13}b_{13} + 6a_{22}b_{22} - 6a_{33}b_{22} - 8a_{23}b_{23} + 6a_{11}b_{33} - 6a_{22}b_{33}), \tag{G.11}$$

$$c_4 = (3\beta_2^2 - 6\beta_2\beta_3), \tag{G.12}$$

$$c_5 = (3\beta_1^2 - 6\beta_1\beta_3), \tag{G.13}$$

$$c_6 = 3(2a_{12}b_{12} + a_{13}b_{13} + a_{23}b_{23}), \tag{G.14}$$

$$c_7 = 6a_{12}b_{12}, \tag{G.15}$$

$$c_8 = 3(a_{13}b_{13} + a_{23}b_{23}), \tag{G.16}$$

$$c_9 = (3\beta_3^2 - 3a_{11}b_{11} + 3a_{33}b_{11} + a_{13}b_{13} - 3a_{22}b_{22} +$$

$$3a_{33}b_{22} + a_{23}b_{23} + 3(a_{11} + a_{22} - 2a_{33})b_{33}). \tag{G.17}$$

The final expression for $\mathcal{T}_\Omega$ is

$$\mathcal{T}_\Omega = -\frac{512\pi^4}{3(\beta_1 - \beta_2)^5 R^8} \int_0^1 \frac{1}{(-1+y^2)^3} \exp\left[-\frac{xx\left((\beta_1+\beta_2)(1-y^2) - 2\beta_3 y^2\right)}{(\beta_1-\beta_2)(-1+y^2)}\right]$$

$$xx^2y^2\Big\{2(-1+y^2)\Big[c_1(1-y^2) + 4xx(c_2 + c_3y^2)\Big]I_c[xx]$$

$$+ xx\Big[c_4(-1+y^2)\big(3 - (9-4xx)y^2\big) + c_5(-1+y^2)\big(-3 + (9+4xx)y^2\big)$$

$$+8xx\big(c_6 - c_7y^2 + c_8y^4 - c_9(y^2 - y^4)\big)\Big]I_1(xx)\Big\}\,dy, \tag{G.18}$$

where we defined

$$I_c[xx] = \frac{xx}{2}I_0[xx] - I_1[xx]. \tag{G.19}$$

We still need to evaluate the matrix elements corresponding to the couplings

$$P_{BA}(R) = \langle B|\frac{d}{dR}|A\rangle\Big|_R, \tag{G.20}$$

$$Q_{BA}(R) = \langle\frac{dB}{dR}|\frac{dA}{dR}\rangle\Big|_R. \tag{G.21}$$

Using the standard tricks, we obtain

$$P_{BA}(R) = -\frac{(4\pi)^3}{R^9}\int \exp(-\frac{\beta_1 y_1^2+\beta_2 y_2^2+\beta_3 y_3^2}{2})\overline{\vec{y}.D.\vec{y}}\, y_1^2 y_2^2 y_3^2 dy_1 dy_2 dy_3 \tag{G.22}$$

$$Q_{BA}(R) = \frac{(4\pi)^3}{R^{10}}\int \exp(-\frac{\beta_1 y_1^2+\beta_2 y_2^2+\beta_3 y_3^2}{2})(\overline{(\vec{y}.K.\vec{y})(\vec{y}.D.\vec{y})})y_1^2 y_2^2 y_3^2 dy_1 dy_2 dy_3 \tag{G.23}$$

where $D = T^T.A.T$ and $K = T^T.B.T$ and

$$\overline{\vec{y}.D.\vec{y}} = d_{11}y_1^2 + d_{22}y_2^2 + d_{33}y_3^2, \tag{G.24}$$

$$\overline{(\vec{y}.K.\vec{y})(\vec{y}.D.\vec{y})} = \sum_{i=1}^{3} k_{ii}d_{ii}y_i^4 + \sum_{i>j}^{3}\left(k_{ii}d_{jj} + d_{ii}k_{jj} + \frac{4}{3}d_{ij}k_{ij}\right)y_i^2 y_j^2. \tag{G.25}$$

Equations (G.22, G.23) can be written in spherical coordinates, and one of the integrations can be done analytically leading to equations similar to Eq. (G.18).